On the electronic structure of layered sodium cobalt oxides

Dissertation

zur Erlangung des akademischen Grades
Doctor rerum naturalium (Dr. rer. nat.)

vorgelegt

der Fakultät Mathematik und Naturwissenschaften
der Technischen Universität Dresden

von

Thomas Kroll

geboren am 06. Februar 1976 in Münster

Dresden, im Dezember 2006

Contents

Introduction **1**

1 Experimental methods **3**
1.1 Near–edge X–ray absorption fine structure spectroscopy 4
1.1.1 Introduction 4
1.1.2 Selection rules and polarisation dependence 7
1.2 Magnetisation and transport measurements 13
1.3 High energy and resonant X–ray scattering 13
1.3.1 Elastic non-resonant scattering 14
1.3.2 Elastic resonant scattering 15

2 Some theoretical aspects **17**
2.1 Theory of atomic spectra 17
2.2 Group theory 22

3 The layered cobaltates Na_xCoO_2 and their hydrated derivatives **30**
3.1 Introduction 30
3.2 Sample preparation 35
3.3 The low doping regime (x<0.5) 37
3.3.1 Superconductivity 38
3.4 The special case x=0.5 39
3.5 The high doping nonmagnetic regime (0.5<x<0.75) 42
3.5.1 Magnetism and transport 42
3.5.2 Na ordering 44
3.6 The magnetic regime of the phase diagram (x>0.75) 45

4 Experimental results: X–ray diffraction and magnetisation **53**
4.1 High energy X–ray scattering on $Na_{0.5}CoO_2$ 53
4.2 Resonant X–ray scattering on $Na_{0.66}CoO_2$ 55
4.3 Measurements of the magnetisation and of the transport properties . 57

5 At the microscopic scale: The electronic structure of Na_xCoO_2 60
5.1 Introduction 61
5.2 Spectroscopy 66
5.2.1 X–ray photoemission spectroscopy 67
5.2.2 X–ray absorption spectroscopy 72
5.3 The electronic structure derived from cluster calculations 85
5.3.1 Method 86
5.3.2 Results 96
5.4 Electronic structure and Fermi surface topology of Na_xCoO_2 109

Summary 112

A Theoretical tools 115
A.1 The d-d interaction matrix elements 115
A.2 The hopping integrals 117
A.3 The Hamiltonian concerning d-d interaction 118
A.4 Clebsch-Gordon coefficiants 120

Bibliography 121

Introduction

The electronic properties of solid state materials do not only attract interest for technological reasons, but are also important for the fundamental research in solid state physics. For many solids, they are described by the electronic band structure. In the case of insulators and simple metals the band structure is well understood experimentally and theoretically. More interesting and therefore the object of intensive research activities these days are systems in between the limiting insulator and metal systems. As an example, in the transition metal oxides phenomena like high temperature superconductivity or phase segregation occur. For many phenomena, a situation in a crossover state of itinerant and localised electrons is achieved. The reason for that are correlation effects between the electrons that arise from Coulomb interaction, and thus the Fermi liquid approximation as it has been used successfully for some metals fails. As a consequence of these correlations some transition metal oxides have been found to be insulators although their valence band is only partially filled. The localisation of electrons may lead to local magnetic moments so that an interplay between charge mobility and magnetism becomes important. Such an interplay between charge and magnetic degrees of freedom leads to interesting phenomena such as the colossal magneto–resistance in the manganites or probably to high temperature superconductivity in the doped cuprates. Experimentally, an important tool for the investigation of the electronic structure are spectroscopic methods such as X-ray absorption spectroscopy, photoemission, optical spectroscopy and X-ray diffraction. Backed by a good theoretical description reliable results can be achieved.

In this context, the sodium cobalt oxides Na_xCoO_2 are an interesting system which is the subject of this work. Na_xCoO_2 shows many unusual properties such as an unexpectedly high thermopower accompanied by low resistivity, magnetic ordering together with itinerant electrons or superconductivity when hydrated with water at temperatures below 5 K. The discovery of superconductivity raised a broad interest in this system since it is the only $3d$ transition metal oxide that shows superconductivity beside the high temperature cuprates and the titanates. Like the high temperature cuprates, its crystal structure consists of stacked quasi two-dimensional $(Cu, Co)O_2$ planes. This analogy raised hope to learn more about the mechanism of high temperature superconductivity, especially when considering that superconductivity in Na_xCoO_2 only occurs when it is hydrated, i.e. superconductivity could in principle be switched on and off. However, it is not only the discovery of su-

perconductivity that raised research interest in this system. Some years before this discovery, the non–hydrated compound already attracted attention because of its anomalous high thermopower together with low resistivity. These unusual properties make this material a favourable candidate for technical applications in refrigeration.

As noted above, both the high T_c cuprates and the Na cobaltates consist of stacked quasi two–dimensional $(Cu, Co)O_2$ layers. In contrast to the high T_c cuprates however, the CoO_2 layers consist of edge sharing CoO_6 octahedra which are distorted lowering their symmetry from cubic to trigonal. Due to the trigonal distortion, the former threefold degenerate t_{2g} levels split into an a'_{1g} level with a $3z^2 - r^2$ like orbital oriented parallel to the c–axis and a twofold degenerate e'_g level (the prime represents the trigonal distortion).

In this work, the electronic structure of non–hydrated Na_xCoO_2 has been investigated experimentally and theoretically. Mainly X–ray absorption spectroscopy and photoemission as well as X–ray diffraction and magnetisation experiments have been performed, while the theoretical treatment involved cluster calculations seeking to explain the results of the X–ray absorption experiments.

The present thesis is organised in four chapters. The first chapter deals with an introduction to the experimental methods, especially to some selected aspects of X–ray absorption spectroscopy that are not widely discussed in textbooks. Some theoretical aspects are addressed in the second chapter, namely the theory of atomic spectra and group theory. Both are important tools for the calculation of the X–ray absorption spectra presented later. The next three chapters are devoted to the investigated system Na_xCoO_2. In the third chapter every part of the rich phase diagram will be discussed in great detail, while in chapter four some experimental results of X–ray diffraction and magnetisation measurements will be discussed. In the main and final chapter the electronic structure of Na_xCoO_2 will be treated in great detail. After an overview of the present state of research, the results of X–ray photoemission and X–ray absorption experiments are presented and discussed which provides a first picture. The deeper insight into the electronic structure, however, is achieved from the results of the cluster calculations, then following.

Chapter 1

Experimental methods

Compounds of the $3d$ transition metal elements exhibit an astonishing variety of physical properties. They range from large band gap insulators and ferroelectrics to semiconductors and metals, and even superconductors. With regard to magnetic properties, antiferromagnets, ferrimagnets and ferromagnets have been found. The reason for this wide range of properties can be found in the sensitivity of the electronic structure to the details of the crystal structure, the chemical composition and the detailed stoichiometry. A famous example for this sensitivity are the high T_c superconductors, where a small change of the electron concentration turns an antiferrmoagnetic insulator into a high temperature superconductor. Therefore, a detailed knowledge of the electronic structure and its dependence on the crystal structure, on spin and charge is crucial for the understanding of these phenomena.

The physical properties of the $3d$ system of Na cobaltates are governed by the interplay between lattice, spin, charge and orbital degrees of freedom. In particular, charge separation, lattice distortion and orbital ordering play an essential role in the understanding of the various interesting phenomena in Na_xCoO_2. In order to investigate the electronic structure, near–edge X–ray absorption fine structure (NEXAFS) and photoemission spectroscopy (XPS) are two powerful methods since they reveal important information about the d–d Coulomb interaction U, the band dispersion width W, the charge transfer energy Δ and the crystal and ligand field influence [1–8]. NEXAFS probes the unoccupied levels near the Fermi surface while photoemission excites electrons into the vacuum and thus probes the occupied states which are influenced by the local surroundings. Additionally, both methods are very "fast" experiments with an excitation time scale of the order of a few femtoseconds. This allows to distinguish between two ions with the same atomic number but different oxidation states even for a metal, which makes these methods site selective.

Therefore, the main experimental methods used during this thesis were optical spectroscopic methods, especially near edge X–ray absorption fine structure (NEXAFS) spectroscopy and X–ray photoemission spectroscopy (XPS). Both techniques are already described in detail in various works [9–11]. In this chapter, the focus will be set on two special topics in NEXAFS spectroscopy, which are not commonly

explained in the literature in detail - the polarisation dependence and the selection rules, especially for trigonally distorted systems.

First, the principle of NEXAFS and XPS will be briefly and basically described as an introduction, before the polarisation dependence and the selection rules will be discussed in detail.

1.1 Near–edge X–ray absorption fine structure spectroscopy

1.1.1 Introduction

The principle underlying NEXAFS can be explained in a few words. Basically, it is an excitation from an occupied core level into an unoccupied level close to the Fermi energy by the absorption of a photon, so that the required energies are close to the absorption edge depending on the local electronic structure. The main information gained from such an experiment is the absorption coefficient $\mu(E)$ as a function of the photon energy E close to the absorption edge (hence, the experiment probes the *near edge X–ray absorption fine structure*). $\mu(E)$ is defined by

$$I(E) = I_0 e^{-\mu(E)d}, \tag{1.1}$$

with I_0 being the intensity of the incoming light, $I(E)$ the transmitted intensity at energy E, and d being the thickness of the probed sample. The absorption coefficient $\mu(E)$ is given by Fermi's Golden Rule

$$\mu(\hbar\omega) \propto \sum_{i,f} |\langle f|H'|i\rangle|^2 \delta(E_f - E_i - \hbar\omega), \tag{1.2}$$

where $|i\rangle$ and $|f\rangle$ describe the initial and final state of the system with their energies E_i and E_f, respectively. $\hbar\omega$ is the energy of the incoming light. The electron–photon interaction is described by the Hamiltonian H' using photons with a wave vector $\mathbf{k}$:

$$H' = -i\hbar\frac{e}{c}A\sum_{j=1}^{N} e^{i\mathbf{k}\mathbf{r}_j}\mathbf{e}\nabla_j, \tag{1.3}$$

with A being the vector potential of the incoming light, $\mathbf{e}$ the unit vector of the polarisation of the photons, and $\mathbf{r_j}$ and $\mathbf{p_j} = -i\hbar\nabla_j$ being the position and momentum operators of the j–th electron. N is the number of electrons in the system.

Due to the small spatial extension of the core level wave function and the use of soft X–ray radiation, the assumption $\mathbf{k}\cdot\mathbf{r}_j \ll 1$ is valid. This allows to approximate the term $e^{i\mathbf{k}\mathbf{r}_j}$ as equal to 1:

$$\langle f|e^{i\mathbf{k}\mathbf{r}_j}\mathbf{e}\cdot\mathbf{p}|i\rangle \simeq \langle f|\mathbf{e}\cdot\mathbf{p}|i\rangle. \tag{1.4}$$

Furthermore, it is $2m\big[H_0, \mathbf{r}\big] = -i\hbar\mathbf{p}$, where H_0 describes the isolated atom. $\langle f|\mathbf{e}\cdot\mathbf{p}|i\rangle$ can be rewritten as

$$\begin{aligned}\mathbf{e}\cdot\langle f|\mathbf{p}|i\rangle &= \frac{im}{\hbar}\mathbf{e}\cdot\langle f|\big[H_0,\mathbf{r}\big]|i\rangle \\ &= im\frac{E_f^0 - E_i^0}{\hbar}\mathbf{e}\cdot\langle f|\mathbf{r}|i\rangle. \end{aligned} \tag{1.5}$$

This approximation is known as the dipole approximation and reduces the Hamiltonian H' to the dipole operator. If one additionally assumes that the absorption process does not influence the electrons that are not directly involved as well as the unoccupied states (*sudden approximation*), equation (1.2) can be reduced to

$$\mu(\hbar\omega) \propto \sum_{i,f} |\langle f|\mathbf{er}|i\rangle|^2 \delta(E_f - E_i - \hbar\omega). \tag{1.6}$$

Crucial parameters that determine the electronic structure and thus, have a great influence on the NEXAFS and XPS spectra are the d–d Coulomb interaction U_{dd}, the band dispersion width W, the charge transfer energy Δ and the crystal and ligand field influence. The charge transfer energy Δ describes a charge fluctuation between the $3d$ central ion and its ligands $d^n \rightarrow d^{n+1}\underline{L}$, where the term d^n represents a $3d$ shell with n electrons. $d^{n+1}\underline{L}$ represents a configuration with $n+1$ electrons at the $3d$ ion site and one ligand hole, the letter c denotes a core hole. The main questions one would like to answer are: how large are U_{dd}, Δ, W, and how large is

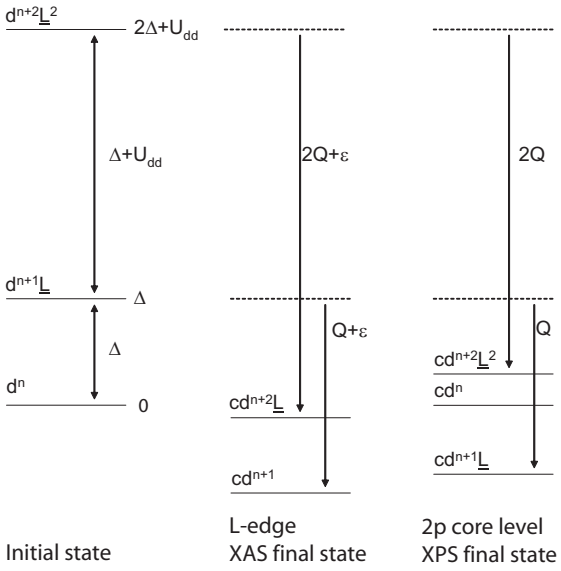

Figure 1.1: On–site energies of the bare configurations for the initial states and the final states of L–edge NEXAFS and $2p$ core level XPS. U_{dd} is the repulsive Coulomb energy between two electrons in the $3d$ shell. The charge transfer energy Δ describes the energy that costs an electron to hop from an oxygen site to the transition metal d site. Q is the Coulomb potential between an electron in the $3d$ shell and the $2p$ core hole. The ligand ionisation energy ϵ describes the energy difference between $cd^{n+1}\underline{L}$ final states in XPS and cd^{n+1} final states in NEXAFS. The horizontal dashed lines represent the energy level of the $d^{n+1}\underline{L}$ and $d^{n+2}\underline{L}^2$ initial states in the scheme for NEXAFS and XPS. The energy difference between cd^{n+1}(XAS) and $cd^{n+1}\underline{L}$(XPS) is the ligand ionisation potential ϵ. The scheme is taken from van Elp *et al* [12].

the covalency (T). In figure 1.1 the energy level diagram of the $3d$ states for the initial state and for the final states of L–edge NEXAFS and $2p$ core level XPS is shown. For the initial state only the few lowest states are important while for the final states in principal all different configurations can be reached and are therefore important. The letter c in the final state configurations represents a core hole. As it can be seen in figure 1.1, the influence of the core hole is very different for X–ray absorption and $2p$ core level photoemission. In the core hole final state in the XPS spectra, the core hole potential Q lowers the energy of the $d^{n+1}\underline{L}$ and $d^{n+2}\underline{L}^2$ states by Q and $2Q$, respectively, as compared to the d^n state. Note that the energy scale of the different columns in figure 1.1 is set in relation to each other. The energy of the d^n initial state and cd^n XPS final state is set to zero, so that the influence of the core hole potential becomes more illustrative. The NEXAFS final states energies are shifted in a very similar way. However, in the NEXAFS final states also the ligand ionisation potential ϵ has to be taken into account, which describes the energy difference between $cd^{n+1}\underline{L}$ final states in XPS and cd^{n+1} final states in NEXAFS.
If $Q > \Delta$ the first two lowest energy levels in the XPS final states are inverted compared to the initial state which results in a large satellite peak in the spectra. This is different in the NEXAFS final states, where the lowest energy levels keep their ordering.

In many publications, term symbols are used for the description of the ground or excited states, especially in the theory describing X–ray absorption and photoemission experiments. Therefore, the term symbols shall be introduced briefly. The main quantum number n is not important for the angular symmetry of a state and does not appear in the term symbol. As an example a 2–electron configuration shall be treated. The maximum orbital momentum L is equal to the sum of two individual orbital momenta, l_1 and l_2 with $L_{max} = l_1 + l_2$, $L_{min} = |l_1 - l_2|$ and $|\Delta L| = 1$. The same rules apply to the spin momentum, implying that the spin momentum of two spins can be either 1 or 0. Without spin–orbit coupling all terms are degenerate, i.e. the energy level is $(2L+1)(2S+1)$ fold degenerate. Including spin–orbit coupling the terms are split in energy according to their J value with a degeneracy $(2J+1)$, with $J_{max} = L + S$, $J_{min} = |L - S|$ and $|\Delta J| = 1$. A term symbol is written as ${}^{2S+1}X_J$, where X corresponds to a letter according to the value of L. The quantity $2S+1$ is called the spin multiplicity of the term: singlet, doublet, triplet, etc. A single s electron has an orbital moment $L = 0$, a spin moment $S = 1/2$ and a total moment $J = 1/2$ with the only term symbol ${}^2S_{1/2}$, whereas a single d electron has the term symbols ${}^2D_{3/2}$ and ${}^2D_{5/2}$. As an easy example for the absorption process, one can look at an ion like Ca^{2+} with an empty $3d$ shell in the ground state. The $2p^6 3d^0$ ground state of such an ion is ${}^1S_0$. In the final state, the electronic configuration is $2p^5 3d^1$, one hole in the $2p$ shell (${}^2P$) and one electron in the $3d$ shell (${}^2D$). In order to find the right term symbols one has to multiply ${}^2P \otimes {}^2D$. For the spin, this leads to $S = 0, 1$ and for the angular momentum it gives $L = 3, 2, 1$. In total, as the term symbols of the final state one finds ${}^1P_1$, ${}^3P_{2,1,0}$, ${}^1D_2$, ${}^3D_{3,2,1}$, ${}^1F_3$, and ${}^3F_{4,3,2}$. Since $J = 0$ in the initial state, the optical selection rule gives $J = \pm 1$, leading

to the only possible final states $^1P_1$, $^3P_1$, and $^3D_1$ that can be reached in such an experiment. Therefore, one expects a maximum of three lines that reduce to two lines with $j = 3/2$ and $j = 1/2$ for the core hole with an intensity ratio $2 : 1$ for negligible spin–orbit coupling of the d electrons as well as negligible p–d Coulomb and exchange interactions. If initial state spin–orbit coupling and electrostatic interactions between the core–hole and valence electrons are included, the intensity ratio of $I(L_3)/I(L_2)$ appears to be different from the statistical value [13, 14] and yields valuable information about these interactions and the ground state.

1.1.2 Selection rules and polarisation dependence

As described above, an excitation of a core electron into an unoccupied site follows the rules of a dipole, i.e. during such a process the excitation has to obey the *dipole selection rules*. These rules are a very powerful tool for the interpretation of NEXAFS spectra since they provide information about possible final states as well as about the polarisation dependence of the system.

The initial and final states $|i\rangle$ and $|f\rangle$ can be expressed as a product of the radial and the angular part using the quantum numbers n, l and m. Therefore, the matrix element $\langle f|\mathbf{er}|i\rangle$ can be written as

$$\begin{aligned}\langle f|\mathbf{e}\cdot\mathbf{r}|i\rangle &= \int_0^\infty r^2 dr \int d\Omega R^*_{n_f l_f} Y^*_{l_f m_f}(\theta,\phi)\mathbf{e}\cdot\mathbf{r} R_{n_i l_i} Y_{l_i m_i}(\theta,\phi) \\ &= \int_0^\infty r^2 dr R^*_{n_f l_f}\mathbf{r} R_{n_i l_i} \times \int d\Omega Y^*_{l_f m_f}(\theta,\phi)\mathbf{e} Y_{l_i m_i}(\theta,\phi).\end{aligned} \tag{1.7}$$

The radial part can be very complicated since it contains many Coulomb and exchange terms and cannot be easily predicted. Later in the text, a way of calculating the required matrix elements will be explained. At this point, one can already gain many information about the polarisation dependence from the angular part alone. The selection rules for a dipole are in principle well known [15, 16] and are thus not mentioned in most articles and textbooks about X–ray absorption spectroscopy. Therefore, just as a reminder and a tool for the arguments used below, the selection rules are briefly summarised. In spherical coordinates it is

$$\mathbf{e}\cdot\mathbf{r} = e_x \sin(\theta)\cos(\phi) + e_y \sin(\theta)\sin(\phi) + e_z \cos(\theta). \tag{1.8}$$

With the knowledge of the spherical harmonics $Y_{1,0}(\theta,\phi) = \sqrt{\frac{4\pi}{3}}\cos(\theta)$ and $Y_{1,\pm1}(\theta,\phi) = \mp\sqrt{\frac{8\pi}{3}}\sin(\theta)e^{\pm i\phi}$ one gets for equation (1.8):

$$\mathbf{e}\cdot\mathbf{r} = \sqrt{\frac{4\pi}{3}}\Big(e_z Y_{1,0} + \frac{-e_x + ie_y}{\sqrt{2}} Y_{1,1} + \frac{e_x + ie_y}{\sqrt{2}} Y_{1,-1}\Big). \tag{1.9}$$

Therefore, the angular part of equation (1.7) looks like

$$\int d\Omega Y^*_{l_f m_f}(\theta,\phi) Y_{1,m} Y_{l_i m_i}(\theta,\phi) \tag{1.10}$$

with $m = 1{,}0$, or -1. From the azimuthal integration one gets

$$\int_0^{2\pi} d\phi e^{-im_f\phi} e^{im\phi} e^{im_i\phi} = 2\pi\delta_{m=m_f-m_i}, \tag{1.11}$$

which yields the first *selection rule*

$$m_f - m_i = m = 1, 0, -1. \tag{1.12}$$

Another selection rule can be found through the integration over θ. For the integration of equation (1.10), the addition theorem of the spherical harmonics is very helpful. In general, one has [16]

$$\begin{aligned} Y_{l_1 m_1}(\theta,\phi) Y_{l_2 m_2}(\theta,\phi) &= \sum_{l=|l_1-l_2|}^{l_1+l_2} \sum_{m=-l}^{l} \sqrt{\frac{(2l_1+1)(2l_2+1)}{4\pi(2l+1)}} \langle l_1, l_2; 0, 0 | l, 0\rangle \\ &\quad \times \langle l_1, l_2; m_1, m_2 | l, m\rangle Y_{l,m}(\theta,\phi), \end{aligned} \tag{1.13}$$

where the terms $\langle l_1, l_2; m_1, m_2 | l, m\rangle$ represent the Clebsch-Gordan coefficients. $\langle l_1, l_2; 0, 0 | l, 0\rangle$ is different from zero only in the special case where $l_1 + l_2 - l$ is even. Note that the summation over m is not necessary since the only non vanishing terms belong to $m = m_1 + m_2$. Here the reader is asked to distinguish between m used in equation (1.12) and this part. Since we are interested in a case such as

$$I = \int d\Omega Y_{l_1 m_1}(\theta,\phi) Y_{l_2 m_2}(\theta,\phi) Y_{l_3 m_3}(\theta,\phi), \tag{1.14}$$

one has to insert equation (1.13) into equation (1.14), which leads to an expression such as

$$K(l, m; l_3, m_3) = \int d\Omega Y_{lm}(\theta,\phi) Y_{l_3 m_3}(\theta,\phi). \tag{1.15}$$

Due to the orthogonality of the spherical harmonics, the solution of this equation can be found as

$$K(l, m; l_3, m_3) = (-1)^m \delta_{l,l_3} delta_{m,-m_3}, \tag{1.16}$$

so that equation 1.14 can be calculated as

$$\begin{aligned} I &= \int d\Omega Y_{l_1 m_1}(\theta,\phi) Y_{l_2 m_2}(\theta,\phi) Y_{l_3 m_3}(\theta,\phi) \\ &= (-1)^{m_3} \sqrt{\frac{(2l_1+1)(2l_2+1)}{4\pi(2l_3+1)}} \times \langle l_1, l_2; 0, 0 | l_3, 0\rangle \langle l_1, l_2; m_1, m_2 | l_3, -m_3\rangle. \end{aligned} \tag{1.17}$$

This equation is different from zero, only if

- $m_1+m_2+m_3 = 0$. This relation is exactly the same result as given in equation (1.12) since $Y^*_{l,m}(\theta,\phi) = (-1)^m Y_{l,m}(\theta,\phi)$ and $m_1 = m_f$, $m_2 = m$, and $m_3 = m_i$,
- $|l_1 - l_2| \leq l_3 \leq l_1 + l_2$ and
- $l_1 + l_2 - l_3 = even$.

Adopting this general result to the special case as given in equation (1.10), one finds the dipole transition selection rules

$$\Delta l = \pm 1, \qquad \Delta m = 0, \pm 1. \tag{1.18}$$

These selection rules result as a consequence of the properties of the spherical harmonics.

Additionally, one gets the selection rule

$$\Delta S = 0, \tag{1.19}$$

if one (realistically) assumes that the only interaction of the systems is spin independent as given in equation (1.3).

Note that this result is valid only if the assumption $e^{-i\mathbf{kr}} \approx 1$ is true. Otherwise, higher orders play a role (electric quadrupole, magnetic dipole transition). In such a case, a transition like $1s \rightarrow 3d$ could be possible, even though it is very unlikely to occur in NEXAFS.

Up to now, we neglected spin–orbit coupling in the derivation of the dipole transition selection rules. In fact, the spin-orbit coupling of the $2p$ core hole in a NEXAFS experiment is rather large and cannot be neglected easily. Therefore, a j,j–representation is more appropriate to work in (c.f. Ref. [17]). If H_0 contains a spin orbit coupling term $\lambda L \cdot S$, then the eigenstates of H_0 are $|l,s;j,m_j\rangle$, with $\mathbf{j} = \mathbf{l} + \mathbf{m}$ and not $|l,s;m,m_s\rangle$. The dipole selection rules become $\Delta j = 0, \pm 1$, (except $j_i = j_f = 0$), $\Delta l = \pm 1$, and $\Delta m_j = 0, \pm 1$. The selection rules are just stated here without further explanation. They follow from the Wigner-Eckart theorem which is well explained for example in Ref. [16].

The dipole selection rules directly lead to another important point in X–ray absorption spectroscopy: the polarisation dependence. This will be shown in two examples. First, lets have a look on a transition from a p_z orbital to a $d_{3z^2-r^2}$ orbital. In spherical harmonics[1] it is $d_{3z^2-r^2} = d_{l=2,m=0}$ and $p_z = p_{1,0}$. Therefore, if the selection rule $\Delta m = 0, \pm 1$ holds, the only allowed transitions are those with $\Delta m = 0$ which corresponds only to z–polarised light (see equation (1.9)). An example that is a bit more complicated is a transition from a p_x orbital to a $d_{x^2-y^2}$ orbital. Again, first one has to know how they are expressed in spherical harmonics: $d_{x^2-y^2} = 1/\sqrt{2}(d_{2,2} + d_{2,-2})$ and $p_x = -1/\sqrt{2}(p_{1,1} - p_{1,-1})$. From a first view, only the selection rule $\Delta m = \pm 1$ holds true, which does not tell which polarisation

[1] The spherical harmonics are described by the quantum numbers l and m. Therefore, the d and p orbitals can be expressed as linear combinations of $d_{l,m}$ and $p_{l,m}$.

is needed for such a transition. But knowing that $Y_{l,-m} = (-1)^m Y^*_{l,m}$ and therefore, $\int Y^*_{1,-1} Y_{1,1} Y_{2,-2} d\Omega = \int Y^*_{1,1} Y_{1,-1} Y_{2,2} d\Omega$, it follows that such a transition is only allowed for light polarised along the ϵ_y direction and is forbidden for ϵ_x and ϵ_z.

A picture that is a bit more descriptive concerns the parity of the orbital functions. Taking the same examples as above, one first notes that the intensity is given as the square of the integral 1.10. Since the integral over an odd function is zero, one can only detect an intensity if the integrand is even. For the first transition from p_z to $d_{3z^2-r^2}$ using z–polarised light, one finds that $d_{3z^2-r^2}$ is even in z, z is odd in z and p_z is again odd in z. In total, the whole function is even and therefore such a transition is allowed. For x– and y–polarised light, the integrand becomes odd and therefore the intensity is zero. The same can be done for the second example for a transition from $d_{x^2-y^2}$ to p_x. For x–polarised light, $d_{x^2-y^2}$ is even in x, x is odd in x and p_x is again odd in x, in total the whole function is even in x so that intensity can be detected.

With the help of the description given above, one can calculate all matrix elements for different transitions. In the following, all transitions which lead to an intensity different from zero are listed for light polarised parallel x, y, and z.

$$\begin{aligned}
\langle p_x|y|d_{xy}\rangle &= \frac{1}{\sqrt{5}} & \langle p_x|x|d_{x^2-y^2}\rangle &= \tfrac{1}{\sqrt{5}} \\
\langle p_x|z|d_{zx}\rangle &= \frac{1}{\sqrt{5}} & \langle p_y|y|d_{x^2-y^2}\rangle &= \tfrac{1}{\sqrt{5}} \\
\langle p_y|x|d_{xy}\rangle &= \frac{1}{\sqrt{5}} & \langle p_x|x|d_{3z^2-r^2}\rangle &= -\tfrac{1}{\sqrt{15}} \\
\langle p_y|z|d_{yz}\rangle &= \frac{1}{\sqrt{5}} & \langle p_y|y|d_{3z^2-r^2}\rangle &= \tfrac{1}{\sqrt{15}} \\
\langle p_z|x|d_{zx}\rangle &= \frac{1}{\sqrt{5}} & \langle p_z|z|d_{3z^2-r^2}\rangle &= \tfrac{2}{\sqrt{15}} \\
\langle p_z|y|d_{yz}\rangle &= \frac{1}{\sqrt{5}}
\end{aligned} \tag{1.20}$$

In the case of a cubic crystal field, the formerly degenerate $3d$ states split into lower lying 3–fold degenerate states with t_{2g} symmetry and higher lying 2–fold degenerate states with e_g symmetry. Note that there is no polarisation dependence observable, as long as the t_{2g} and e_g states are degenerate (as they are for cubic symmetry). This partially changes when the symmetry is lowered. In tetragonal symmetry, the t_{2g} and e_g states are not degenerate anymore, but split into states with b_1, a_1, b_2, and e symmetry (see figure 1.2). For the nomenclature of the b_1, a_1, b_2, and e states see section 2.2 about group theory. These irreducible representations are typified by the orbitals $3d_{x^2-y^2}$, $3d_{3z^2-r^2}$, $3d_{xy}$, and $3d_{yz,zx}$, respectively. If, for example, the ligands are octahedrally arranged around a central ion and if the octahedron is elongated along the z axis, then the energy states split in such a way that the d_{yz} and d_{zx} orbitals are in fact still degenerate, but lower in energy than the d_{xy}

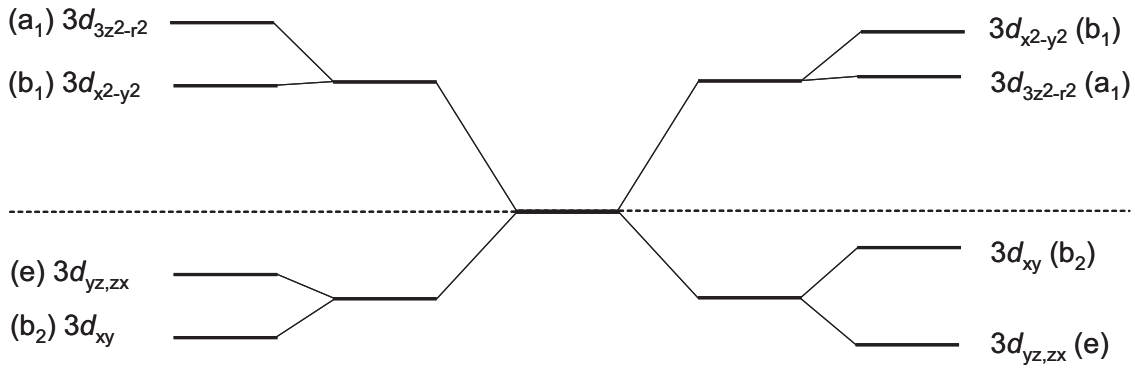

Figure 1.2: Diagram of the energy splitting for a tetragonal distortion (D_{4h} symmetry group) for a pressed (left) and elongated (right) octahedron. a_1, b_1 etc. denote the symmetry of the subspaces. The deeper meaning of these symmetry symbols is given in the chapter dealing with group theory (see chapter 2.2).

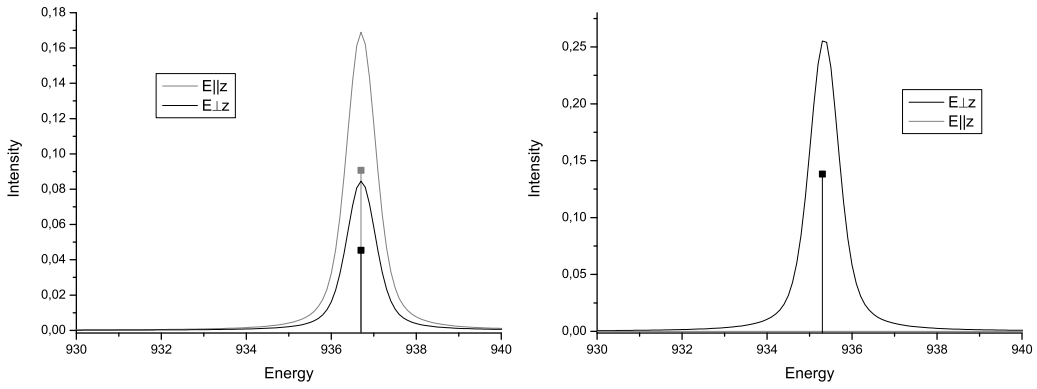

Figure 1.3: Calculations of the NEXAFS spectra of the Cu^{2+} L_3–edge as a d^9 system in tetragonal symmetry for a compressed (left) and an elongated (right) octahedron.

orbital. Also, the $d_{x^2-y^2}$ and $d_{3z^2-r^2}$ split with the latter one being higher in energy (figure 1.2). Therefore, due to the loss of degeneracy a polarisation dependence can occur. Here, the easiest example is a d^9 central ion with all but one states occupied. Depending on the distortion (elongation or compression) either a site in a $3d_{x^2-y^2}$ or a $3d_{3z^2-r^2}$ orbital is unoccupied. With z–polarised light one cannot reach a $3d_{x^2-y^2}$ orbital and therefore for an elongated octahedron with a d^9 central ion one expects an intensity only for polarisation along x and y. For the other case (compressed octahedron, $3d_{3z^2-r^2}$ orbital), one expects a two times larger intensity for z–polarised light than for light polarised perpendicular to z. This example is shown in figure 1.3 for the Cu L_3–edge, where spectra of a Cu^{2+} ion in a tetragonal environment (D_{4d} symmetry group) have been calculated for the two cases of an elongated and a compressed octahedron by atomic multiplet calculations [18]. One

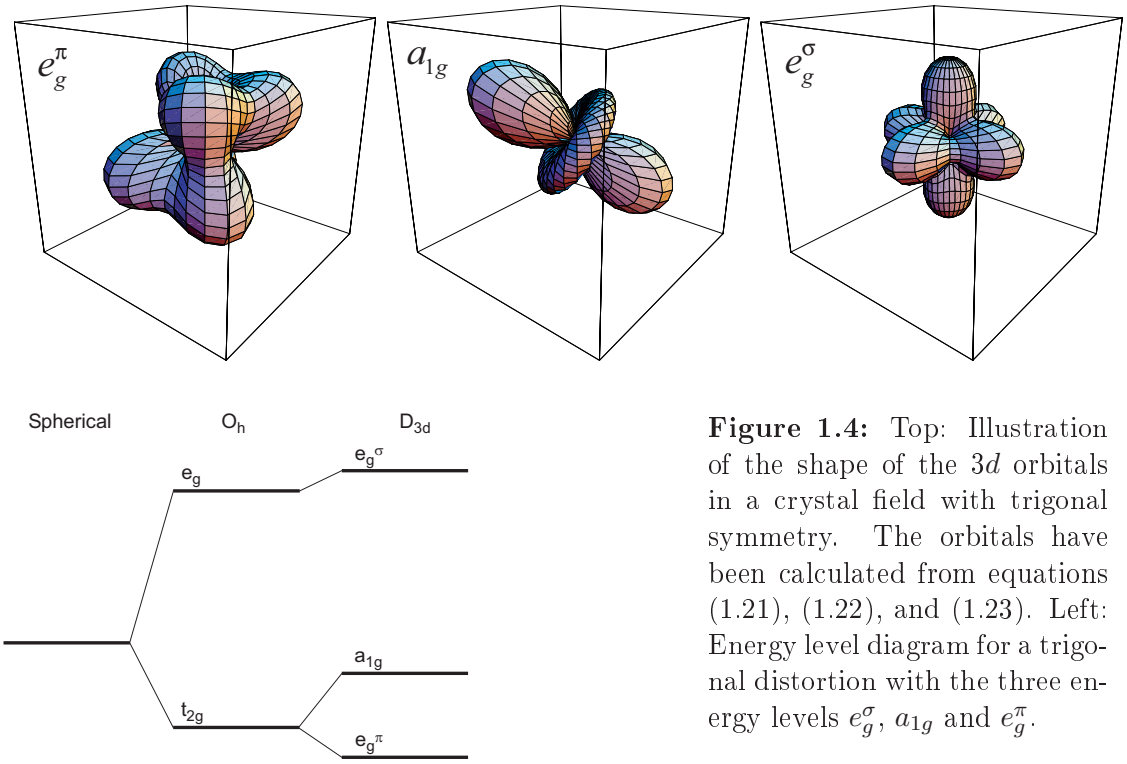

Figure 1.4: Top: Illustration of the shape of the $3d$ orbitals in a crystal field with trigonal symmetry. The orbitals have been calculated from equations (1.21), (1.22), and (1.23). Left: Energy level diagram for a trigonal distortion with the three energy levels e_g^σ, a_{1g} and e_g^π.

easily recognises the two different polarisation dependencies. Experimentally, such a behaviour has been measured by Chen *et al.* on $La_{1.85}Sr_{0.15}CuO_4$ [19]. This high T_c superconductor has a CuO plane, where the valence of the Cu is d^9 and the only hole site is in the $d_{x^2-y^2}$ orbital, similar to the example given above.

The system Na_xCoO_2 which has been investigated in this work contains CoO_6 octahedra which are trigonally distorted. Under trigonal symmetry (D_{3d} symmetry group) the t_{2g} states split into states with e_g^π and a_{1g} symmetry, which can be represented as

$$|e_{g\pm}^\pi\rangle = \mp\frac{1}{\sqrt{3}}\big(|xy\rangle + exp^{\pm i2\pi/3}|yz\rangle + exp^{\pm i4\pi/3}|zx\rangle\big) \quad \text{and} \tag{1.21}$$

$$|a_{1g}\rangle = \frac{1}{\sqrt{3}}\big(|xy\rangle + |yz\rangle + |zx\rangle\big). \tag{1.22}$$

The cubic e_g states remain degenerate and will be named e_g^σ in the following in order to avoid confusion. The superscripts π and σ are motivated by the kind of their binding to the ligand oxygen states. For trigonal symmetry, the degenerate e_g^σ states can be written as

$$|e_{g\pm}^\sigma\rangle = \mp\frac{1}{\sqrt{2}}\big(|3z^2 - r^2\rangle \pm i|x^2 - r^2\rangle\big). \tag{1.23}$$

In figure 1.4 the resulting orbitals are illustrated. It is seen that the $e_{g\pm}^\pi$ and $e_{g\pm}^\sigma$ orbitals are highly symmetric whereas the a_{1g} orbital looks like a $3z^2-r^2$ orbital but is rotated towards the (1 1 1) direction. Thus, for trigonal symmetry one expects only a strong polarisation dependence for excitations into unoccupied states with an

a_{1g} symmetry. When the example given above with a d^9 central ion in a tetragonal symmetry environment is applied to trigonal symmetry, then, different from the tetragonal case, no strong polarisation dependence will be expected for any trigonal distortion. Here, an interesting example is the polarisation dependence of a d^5 configuration in high and low spin states, respectively. For weak crystal fields, Hund's exchange energy (J_H) is comparably strong and therefore the system will be in a high spin state with $S = 5/2$. For crystal fields of about 3 eV this situation changes and the system reorganises its spin state to a low one with $S = 1/2$. In the latter case, one main peak is expected for excitations into e_g^σ levels and a weaker peak at lower energies for excitations into a_{1g} levels, whereas the high spin case allows all different excitation levels and therefore should show more than two peaks in its spectrum.

1.2 Magnetisation and transport measurements

In this work, not only spectroscopic methods were used, but also some magnetisation and transport measurements will be presented. Obviously, these measurements are not the main part of this thesis and therefore should be addressed only briefly. Measurements of the magnetisation have been either carried out in a Quantum Design MPMS system (SQUID) or in a home–made vibrating sample magnetometer which allows measurements in external magnetic fields up to 15 T [20]. The underlying principle of this instrument is to move the (magnetic) sample in an external field. The magnetic sample vibrates in the center of a pair of coils, which induces a periodical modulated voltage in these coils. The induced signal is proportional to the (known) frequency and amplitude of the movement of the sample as well as to its magnetic moment. A very detailed description of this magnetometer can be found in the doctoral thesis of Markus Hücker [20], but also (less detailed) in some other doctoral and Diploma theses (c.f. [21, 22]). Measurements of the specific heat were carried out in a Quantum Design PPMS system.

1.3 High energy and resonant X–ray scattering

Beside spectroscopic methods and magnetisation and transport measurements, high energy and resonant X–ray scattering has been applied in this work. The high energy X–ray scattering experiments were performed at the BW5 beamline at HASYLAB at DESY, Hamburg, on a triple–crystal diffractometer for high energy X–ray scattering together with J. Geck, and with M. v. Zimmermann as the beamline scientist (a detailed experimetal setup is described in the literature [23]). The resonant X–ray experiments were performed at the Mags7 beamline at Bessy II, Berlin, together with J. Geck, and with R. Feyerherm as the beamline scientist.

In the following, a short introduction to the theory of scattering and its advantages will be given. It is the aim of this section to provide the reader with the basic

knowledge of X–ray scattering so that he or she can easily follow the discussion of the data given below and understand the arguments. Since this work is not primarily dealing with X–ray scattering, a full and advanced description of this powerful method is beyond the scope of the thesis. For a deeper insight some textbooks and doctoral theses are recommended (c.f. [24–28]).

1.3.1 Elastic non-resonant scattering

Under the influence of the electromagnetic field of the incoming wave the electrons of the ions inside a crystal start to vibrate and emit light of the same frequency. These rays interfere with each other, leading to an intensity pattern that depends on the structure of the crystal. The most general description of the interference while assuming translational symmetry, is the Bragg equation

$$n\lambda = 2d\sin\theta, \tag{1.24}$$

where the difference in path length between beams scattered by two adjacent lattice planes with distance d has to be a multiple n of the wavelength λ, 2θ is the scattering angle, i.e. the angle between the incoming and outgoing beam. In order to describe the reciprocal space, the Miller indices h, k, l have been introduced that describe the coordinates of points in the reciprocal space. The distance d between two adjacent planes in the real space is connected to the Miller indices; the easiest example is a system with cubic symmetry so that

$$\frac{1}{d_{hkl}^2} = \frac{h^2 + l^2 + k^2}{a^2}, \tag{1.25}$$

where a is the lattice parameter in real space.
Since the incoming light is scattered by the electrons in the crystal, the measured intensity of a given reflection (h k l) depends on the electron density distribution. Its Fourier transform yields the structure factor which represents the total of a scattered wave corresponding to a given (h k l) reflection:

$$F_{hkl} = \int_0^a \int_0^b \int_0^c \rho(x,y,z) \exp\big[-2\pi i\big(\frac{hx}{a} + \frac{hy}{b} + \frac{hz}{c}\big)\big]\,dx\,dy\,dz. \tag{1.26}$$

In practice, this equation is difficult to solve. Therefore, an approximation is applied, in which the atoms in the unit cell are treated as point charges to which specific atomic scattering factors f are attached. This reduces the equation above to

$$F_{hkl} = \sum_j^N f_j \exp\big[-2\pi i\big(hx_j + ky_j + lz_j\big)\big]. \tag{1.27}$$

The measured intensity is proportional to the square of the structure factor:

$$I_{hkl} \propto |F_{hkl}|^2. \tag{1.28}$$

The intensities of the measured reflections depend on the crystal structure. This is best illustrated by way of an easy example like a system having only one kind of atom in a body centered cubic structure. In this structure atoms with the same scattering factor f are located at two positions: $r_1 = (0, 0, 0)$ and $r_2 = (1/2, 1/2, 1/2)$. Equation (1.27) then becomes

$$F_{hkl} = f(1 + e^{-i\pi(h+k+l)}) = \begin{cases} 0 & \text{for } h+k+l = \text{odd} \\ 2\pi & \text{for } h+k+l = \text{even} \end{cases} \tag{1.29}$$

Consequently, systematic reflections with zero intensity called "forbidden" reflections are generated.

In general, forbidden reflections become important when the structure changes due to variations of the external conditions such as temperature and pressure. In this work, X–ray scattering was used mainly to investigate ordering effects as a function of temperature. The idea behind the method is very simple. Let us assume that only one atomic species is involved and that there are two symmetrically non-equivalent sites that the atoms can occupy. At high temperatures, these sites are randomly occupied leading to a structure characterised by allowed and forbidden reflections. At decreasing temperatures these atoms start to order in such a way that one site is energetically preferred over the other. This leads to a change in the structure and a different (larger) unit cell. However, since the same indexing scheme is used for the high and low temperature structures, formerly forbidden reflections begin to show up which is a strong evidence for ordering effects. From a collection of formerly forbidden reflections one can estimate the kind of the ordering pattern.
For such investigations high energy X–rays (∼100 keV) are advantageous since there the penetration depth is very large so that true bulk properties can be measured. In addition, there will be no absorption and extinction effects.

1.3.2 Elastic resonant scattering

As mentioned earlier, the structure factor and thus the reflection intensity depend on the electron density. In the investigated system Na_xCoO_2 the Na sites are only partially occupied possibly leading to ordering effects whereas the Co and O sites are fixed and therefore cannot contribute to the ordering reaction. However, because the valence of the Co ions is either 4+ or 3+, charge order may occur. Such an ordering in which effectively only one electron is involved, is easily screened by Na ordering and is therefore difficult to observe. The main trick to verify charge ordering is to tune the energy of the incoming X–ray beam to a resonance energy of the ion in question, e.g. cobalt at the Co K–edge at about 7710 eV. Due to resonance at the Co K–edge an electron is excited from an $1s$ core level to an unoccupied $4p$ state. In a charge ordered phase, the valence state of different ions varies. This may lead to different resonance energies and polarisation dependencies as well as to to form factors that depend on the valency. Therefore, resonant X–ray scattering is very sensitive to charge, spin, and orbital ordering. Again, the most interesting reflections

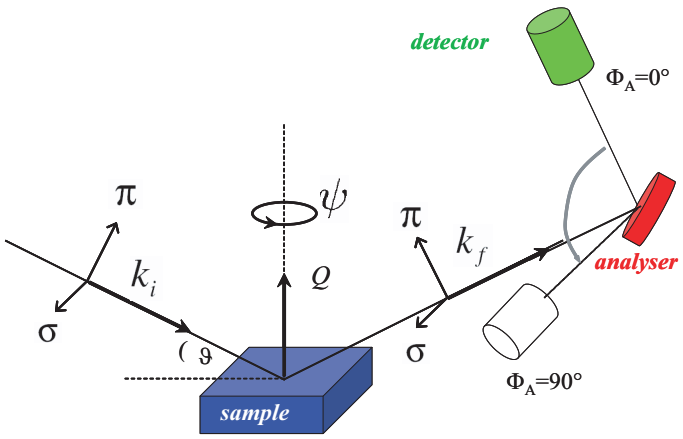

Figure 1.5: Sketch of the geometry in a resonant X–ray scattering experiment. σ and π denote the polarisation of the incident and outgoing light wave, k_i and k_f are the initial and final wave vectors, ϑ is the scattering angle. The analyzer can be changed from detection of π polarised light ($\Phi_A = 0°$) to σ polarised light ($\Phi_A = 90°$). Figure taken from Ref. [27].

are the ones that are forbidden by symmetry when the energy of the incident photons is tuned through the Co K–edge. In the scattering process for energies off the resonance, the particles (electrons) are accelerated by the incident wave and therefore start to emit radiation so that the wave is scattered (Thomson scattering). The particle moves in the direction of the oscillating electric field of the incoming light wave, resulting in electromagnetic dipole radiation. In the non–relativistic case, the moving particle radiates most strongly in a direction perpendicular to its motion. Therefore, the light scattered from a small volume element will be more or less polarised. In figure 1.5 the scattering process is illustrated. If the incoming light is σ polarised (as it was during the experiment), the outgoing light should be π polarised due to Thomson scattering. The analyzer can be switched between detection of π and σ polarised light. If the energy of the incoming beam is set to the resonance, the absorption process takes place, too. Since the $1s$ orbital has a spherical shape, its electrons can be equally excited for any polarisation. In the $4p$ final state, the electrons can be excited into the p_x, p_y, and p_z orbitals, obeying the selection rules (see the first section). Therefore, in resonant scattering the omitted light is mainly σ polarised. This fact reduces the ions that are involved in the scattering process to only one species, namely the one which is involved in the absorption process (i.e. the transition metal ion) so that its charge, spin and/or orbital ordering can be investigated.

Chapter 2

Some theoretical aspects

In this chapter a short introduction to some theoretical methods applied in this work will be given. This helps to better understand the methods and tricks used in the calculation of X–ray absorption and photoemission spectra explained later in the text. The theory of atomic spectra plays an important role in the calculation of the energies of different electronic configurations and in the understanding of the origin of multiplet splitting due to Coulomb interactions between two electrons (or holes). The theory of symmetry as outlined in section 2.2 is of great help when in chapter 5.3 the various basis functions are constructed and the spectra are calculated.

2.1 Theory of atomic spectra

The theoretical description of experimental spectra also requires a basic knowledge of the internal interactions in the electronic configuration. An important part in this field is played by the Coulomb and exchange interactions between the outer electrons (holes) which lead to the well known multiplet structure in optical spectra. In this chapter, these interactions as well as their calculation and also the calculation of energy levels will be shortly explained as they become necessary for the calculation of X–ray absorption spectra as explained later on. For a deeper insight into this huge and interesting field the books by E.U. Condon and G.H. Shortely [29], W.A. Harrison [30], C.L. Ballhausen [31], or J.W. Negele and H. Orland [32] are recommended.

Evaluation of the matrix elements $\langle \mathbf{ab}|\frac{\mathbf{1}}{\mathbf{r}}|\mathbf{cd}\rangle$

Not considering the Coulomb and exchange interactions all d orbitals have the same energy. The Coulomb repulsion $\mathrm{g(i,j)} = \sum_{\mathrm{i>j}}(\mathrm{e}^2/\mathrm{r_{ij}})$ with $r_{ij} = |r_i - r_j|$ destroys the degeneracy. This interaction thus is responsible for the separation of different groups of multiplets in the spectrum of an ion. The main task now is the calculation of the matrix elements $\langle ab|\frac{e^2}{r_{12}}|cd\rangle$ between two electrons (or holes) 1 and 2 in the

m_l	m'_l	$k=0$	$k=2$	$k=4$	m_l	m'_l	$k=0$	$k=2$	$k=4$
±2	±2	$+1$	$-\frac{\sqrt{4}}{7}$	$+\frac{1}{21}$	0	0	$+1$	$+\frac{\sqrt{4}}{7}$	$+\frac{\sqrt{36}}{21}$
±2	±1	0	$+\frac{\sqrt{6}}{7}$	$-\frac{\sqrt{5}}{21}$	±2	∓2	0	0	$+\frac{\sqrt{70}}{21}$
±2	0	0	$-\frac{\sqrt{4}}{7}$	$+\frac{\sqrt{15}}{21}$	±2	∓1	0	0	$-\frac{\sqrt{35}}{21}$
±1	±1	$+1$	$+\frac{1}{7}$	$-\frac{\sqrt{16}}{21}$	±1	∓1	0	$-\frac{\sqrt{6}}{7}$	$-\frac{\sqrt{40}}{21}$
±1	0	0	$+\frac{1}{7}$	$+\frac{\sqrt{30}}{21}$					

$\lvert m_l\rvert$	$\lvert m'_l\rvert$	$k=2$	$k=4$
2	2	$\frac{4}{49}$	$\frac{1}{441}$
2	1	$-\frac{2}{49}$	$-\frac{4}{441}$
2	0	$-\frac{4}{49}$	$\frac{6}{441}$
1	1	$\frac{1}{49}$	$\frac{16}{441}$
1	0	$\frac{2}{49}$	$-\frac{24}{441}$
0	0	$\frac{4}{49}$	$\frac{36}{441}$

Table 2.1: Top: Values of c^k for $l = l' = 2$. A complete list for $l = 0...3$ is given in the book of J.C. Slater [33]. Left: Values of $a^k(nm_l, l'm'_l) = a^k(l'm'_l, nm_l)$ for $l = l' = 2$, and $k = 2$ and $k = 4$.

orbitals a, b, c, or d (a and b in the state ab, and c and d in the state cd):

$$\langle ab|\frac{1}{r_{12}}|cd\rangle = \int\int a^*(1)b^*(2)\,\frac{e^2}{r_{12}}\,d(2)c(1)d\tau_1 d\tau_2 \tag{2.1}$$

with the single electron wave function $a(i) = R_{nl}(r_i)Y_l^{m_l}(\theta_i,\phi_i)$ as for the hydrogen–like atom. $Y_l^{m_l}(\theta_i,\phi_i)$ is a normalised spherical harmonic, and $d\tau = r\sin\theta d\theta d\phi$ is the space element. Expanding $\frac{1}{r_{12}}$ in spherical harmonics and using $Y_l^m = P_l^m(\cos(\theta))\frac{1}{\sqrt{2\pi}}e^{im\phi}$, where $P_l^m(\cos(\theta))$ is a normalised Legendre function, yields

$$\begin{aligned}\langle ab|\frac{1}{r_{12}}|cd\rangle &= \delta(m_s^a,m_s^c)\delta(m_s^b,m_s^d)\delta(m_l^a+m_l^b,m_l^c+m_l^d)\\ &\quad\times\sum_{k=0}^{\infty}c^k(l^am_l^a,l^cm_l^c)c^k(l^dm_l^d,l^bm_l^b)\cdot R^k(abcd).\end{aligned} \tag{2.2}$$

$c^k(lm_l,l'm'_l)$ and $R^k(abcd)$ can be calculated from the following expressions,

$$\begin{aligned}c^k(lm_l,l'm'_l) &= \sqrt{\frac{2}{2k+1}}\int_0^\pi P_k^{m_l-m'_l}(\cos\theta)P_l^{m_l}(\cos\theta)P_{l'}^{m'_l}(\cos\theta)\sin\theta d\theta\\ R^k(abcd) &= e^2\int_0^\infty\int_0^\infty\frac{r_<^k}{r_>^{k+1}}R_1(a)R_2(b)R_1(c)R_2(d)r_1^2r_2^2dr_1dr_2,\end{aligned} \tag{2.3}$$

with $r_<$ being the smaller and $r_>$ being the larger of r_1 and r_2. Note that $c^k(lm_l,l'm'_l) = 0$ if either $k > l+l'$ or if k is odd for $l = l'$ as for $d-d$ interaction. In Table 2.1 the resulting values for c^k are listed for $l = l' = 2$. Therefrom the Coulomb integral J

Slater–Condon	Normalised	Racah
F^0	$F_0 = F^0$	$A = F_0 - 49F_4$
F^2	$F_2 = F^2/49$	$B = F_2 - 5F_4$
F^4	$F_4 = F^4/441$	$C = 35F_4$
$F^0 = 8.0$	$F_0 = 8.0$	$A = 7.3$
$F^2 = 10.0$	$F_2 = 0.21$	$B = 0.13$
$F^4 = 6.2$	$F_4 = 0.014$	$C = 0.49$

Table 2.2: A comparison of the Slater–Condon parameters F^k with the normalised Slater–Condon parameters F_k and the Racah parameters. Numbers are in eV.

and and the exchange integral K are defined as

$$\begin{aligned} J(a,b) &= \langle ab|\frac{1}{r_{12}}|ab\rangle \\ K(a,b) &= \langle ab|\frac{1}{r_{12}}|ba\rangle. \end{aligned} \tag{2.4}$$

Further definitions include

$$\begin{aligned} a^k(l^a m_l^a, l^b m_l^b) &= c^k(l^a m_l^a, l^a m_l^a) c^k(l^b m_l^b, l^b m_l^b) \\ b^k(l^a m_l^a, l^b m_l^b) &= \left[c^k(l^a m_l^a, l^b m_l^b)\right]^2. \end{aligned} \tag{2.5}$$

For equivalent electrons it is

$$\begin{aligned} F^k &= R^k(n^a l^a n^b l^b, n^a l^a n^b l^b) \text{ and} \\ G^k &= R^k(n^a l^a n^b l^b, n^b l^b n^a l^a). \end{aligned} \tag{2.6}$$

Sometimes normalised values are used for F^k in such a way that $F_k = F^k/D_k$, where D_k is the denominator of the corresponding a's and b's, for example $F_2 = F^2/49$ or $F_4 = F^4/441$. They are called the Slater–Condon parameters. It turns out that F_2 and F_4 are hardly screened and therefore differ only slightly from the values of the free ion. Additionally, the Slater–Condon parameters have approximately a constant ratio: $F^4 \approx 0.62F^2$ or $F_4 \approx 0.07F_2$.
In some publications the so–called Racah parameters are used. They have a fixed relation to the Slater–Condon parameters. In table 2.1 the Slater–Condon, the normalised Slater–Condon, and the Racah parameters are listed. The value $F_0 = 8.0\,\text{eV}$ is just an example, whereas F_2 and F_4 are real values.

When a formerly free ion is incorporated into a crystal, it is not 'free' any more, but feels the influence of the surrounding ligands. Therefore, the Hamiltonian describing such an anion has to be expanded as

$$\mathcal{H} = \mathcal{H}_f + \mathcal{V}, \tag{2.7}$$

where $\mathcal{H}_f$ describes the free ion and $\mathcal{V}$ the potential provided by the ligands. It perturbs the eigenvalues of the free ion. The first question arising from equation

(2.7) is how $\mathcal{V}$ compares to the two other perturbing quantities in the Hamiltonian of the free ion, namely the electron repulsion $\sum e^2/r_{ij}$ and the spin–orbit coupling term $\sum \xi(r)_i \mathbf{l} \cdot \mathbf{s}$. Here, three cases can be realised:

$$\begin{aligned} (i) \qquad & \mathcal{V} < \xi(r)\mathbf{l} \cdot \mathbf{s} \\ (ii) \qquad & \xi(r)\mathbf{l} \cdot \mathbf{s} < \mathcal{V} < \frac{e^2}{r_{ij}} \\ (iii) \qquad & \mathcal{V} > \frac{e^2}{r_{ij}} \end{aligned} \tag{2.8}$$

In the literature the second case is called 'weak crystalline field case' and the third case 'strong crystalline field case'. Analytically, there is a smooth crossover between the three cases, the difference between them is mainly a different choice of the starting point. The complexes of the rare earth elements are found in case (i), while the complexes of the first transition group are found between case (ii) and (iii). The complexes of the second and third transition series are approximated best as 'covalent' complexes, i.e. case (iii).

Obviously the symmetry of $\mathcal{V}$ plays an important role since $\mathcal{V}$ must transform as the representations in the symmetry group of the complex (c.f. section 2.2). This follows to the fact, that the Hamiltonian for the system must remain invariant under all symmetry operations.

The $3d$ transition metal complexes of the Na_xCoO_2 system are known for their strong crystalline fields. Therefore, the calculations of the spectra of the system Na_xCoO_2 presented later correspond to an intermediate case between the second and third cases. In the strong field case, the crystalline field splitting parameter Dq is large enough to cause the orbital motion of the electrons to be determined by the lattice site symmetry rather than by the interactions between the electrons. In simple words, the crystal field wins over Hund's rule. In a cubic field, first, the lower lying t_{2g} states (for electrons) will be filled and only then the higher lying e_g levels will be occupied. The Coulomb repulsions are responsible for the separations of the different groups of multiplets in the spectrum of the free ion. In order to calculate the energies one simply has to count the number of electrons in the t_{2g} and e_g orbitals with $E(t_{2g}) = -4Dq$ and $E(e_g) = 6Dq$ and needs to know the Coulomb (J) and exchange (K) integrals using the orbitals of the t_{2g} and e_g states as a basis.

In order to explain how to calculate the Coulomb and exchange integrals, two examples (one for each integral) will be given.
From group theoretical considerations it is known that there are two irreducible representations e_g (two dimensional) and t_{2g} (three dimensional) in the O_h symmetry group, so that there are five linear combinations of the d orbitals in the group O_h.

	a	b	c	d	$\langle ab\|1/r_{12}\|cd\rangle$
$J(z^2, z^2)$	z^2	z^2	z^2	z^2	$F_0 + 4F_2 + 36F_4 = U_{dd}$
$J(x^2-y^2, x^2-y^2)$	x^2-y^2	x^2-y^2	x^2-y^2	x^2-y^2	$F_0 + 4F_2 + 36F_4 = U_{dd}$
$J(xy, xy)$	xy	xy	xy	xy	$F_0 + 4F_2 + 36F_4 = U_{dd}$
$J(zx, zx)$	zx	zx	zx	zx	$F_0 + 4F_2 + 36F_4 = U_{dd}$
$J(yz, yz)$	yz	yz	yz	yz	$F_0 + 4F_2 + 36F_4 = U_{dd}$
$K(xy, yz)$	xy	yz	yz	xy	$3F_2 + 20F_4 = J_H(t_{2g})$
$K(xy, zx)$	xy	zx	zx	xy	$3F_2 + 20F_4 = J_H(t_{2g})$
$K(zx, yz)$	zx	yz	yz	zx	$3F_2 + 20F_4 = J_H(t_{2g})$
$K(z^2, x^2-y^2)$	z^2	x^2-y^2	x^2-y^2	z^2	$4F_2 + 15F_4 = J_H(e_g)$

Table 2.3: Examples of the matrix elements $\langle ab|\frac{1}{r_{12}}|cd\rangle$ different from zero. Only the values of the t_{2g} and e_g on–site Coulomb energy U_{dd} and the Hund energy J_H are given. A complete list of all $3d$ interactions is given in appendix A.1.

For $l = 2$ they are

$$\begin{aligned}
d_{x^2-y^2} &= \frac{1}{\sqrt{2}}(d_2 + d_{-2}) = \frac{\sqrt{3}}{2}(x^2 - y^2) \\
d_{3z^2-r^2} &= d_0 = \frac{1}{2}(3z^2 - r^2) \\
d_{xy} &= \frac{1}{i\sqrt{2}}(d_2 - d_{-2}) = \sqrt{3}(xy) \\
d_{yz} &= -\frac{1}{i\sqrt{2}}(d_1 + d_{-1}) = \sqrt{3}(yz) \\
d_{zx} &= -\frac{1}{\sqrt{2}}(d_1 - d_{-1}) = \sqrt{3}(zx)
\end{aligned} \tag{2.9}$$

Note that the e_g and t_{2g} orbitals are real by taking linear combinations of d_m and d_{-m}. With these equations, equation (2.2), table 2.1, and normalised F_k's one can calculate for example $J(zx, yz)$ and $K(zx, yz)$ as:

$$\begin{aligned}
J(zx, yz) &= \langle zx, yz|\frac{1}{r}|zx, yz\rangle \\
&= \int (zx)^*(1)(yz)^*(2)\frac{1}{r}(zx)(1)(yz)(2)d\tau \\
&= \frac{1}{4}\int (d_1 - d_{-1})^*(1)(d_1 + d_{-1})^*(2)\frac{1}{r}(d_1 - d_{-1})(1)(d_1 + d_{-1})(2)d\tau \\
&= F_0 - 2F_2 - 4F_4 \qquad \text{and}
\end{aligned} \tag{2.10}$$

$$\begin{aligned} K(zx,yz) &= \langle zx,yz|\frac{1}{r}|yz,zx\rangle \\ &= \int (zx)^*(1)(yz)^*(2)\frac{1}{r}(yz)(1)(zx)(2)d\tau \\ &= \frac{1}{4}\int (d_1-d_{-1})^*(1)(d_1+d_{-1})^*(2)\frac{1}{r}(d_1+d_{-1})(1)(d_1-d_{-1})(2)d\tau \\ &= 3F_2+20F_4 \end{aligned} \tag{2.11}$$

In this way all matrix elements can be calculated. In table 2.3 examples of the matrix elements $\langle ab|\frac{1}{r_{12}}|cd\rangle$ different from zero are given for the t_{2g} and e_g on–site Coulomb energy U_{dd} and the Hund energy J_H. In appendix A.1 a complete list for all integrals between d–d electrons (holes) can be found.

2.2 Group theory

Group theory is an important tool in ligand field theory and simplifies the calculations dramatically. Even though there are lots of good textbooks dealing with group theory, for reasons of completeness a short introduction to this topic is given here. It will help the reader to understand the arguments used later in chapter 5.3. For a deeper insight into group theory the books from Landau and Lifshitz (Ref. [34]), Cornwell (Ref. [35]) or Tinkham (Ref. [36]) are recommended. All proofs of the theorems given below can be found in these references.

In this section, important definitions and terms are given and explained, followed by an introduction into the concept of representations of groups. After general remarks, an example for D_4 symmetry will be presented to clarify what will have been explained. In order to find the correct basis functions of a system, the main role is played by the projection operators that are explained next, followed by the multiplication tables used for the combination of states in different symmetries.

Introduction

Group theory provides the mathematical framework that allows to dead with symmetry properties of systems. The main goal of group theory in X–ray absorption spectroscopy is a systematic method to classify the ground, intermediate and final states within a certain symmetry.

A group is defined as a set of elements that satisfy four requirements:

- A group is closed, i.e. the product of two elements of a group is also an element of this group.

- Multiplication is associative, i.e. the product of three elements e_1, e_2 and e_3 leads to the same result wether the calculation is carried out as $(e_1e_2)e_3$ or $e_1(e_2e_3)$. Note that a commutative multiplication $e_1e_2 = e_2e_1$ only exists in Abelian groups.
- There is a unit element, i.e. a unit element multiplied with any element yields that element again.
- There is an inverse element, i.e. the inverse element multiplied with its corresponding element yields the unit element.

Typically, the elements contained in point groups like O_h, D_{4h}, or D_{3d} are the relevant symmetry operations of the object under study such as the identity operation E, rotations C, for example a C_{2z} operation that represents a two-fold rotation (180 degrees) around the z-axis , inversion in the center of symmetry I, reflections σ, and rotary reflections S. The total number of elements in a group is called its *order*. Two elements A and B are said to be conjugate if

$$A = CBC^{-1}$$

where C is also an element of the group. From this it follows that $B = C^{-1}AC$. An important property of conjugate elements is the following. When A is conjugate to B, and B to C, then A is conjugate to C, too. If $B = P^{-1}AP$, $C = Q^{-1}BQ$ (P and Q being elements of the group), it follows that $C = (PQ)^{-1}A(PQ)$ [1], which denotes sets of conjugate elements of a group. Such sets are called *classes of conjugate elements*, or simply *classes* of the group. Each class is determined by any element of it, by a given A. The whole class is obtained by forming the products DAD^{-1}, where D is successively every element of the group. Thus one can divide the whole group into classes where each element can appear only in one class. The unit element is a class of its own since for any element of the group it is $DED^{-1} = E$. In the O_h symmetry group for example, there are five classes with their elements being the unit element, 8 three-fold rotations, 3 two-fold rotations, 6 four-fold rotations and another 6 two-fold rotations, in total 24 elements, i.e. the order is 24.

Representation of groups

By applying a symmetry operation $P(T)$ of a group element T of a group G on a function ψ_i, one gets another function, usually different from the original one. Every possible operation will lead to another function so that one gets a number of functions that is equal to or less than the order g of the group. It can happen that some of these functions are linearly dependent so one finally gets f linearly independent (basis) functions $\psi_1, ..., \psi_f$ with $f \leq g$. In other words, the $P(T)$ operators can be seen as operators that act on ψ_i which can be written as

$$P(T)\psi_i = \sum_k \Gamma_{ki}(T)\psi_k \tag{2.12}$$

[1] here the relation $(AB)^{-1} = B^{-1}A^{-1}$ has been used

with $\Gamma_{ki}(T)$ being constants that depend on the transformation T in such a way that $\Gamma_{ki}(T) = \int \psi_k^* \Gamma(T) \psi_i dq$, where all basis functions ψ_i are orthonormal. Each symmetry element is identified with a certain matrix that follows the known matrix multiplication rule for the product of two matrices (elements) $\Gamma(T)$ and $\Gamma(Q)$; $\Gamma(TQ)_{ik} = \sum_l \Gamma_{il}(T)\Gamma_{lk}(Q)$. Such a set of matrices is called a *representation of a group*. The functions $\psi_1, ..., \psi_f$ that define the matrices are called the *basis* and their number f is called the *dimension* of the representation.

Representations that can be constructed by linear transformations of the same sets of basis functions are called *equivalent*. All matrices of the same class of equivalent representations have in common that their traces are identical. Therefore, the trace is a useful description of a set of equivalent representations of the group. It is called character and will be denoted with $\chi(T)$ in the following.

A representation is called *reducible*, if the basis functions of a representation of dimension f can be divided into sets of functions of dimension $f_1, f_2, ...$ and in such a way that, if any element of the group acts on them the functions in each set are transformed only into combinations of themselves. If the number of basis functions of a given representation that are transformed only into combinations of themselves cannot be reduced by any linear transformation of them, the representation is called *irreducible*. Therefore, reducible representations are linear combinations of irreducible representations. It can be shown, that the number of irreducible representations is equal to the number of classes in a group (see for example Ref. [35]).

For α and β being two irreducible representations of a group G with group elements T one finds

$$\sum_{T \in G} \Gamma_{ik}^{(\alpha)}(T) \Gamma_{lm}^{(\beta)}(T)^* = \frac{g}{f_\alpha} \delta_{\alpha\beta} \delta_{il} \delta_{km}. \tag{2.13}$$

If both sides of the above equation are summed over the pairs of indices i, k and l, m, one gets the orthogonality relation of the characters of the group

$$\sum_{T \in G} \chi^{(\alpha)}(T) \chi^{(\beta)}(T)^* = g \delta_{\alpha\beta}. \tag{2.14}$$

Naturally, an important point is how to find the irreducible representations of a given group. From the equation above, from $\chi(T)$ being the characters of a *reducible* representation of dimension f, and the numbers $n^{(1)}, n^{(2)}, ..., n^{(r)}$ giving the multiplicity of their corresponding irreducible representations within the reducible representation, it is

$$\sum_{\beta=1}^{r} n^{(\beta)} f_\beta = f. \tag{2.15}$$

Then the characters $\chi(T)$ can be written as

$$\chi(T) = \sum_{\beta=1}^{r} n^{(\beta)} \chi^\beta(T). \tag{2.16}$$

If this equation is now multiplied by $\chi^{(\alpha)}(T)^*$ and summed over all T, one gets with equation (2.14)

$$n^{(\alpha)} = \frac{1}{g}\sum_{T\in G}\chi(T)\chi^{(\alpha)}(T)^*. \tag{2.17}$$

If the elements T and Q are conjugate, then they have the same character $\chi(T) = \chi(Q)$. From this it follows, that

$$n^{(\alpha)} = \frac{1}{g}\sum_{k=1}^{r} N_k\chi(C_k)\chi^{(\alpha)}(C_k)^*, \tag{2.18}$$

where the summation is over the classes C, N_k is the number of elements in the kth class C_k with $\sum N_k = g$. This equation allows to easily divide reducible into irreducible representations if their characters are known. If the number of classes (and irreducible representations) of a group is n, then it can be shown that $f_1^2 + f_2^2 + ... + f_n^2 = g$.

For a better understanding of the usefulness of the above derived equations, a special example with a $3d$ electron in the middle of a square lattice, will be outlined. For a free ion, the d orbitals are fivefold degenerate with their wave functions being

$$\psi_{3,2,m_l} = R_{3,2}(r)P_2^{m_l}(cos\theta)\frac{e^{im_l\phi}}{\sqrt{2\pi}} \tag{2.19}$$

with $|\mathrm{m_l}| \leq 2$. The point group that describes the symmetry is D_{4h}, but for simplicity we use the subgroup D_4, its character table is given in table 2.4. A rotation around an axis through the angle ϕ so that $\psi_1 \cdots \psi_5$ are quantized with respect to that axis carries ϕ over in $\phi + \Phi$. That changes equation (2.19) into

$$\psi_{3,2,m_l} = R_{3,2}(r)P_2^{m_l}(cos\theta)\frac{e^{im_l(\phi+\Phi)}}{\sqrt{2\pi}}. \tag{2.20}$$

Such a rotation is given by the 5×5 matrix

$$\begin{pmatrix} e^{il\Phi} & \cdots & & 0 \\ 0 & e^{i(l-1)\Phi} & & \vdots \\ \vdots & & \ddots & \\ 0 & \cdots & & e^{-il\Phi} \end{pmatrix} \tag{2.21}$$

that is, the character of a rotation $\chi(\Phi)$ is given by

$$\chi(\Phi) = e^{il\Phi} + e^{i(l-1)\Phi} + \cdots + e^{-il\Phi} = e^{-il\Phi}\sum_{n=0}^{2l}(e^{i\Phi})^n = \frac{\sin(l+1/2)\Phi}{\sin(\Phi/2)} \tag{2.22}$$

As a result, one finds

$$\begin{aligned} \Phi = \pi \qquad & \chi(C_2) = (-1)^l \\ \Phi = \frac{\pi}{2} \qquad & \chi(C_4) = \begin{cases} 1 & l = 0, 1, 4, 5, ... \\ -1 & l = 2, 3, 6, 7, ... \end{cases} \end{aligned}$$

D_4		E	$2C_4$	C_2	$2C_2'$	$2C_2''$
A_1	Γ_1	1	1	1	1	1
A_2	Γ_2	1	1	1	-1	-1
B_1	Γ_3	1	-1	1	1	-1
B_2	Γ_4	1	-1	1	-1	1
E	Γ_5	2	0	-2	0	0

O		E	$8C_3$	$3C_2$	$6C_4$	$6C_2'$
A_1	Γ_1	1	1	1	1	1
A_2	Γ_2	1	1	1	-1	-1
E	Γ_3	2	-1	2	0	0
T_1	Γ_4	3	0	-1	1	-1
T_2	Γ_5	3	0	-1	-1	1

Table 2.4: Character table for the point groups D_4 (left) and O (right). The Bethe notation (Γ_1, etc.) is most common in physics while the Mullikan notation (A_{1g},...) is most familiar in chemistry. In this work mainly the Mullikan notation will be used, the Bethe notation is mentioned for completeness. Note that the Bethe symbols Γ_1 ... Γ_n describe only one symmetry group, for example Γ_2 in the O_h symmetry group describes a different irreducible representation than Γ_2 in the D_4 symmetry group. In the Mullikan notation, A and B represent one dimensional representations with symmetric (A) and antisymmetric (B) basis functions with respect to rotations about a principal axis of the nth order, E stands for two–dimensional representations and T for three–dimensional ones. The primes distinguish between different classes and g (gerade) and u (ungerade) denote the symmetry with respect to inversion. The numbers written together with the classes give the umber of elements within one class, for example $6C_2$ means that there are 6 two–fold rotational axis in this class.

The characters of the 5 classes of the representation spanned by the five d orbitals are then

E	$2C_4$	C_2	$2C_2'$	$2C_2''$
5	-1	1	1	1

Using formula 2.18 and the character table for D_4 (table 2.4), it is

$$\begin{aligned}
n^1 &= n(\Gamma_1) = n(a_1) \\
&= 1/8(1\cdot 5\cdot 1 + 2\cdot(-1)\cdot 1 + 1\cdot 1\cdot 1 + 2\cdot 1\cdot 1 + 2\cdot 1\cdot 1 && = 1 \\
n^2 &= n(\Gamma_2) = n(a_2) \\
&= 1/8(1\cdot 5\cdot 1 + 2\cdot(-1)\cdot 1 + 1\cdot 1\cdot 1 + 2\cdot 1\cdot(-1) + 2\cdot 1\cdot(-1) && = 0 \\
n^3 &= n(\Gamma_3) = n(b_1) \\
&= 1/8(1\cdot 5\cdot 1 + 2\cdot(-1)\cdot(-1) + 1\cdot 1\cdot 1 + 2\cdot 1\cdot 1 + 2\cdot 1\cdot(-1) && = 1 \\
n^4 &= n(\Gamma_4) = n(b_2) \\
&= 1/8(1\cdot 5\cdot 1 + 2\cdot(-1)\cdot(-1) + 1\cdot 1\cdot 1 + 2\cdot 1\cdot(-1) + 2\cdot 1\cdot 1 && = 1 \\
n^5 &= n(\Gamma_5) = n(e) \\
&= 1/8(1\cdot 5\cdot 2 + 2\cdot(-1)\cdot 0 + 1\cdot 1\cdot(-2) + 2\cdot 1\cdot 0 + 2\cdot 1\cdot 0 && = 1
\end{aligned}$$

In other words, the representation spanned by five d orbitals is a reducible representation made up by the irreducible representation $a_1, b_1, b_2,$ and e. The fivefold degeneracy of the d orbitals is removed in the D_4 point group, and we get three non-degenerate levels and one two-fold degenerate level.

The nomenclature of the different representations (for example $a_1, b_1, b_2,$ and e in the D_4 point group) is rather simple. a and b represent one–dimensional representations where a corresponds to symmetric base functions and b to antisymmetric

base functions. e stands for two–dimensional, f (or more commonly t) for three–dimensional, and g for four-dimensional representations. In order to distinguish within the various one–, two–, three–, or four–dimensional groups between the representations, a number (1 or 2) put down as a subscript is used. The subscripts g (gerade) and u (ungerade) explain the symmetry with respect to the inversion; if the representations do not change sign under the inversion operator i, it is called *gerade* (g), if it changes its sign, it is called *ungerade* (u).

Projection operators

An important tool given by group theory is the projector $\mathcal{P}$. It is particularly important in the applications on quantum mechanics, especially for the generation of basis functions of irreducible representations of crystallographic point groups. If Γ_α is a unitary irreducible representation of dimension f_α of a finite group G of order g. $\Gamma^{(\alpha)}_{mn}(T)$ represents the (m,n)th element of the matrix $\Gamma(T)$ of the symmetry element T. The subscript (α) denotes the irreducible representation. Then the projection operators are defined by

$$\mathcal{P}^{(\alpha)}_{mn} = \frac{f_\alpha}{g} \sum_{T \in G} \Gamma^{(\alpha)}_{mn}(T)^* P(T), \tag{2.23}$$

with $P(T)$ being the symmetry operator that transforms a function ψ such that $\psi' = P(T)\psi$. In some cases it is practical to use $P(T)\psi^{(\alpha)}_n(\mathbf{r}) = \sum_{m=1}^{f_\alpha} \Gamma^{(\alpha)}_{mn}(T)\psi^{(\alpha)}_m(\mathbf{r})$ (c.f. equation (2.12)). Then equation (2.23) can be expanded as

$$\mathcal{P}^{(\alpha)}_{mn}\psi^{(\alpha)}_n(\mathbf{r}) = \frac{f_\alpha}{g} \sum_{T \in G} \Gamma^{(\alpha)}_{mn}(T)^* \Big(\sum_{m=1}^{f_\alpha} \Gamma^{(\alpha)}_{mn}(T)\psi^{(\alpha)}_m(\mathbf{r})\Big). \tag{2.24}$$

Together with the following rules this equation is a very powerful tool for the finding of the basis functions of a given problem.

The projection operators $\mathcal{P}$ follow four important properties:

(i) For any two functions $\phi(\mathbf{r})$ and $\psi(\mathbf{r})$ it is

$$(\mathcal{P}^{\alpha}_{mn}\phi, \psi) = (\phi, \mathcal{P}^{\alpha}_{mn}\psi). \tag{2.25}$$

(ii) For any two projection operators $\mathcal{P}^{\alpha}_{mn}$ and $\mathcal{P}^{\beta}_{jk}$, it is

$$\mathcal{P}^{\alpha}_{mn}\mathcal{P}^{\beta}_{jk} = \delta_{\alpha\beta}\delta_{nj}\mathcal{P}^{\alpha}_{mk}. \tag{2.26}$$

(iii) If $\psi^{\beta}_1(\mathbf{r})$, $\psi^{\beta}_2(\mathbf{r})$, ... are basis functions transforming as the unitary irreducible representation Γ^α of G, then

$$\mathcal{P}^{\alpha}_{mn}\psi^{\beta}_j(\mathbf{r}) = \delta_{\alpha\beta}\delta_{nj}\psi^{\alpha}_m(\mathbf{r}). \tag{2.27}$$

(iv) For any function $\psi(\mathbf{r})$, it is

$$\mathcal{P}^{\alpha}_{nn}\psi(\mathbf{r}) = a^{\alpha}_{n}\psi^{\alpha}_{n}(\mathbf{r}), \tag{2.28}$$

where a^{α}_{n} and $\psi^{\alpha}_{n}(\mathbf{r})$ are the coefficient and basis function of the expansion of $\psi(\mathbf{r})$[2] that relate to the nth row of Γ^{α}.

These equations are a very powerful tool in order to find all basis functions since only one basis function is necessary to find the unknown basis functions from a symmetry transformation. As an example one could think of the still missing basis functions of the example given above of the D_4 point group. We know that its symmetry group is D_4 and we also know the four irreducible representations to be a_1, b_1, b_2, and e. If the projector acts on a function ψ_{lm}, it can yield zero. If it leads to a non vanishing result, the first basis function has been found (it may not be normalised yet). The other basis functions for symmetries with a dimension greater than one can be obtained by applying a symmetry transformation to the former.

Multiplication tables

Finally, the multiplication of elements of different symmetries will be explained, since it will become important in the theory of X–ray absorption spectra.
The direct product of two matrices $\mathbf{A}$ and $\mathbf{B}$ with $\mathbf{A}$ being a $m \times m$ matrix and $\mathbf{B}$ being a $n \times n$ matrix, is given by

$$(\mathbf{A} \times \mathbf{B})_{ks,lt} = A_{kl}B_{st}. \tag{2.29}$$

If Γ^{α} and Γ^{β} are two unitary irreducible representations of a group G of dimensions f_{α} and f_{β}, then their direct product

$$\Gamma(T) = \Gamma^{\alpha}(T)\Gamma^{\beta}(T) \tag{2.30}$$

[2]Any function $\psi(\mathbf{r})$ can be written as a linear combination of basis functions of the unitary irreducible representations of a group G of coordinate transformations in $\mathbb{R}^3$. That is

$$\psi(\mathbf{r}) = \sum_{\alpha}\sum_{j=1}^{f_{\alpha}} a^{\alpha}_{j}\psi^{\alpha}_{j}(\mathbf{r}),$$

where $\psi^{\alpha}_{j}(\mathbf{r})$ is a normalised basis function transforming as the jth row of the d_{α}–dimensional unitary irreducible representation Γ^{α} of G, a^{α}_{j} are a set of complex numbers and the sum over α is over all the inequivalent unitary irreducible representations of G.

O	A_1	A_2	T_1	T_2	E
A_1	A_1	A_2	T_1	T_2	E
A_2	A_2	A_1	T_2	T_1	E
T_1	T_1	T_2	$T_1+T_2+E+A_1$	$T_1+T_2+E+A_2$	T_1+T_2
T_2	T_2	T_1	$T_1+T_2+E+A_2$	$T_1+T_2+E+A_1$	T_1+T_2
E	E	E	T_1+T_2	T_1+T_2	A_1+A_2+E

Table 2.5: Multiplication table for O symmetry

for all $T \in G$ gives a unitary representation of G of dimension $f_\alpha f_\beta$. The character $\chi(T)$ of $T \in G$ in this representation is given by

$$\chi(T) = \chi^\alpha(T)\chi^\beta(T). \tag{2.31}$$

Knowing the characters of the direct product representation, we can decompose it into irreducible representations using equation (2.18). So practically, the multiplication of two representations can be constructed directly from their character tables. For example, $E \otimes E = A_1 + A_2 + E$, a result that can be derived by multiplying the characters belonging to the same class of the two multiplied representations. Here $E \otimes E$ gives the characters 4,1,4,0,0. As one can see in the character tables that such a combination can only be derived for $A_1 + A_2 + E$. In the same way a multiplication table for a symmetry can be derived. In table 2.5 such a table is given for O symmetry.

Chapter 3

The layered cobaltates Na_xCoO_2 and their hydrated derivatives

In recent years, investigations of the system Na_xCoO_2 have been very active due to its many interesting and unusual transport, magnetic and superconducting properties of this system. For example, Na_xCoO_2 shows an exceptionally high thermopower over the doping range of $0.5 \leq x \leq 0.9$, while also displaying low resistivity and low thermal conductivity [37–39]. Such properties are wanted in materials which have potential technological applications in refrigeration. In 2003, Takada and co-workers found a superconducting state in $Na_{0.35}CoO_2 \cdot 1.3H_2O$ at temperatures lower than 5 K [40]. Especially the discovery of superconductivity in a layered system that does not contain copper triggered an enormous interest in this compound.

In this thesis, the physics of the system Na_xCoO_2 will be described in detail. In this chapter an introduction to the material will be given first (section 3.1), followed by an introduction to the sample preparation (section 3.2) and a discussion of the magnetic and transport properties. Possible ordering effects for each region of the phase diagram together with results of X–ray scattering experiments and magnetisation measurements will also be discussed (section 3.3-3.6). In the following main chapter the electronic structure will be described in great detail using experimental (NEXAFS and XPS) and theoretical results (cluster calculations).

3.1 Introduction

The system Na_xCoO_2 was mentioned for the first time in 1974 by M. von Jansen and R. Hoppe [41] in their article 'Notiz zur Kenntnis der Oxocobaltate des Natriums'. In this article, they report about the crystal structure and results of magnetisation measurements of $NaCoO_2$ and $NaCo_2O_4$. They found $NaCoO_2$ to crystallise in the α–$NaFeO_2$ structure type with the space group $D^5_{3d} - R\bar{3}m$ in a low spin configuration, and $NaCo_2O_4$ to belong to the space group $D^6_6 - P6_322$.
The crystal structure of Na_xCoO_2 consists of quasi two dimensional CoO_2 layers stacked along the crystallographic c–axis, separated by Na layers. Within the CoO_2

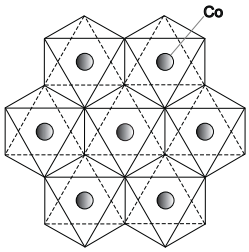

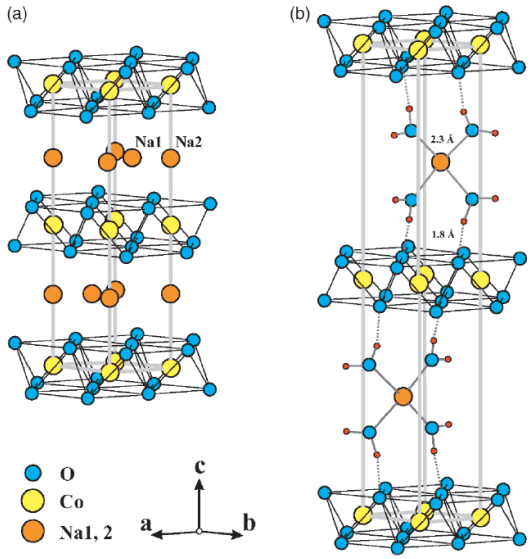

Figure 3.1: Right: Illustration of the crystal structure of the non-hydrated parent compound $Na_{0.61}CoO_2$ (a) and the fully hydrated compound $Na_{0.33}CoO_2 \cdot 1.3H_2O$ (b). The water molecules are placed above and below the Na planes. Figure taken from Ref. [44]. Top: Sketch of a top view of a CoO_2 plane.

layers the Co ions are surrounded by O_6 "octahedra" (see figure 3.1), that are trigonally distorted [42,43]. As a layered transition–metal oxide this system looks similar to the high temperature superconductors (HTSC's). However, the CoO_2 layers are different in structure from the CuO_2 layers of the HTSC's since the cobaltates contain a 2D triangular lattice, while the CuO_2 layers are built of a 2D square lattice.

During the end of the 1990's the system Na_xCoO_2 was touched by a first bigger wave of interest because of its unusually large thermopower. First Terasaki and co–workers found a large thermoelectric power in $NaCo_2O_4$ single crystals in 1997 [37]. Different from what has been published by other groups later on, they found the system to be metallic and with a highly anisotropic transport behaviour. The crystals used were $NaCo_2O_4$ single crystals prepared by a NaCl–flux technique. The anisotropy of the resistivity follows from the anisotropy of the crystal structure as described above. As Terasaki *et al.* report, $NaCo_2O_4$ exhibits a thermoelectric power one order of magnitude larger than have typical metals and high temperature superconductors (HTSC), while at the same time it has a lower resistivity (ρ_a) as HTSC's. The large thermoelectric power accompanied by low ρ_a suggests that $NaCo_2O_4$ is applicable to thermoelectric devices that convert heat into electric energy through the thermoelectric power of solids. It should also be noted that the results show a strong anisotropy between the in-plane (ρ_a) and out–of–plane (ρ_c) resistivity both in magnitude and in the nature of the temperature variation. At decreasing temperature, ρ_c shows a crossover from a semiconducting to a metallic phase around 200 K, whereas ρ_a corresponds to metallic conduction at all temperatures [37]. Additionally, Motohashi and co–workers found that with increasing x, the absolute value of ρ monotonically decreased, while the value of the thermoelectric power S increased [45]. Different from later reports, $NaCo_2O_4$ was found to be metallic [37, 46]. It is believed that the CoO_2 layers are the conducting planes

since they are a common structural component for all known thermoelectric layered cobaltates, i.e. Na_xCoO_2, $Ca_3Co_4O_9$ [47–49], and $Bi_2Sr_2Co_2O_y$ [50–52].
The assumption of Co^{3+} and Co^{4+} ions existing in the low spin state is supported by Koshibae *et al.* in their theoretical work about the origin of the large thermopower in $NaCo_2O_4$ and also in $La_{1-x}Sr_xCoO_3$. By generalising Heikes formula [53,54], they show that the degeneracy of carriers, together with the strong electron correlation in cobalt oxides, leads to a large thermopower. That means, not only the degeneracies of electronic states of Co^{3+} and Co^{4+} ions but also the ratio between the two different valances is important for the enhancement of the thermopower. The authors found the highest values for low spin Co^{3+} ions and either low spin Co^{4+} ions or a mix of Co^{4+} low spin and high spin ions, excluding the possibility of a high spin state for both ions [55].
Experimentally, Wang *et al.* explain the origin of the enhanced thermopower from measurements of the thermopower and the magnetisation by spin entropy, i.e the motion of charge tied to local moments of spin 1/2 in a background of Co^{3+} ions that are magnetically inert (diamagnetic) [56]. From their magnetisation measurements, they found the existence of large local moments that are antiferromagnetically coupled and a magnetic moment around 0.87 μ_B averaged over all Co ions, resulting in a picture with non magnetic Co^{3+} ions (S=0) and Co^{4+} ions in a low spin state (S=1/2) and a moment $\sqrt{3}\mu_B$ [56].
From density functional calculations within the local density approximation D.J. Singh gets an energy difference between the lower lying t_{2g} and the upper lying e_g bands of approximately 2.5 eV, and a width of the t_{2g} bands of 1.6 eV and of the e_g bands of 1.2 eV [57]. An effective on–site Hubbard U of 5-8 eV is suggested. As another possible origin of the high thermopower Singh mentions the mechanism through a high effective mass. The calculations yield a strongly energy dependent transport function and very high density of states (DOS) at the fermi energy ($N(E_F)$) which could explain the specific heat and thermopower of $NaCo_2O_4$ with only a modest many–body renormalisation [57].
In order to address the question of the valence state of the Co ions, Ray and co–workers performed transport, magnetisation and Co^{59} NMR measurements. Using conduction and susceptibility data, they were able to explain their data by two possible pictures: In the first, the cobalt ions behave effectively as $Co^{3.5}$, while in the second the cobalt ions exist as Co^{3+} and Co^{4+} in a low spin state with $S = 0$ and $S = 1/2$, respectively [58]. However, by performing Co^{59} NMR measurements they found two different Co sites in $NaCo_2O_4$ that they assigned to Co^{3+} and Co^{4+} sites [58], pointing indeed towards a charge separation picture as it has been suggested by Koshibae *et al.*

A huge wave of interest hit the sodium cobaltates research after the discovery of superconductivity in the hydrated compound $Na_{0.35}CoO_2 \cdot 1.3H_2O$ by Takada and co–workers [40], since this is the only known layered transition metal oxide which exhibits superconductivity other than high T_c cuprates and Sr_2RuO_4. The transition temperature T_c was at $\approx 5\,\mathrm{K}$ and the critical field $H_c \approx 100$ Oe. The introduction of water into the system is responsible for an increase of the crystallographic c–axis

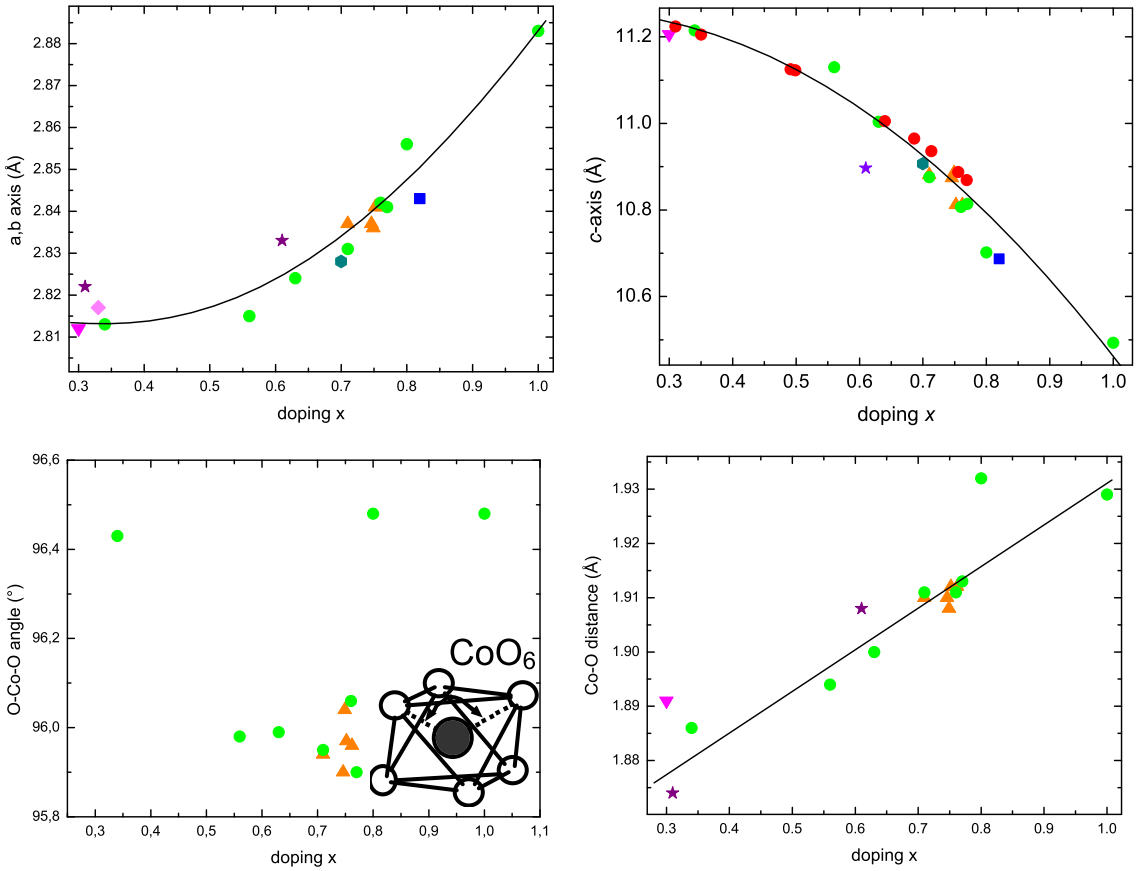

Figure 3.2: Dependence on doping of the a and c–axes length, of the Co-O distance, and the O-Co-O binding angle at room temperature, the data is taken from various publications: ▼ Ref. [42], ★ Ref. [43], ◆ Ref. [59], ▲ Ref. [60], ● Ref. [61], ● Ref. [44], ■ Ref. [62], and ● Ref. [63]. The straight lines may work as a guide to the eye.

(perpendicular to the CoO_2 layers) emphasising the two dimensional character of these layers. The similarity between sodium cobaltates and high temperature superconductors is an important aspect of the research activities. Both compounds contain quasi two–dimensional CoO_2 and CuO_2 planes, respectively, which are, however, different in their construction. While the copper oxide planes are constructed of CuO_4 plaquettes, the CoO_2 layers consist of edge sharing CoO_6 octahedra which are distorted in such a way that the resulting symmetry is trigonal. The trigonal coordination of the Co-sites may result in geometric frustration which favours unconventional electronic ground states. The geometrically frustrated CoO_2-sublattice exists not only in the hydrated compound, but also in the non-hydrated parent compound Na_xCoO_2.

It has been found that the length of the crystallographic a and b–axes are only slightly dependent on doping, whereas the c–axis depends strongly on the doping level. Therefore, the determination of the c axial length provides a useful indication about the actual stoichiometry of the sample. In figure 3.2 the doping dependence of the crystallographic a and c–axes is shown as well as the doping dependence of

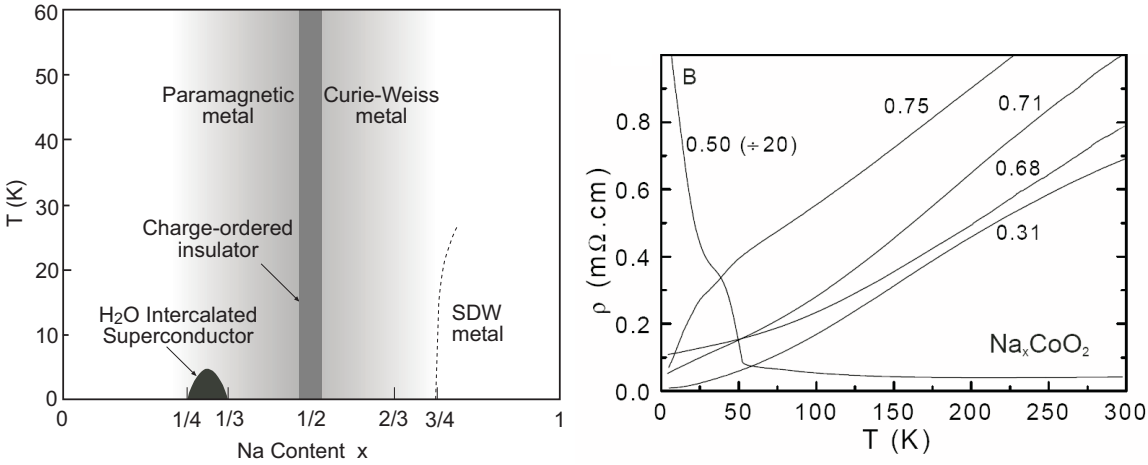

Figure 3.3: Left: Phase diagram of non-hydrated Na_xCoO_2. Right: Temperature dependent in-plane resistivity ρ of single crystals of Na_xCoO_2. Figures are taken from Ref. [63].

the Co-O distance and the angle of an O-Co-O bond. The Co-O distance increases linearly up to a value of $x \approx 0.75$ from where it jumps to a significantly higher value at $x = 0.8$, but returns to the linear dependence near $x = 1.0$ [61]. Note that $x = 0.8$ is the only representative of the magnetic phase in this graph. Therefore, it is not known weather this variation of the linear dependence is intrinsic or due to an error in the interpretation of the measurements. An increase in the Co-O bond distance also results in a weaker crystal field influence and thus weaker hybridisation which may result in a weaker energy splitting of the t_{2g} and e_g energy levels. The region at $x > 0.75$ shows also a change in the bond angle, it is more or less constant for lower x concentrations, but jumps to a higher value [61] indicating a stronger trigonal distortion in that doping region. Interestingly, an increase in the O-Co-O bond angle is also observed for $x \approx 0.35$.

The trigonal distortion of the CoO_6 octahedra leads to an energy splitting of the t_{2g} states into a twofold degenerate a_{1g} level and a fourfold degenerate e'_g level, whereas the e_g states remain degenerate. In the following, in order to avoid confusion, the e_g states will be named e_g^σ and the e'_g states e_g^π. Although the a_{1g} and e_g^π states overlap, and mix to some extent, these states are roughly separated in energy by the rhombohedral crystal field [57]. In $NaCo_2O_4$ the states at the top of the t_{2g} manifold where E_F sits have dominant a_{1g} character [57].

From all that is mentioned above it is not a big surprise that Na_xCoO_2 exhibits a rich phase diagram. Foo *et al.* published in 2004 the first phase diagram of this class of material where they found superconductivity and different metallic states as well as different magnetic behaviour depending on the Na concentration (see figure 3.3 and Ref. [63]), which emphasises the strong influence of the Na ions on the electronic structure. The authors give a dome-shaped superconducting phase for $1/4 \leq x \leq 1/3$ with a maximum transition temperature $T_c \approx 5\,\mathrm{K}$. Away from the superconducting phase which only occurs in the hydrated compound, the system can

be divided into three distinct phases: One with $0 < x < 0.5$, the special case $x = 0.5$, and the phase with $0.5 < x < 1.0$. In all phases but the special case $x = 0.5$ the system's conductivity ρ appears to be metallic in its temperature dependence (see figure 3.3). Note that the insulating $x = 0.5$ state has been found to be metallic by Terasaki *et al.* [37] or Ray and co-workers [58], they also found a different magnetic behaviour.
In the low doping region (i.e. $x < 0.5$), the conductivity ρ below 30 K follows a T^2 behaviour [63] and the susceptibility χ appears to be paramagnetic, where its magnitude remains large compared with the Pauli susceptibility in conventional metals [63]. This regime is therefore called paramagnetic metal.
At a doping of $0.5 < x < 0.75$, where a Curie–Weiss state has been found, the resistivity ρ exhibits a characteristic T-linear profile below 100 K [56], whereas at higher doping ($x > 0.75$), ρ shows a distinct change in the slope near 20 K which reflects the onset of a weak magnetic order [63]. In the magnetic regime $x > 0.75$ a weak magnetisation has been found below 20 K which has been interpreted in terms of a spin density wave (SDW) [64, 65] (see also section 3.6). Outside this magnetic regime χ vs. T follows the Curie-Weiss law $\chi = C/(T - \Theta)$ [56, 58] and therefore this part of the phase diagram is called Curie-Weiss metal. To the nature of the insulating state at $x = 0.5$ Foo *et al.* suggest a long range Na order which they found in electron diffraction studies. Such a long range order should influence the thermal conductivity κ, since the thermal conductivity in layered oxides is dominated by phonons. Because phonons are strongly scattered by disorder in the Na sublattice, the phonon mean-free-path is expected to be much longer at $x = 0.5$ than at neighbouring x values without such a long range order, and therefore should have a strong influence on the thermal conductivity κ what they indeed found [63]. A detailed description of the special case $x = 0.5$ will be given in section 3.4.

3.2 Sample preparation

As reported, the preparation of high quality crystals in the family of the sodium cobaltates has been found to be a very difficult task. Stoichiometric homogeneity and stability even of small crystal pieces appear to pose the largest problems. In the literature and also in this work the stoichiometry is given by exact numbers, even though there is always some uncertainty in the true value of x. This point will also be addressed in the experimental part in the chapter 5.2.2 which deals with the electronic structure of Na_xCoO_2. There are many different methods of growing crystals such as a modified solid state reaction technique called 'rapid heat–up' technique [45], the floating–zone technique employing an optical furnace [44, 66–68] or the flux method [69]. In this work, only crystals grown by the two latter methods were used and therefore these two techniques and their doping procedures shall be addressed briefly in the following.

A composition around $Na_{0.75}CoO_2$ seems to be stable, but higher doping levels can also be achieved rather easily as reported by Chen *et al.* [44] who used the

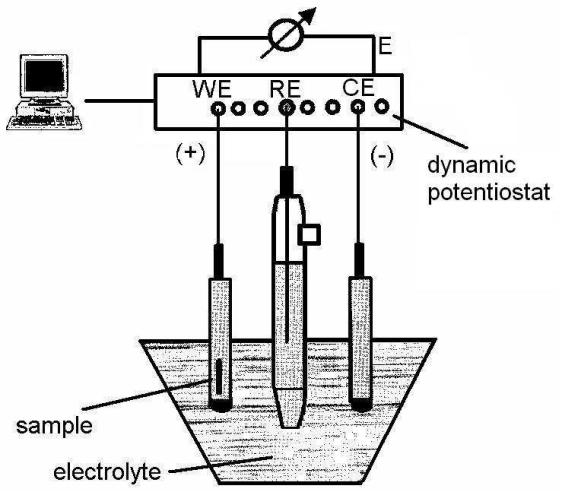

Figure 3.4: Sketch of the experimental setup and the reaction process for electrochemical de–intercalation as used for Na_xCoO_2. Figure is taken from Ref. [70]

floating–zone technique. In contrast, they report it to be hard to grow a compound with $x = 0.50 - 0.60$. In order to reach doping levels with a lower Na content, single crystals of $Na_{0.7}CoO_2$ were placed in the oxidizing agent Br_2/CH_3CN and then washed with acetonitrile. The change of the Na content of the resulting crystals is generally proportional to the bromine concentration in the CH_3CN agent [44]. Single crystals grown by the floating–zone method that have been used during this work were grown at the IFW Dresden by C. Sekar, at the Max Planck Institute for Solid State Research in Stuttgart by D.P. Chen and C.T. Lin, as well as at Princeton University in the group of R.J. Cava. Maybe the highest single crystal quality can be reached in crystals grown by the sodium chloride flux method [69], but this technique has the disadvantage that only a stoichiometry of $x \approx 0.7$ can be grown. In order to reach different doping levels, electrochemical de–intercalation or intercalation has to be used [68, 71]. At the IFW Dresden these experiments have been done by C. Malbrich in the group of Prof. L. Dunsch. A three–electrode electrochemical cell was set up using the Na_xCoO_2 sample as a working electrode, platinum net as a counter electrode, Ag/AgCl as a reference electrode ($E_0 = +0.2\,V$ versus the standard hydrogen electrode), and 0.1M $TBAPF_6$ [1] as an electrolyte, and a constant potential of 1.7 eV between the working and counter electrodes. The proposed half reaction at the anodically polarised Na_xCoO_2 electrode responsible for Na extraction is

$$Na_xCoO_2 + \delta(PF_6)^- \rightarrow Na_{x-\delta}CoO_2 + \delta(NaPF_6) + \delta e^-. \qquad (3.1)$$

In figure 3.4 a sketch of an experimental setup and a reaction process for de–intercalation is shown. The sample is attached to the positive working electrode (WE). The electrolyte connects the working electrode with the counter electrode (CE) where the reaction takes place. The reference electrode (RE) is used to determine the exact voltage set at the potentiostat.

Electrochemical de–intercalation has been performed successfully down to different

[1] Tetrabutylammoniumhexafluorophosphat

doping, but the intercalation of Na into the system turned out to be a more difficult task and did not work out so far.

3.3 The low doping regime (x<0.5)

In the low doping regime, the superconducting phase in the hydrated compound with x around 0.3 [72] is located. Many works have been dovoted to the hydrated compound, while only a few papers deal with the unhydrated compound with $x < 0.5$. This is rather surprising since also the unhydrated system shows interesting physical properties which are worth being investigated in their own right. A low Na concentration corresponds to a high Co^{4+} concentration with more than 50% Co^{4+} ions and a large spin 1/2 hole density in this doping regime. As shown in the phase diagram by Foo *et al.* [63], the susceptibility χ and the in–plane resistivity ρ (figure 3.5(a,b)) display a paramagnetic and metallic behaviour, respectively. The profile of χ becomes rather featureless, although its magnitude remains large compared to the Pauli susceptibility in conventional metals. At low temperatures the conductivity σ is ~ 5 times larger than that for crystals with $x > 0.5$ [63]. In a sample with $x = 0.31$, Foo *et al.* found a nearly T–independent value of the Hall constant R_H at low temperatures (figure 3.5(d)) giving a Hall density of $2.8 \times 10^{22}\mathrm{cm}^3$, that is about ten times larger than that observed in the cuprates doped at 0.3. From the large hole density and high conductivity at low temperature they concluded that screening of charge fluctuations is quite effective at $x = 0.31$ [63].
Theoretically, by investigating an extended Hubbard model it has been found that on the triangular lattice the electrons (holes) crystallise into a $\sqrt{3} \times \sqrt{3}$ structure at $x = 1/3$ [73]. Using LDA+U calculations, Kunes *et al.* found that a charge-

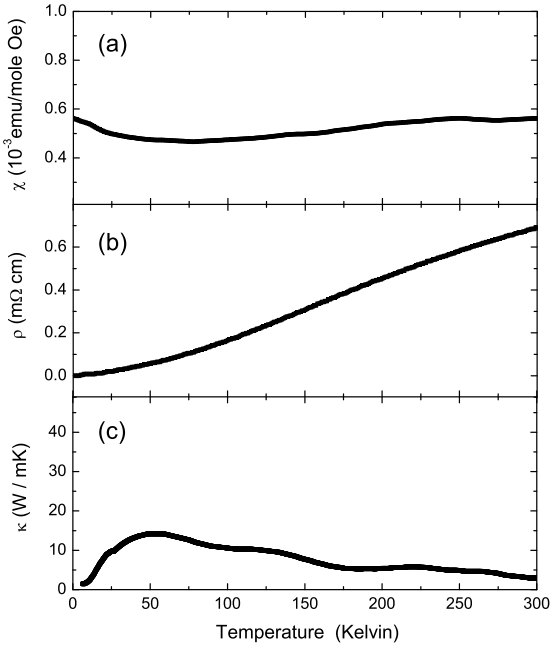

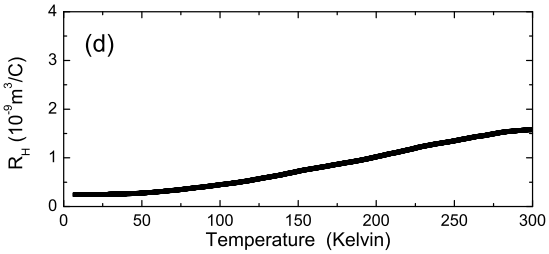

Figure 3.5: Susceptibility χ, conductivity ρ, thermal conductivity κ and Hall constant R_H of $Na_{0.31}CoO_2$, data taken from Ref. [63].

ordered state and antiferromagnetic coupling is favoured over ferromagnetism above a critical $U_c = 3eV$ for $x = 1/3$, while below U_c ferromagnetism is favoured [74].
Regarding a possible Na ordering, Mukhamedshin *et al.* found evidence from NMR measurements that there cannot be a perfect ordering of Na ions in $Na_{0.35}CoO_2$ [75]. This finding is supported by electron diffraction measurements where any ordering is absent for doping at $x = 0.35$, whereas there is a weak superstructure for $x = 0.3$ and a strong superstructure has been found for $x = 0.15$, which can be described with an $a\sqrt{3} \times a\sqrt{3}$ superstructure [76].

3.3.1 Superconductivity

As mentioned above, the layered transition metal oxide Na_xCoO_2 attracts considerable interest not only because of its unusual magnetic and transport properties, but mainly because of the superconductivity discovered in its hydrated compound $Na_{0.35}CoO_2 \cdot 1.3H_2O$ in 2003 [40]. Several experiments have been performed since then, finding evidence of unconventional superconductivity in this class of material [77–81]. The sodium cobaltates have been thought of superconductors that can be understood from the Anderson resonating valence bond (RVB) model [82], which describes a singlet quantum spin liquid ground state stabilised by frustration [83–87]. Although singlet pairing has not yet been definitely excluded [88], mainly spin–triplet superconductivity has been treated theoretically [83, 89–91] which finds support from several experiments [77–81, 92]. These findings lead to the idea that spin fluctuations [77, 79, 89, 93, 94] mediate superconductivity, as it is the case in other layered superconducting transition metal oxides like the high T_c cuprates or Sr_2RuO_4. However, these systems have a strongly two–dimensional electronic and magnetic structure other than Na_xCoO_2 [95–99].
Based on further studies a dome–shaped phase diagram of the superconducting regime could be drawn with an optimal doping $x \approx 0.30$ and a maximum transition temperature $T_c = 4.3\,K$ [72]. As the Na content increases in the superconducting regime from $x = 0.26$ to $x = 0.35$, the formal oxidation state of the Co ion decreases from +3.74 to +3.65 with the optimum for superconductivity at +3.70. In 2004, Takada *et al.* revised the published stoichiometry of the superconductor to be $Na_{0.337}(H3O)_{0.234}CoO_2 \cdot yH_2O$ [100]. They found that oxonium ions, $(H_3O)^+$, can occupy the same crystallographic sites as the Na ions [100]. The occupation of $(H_3O)^+$ in the Na^+ layers in superconducting $Na_xCoO_2 \cdot yH_2O$ changes the Co valence to $\approx +3.43$, much lower than $\approx +3.7$ deduced from the Na content. Independently Milne *et al.* [101] reached very similar conclusions.
Therefore, in recent superconducting phase diagrams the transition temperature T_c is plotted against the Co oxidation state rather than against the Na content x. Here, an optimal doping has been found for an oxidation state of $\approx +3.5$ [102, 103]. In addition, it has been reported, that the superconductivity with the highest T_c is observed in the vicinity of a magnetic phase, strongly suggesting that magnetic fluctuations play an important role in the occurrence of superconductivity [104, 105]. It has been emphasised, that this oxidation state corresponds with the nonhydrated

compound $Na_{0.5}CoO_2$, where a charge ordered phase has been found [63]. Therefore it has been suggested, that the superconducting state could compete with the charge–ordered state, similar to the high T_c cuprates.

3.4 The special case x=0.5

As pointed out in the phase diagram by Foo *et al.* [63], the stoichiometry $x = 0.5$ is special in many ways. The greatest difference to all other doping situations is the fact that $Na_{0.5}CoO_2$ is an insulator while all other compositions turn out to be metals. It is widely believed that the reason for this difference in basic physical properties originates in a charge and spin order. In the data of the resistivity and magnetisation (figure 3.6(a)-(c)) one finds two important transition temperatures: One at $T_1 \approx 53\,\mathrm{K}$ and one at $T_2 \approx 87\,\mathrm{K}$ [63, 107]. Below $T = 51\,\mathrm{K}$, the resistivity measured in the CoO_2 plane dramatically increases due to an assumed onset of charge ordering below $T_{co} \approx 53\,\mathrm{K}$ as it has been found from infrared spectroscopy [108]. In these measurements, an optical gap below $T_{co} \approx 50\,\mathrm{K}$ could be observed to develop, evidencing an insulating charge density wave ground state [108].
The magnetic susceptibility decreases with decreasing temperature and shows kinks at the transition temperatures $T_2 = 87$ and $T_{co} = 53\,\mathrm{K}$ and is anisotropic [109, 110]. In external fields $H||ab$, a negative magnetoresistance is observed below $\sim 53\,\mathrm{K}$ [106, 111]. The kink in the data near 50 K is caused by a shift in the onset temperature of the resistivity upturn. For $H||c$, the data exhibit a positive magnetoresistance below $T_2 = 88\,\mathrm{K}$ which coincides with the antiferromagnetic phase transition at $T_N \approx 87\,\mathrm{K}$

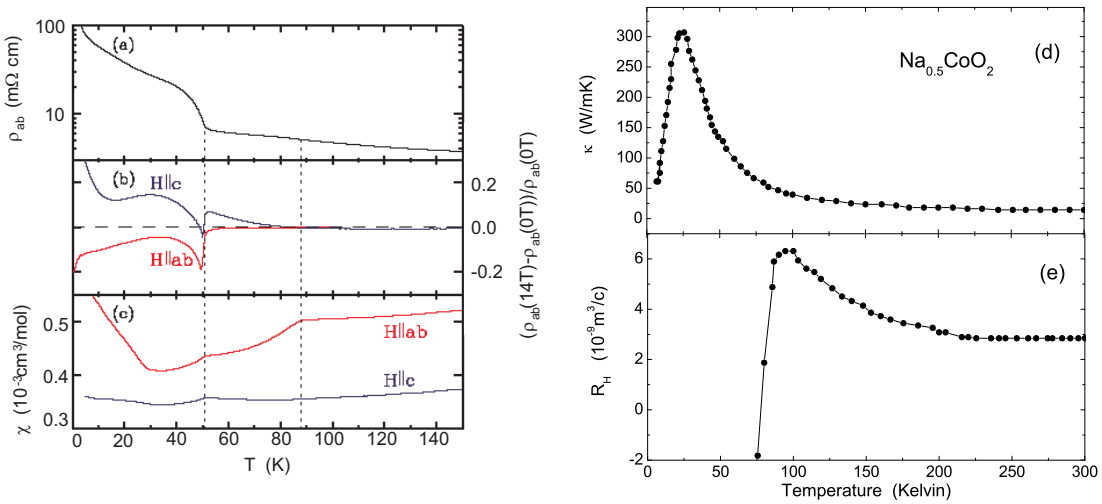

Figure 3.6: $Na_{0.5}CoO_2$: (a) In–plane resistivity ρ_{ab}, (b) fractional change of ρ_{ab} measured in a magnetic field of 14 T with $H||c$ and $H||ab$. (c) Anisotropic magnetic susceptibility in a field of 1 T. The vertical dashed lines denote the temperatures of $T = 51\,\mathrm{K}$ and $T_N = 87\,\mathrm{K}$. Figure taken from Ref. [106]. (d) In–plane thermal conductivity κ and (e) Hall coefficient R_H. Data taken from Ref. [63].

which has been found from neutron scattering data [106] (see below).

Data from NMR/NQR and neutron scattering experiments suggest two kinds of Co ions showing two different magnetic moments. Here, the Co ions having a larger moment align antiferromagnetically at $T_N \sim 87\,\mathrm{K}$ with their direction within the *ab* plane, while the Co ions with smaller moments align in the direction parallel to the *c*–axis [110]. Such a picture finds support from polarised and unpolarised neutron scattering experiments on electrochemically de–intercalated floating–zone grown crystals [68], indicating that below $T_N = 87\,\mathrm{K}$ the spins form an antiferromagnetic pattern within the CoO_2 planes, consisting of alternating rows of ordered and disordered Co ions [106] (see figure 3.7). One possible interpretation of the different behaviour of the Co ions is a charge separation into nonmagnetic Co^{3+} ions (S=0) and magnetic S=1/2 Co^{4+} ions as it has been found from correlated band theory LDA+U calculations [112] or an extended Hubbard model [113]. Similar to that, studies by high–resolution powder neutron diffraction also show that Na ordering creates two distinct Co sites located in parallel chains running along one crystallographic direction. The structural results, however, suggest that there is only a slight difference in electron density at the two Co sites in $Na_{0.5}CoO_2$ and that spontaneous (or Na order–assisted) full Co^{3+}/Co^{4+} charge ordering is not seen down to 10 K [114]. Note that for $Na_{0.5}CoO_2$ the spins are assumed to be aligned in the *ab* plane, different from what has been found for doping at $x > 0.5$.
Interestingly, the magnetic transition temperature T_N is higher than the charge ordering temperature T_{co}. In order to solve this discrepancy, Gasparovic *et al.* suggest that only those charges participate in the charge order below T_{co} that are not involved in the magnetic order below T_N [106].

Electron diffraction studies suggest that the 87 K transition has a structural component [107]. The necessity of long–range ordering of the Na ions can be seen indirectly by measuring the thermal conductivity κ parallel to the *ab* layers, since phonons are strongly scattered by disorder in the Na sublattice. The thermal conductivity κ in $Na_{0.5}CoO_2$ is strongly temperature dependent with an exceptional high value at its maximum (figure 3.6(d)), whereas for other doping levels κ is only weakly temperature dependent [63]. Therefore the phonon mean–free path length has to be much longer for $x = 0.5$ than for neighbouring values of x, leading to the picture of long–range ordered Na ions for $x = 0.5$ and less well or disordered for x away from 0.5 [63][2].
Theoretically, Na ordering is predicted from different methods. Density functional theory (DFT) suggests that the primary driving force for Na ordering is the screened Coulomb interaction among Na ions [115]. For different x non–trivial ordering patterns have been found that are sensitive to the Na concentration [115]. Additionally, it has been found, that the electronic structure of the CoO_2 layers does not affect the ordering of the Na ions since the coupling between the CoO_2 planes and the

[2] Here, Foo *et al.* compare their data to measurements done on crystals with $x = 0.31$ and $x = 0.7$.

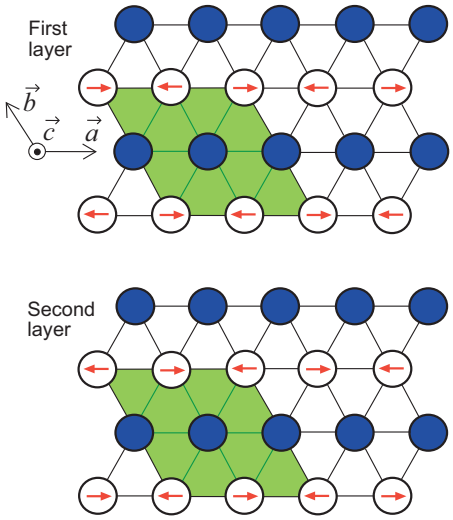

Figure 3.7: $Na_{0.5}CoO_2$: Model of the spin arrangement for two CoO_2 layers in the magnetic unit cell. The solid circles represent 'nonordered' Co ions, the hollow circles represent magnetically ordered Co ions with arrows indicate the directions of the magnetic moments. The green shaded parallelogram outlines the magnetic unit cell. Figure taken from Ref. [106]

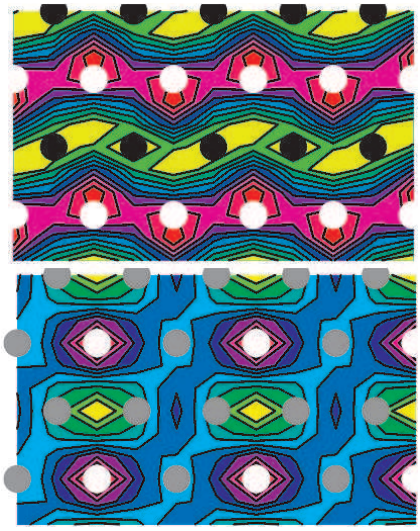

Figure 3.8: $Na_{0.5}CoO_2$: Calculations of the Na potential in Co planes with (top) a cluster of two Na vacancy sites, in successive layers displaced by the lattice vector **b** and (bottom) an alignment along the c direction. The white (black) circles represent Co^{3+} (Co^{4+}) ions. The gray circles represent conducting Co ions at intermediate valencies. Figures are taken from Ref. [117].

Na planes is much weaker than the intraplane Na–Na interaction [115], whereas the inverse effect is likely to happen since charge and magnetic ordering within the CoO_2 planes happen on an extremely low energy scale [116]. Monte–Carlo simulations also predict different ordering pattern for different doping level [118]. Na ordering induces a periodic Coulomb potential in the Co layers. The Monte–Carlo simulations imply that the depth of the electrostatic potential, ≈100 meV, is substantially larger than the single–particle hopping t ≈10 meV [95, 96] and thus will localise holes. While total energy differences are insignificant (≈0.1 meV) [117], the Coulomb landscape varies drastically in terms of position of Na vacancy clusters in successive layers along c due to a coupling between Na and Co charges, which leads to two configurations in $x = 0.5$ [117]. The two configurations are shown in figure 3.8. The top picture corresponds to a cluster of two Na vacancy sites in successive layers displaced by the lattice vector **b**. It has a one–dimensional character with high (black filled circles) and low (white filled circles) Coulomb potential stripes in agreement with the low and high spin charge–ordered stripes found using neutron diffraction [110]. A large magnetic field parallel to the ab plane favours alignment of holes in the c–direction corresponding to figure 3.8 (bottom) with 2D character and conducting Co ions at intermediate valencies (gray circles) [117]. The authors concluded that this could explain the abrupt change from an insulating antiferro-

magnet to a conducting state with reconstruction of a 2D Fermi surface when a field of 40 T is applied at $T = 50\,\mathrm{K}$ [111].

3.5 The high doping nonmagnetic regime (0.5<x<0.75)

3.5.1 Magnetism and transport

$Na_{0.7}CoO_2$ has been found bo be a starting material for most doping levels of Na_xCoO_2 [69, 109], from where various compositions can be achieved by different methods. The region of $0.5 > x > 0.75$ is described as a Curie–Weiss metal in the phase diagram given by Foo *et al.* [63], showing an anisotropic magnetic susceptibility and an anisotropic g–factor ratio g_{ab}/g_c [109]. From fits to the Curie-Weiss law of magnetisation measurements, Chou *et al.* [109] found that the Curie constant decreases with decreasing x. They concluded that while almost all of the Co^{4+} spins are localised for x=0.75 with a value g=2.5, the fraction of localised spins drops sharply as the Na content is reduced until local moment behaviour disappears almost entirely for x=0.5 [109]. Parallel to the loss of local moments, the Weiss temperature decreases drastically with decreasing x as it is shown in figure 3.9 for powder samples. They found a clear reduction in the strength of the antiferromagnetic correlations as x decreases towards $x = 0.5$. These results demonstrate that de–intercalating Na from $Na_{0.75}CoO_2$ modifies the spin system from one described by localised spins to one described by delocalised spins with weaker magnetic coupling [109]. Such a behaviour is unexpected and disturbing at first glance. Calculations using the local density approximation method found that a magnetically ordered state and a non–magnetic solution are very close in energy leading to a picture that via fluctuations both possibilities become important and determine the ground state [119].

In a sample with $x = 0.7$ Ihara *et al.* did not detect any magnetic anomaly down to 1.5 K from ^{23}Na NMR measurements, but found competing magnetic fluctuations at low temperatures which they assign to two different hole Fermi surfaces (FS), six small hole pockets near the K point, which have an e_g–orbital character, and a large cylindrical hole FS, which has a dominant a_{1g}–orbital character, as they have been predicted from band structure calculations [57]. Note that these hole pockets have not been observed in angle resolved photoemission (ARPES) experiments at the Fermi surface, but shifted to energies below the Fermi surface (see also chapter 5.1). In addition to that, Gavilano *et al.* found charge ordering at $T = 295\,\mathrm{K}$ also from ^{23}Na NMR experiments. They interpret their data suggesting that with decreasing temperature the Co ions adopt the integral valent configurations of Co^{3+} and Co^{4+}, whereas they have an average valency of +3.3 above the ordering temperature. This is completed only below 250 K, leading to a slight rearrangement of the Na ions [120]. Further ^{23}Na NMR measurements identified three Na sites from their single valued quadrupole effects and magnetic shifts, which points to a definite order of the Na^+ ions and of the Co charges in the CoO_2 planes [75]. Carretta *et al.* [121] combined various methods, viz. NMR, EPR and magnetisation measurements, to investigate

Na_xCoO_2 in the range $0.65 < x < 0.75$. The authors found the EPR signal to arise from the Co^{4+} magnetic moments that order at $T_c = 26\,K$, the ^{59}Co NMR signal originates from cobalt nuclei in metallic regions with no long range magnetic order, characterised by a generalised susceptibility typical for strongly correlated metallic systems. Such a phase separation in metallic and magnetic insulating regions is argued to occur below a transition temperature T^* in a temperature range of 220–270 K [121]. A similarity to a spin–density–wave metallic state in $Na_{0.7}CoO_2$ has also been found from optical experiments [122]. Above T^* an anomalous decrease in the intensity of the EPR signal is observed and associated with the delocalisation of the electrons. Since the exchange coupling constant J is much less than T^*, antiferromagnetic exchange as a driving force for this phase separation can be excluded [121].

Important thermodynamic information is given by Li and co–workers [123]. In–plane resistivity ρ and thermal conductivity κ measurements of a $Na_{0.7}CoO_2$ single crystal down to 40 mK show the existence of a well–defined Fermi–liquid state. A different view is presented by Bruehwiler *et al.* [124], thermodynamic and transport measurements on Na_xCoO_2 ($x \sim 0.7 - 0.75$) over a wide temperature range reveal a strongly enhanced low energy excitation spectrum. The zero–field specific heat and resistance at low temperature are proportional to a T^n law with $1 < n$, which is in contrast to ordinary Landau Fermi–liquid metals. Together with a suppression of the specific heat in a magnetic field and magnetoresistance data, Bruehwiler *et al.* concluded that a single band model cannot describe the system [124].

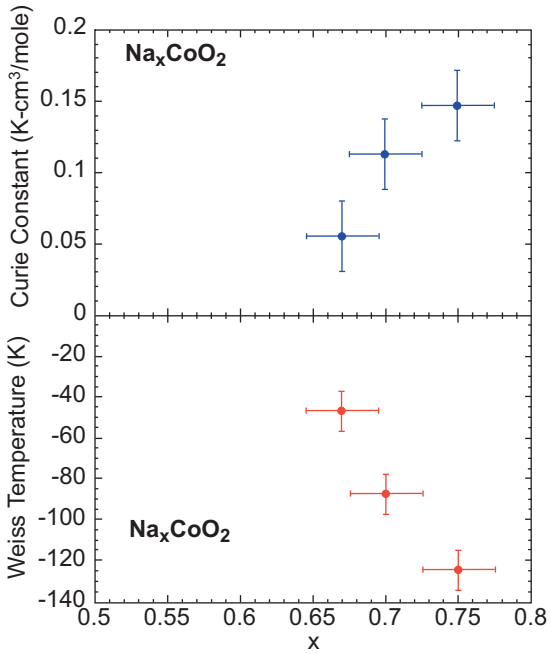

Figure 3.9: Top panel: Curie constant vs x. Bottom panel: the Weiss temperature vs x. Both are taken from powder averaged values. Figure taken from Ref. [109].

3.5.2 Na ordering

An important aspect regarding the physical properties of most systems is the occurrence of possible ordering effects in the Na sublattice and their influence on the magnetisation and transport properties. Several experimental and theoretical investigations have been performed that address this question [76, 115, 118, 126]. They all confirm that Na ordering exists, but the correct ordering pattern is still under discussion. From electron diffraction studies on a large doping range Zandbergen *et al.* [76] observe an incommensurate superstructure in a $Na_{0.64}CoO_2$ crystal, but the absence of any indication of superstructure for $Na_{0.55}CoO_2$. On the other end of this regime of the phase diagram, at $x = 0.75$, superstructure reflections have been found indicating an incommensurate vector q, which is oriented along [110] with a length of 0.135[110]. In real space, $1/q = Q$ has a length of $7.4\,d\,(110)$ [76]. Combining detailed studies using density functional theory (DFT) with model calculations based on the results given in Ref. [76], Zhang *et al.* [115] suggest that the primary driving force for Na ordering is the screened Coulomb interaction among Na ions.

Different possible unit cells have been found by Geck *et al.* [125] from high–energy X-ray diffraction combined with local density approximation studies in a $Na_{0.75}CoO_2$ single crystal. This stoichiometry is at the high end of the nonmagnetic part of the phase diagram or at the low end of the magnetic regime, but since the investigated

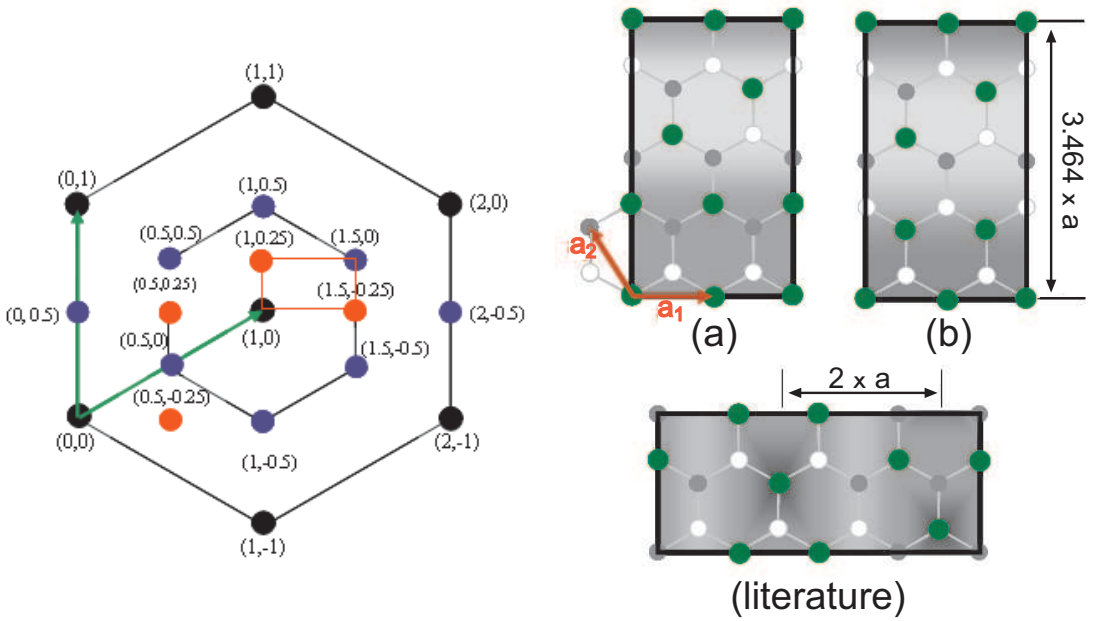

Figure 3.10: Results of high energy X–ray diffraction on $Na_{0.75}CoO_2$. Left: Summary of observed superstructure peaks around (1 0 0). The red rectangle marks the assumed unit cell of the reciprocal lattice. Right: Models for the Na superlattice. Projections of superstructure unit cells on the (a_1a_2) plane are shown. Small gray and white circles indicate Na1 and Na2 sites, respectively. The occupied Na sites are indicated by big green circles. Figures are taken from Ref. [125].

crystal did not show the magnetic phase transition at $\approx 20\,\mathrm{K}$ [127], it is treated in this part of the thesis rather than in the one on magnetism. The right stoichiometry of $x = 0.75$ could be confirmed easily by determining the room temperature lattice parameters $a = 2.83$ Å and $c = 10.84$ Å. A resolution limited radial scan through the (004) reflection (FWHM = 0.011°) at $\mathrm{T} = 8\,\mathrm{K}$ verified a well defined and homogeneous Na concentration in the probed sample volume. The observed superstructure in this compound shows a commensurate structure with peaks for example at (1.5, −0.25, 0) or (2, −0.5, 0). A summary of a survey in reciprocal space at 8 K is given in figure 3.10 (left). The correlation length of the superstructure modulation could be estimated to be about 300 Å. From temperature scans at the (1.5, −0.25, 0) and (2, −0.5, 0) peaks it was found that the observed ordering is related to an ordering of the Na ions. Here the doubling of the unit cell occurs well above 360 K, whereas the structural modulation related to the (1.5, −0.25, 0) peak appears below the transition temperature $T = 350\,\mathrm{K}$ [125]. Possible Na ordering patterns were investigated by performing a local density approximation (LDA) based on supercells as shown in figure 3.10 (right). It turned out, that configuration (a) leads to the lowest energy whereas the other possibility (including the one suggested in literature [76]), corresponds to higher energies due to an increased Coulomb energy. Interestingly, the lowest energy configuration exhibits Na density stripes within the Na planes, similar to the doped high temperature superconducting cuprates [125].

3.6 The magnetic regime of the phase diagram (x>0.75)

As mentioned in chapter 3.3.1, the origin of superconductivity in the hydrated compound is still under discussion. One point that seems to be well accepted is the presence of H_3O^+ in the superconducting compound, which would affect the electronic structure and lead to a doping level for superconductivity similar to that in $Na_{0.75}CoO_2$ [101], i.e. similar to the doping level in the magnetic regime. Therefore, a good knowledge of the magnetic and transport as well as other characteristic properties may be important for the understanding of superconductivity in the sodium cobaltates.

In this section first a detailed introduction and summary of the situation for doping levels larger than $x = 0.75$ will be given, followed by own results obtained from magnetisation and transport measurements mainly using a SQUID and a vibrating sample magnetometer as they are briefly described in chapter 4.3.

The system Na_xCoO_2 became famous for its unexpected high thermopower accompanied by a low resistivity [37] and unconventional superconductivity [40, 93], but also for its magnetic properties that were found to be unconventional. Motohashi and co–workers found in a $Na_{0.75}CoO_2$ sample a second–order magnetic phase transition at $\mathrm{T_m} \sim 22\,\mathrm{K}$ and a large positive magnetoresistance effect below T_m [64] in a sample grown using a sample preparation method named 'rapid heat–up' technique [45]. The magnetic transition is observable in the magnetisation, but also in

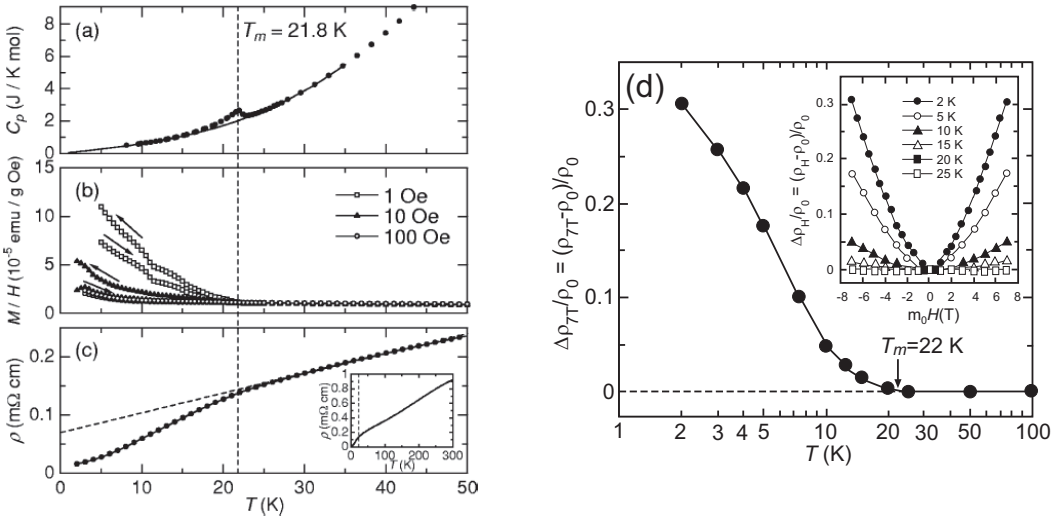

Figure 3.11: $Na_{0.75}CoO_2$: (a) Specific heat C_p, (b) magnetic susceptibility M/H and (c) electrical resistivity ρ plotted versus temperature. The inset in (c) shows the $\rho - T$ relation for temperatures up to 300 K. Figure (d) displays the degree of the magnetoresistance (MR) effect in a field of 7 T. The inset shows the field dependence of the degree of MR for different temperatures. Figures taken from Ref. [64].

the specific heat and the resistivity. As shown in figure 3.11(a), the specific heat (C_p) exhibits a jump at the transition temperature $T_m = 21.8$ K with a shape typical for a second order phase transition. Motohashi *et al.* [64] fitted the specific heat data by applying the formula $C_p(T) = f_D(T/\Theta_D) + \gamma T$, where Θ_D, γ, and f_D denote, respectively, the Debye temperature, the electronic specific heat coefficient, and Debye's formula for which the degree of freedom was assumed to be three per atom. They reported values of $\Theta_D = 553$ K and $\gamma = 25.9$ mJ/K^2 After subtracting a baseline generated from these values (shown in figure 3.11(a) as a solid line) Motohashi *et al.* calculate the enthalpy and entropy changes as $\Delta H = 0.975$ J/mol and $\Delta S = 0.0481$ J/mol K, respectively [64].

Below T_m the magnetic susceptibility exhibits a distinct hysteresis between the zero-field-cooled (ZFC) and field-cooled (FC) curves (figure 3.11(b)). From fitting the temperature dependence of the inverse susceptibility (a straight line above T_m) Motohashi *et al.* [64] found that the susceptibility follows the Curie–Weiss law $\chi = C/(T - \Theta)$ above T_m where the values for C and Θ have been determind to be 0.234 emu K/mol Oe and -166.4 K, respectively. The negative value of Θ suggests an antiferromagnetic spin coupling interaction (negative values of Θ were also reported in previous works [58,128]). The resistivity shown in figure 3.11(c) decreases linearly down to the transition temperature, yielding a kink around T_m.

Another characteristic of the investigated sample is its large positive magnetoresistance (MR) effect seen in the magnetically ordered state (figure 3.11(d)). The magnetoresistance effect is defined as $\Delta\rho_H/\rho_0 \equiv (\rho_H - \rho_0)/\rho_0$, where ρ_H is the resistivity in an applied field H. The onset temperature of the MR effect is in good

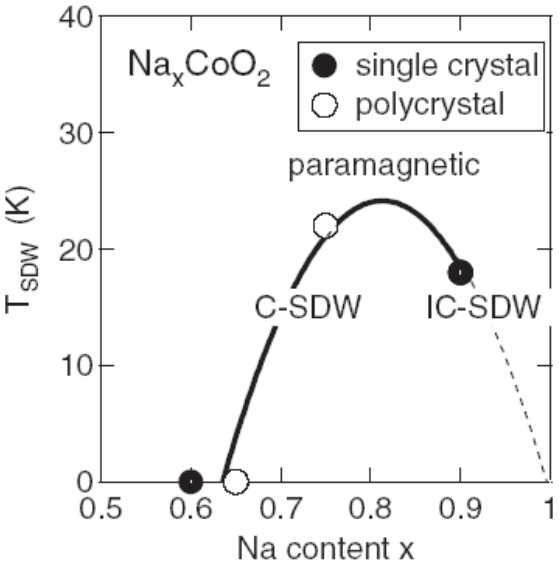

Figure 3.12: Phase diagram of Na_xCoO_2 determined by μ^+SR experiments. Solid and open circles represent results on single crystals (flux grown crystals [39]) and polycrystalline samples (synthesised by a solid state reaction technique [130–134]), respectively. The point at $x = 1$ is extrapolated from the data on the related compound $LiCoO_2$ [135]. C-SDW stands for a commensurate spin–density wave whereas IC-SDW denotes an incommensurate spin–density wave. The figure is taken from Ref. [129].

agreement with the transition temperature $T_m = 22\,\mathrm{K}$, which indicates that the positive MR effect is triggered by the magnetic transition. In total, a magnetic transition has been found for doping levels around $x = 0.8$. This has been summarised in a magnetic phase diagram as shown in figure 3.12 [129].

The ground state of Na_xCoO_2 for $x > 0.75$ is still not clear. Sugiyama and coworkers [129,136] carried out muon-spin-rotation experiments (μSR) on $Na_{0.65}CoO_2$ and $Na_{0.75}CoO_2$ polycrystalline samples synthesized by a modified solid state reaction technique, the 'rapid heat–up' technique [45] and on a $Na_{0.9}CoO_2$ single crystal prepared by a flux method [39]. The $Na_{0.65}CoO_2$ sample did not undergo a magnetic phase transition down to 2.5 K, whereas a transition at $T_m = 22\,\mathrm{K}$ for the $x = 0.75$ sample has been found. However, although the sample was in a structurally single phase it turned out to be partially nonmagnetic, i.e. magnetically inhomogeneous, probably because of a low local Na concentration. It has been estimated that only ∼20% of the sample exhibits the transition to the ordered phase at 22 K. Furthermore, the volume of the ordered phase does not change down to 2.5 K [136]. From calculations, Sugiyama *et al.* concluded that the ordered phase is either a ferrimagnet or a commensurate spin–density–wave (C-SDW) but not an incommensurate spin–density–wave (IC-SDW) [136], as found, for example, for $Ca_3Co_4O_9$ [133] and the Zn and Si doped $CuGeO_3$ system [137]. For the $Na_{0.9}CoO_2$ single crystal it has been found that the μSR signal was fitted best by a zeroth-order Bessel function, leading to the conclusion that $Na_{0.9}CoO_2$ undergoes a transition from a paramagnetic to an incommensurate spin density wave (IC-SDW) state at $T_{SDW} = 19\,\mathrm{K}$, different from what has been found for the two samples with $x = 0.65$ and $x = 0.75$. (cf. the phase diagram figure 3.12). Furthermore, Sugiyama *et al.* claimed that the IC-SDW state occurs within the CoO_2 plane and that the oscillating moments point along the c–axis. However, Bayrakci *et al.* [62] found that $Na_{0.82}CoO_2$ exhibits bulk antiferromagnetic (AF) long range order with a Néel temperature of about 20 K, employed by susceptibility, specific heat, and μSR measurements on single crystals

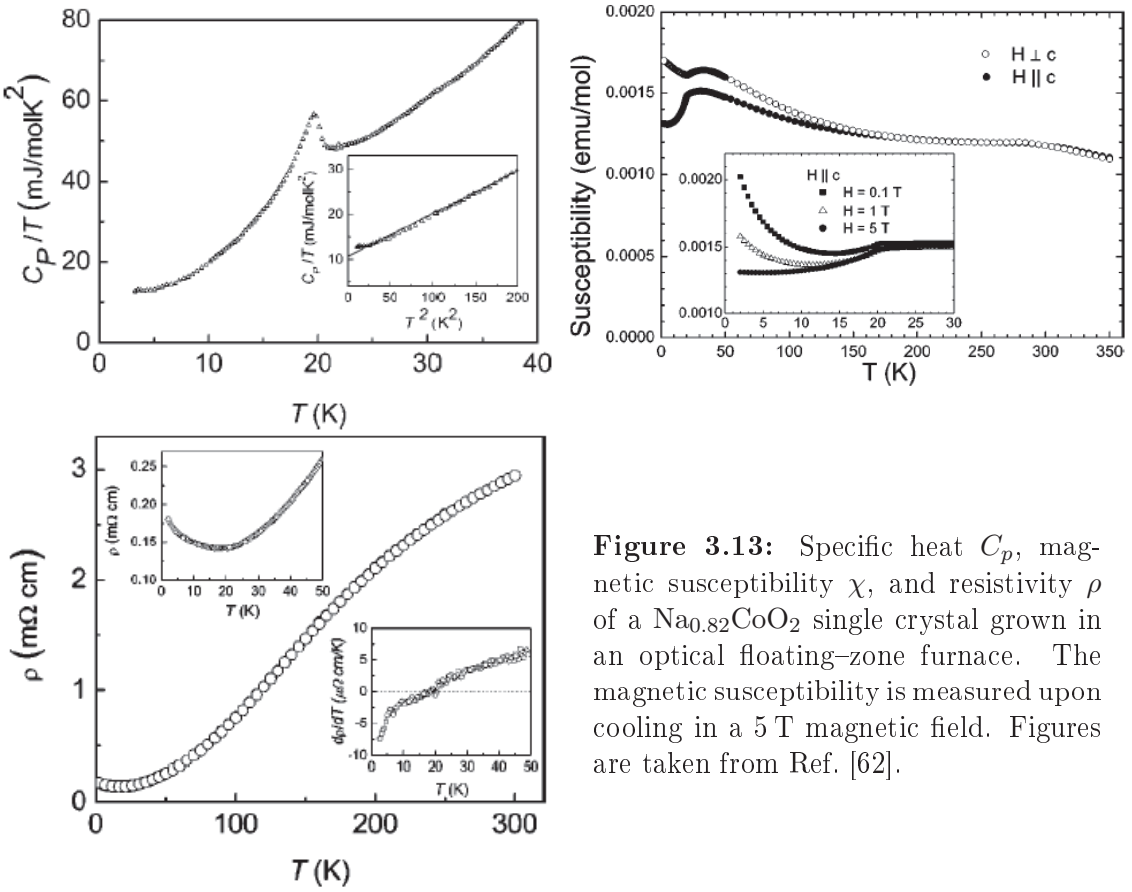

Figure 3.13: Specific heat C_p, magnetic susceptibility χ, and resistivity ρ of a $Na_{0.82}CoO_2$ single crystal grown in an optical floating–zone furnace. The magnetic susceptibility is measured upon cooling in a 5 T magnetic field. Figures are taken from Ref. [62].

prepared by the floating-zone method. They observed that the magnetic order encompasses nearly 100% of the crystal volume, which disappears rapidly above T_N. The large difference in volume fractions observed by Bayrakci *et al.* and Sugiyama *et al.* [136] is explained by a less homogeneity of the samples of Sugiyama *et al.*, possibly caused by an inhomogeneous Na content or intercalation of water which is known to occur rather rapidly under moist conditions, especially in powder samples [62].

Furthermore, Bayrakci *et al.* [62] found hints towards a commensurate spin order by employing myon spin rotation experiments. As a possible explanation of a commensurate spin order they suggest that the same local field is repeated in every third crystallographic unit cell. However, their results do not support an interpretation in terms of an incommensurate order as suggested by Ref. [62, 136]. From measurements of the magnetic susceptibility on cooling in a 5 T magnetic field oriented either along the c–axis or perpendicular to it, a broad peak at 31 ± 3 K has been found which has been interpreted as short-range, Ising-type, quasi two–dimensional antiferromagnetic correlations [62]. A sharp decrease of the c–axis susceptibility around 20 K represents the onset of an antiferromagnetic transition with ordered moments along c. The onset of long–range antiferromagnetic ordering at 19.8 ± 0.1 K is also indicated by a sharp anomaly in the specific heat as shown in figure 3.13(a).

Bayrakci *et al.* [62] analysed the specific heat data by determining the entropy contained in this anomaly. They that the entropy contained in this anomaly amounts to 0.08(1) J/molK and corresponds to about 10% of the entropy of the Co^{4+} spin-1/2 system, which is consistent with the short–range magnetic fluctuations above T_N visible in the magnetic susceptibility measurements [62]. The in–plane resistivity shows a metallic character for temperatures above T_N, but changes its sign in the temperature derivative of the resistivity below T_N (see figure 3.13(c) and the inset) Such a behaviour is expected if a spin–density wave opens a small gap at the Fermi surface [62]. In the susceptibility data as shown in figure 3.13(c) a broad hump at around $285 \pm 5\,\mathrm{K}$ can be seen. Together with information from Raman data, the authors explain this feature by a structural phase transition intrinsic to $Na_{0.82}CoO_2$, rather than by an impurity phase such as CoO which is an antiferomagnet with $T_N = 292\,\mathrm{K}$. From spectral ellipsometry on a very similar crystal $Na_{0.82}CoO_2$ Bernhard *et al.* found indications of charge ordering in the CoO_2 layers below that transition temperature of 280 K [138]. The data is discussed in terms of charge ordering and formation of magnetopolarons due to a charge–induced spin–state transition of adjacent Co^{3+} ions similar to the related compound $La_{1-y}Sr_yCoO_3$ [139–143]. This mechanism would be driven by a displacement of the neighbouring oxygen ligands towards the central Co^{4+} ion which may favour an intermediate–spin (IS) state with S=1 over a low–spin (LS) state with S=0 of the Co^{3+} ions. Below the Néel temperature, the self–trapping energy of the magnetopolarons is increased in the antiferromagnetic state where polaron hopping requires spin–flip excitations and therefore are not dynamic anymore [138].

Inelastic neutron scattering experiments on $Na_{0.75}CoO_2$ single crystals grown by the floating–zone method [66] showed that there exists strong in–plane ferromagnetic (FM) correlations with an energy scale much higher than 20 K [98]. The existence of strong in-plane FM correlations is also consistent with the band structure calculations [57, 93]. There, a weak itinerant ferromagnetic ground state for all doping levels in the range $x = 0.3 - 0.7$ is predicted where quantum spin fluctuations would in practice suppress the tendency for ordering. Since full 3D ferromagnetic order is excluded by the magnetisation data [62,64], a spin arrangement with in–plane ferromagnetic order and a spin-density wave modulation perpendicular to the planes, as an antiferromagnetic stacking along the c–axis, would be compatible with these results. And indeed, such antiferromagnetic correlations perpendicular to the layers, consistent with an A–type antiferromagnetic ordering, were found from polarised neutron scattering [99, 144]. From a fit of the magnon dispersion (shown in figure 3.14(a)) using a minimal spin–wave model, with a Hamiltonian containing only nearest–neighbour Heisenberg exchange interactions, Helme *et al.* estimate the interlayer and intralayer exchange constants to be 12.2 ± 0.5 meV and -6 ± 2 meV, respectively, which means that the magnetic fluctuations in $Na_{0.75}CoO_2$ are highly three–dimensional (figure 3.14(b)). The spin–wave modes propagating along the c–axis are found to be sharp, indicating a well correlated ground state [144]. Bayrakci *et al.* used a similar Hamiltonian, but added another term including the anisotropy

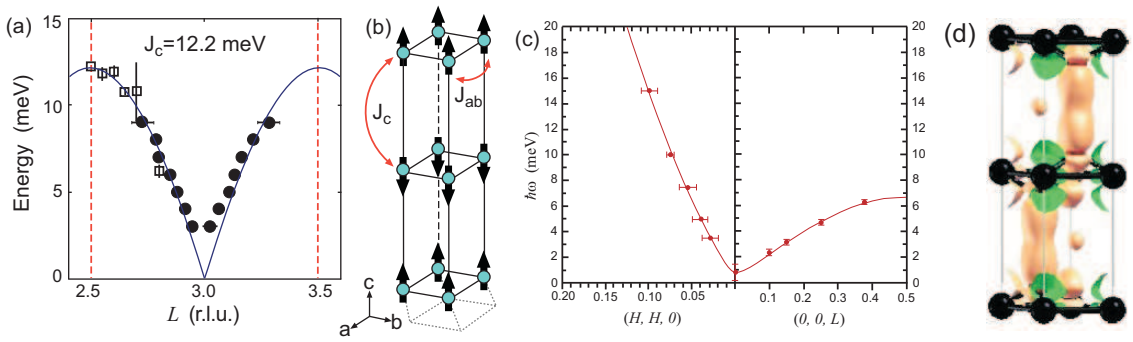

Figure 3.14: Magnon dispersion and the magnetic structure showing the two exchange constants, J_{ab} and J_c, and the spin direction. Figure (a) and (b) are taken from Ref. [144], solid circles are from constant–energy scans and open squares from constant–L scans. The solid curve is calculated from the spin-wave dispersion with exchange constant $J_c = 12.2$ meV. Figure (c) shows the spin–wave dispersion along $(hh0)$ and along $(00l)$, it is taken from Ref. [99]. The right figure (d) illustrates possible exchange paths between Na and O. Figure (d) is taken from Ref. [145].

constant D

$$H = J_{||} \sum_{\substack{i,j \\ in-plane}} \mathbf{S_i S_j} + J_{\perp} \sum_{\substack{i,j \\ \perp plane}} \mathbf{S_i S_j} - D \sum_i S_i^z, \tag{3.2}$$

where $\mathbf{S_i}$ is the spin 1/2 operator for the magnetic ion at lattice site i and the coupling constants $J_{||}$ and $J_{\perp}$ characterise the exchange interactions within the ab plane and between adjacent planes, respectively. The anisotropy constant D models the exchange anisotropy where its sign alters from layer to layer. From a fit of the dispersion data in the $(H\,H\,0)$ and $(0\,0\,L)$ directions (cf. figure 3.14(c)) they extract the values $J_{||} = -4.5 \pm 0.3$ meV, $J_{\perp} = 3.3 \pm 0.3$ meV, and $|D| = 0.05 \pm 0.05$ meV [99]. From figure 3.14(c) the existence of an energy gap appears to be possible, but cannot be judged from that data. However, using low–energy inelastic neutron scattering, Helme *et al.* actually observed two gaps in the magnetically ordered phase of $Na_{0.75}CoO_2$. The gap energies decrease with increasing temperature and both gaps are found to be closed when the temperature exceeds the magnetic ordering temperature $T_m \approx 22$ K [146]. This relative isotropy of the magnetic coupling constants is surprising in light of the two–dimensionality of the Na_xCoO_2 crystal structure. In other layered magnets with comparable bond length anisotropies, such as $YBa_2Cu_3O_6$, the magnitudes of the in–plane and out–of–plane exchange parameters differ by orders of magnitude [147]. A required necessity for the validity of this model would be an unusually strong c–axis superexchange coupling through Na or an unusually weak nearest–neighbour in–plane exchange coupling.
The possibility for such a coupling has been found theoretically by Johannes *et al.* [145] from first–principles calculations and an analysis of the exchange mechanism. The superexchange via direct O-O hopping and through intermediate Na sp_2 hybrids couples each Co to its nearest and six *next*–nearest interplanar neighbours (see figure 3.14(d)), which plays an important role in the out–of–plane magnetism,

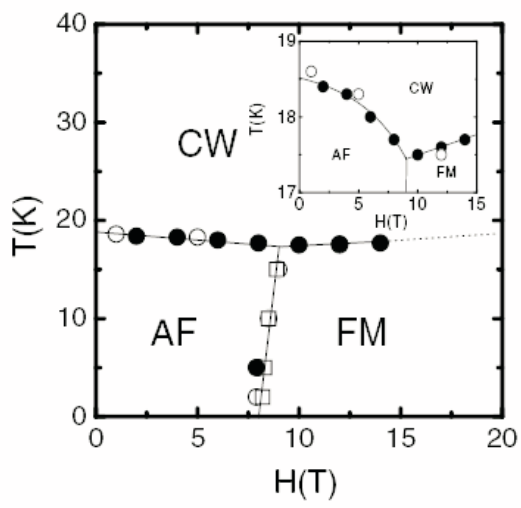

Figure 3.15: The magnetic phase diagram of $Na_{0.85}CoO_2$. The inset shows the data around the tri–critical point in an enlarged scale. CW, AF, and FM represent a Curie–Weiss, an antiferromagnetically ordered, and a ferromagnetically spin polarised state, respectively. The phase boundary points are obtained from the susceptibility (open circles), specific heat (solid circles), and magnetoresistance (open squares) measurements. Figure taken from Ref. [67].

via equivalent paths. The individual exchange constants are rather two–dimensional, like the lattice itself, but due to multiple c–axis exchange paths, the magnetism becomes effectively three–dimensional [145]. From X–ray absorption spectroscopy one clearly finds a significant O-Na hybridisation which supports the possibility of O-O hopping through intermediate Na sp_2 hybrid orbitals [148] (see also chapter 5.2.2). In addition to the hopping path along c, LDA calculations found the in–plane coupling to be weak, obtained from an itinerant picture. Here, the ground state shows the observed magnetic order ferromagnetic layers in an antiferromagnetic stack but is only 3 meV lower than a ferromagnetic state which is half–metallic and 9 meV below the nonmagnetic solution [119]. This leads to a high sensitivity of the electronic state both to temperature changes and to applied magnetic fields [119]. Note that such a superexchange drops with the distance more strongly than other coupling mechanisms, such as double exchange. Thus, although the interplanar coupling is surprisingly strong in Na_xCoO_2, it would be expected to be very weak in the hydrated superconducting compound. It is even possible that a crossover from AFM to FM coupling occurs with hydration due to the suppression of the superexchange interaction [145] since dimensionality plays an important role in spin–fluctuation–mediated superconductivity [149–151]. Another interesting point in the neutron scattering data is the fact, that the Curie–Weiss temperature $-(3J_{||} + J_{\perp})/k_B$ as calculated with the values given by Bayrakci *et al.* is positive [99], whereas a temperature extracted from the magnetic susceptibility measurements is negative [62]. As a possible explanation of this point Bayrakci *et al.* describe a scenario in which the Co^{3+} ions in the superstructure are in an intermediate–spin state with S=1 and interact antiferromagnetically [138] which could explain why the bulk DC susceptibility in $Na_{0.82}CoO_2$ is antiferromagnetic, despite the fact that $-(3J_{||} + J_{\perp}) > 0$.

From measurements of the magnetisation, specific heat and magnetoresistance on a $Na_{0.85}CoO_2$ single crystal prepared in flowing oxygen in a floating–zone optical image furnace, Luo and co–workers found a metamagnetic transition from an antiferromagnetic state to a quasi ferromagnetic state at about 8 T at low temperatures which is driven by a spin–flop transition along the c–axis [67]. However, the observed

spin–flop jump is small compared with that in conventional antiferromagnets; from the transition field, the characteristic energy of the interlayer antiferromagnetic coupling has been estimated to be ~ 1 meV [67]. From these results Luo *et al.* are able to draw the low temperature magnetic phase diagram of $Na_{0.82}CoO_2$ as shown in figure 3.15. A confirmation of a spin–flop transition could be made from neutron diffraction studies of a $Na_{0.85}CoO_2$ single crystal grown by the floating–zone method [66]. Helme *et al.* [146] found a spin–flop transition at $\approx 8\,\mathrm{T}$ and support the assumption that the spins are aligned along the c–axis for $B = 0\,\mathrm{T}$. From calculations, they found the observed spin–flop transition field to be in good agreement with the field that is needed to overcome the anisotropy associated with the gap in the spin–wave dispersion, as described above.

Chapter 4

Experimental results: X–ray diffraction and magnetisation

4.1 High energy X–ray scattering on $Na_{0.5}CoO_2$

As explained above, ordering of the Co ions may play a crucial role in the physics of the magnetic and transport properties in the special case of $Na_{0.5}CoO_2$. However, a direct observation of such an ordering by resonant X–ray scattering using soft X–rays (i.e. at the Co L–edge), is very difficult since such an ordering occurs within the ab planes with a crystallographic a–axis of ≈ 2.8 Å. Therefore, the reciprocal lattice vector a' is rather large so that the reciprocal Q space is very large, too, which makes a detailed investigation impossible since $\lambda/2 > d$. An easier path to follow is high energy X–ray scattering (in an energy range of about 100 keV) in order to address a possible Na ordering. When using high energy X–rays mainly the Na ions play an important role since X–rays are scattered by electrons and thus an additional Co^{3+}/Co^{4+} ordering only changes the number of electrons at the Co sites at most by one and is therefore very weak and nearly undetectable. Previous electron diffraction experiments [76] show a strong superstructure, indicating the presence of a well ordered superlattice structure with a commensurate vector q oriented along [110] with a length of 0.25[110]. The [001] electron diffraction pattern of $Na_{0.5}CoO_2$ is shown in figure 4.1. From the obtained data a structure model was derived that describes the data fairly well (figure 4.1(b)). The model includes the two different types of Na sites, Na1 and Na2, both of which are only partly occupied and have a prismatic sixfold coordination of O. They are positioned directly above the Co ions (Na1) and at the other prismatic position, above the centers of the Co triangles (Na2), respectively. The existence of two different Na sites and occupation behaviour with doping has also been found by X–ray photoemission spectroscopy. These data will be described in more detail in chapter 5.2.1. The model that is given by Zandbergen *et al.* shows that one out of four Na1 as well as one out of four Na2 sites are occupied. Their model is supported by neutron powder diffraction where zigzag chains of Na running along one crystallographic direction were found at 300

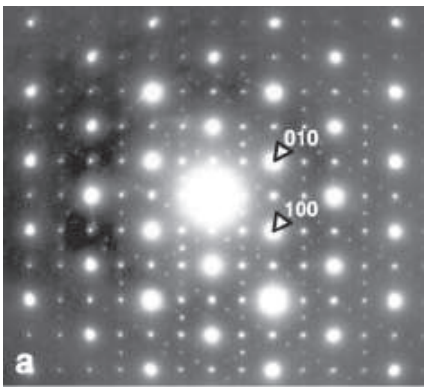

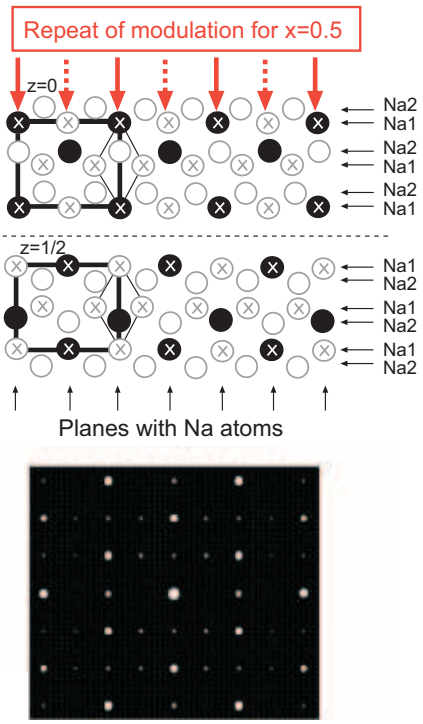

Figure 4.1: (a) Electron diffraction pattern of $Na_{0.5}CoO_2$ (b) Models for the Na planes of $Na_{0.5}CoO_2$, both the Na planes at z=0 and z =1/2 are given. Occupied Na positions are indicated by black dots, Na vacancies by open circles. X indicates the positions of the Co atoms lying below. Figures are taken from Ref. [76].

and 3.5 K [107].

A high energy X–ray diffraction experiment performed at beamline BW5 at the synchrotron facility DESY in Hamburg, Germany, confirmed the results from electron diffraction. The crystal that has been used had been grown by H. Berger, Lausanne, Switzerland, by the flux method with a stoichiometry $x = 0.7$ and had been electrochemically de–intercalated by C. Malbrich at the IFW Dresden, Germany. A rocking scan (figure 4.2(a)) proves the high quality of the crystal given by the full width at half maximum (FWHM) of 0.261° at the (004) Bragg–reflection. A ϑ–2θ scan at the (004) Bragg–refleflection with a FWHM of 0.006° shows the homogeneous Na distribution along the crystallographic c–axis (figure 4.2(b)). From this it is clear that the Na de–intercalation works very well, producing homogeneous and well distributed Na concentrations. With scans along selected directions in the reciprocal space a map of the structure at 15 K in the (H K 0) plane could be drawn. As an example a short K–scan around the (0 1.5 0) reflection and a longer K–scan along (1.5 K 0) is shown (figure 4.2(c) and (d)), as well as an H–scan along (H 0.5 0) (figure 4.2(e)). The resulting map is shown in figure 4.2(f), where the Bragg–reflections are represented by black filled circles. Additionally, superstructure reflections have been found at half and quarter integer values of H and K (blue and red filled circles, respectively), similar to what has been found from electron diffraction experiments [76]. Note that the map of the (H K 0) plane contains also all reflections that originate from twinning effects.

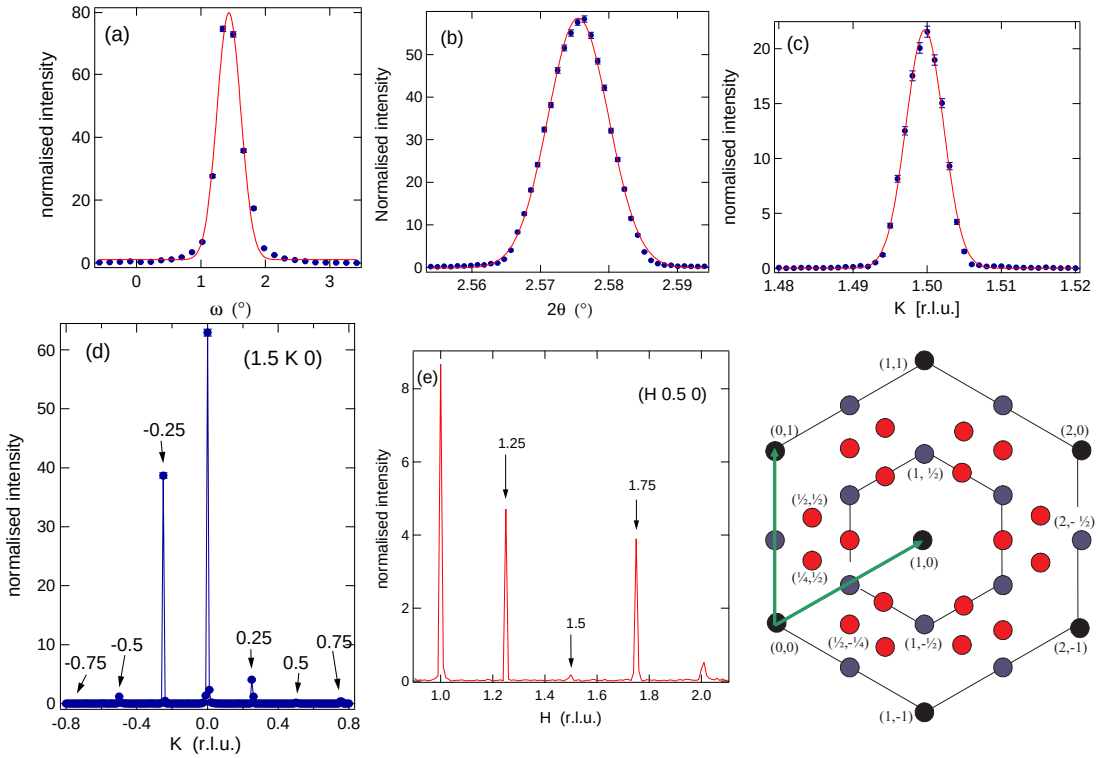

Figure 4.2: Results of high energy X–ray diffraction on $Na_{0.5}CoO_2$: (a) ω– and (b) ϑ–2θ scan at the (0 0 4) reflection, (c) K–scan around the (0 3/2 0) reflection, (d) K–scan along (3/2 K 0), H–scan along (H 1/2 0) (e), and a map of the reciprocal space in the (H K 0) plane.

4.2 Resonant X–ray scattering on $Na_{0.66}CoO_2$

In order to learn more about possible Co ordering and its influence on the physical properties we performed resonant X–ray scattering at the Co K–edge on an electrochemically de–intercalated single crystal $Na_{0.66}CoO_2$. A sample characterisation has been done at energies off the Co K–resonance where the length of the crystallographic c–axis could be determined to be 10.97 Å and that of the crystallographic a–axis to be 2.837Å at room temperature which gives a stoichiometry of $x = 0.66$ for the de–intercalated sample.

In the following, resonant X–ray scattering experiments on this $x = 0.66$ sample will be discussed and compared to resistivity data given in literature. In figure 4.3 the energy dependence of the (0 0.5 4) reflection at T=10 K is shown. Unfortunately, Co is a very good absorber and since the incoming light is mainly scattered at the Co ions, the intensity at energies larger than the resonance at ≈7710 eV rises only weakly, different from what has been found for the manganates [152], for example. Nevertheless, a clear difference between the two polarisations in the analyzer ($\sigma\sigma$– or $\sigma\pi$–channel) is observable which shows that there exist two crystallographically non–equivalent Co sites within the ab plane. This effect may be due to charge ordering, but also explanations such as lattice distortion effects or orbital ordering could

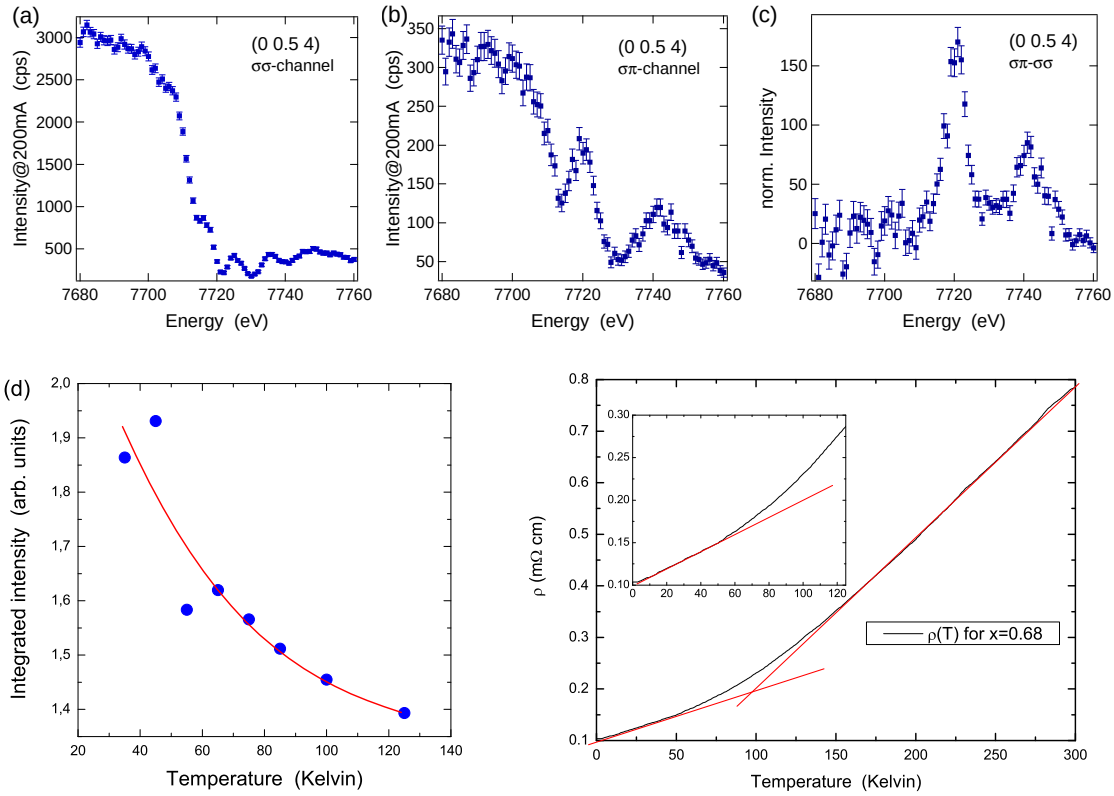

Figure 4.3: $Na_{0.66}CoO_2$: Energy scan at the (0 0.5 4) reflection in the (a) $\sigma\sigma$–channel and (b) in the $\sigma\pi$–channel, (c) shows the difference between (a) and (b) for a normalised intensity. In figure (d) the integrated intensity of the (0 0.5 4) peak at the resonance energy is shown for temperatures up to 125 K. The red line may act as a guide to the eye. The resistivity for a similar doping $x = 0.68$ is shown in figure (e), the behaviour with temperature changes at around 100 K. The red lines are linear fits to the low and high temperature region (the resistivity data has been taken from Ref. [63]).

be possible explanations. Especially the peak at ≈7720 eV is strong for $\sigma\pi$ scattering (figure 4.3(a)), but weak in the $\sigma\sigma$ channel (figure 4.3(b)). This becomes this becomes obvious when the latter case is subtracted from the former (figure 4.3(c)), even though the resonance signal is weak compared to other materials such as the manganite oxides [152]. Interestingly, the (0 0.5 4) peak shows a temperature dependent behaviour in the $\sigma\pi$ channel at the resonance energy; unfortunately, due to lack of time, the $\sigma\sigma$ channel could not be measured as well. For the same reason only this (0 0.5 4) superstructure peak could be measured as a function of temperature at the resonance. In figure 4.3(d), the intensity of the (0 0.5 4) reflection is shown. With increasing temperature the peak intensity in the $\sigma\pi$ channel decreases non linearly in the measured region up to 125 K. The resistivity data of a similar crystal with $x = 0.68$ [63] shows a behaviour that can be connected to the observed temperature dependent superstructure. As shown in figure 4.3, the resistivity increases linearly up to ≈50 K, then has an upturn and increases linearly again from ≈150 K onwards. The intersection point of these two straight lines occures at ≈100 K where the tem-

perature dependent resonant peak also changes the slope. This fact emphasises a connection between a loss of order of the Co ions within the *ab* plane and an increase in conductivity.

4.3 Measurements of the magnetisation and of the transport properties

Unimpressed from what has been published already in the literature, own measurements of the magnetisation up to 15 T have been performed on two single crystals grown by C.T. Lin and D.P. Chen, MPI Stuttgart, using the travelling–zone method, in order to characterise the samples and to learn more about this system.

In the susceptibility data which have been gained by using a SQUID magnetometer all characteristic features of the magnetic low temperature phase transition are observed (figure 4.4(left)): There is a broad peak around 30 K which indicates short-range, Ising-type, quasi–two–dimensional antiferromagnetic correlations [62] as well as the sign of the antiferromagnetic transition at ≈ 20 K. The upturn below $\approx$ 10 K may be due to unpaired paramagnetic spins. Additionally, one observes the hump at 275 K. These features can also be observed in the specific heat data (figure 4.4(right)). Note that C_p shows only a small peak at 19.8 K rather than a well pronounced feature.

A deeper insight into the magnetic ground state can be achieved by performing magnetisation measurements up to 14.5 T. These measurements have been done in a vibrating sample magnetometer (see chapter 4.3) in the laboratories of the IFW Dresden.
In figure 4.5 the magnetisation curves of an $x = 0.82$ single crystal grown by the floating zone method [44] are shown. First, one should look at the temperature dependent magnetisation curves in different constant fields. Figure 4.5(a) shows the magnetisation resulting from an external field of 1 T and 14 T, respectively, applied perpendicular to the crystallographic *c*–axis (i.e. parallel to the *ab* plane) at temperatures up to 100 K. At low temperatures, well below the transition temperature $T_N = 19.8$ K, the curve for H=1 T shows an upturn which does not follow an 1/T law. This upturn may also be caused by uncoupled, paramagnetic spins, since the underlying antiferromagnetic signal is also present and adds to the 1/T law of the paramagnetic spins. This view is supported by the H=14 T curve where this upturn has changed into a more or less horizontal line. Such a behaviour is expected for uncoupled spins, too.
A similar behaviour, although for external fields parallel to the crystallographic *c*–axis, has been observed by Luo *et al.* [67]. They explain this behaviour by a phase transition from an antiferromagnetically ordered state to a spin ferromagnetically polarised state at $\sim$8 T [67]. This interpretation still holds for the observation for fields perpendicular to the *c*–axis and can therefore be attributed to the same phenomenon, i.e. a transition from an antiferromagnetic to a ferromagnetic state.

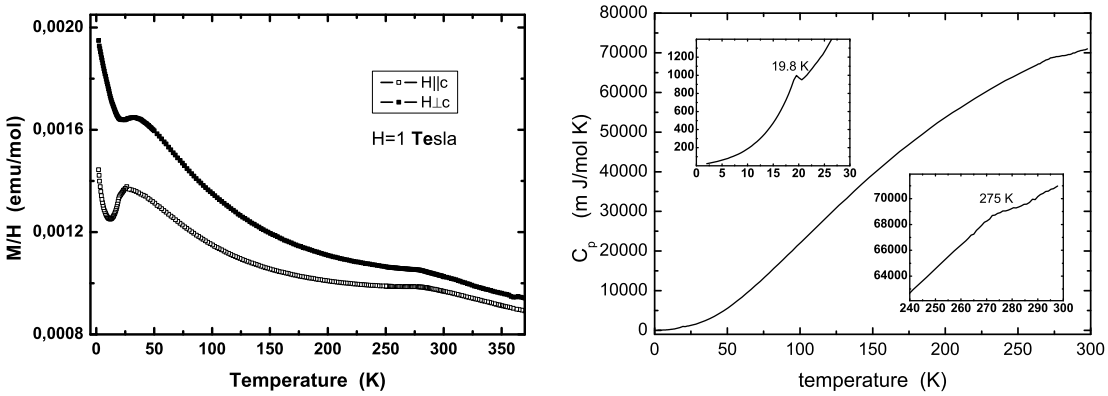

Figure 4.4: Left: Susceptibility data of a $Na_{0.82}CoO_2$ single crystal in a magnetic field of 1 T parallel (open squares) and perpendicular (filled squares) to the c–axis. Right: Specific heat of the same crystal in a temperature range between 2 and 300 K. The insets enlarge the temperature ranges between 2 and 30 K and between 240 and 300 K.

In figure 4.5(b) magnetisation loops up to 14.5 T are shown for the temperature T=4.2 K for the magnetic field perpendicular and parallel to the crystallographic c axis. Note that for both directions (increasing and decreasing fields, respectively) the curves plot directly on top of each other (not shown here).
As it has been pointed out earlier, the Co spins are oriented parallel to the c–axis [62,144]. Therefore, for the dependence of the magnetisation at fields perpendicular to the c–axis a nearly straight line is expected. However, at low temperatures and low fields, the magnetisation curve deviates from a straight line (figure 4.5(b)). This deviation is due to uncoupled, paramagnetic spins since the curve can be described by a straight line plus a Brillouin function. From such a fit, the number of uncoupled spins has been found to amount to 0.3% of all Co ions. The slope $\chi_{0,ab}$ of the straight line has been determined to be $4.7 \cdot 10^{-3} \mu_B/TCo$.

Below the transition temperature $T_N = 19.8$ K for fields parallel to the c–axis, a spin–flop transition at ∼8.5 T occurs, supported by a linear part of the curve that can be extrapolated to zero. The change in magnetisation during the spin–flop amounts to $15.6 \cdot 10^{-3} \mu_B/Co$. Below the spin–flop, the curve can be fitted by a straight line plus a weak signal of a Brillouin function. Again, the number of free spins could be estimated to amount to 0.3% of all Co ions. The slope of the straight line at low fields is $2.9 \cdot 10^{-3} \mu_B/TCo$. At high fields, i.e. above the spin–flop field, the magnetisation curve can be fitted by a straight line running through the origin, emphasising the spin–flop nature of the transition at ∼8.5 T. Its slope $\chi_{0,c}$ could be estimated to be $4.1 \cdot 10^{-3} \mu_B/TCo$. Since the g–factor ratio $(g_{ab}/g_c)^2$ is connected to the fitted slopes χ_0 of the data in figure 4.5(b), the g–factor ratio could be estimated to

$$\frac{g_{ab}}{g_c} = \sqrt{\frac{\chi_{0,ab}}{\chi_{0,c}}} = 1.1 \tag{4.1}$$

With increasing Na intercalation the ratio between Co^{3+} and Co^{4+} ions increases

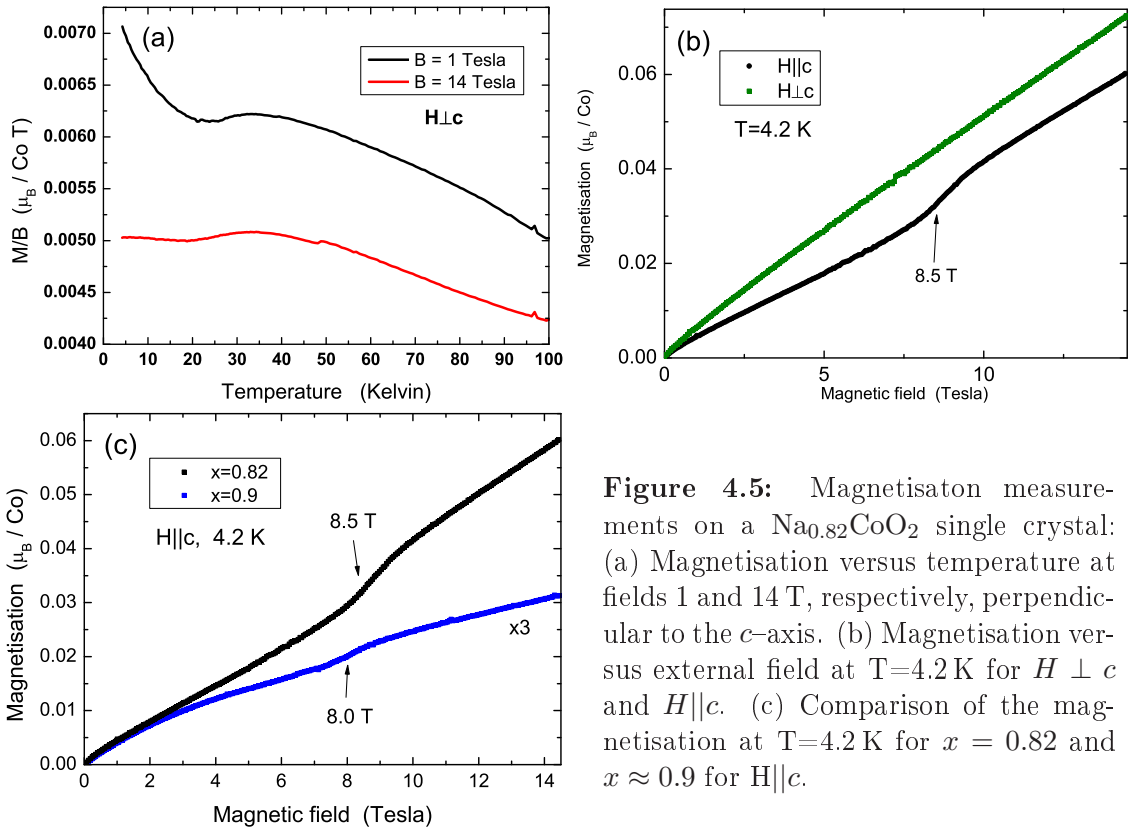

Figure 4.5: Magnetisaton measurements on a $Na_{0.82}CoO_2$ single crystal: (a) Magnetisation versus temperature at fields 1 and 14 T, respectively, perpendicular to the c–axis. (b) Magnetisation versus external field at T=4.2 K for $H \perp c$ and $H||c$. (c) Comparison of the magnetisation at T=4.2 K for $x = 0.82$ and $x \approx 0.9$ for H||c.

until for $x = 1$ only Co^{3+} ions exist. In a low spin state, Co^{3+} is non–magnetic (S=0) and Co^{4+} carries a spin S=1/2. Thus, if only the Co^{4+} ions are responsible for the magnetism, the value of M should decrease with increasing x.
In addition to the measurements of a sample with $x = 0.82$, also a sample with $x \approx 0.9$ [1] has been measured, showing the spin–flop transition at a slightly lower field $B_{SF} \sim 8.0\,\mathrm{T}$ as the one with $x = 0.82$. A shown in figure 4.5(c), this is indeed the case which confirms the idea of a low spin state (especially for the Co^{3+} ions) where only the Co^{4+} ions carry a spin and are thus responsible for the magnetic properties of the system. Note that the magnetisation of the $x = 0.9$ sample has been multiplied by a factor 3. In addition to that, it is obvious that the low field region in the curve of the $x \approx 0.9$ crystal cannot be fitted by a straight line, but by a sum of a straight line and a Brillouin function. For the $x = 0.9$ sample, the amount of free spins could be determined to be 0.7% per Co ion. The existence of unpaired spins at very high doping levels is already understandable in a very basic picture, since at high doping the number of magnetic S=1/2 ions decreases more and more leading to the naive picture that some S=1/2 ions become isolated and thus unpaired.

[1] The $x \approx 0.9$ single crystal was also grown by the floating zone method [44].

Chapter 5

At the microscopic scale: The electronic structure of Na_xCoO_2

In solid state physics, a wealth of different phenomena such as various types of magnetic or transport properties, ordering phenomena, or effects as strange as high temperature superconductivity can be observed. Just looking at the phase diagram of doped cuprates reveals antiferromagnetism, spin–glass behaviour, striped ordered phases, structural and metal–insulator transitions, and, of course, a regime of superconducticity. The driving force behind all of these phenomena determining the material properties, is the electronic structure near the Fermi level. Therefore, it is crucial for an understanding of the physics of these effects to have a very good knowledge of the electronic structure.

There are many ways in gaining information on the electronic structure theoretically and experimentally, for example, band structure or cluster calculations, and various spectroscopic techniques such as angle resolved photoemission (ARPES), optical spectroscopy, (core–level) X–ray photoemission (XPS), X–ray absorption spectroscopy (XAS, NEXAFS or XANES), or resonant inelastic X–ray scattering (RIXS).

In this chapter, the electronic structure of Na_xCoO_2 will be discussed in great detail, starting with an overview of the results already presented in the literature (section 5.1), followed by the results of X–ray absorption and photoemission experiments on a wide doping range (section 5.2) and their interpretation gained from cluster calculations (section 5.3). Finally, an approach from a multiband model explaining the Fermi surface topology is presented (section 5.4).

5.1 Introduction

Motivated by the discovery of superconductivity in $Na_{0.35}CoO_2 \cdot 1.3H_2O$ [40, 68, 72] and its relation to the high temperature superconducting cuprates, intensive work on the electronic structure has been performed. It has been argued that Na_xCoO_2 is probably the only system other than cuprates in which a doped Mott insulator becomes a superconductor, although the fully undoped system Na_0CoO_2 has not yet been synthesised [83, 87]. Usually, the intercalated water molecules are mainly considered as spacer for the CoO_2 planes emphasising the two–dimensionality of the system. However, Milne *et al.* [101] proposed that the intercalated water also acts as a charge donator leading to an off–stoichiometric Co^{3+}/Co^{4+} ratio.

Naturally, the electronic structure of Na_xCoO_2 is strongly influenced by the crystal structure which is composed of stacked quasi two–dimensional CoO_2 planes separated by layers of Na with a nominally valence +1, each Na atom donating one electron to a CoO_2 layer. The CoO_2 layers consist of edge–sharing CoO_6 octahedra, so that a triangular Co layer is sandwiched by two (triangular) O layers (see also figure 3.1 in section 3.1), leading to strong topological frustration [83,84,87]. However, the spacial arrangement of the Na ions also plays a crucial role for the physics of this material. There are two basic positions for the Na ions, one directly above or below a Co site and another one in a center position of a triangle spanned by the Co lattice (see also figure 5.4, 7 pages below). In addition, the CoO_6 octahedra are distorted in such a way that the resulting symmetry is trigonal. In general, due to a cubic crystal field formerly degenerate $3d$ states split into three–fold degenerate t_{2g} states (d_{xy},d_{yz}, and d_{zx}) and two–fold degenerate e_g states ($d_{x^2-y^2}$ and $d_{3z^2-r^2}$). Upon an additional trigonal distortion the e_g states may be lifted somewhat in energy, but remain degenerate, whereas the t_{2g} states are split further into a single a'_{1g} level and a two–fold degenerate e'_g level. Here the prime denotes states due to the trigonal distortion. In order to avoid confusion these states will be named in the following as e_g^σ (formerly e_g), a_{1g} (formerly a'_{1g}) and e_g^π (formerly e'_g). These states can be represented as

$$|e^\sigma_{g\pm}\rangle = \mp\frac{1}{\sqrt{2}}\big(|3z^2 - r^2\rangle \pm i|x^2 - y^2\rangle\big), \tag{5.1}$$

$$|a_{1g}\rangle = \frac{1}{\sqrt{3}}\big(|xy\rangle + |yz\rangle + |xz\rangle\big) \tag{5.2}$$

and

$$|e^\pi_{g\pm}\rangle = \mp\frac{1}{\sqrt{3}}\big(|xy\rangle + \exp^{\pm i2\pi/3}|yz\rangle + \exp^{\pm i4\pi/3}|xz\rangle\big). \tag{5.3}$$

An illustration of the energy diagram and the corresponding orbitals is shown in figure 5.1. Note that the a_{1g} orbital is the only one having only one preferential direction: the (1 1 1) direction, i.e. the crystallographic c–axis.

The first method that have been used to describe the electronic structure of Na_xCoO_2 were local density approximation (LDA) calculations [57, 93]. The calculations show that the e_g and t_{2g} bands are separated approximately by 2.5 eV

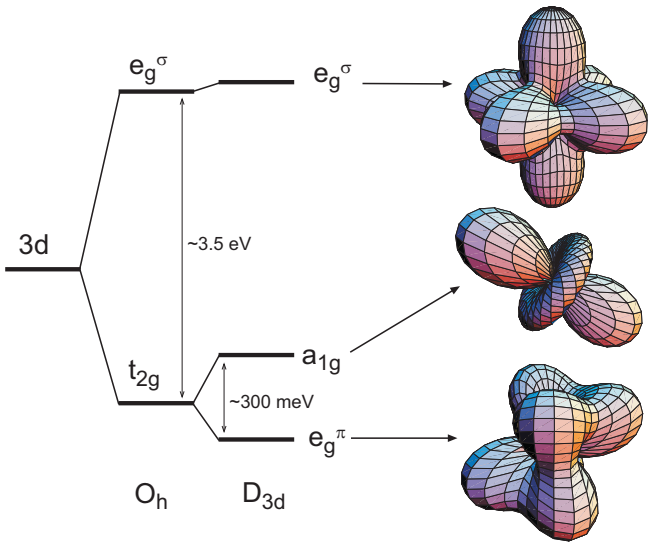

Figure 5.1: Energy diagram of the distorted Co $3d$ levels in trigonal symmetry. As motivated by experiment and theory, the e_g^π states are drawn lower in energy than the a_{1g} state. On the right, an illustration of the corresponding orbitals is given. The a_{1g} orbital is pointing along the (1 1 1) direction of the octahedra, i.e. the crystallographic c–axis. The shape of the orbitals is calculated using equation (5.1), (5.2), and (5.3).

while the t_{2g} bandwidth amounts to 1.6 eV. Although the a_{1g} and e_g^π states overlap and mix to some extend, these states are roughly separated in energy by the rhombohedral field, with the states at the top of the t_{2g} manifold, where the Fermi energy ϵ_F lies, having dominant a_{1g} character in $Na_{0.5}CoO_2$ [57]. The calculated Fermi surface (FS) shows a large cylindrical hole surface with a hexagonal shape around the $\Gamma - A$ line. It has dominant a_{1g} character as well as small hole–like sections centered about 2/3 of the way out on the $\Gamma - K$ and $A - H$ directions that have a mixed a_{1g} and e_g character. A flattening of the large Fermi surface regions along the $\Gamma - K$ directions implies that the hopping giving rise to the dispersion of the a_{1g} derived bands is via the O p_z orbitals [57], while direct a_{1g}-a_{1g} hopping is small, as might be expected from the Co–Co distance. In addition, the c–axis dispersion of a_{1g} derived states is higher than that of e_g^π derived states, as the a_{1g} states are directed along the c–axis and mix with combinations of O $2p$ states that are also directed along c, even though these are weak effects near ϵ_F. Furthermore, the system is assumed to be a strongly correlated system, characterised by $W \ll U_{dd}$, with an effective on–site Hubbard U_{dd} of 5-8 eV [57].

Experimentally, angle resolved photoemission (ARPES) experiments confirmed a Fermi surface with a large hole pocket around the Γ point showing a weak hexagonal character. The predicted small Fermi surface pockets near the K points could not be observed, however, neither in flux grown crystals with $x = 0.7$ [95] nor in crystals grown using the floating–zone technique with $x = 0.6$ [96]. The absence of the hole pockets may result from a shift of the chemical potential due to electron correlation effects that can push these bands away from the Fermi level or wash out their relative intensity [95], or from many–body interactions [96]. This point will be discussed in more detail later on in section 5.4. A low energy peak at about 0.7 eV has been found in photoemission spectroscopy (PES) and together with LDA calculations [57], this excitation has been assigned to Co $3d$ states, whereas the O $2p$ states are somewhat higher in energy. Since these Co $3d$ and O $2p$ peaks are separated, Yang *et al.* conclude that the Co d - O p hybridisation has to be weak [96]. A correlation

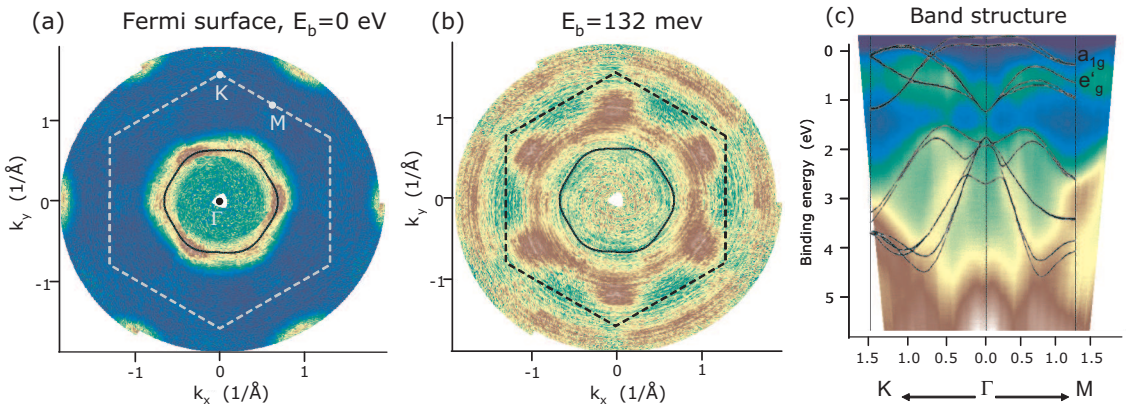

Figure 5.2: $Na_{0.7}CoO_2$: Angle resolved photoemission data show no hole pockets at the Fermi surface (a), but the corresponding bands lie about 133 meV below the Fermi energy (b). In figure (c), the band structure from K via Γ to M is shown. The measurements were done by J. Geck [127].

satellite at 11 eV in the PES spectra indicates a strongly correlated behaviour with a Hubbard $U_{dd} \sim 5\,\text{eV}$ [95]. As an additional parameter, the effective single–particle hopping parameter t_{eff}[1] has been evaluated from a tight–binding band model on the triangular lattice that fits the measured band dispersion. Hasan *et al.* found $t_{eff} = 10 \pm 2\,\text{meV}$ [95] whereas Yang *et al.* quote $t_{eff} = -44\,\text{meV}$ along $\Gamma - M$ and $t_{eff} = 12 - 26\,\text{meV}$ along $\Gamma - K$ [96]. Since the used Hamiltonian is not given in these publications, the difference in sign between these two publications cannot be judged. Both get similar absolute values and it is worth noting that the value of t_{eff} is similar to the (almost isotropic) exchange parameter $|J| \approx 10\,\text{meV}$ [99, 144].

Further information has been derived from ARPES experiments done by J. Geck, S. Borysenko and co–workers, IFW Dresden, on a flux grown single crystal with stoichiometry $x = 0.7$ [127]. Similar to earlier publications, they found a cylindrical hole–like Fermi surface around the Γ point with a hexagonal shape, but could not detect the predicted hole pockets near the Fermi energy either. The bands that are responsible for the hole pockets are pushed below the Fermi surface to higher binding energies as it is shown in figure 5.2(a) and (b) for binding energies $E_B = 0$ and 0.132 eV. In figure (c) an intensity plot down to binding energies of 6 eV along the $K - \Gamma - M$ direction is shown.

A systematic photoemission study on a wide range of Na concentrations ($0.3 \leq x \leq 0.72$) revealed that in all (metallic) samples only a single hole–like Fermi surface centered around the Γ point has been observed. The area of the Fermi surface changes with x according to the Luttinger theorem [153]. The sinking of the hole pockets near the K point has been found to be independent of doping and temperature [97].

High–energy ($h\nu = 5.95\,\text{keV}$) photoemission experiments [154] support a moderate

[1] The effective hopping parameter t_{eff} is a renormalised value from the original band parameter t, estimated to be $t \sim 130\,\text{meV}$ and a total bandwidth $(12t) \sim 1.6\,\text{eV}$ [57, 74], the reduction of t indicates a strong correlation of the electrons.

on–site Coulomb correlation energy $U_{dd} \sim 3 - 5.5\,eV$. From cluster calculations, a mixed character of the electronic structure has been obtained which is more Mott–Hubbard like than charge–transfer like [154] in terms of the ZSA phase diagram [155].

As a further attempt to explain the experimental results, calculations of LDA, local spin density approximation (LSDA), and LSDA+U [156] with a moderate U of 4.0 eV have been done [157]. Here, the Na ions have been treated as a uniform positive background in order to assure charge neutrality. It has been stated, that the presence of a Na potential has little effect on the essential physics [116]. The authors found, that both LDA and LSDA predict a large Fermi surface around the Γ point and small hole pockets near the K points at doping levels $x \leq 0.5$. In contrast, no hole pockets were observed within LSDA+U for all doping levels but the hexagonal shape of the hole–like Fermi surface changes upon doping towards a circle like shape [157].

Furthermore, LSDA+U calculations show that undoped CoO_2 (i.e. Na_0CoO_2) is a charge transfer insulator within LSDA+U and a metal with a high density of states (DOS) at the Fermi level within LSDA. On the other hand, $(CoO_2)^{1.0-}$ (like Na_1CoO_2) is a band insulator with a gap of 2.2 eV, whereas systems with fraction doping are half metal in the absence of charge ordering and assuming a ferromagnetic phase [116]. In the undoped case, a charge transfer gap between the O $2p$ and Co $3d$ (a_{1g}) states has been found. This gap decreases upon electron doping due to a filling of the formerly unoccupied a_{1g} level which is split–off from the former t_{2g} triplet due to on–site Coulomb interaction. At a doping of $x = 0.3$ the Co $3d$ a_{1g} band touches the O p bands in LSDA+U and merges into the rest of the band. For $x = 1.0$ all t_{2g} states are occupied and a new gap (larger than in the undoped case) appears between the t_{2g} and the e_g states leading to a band insulator [116].

However, not only correlation effects change the electronic structure, but it is also highly sensitive to the oxygen height in the CoO_6 octahedra [57, 158]. Ni *et al.* [158] carried out calculations using the pseudopotential method with local spin density functional approximation, finding that at low doping, in particular $x = 0.25$, Na_xCoO_2 is an itinerant ferromagnetic metal with large hybridisation between cobalt and oxygen orbitals. When the Na content is increased, both the ferromagnetism and hybridisation decrease. When $x = 0.5$, only a tiny ferromagnetism is left, and the hybridisation vanishes. Thus, changing the Na content generates a phase transition that leads from the wide band ferromagnetic metal to a narrow band paramagnetic metal. Such a strong suppression of the ferromagnetism is supposed to mainly originate by the local distortions of the oxygen ions around the cobalt atoms [158]. Experimentally, a distortion of the oxygen ions around the Co^{3+} ions and also the existence of strong hybridisation between the cobalt and oxygen ions at low doping levels has indeed been found by X–ray absorption spectroscopy [148]. However, fully different from what is predicted by Ni *et al.*, a strong hybridisation exists for higher doping levels, too (see also the proceeding subsection 5.2.2). Ni *et al.* also claim that the Na ions mainly act as charge donators with a small charge density around the Na ions and conclude that the compounds are clearly two–dimensional [158].

Also from X–ray absorption spectroscopy a hybridisation between the sodium and oxygen ions has been found, indicating a coupling between the Na and CoO_2 layers and therefore, only a weak two–dimensionality [148] is expected, as it is also found in similar coupling constants J from inelastic neutron scattering experiments [99, 144].

Various theoretical attempts have been done, mainly focused on single–band models on the frustrated triangular lattice [83–87, 89, 161], but multi–orbital models [159, 162, 163], and density functional calculations [57, 93, 94, 112, 116, 145, 164] have also been performed as partially described above. At the Γ point, the states with a_{1g} and e_g^π symmetry are clearly split, but on average over the entire Brillouin zone the mixing between a_{1g} and e_g^π is substantial, with the e_g^π states being lower in energy [57]. From a point charge model for a distorted CoO_6 octahedron, Koshibae and Maekawa [159] found the a_{1g} state being stabilised against the e_g^π states by $\sim$0.025 eV and concluded that this discrepancy can only lead to the fact that the energy splitting does not originate in the crystal field due to the distortion, but is determined by the kinetic energy of the electrons. Neglecting the rhombohedral distortion, Koshibae and Maekawa [159] follow the idea that the main hopping path of an electron between Co $3d$ states is via O $2p$ orbitals rather than direct Co $3d$ hopping. Actually, from X–ray absorption spectroscopy spectral evidence has been found that the low–energy excitations of Na_xCoO_2 have significant O $2p$ character [148, 165]. Tight–binding calculations found the direct overlap integral between the cobalt ions to be much smaller than the indirect hopping over the oxygen $2p$ orbitals [162], supporting such a scenario. This prompted Koshibae and Maekawa to constructed a three–band tight–binding model of degenerate t_{2g} orbitals, where the only hopping processes are indirect hopping processes over intermediate oxygen orbitals. This approach leads towards a system of four independent and interpene-

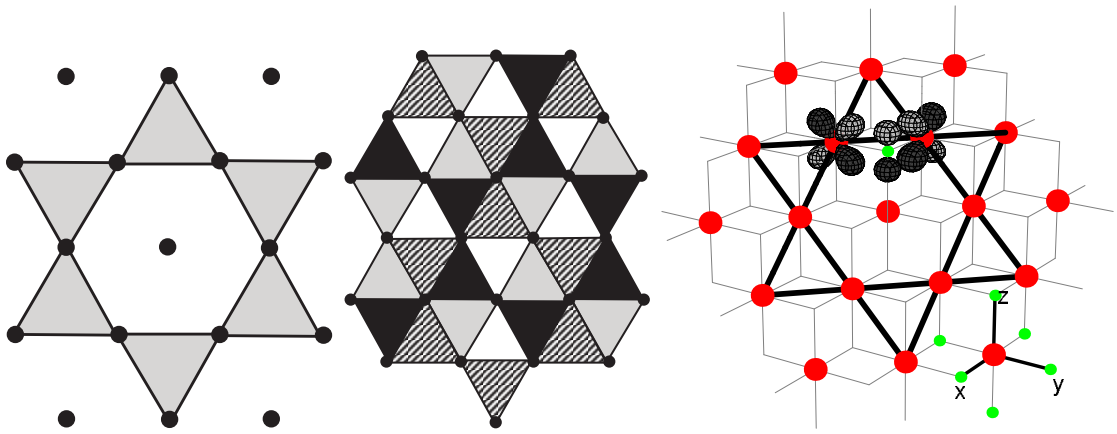

Figure 5.3: Illustration of the Kagomé lattice in the triangular lattice of cobalt ions (a). In figure (b) the four interpenetrating Kagomé lattices are shown, represented as gray, black, hatched, and white (figure (a) and (b) are taken from Ref. [159]). For further illustration, in figure (c) a Kagomé lattice including the cobalt and oxygen ions and also orbitals involved in the effective hopping are shown (figure (c) is taken from Ref. [160].

trating Kagomé lattices. The triangle made of the states $|zx,1\rangle$, $|yz,2\rangle$, and $|xy,3\rangle$, as shown in figure 5.3, is an elementary unit of the Kagomé lattice. This changes the eigenstates of the triangle to

$$|a_{1g}\rangle^K = \frac{1}{\sqrt{3}}\big(|xy,3\rangle + |yz,2\rangle + |xz,1\rangle\big) \tag{5.4}$$

and

$$|e^{\pi}_{g\pm}\rangle^K = \mp\frac{1}{\sqrt{3}}\big(|xy,3\rangle + \exp^{\pm i2\pi/3}|yz,2\rangle + \exp^{\pm i4\pi/3}|xz,1\rangle\big), \tag{5.5}$$

with the eigenstate of $|a_{1g}\rangle^K$ lying higher in energy than that of $|e^{\pi}_{g}\rangle^K$ [159]. As a continuation of this work, Indergand *et al.* [166] calculated a multi–orbital model for the CoO_2 layer in combination with a local Coulomb interaction within a tight–binding approximation including Co–O π hybrisidation as the most relevant hopping process. They confirmed the existence of the Kagomé lattice and were able to reproduce the Fermi surface, but including the hole pockets. In addition, they found a metallic state that allows also charge and spin density ordering together with ferromagnetic tendencies that are dominant compared to the other. This dominance of the ferromagnetic state is enhanced upon an additional trigonal distortion.

5.2 Spectroscopy

Motivated by the discovery of an unexpectedly large thermopower accompanied by low resistivity and low thermal conductivity in Na_xCoO_2 [37] and the discovery of superconductivity in the hydrated compound $Na_{0.35}CoO_2 \cdot 1.3H_2O$ in 2003 [40], experiments using spectroscopic methods such as near edge X–ray absorption fine structure (NEXAFS) at the O K, the Co $L_{2,3}$, and the Na K–edge, as well as X–ray photoemission spectroscopy (XPS) on a wide doping range of Na_xCoO_2 have been performed. The similarity of the Na cobaltates to the high temperature superconductors (HTSC) – both are transition metal oxides and adopt a layered crystal structure with quasi-two-dimensional $(Cu,Co)O_2$ layers – is an important aspect of actual research activities. However, in contrast to the HTSC cuprates, the CoO_2 layers consist of edge sharing CoO_6 octahedra which are distorted in a way that the resulting symmetry is trigonal, as described above. The trigonal coordination of the Co sites results in geometric frustration which may favour unconventional electronic ground states. The geometrically frustrated CoO_2 sublattice also exists in the non–hydrated parent compound Na_xCoO_2, which has been investigated in this work. The intercalation of water is expected to have little effect on the Fermi surface besides the increase in two dimensionality due to the effect of expansion [167, 168] and an off-stoichiometric Co^{3+}/Co^{4+} ratio [100, 101]. The idea of water acting as charge donators to the CoO_2 layers indicating that Na substoichiometry alone does not control the electronic doping of these materials [101] has been recently denied by Co K– edge NEXAFS experiments [169], where no change in the Co valence has been found upon hydration.

As predicted by calculations [159] and shown experimentally [148, 165], the e_g^π states are lower in energy and are therefore filled, while the a_{1g} states are partially filled as a function of x. Therefore, the a_{1g} states govern the relevant low-energy excitations. From magnetisation, specific heat, and conductivity measurements for various doping levels, three phase transitions as a function of temperature have been observed: a low temperature bulk antiferromagnetic transition at $T_N \approx 20\,\mathrm{K}$ for $0.75 \leq x \leq 0.9$ ([39,62,64]) and two high temperature transitions at about 280 K in a $Na_{0.82}CoO_2$ sample [138] and at 323–340 K in samples with $x \approx 0.75$ [60, 170]. The origin of the 280 K transition has been discussed in terms of charge ordering and the formation of magnetopolarons due to a charge induced Co $3d$ spin state transition from a low spin state to an intermediate spin state [138]. Such a spin state transition occurs for instance in the related compounds $La_{1-y}Sr_yCoO_3$ [139–143]. In some samples, a third transition at around 340 K is observed. It has been suggested that this is due to a structural transition involving Na ordering [60, 125, 170], which is supported by Huang *et al.* who found a structural phase transition concomitant with a shift of a large fraction of the Na ions from a high–symmetry position to a lower–symmetry position [60].

In this study, non–hydrated compounds in a wide doping range have been investigated within all three different regions $x < 0.5$, $x = 0.5$, and $x > 0.5$.

The investigated single crystals have been grown by two different methods. First, single crystals of $Na_{0.75}CoO_2$ were grown using the travelling solvent floating–zone method, crystals with a lower Na concentration were produced employing de–intercalation with bromium from the highly doped samples by C. Sekar and G. Krabbes at the IFW Dresden, as well as by C.T. Lin and D.P. Chen at the MPI Stuttgart. The initial characterisation of the samples has been carried out using energy dispersive X–ray analysis (EDX), X–ray diffraction, and chemical analysis done by J. Acker at the IFW Dresden. Details of the crystal growth, de–intercalation, and characterisation of the resulting samples are presented elsewhere [44, 171]. Second, high–quality single crystals were grown by the sodium chloride flux method by H. Berger at EPFL Lausanne, Switzerland, as thoroughly described in Ref. [69]. In order to change the Na concentration of the flux grown crystals, the samples have been treated using electrochemical methods by C. Malbrich and L. Dunsch at the IFW Dresden. Both methods lead to the same spectra.

In the following, the experimental results of X–ray absorption and photoemission spectroscopy on non–hydrated crystals will be presented and discussed in great detail. In part, the following discussion has already been published in Physical Review B, **74** 115123 in 2006 [148].

5.2.1 X–ray photoemission spectroscopy

The X–ray photoemission spectroscopy (XPS) measurements were performed using a Physical Electronics PHI 5600 commercial spectrometer equipped with a monochromatic Al–K_α X–ray source with an energy resolution of about 0.35 eV. The size

of the irradiated spot was about 1mm × 1mm. The samples were cleaved *in–situ* at a pressure of about 2×10^{-9} mbar and measured at $p = 5 \times 10^{-10}$ mbar at room temperature.

As explained above, the crystal structure of Na_xCoO_2 consists of alternating quasi two–dimensional CoO_2 layers separated by insulating Na layers. In this crystal structure, Na occupies two different sites, Na1 and Na2. Both Na ions are surrounded by six O ions, three belonging to the CoO_2 layer on top and three to the layer below. However, while all oxygen neighbours of Na1 belong to different Co ions (i.e. different octahedra), the oxygen ions of the Na2 ion belong to two octahedra (one on top and one below) (figure 5.4(left)). Since the average Na1–O and Na2–O bond length are identical, the Co ion must be responsible for a different site occupation [43]. From first and second nearest neighbour repulsion Jorgensen *et al.* [43] conclude that Na2 has a weaker bonding, which leads to a smaller occupancy of the Na2 site compared to the Na1 site. From a Rietveld refinement of diffraction data they indeed found such a behaviour in $Na_{0.31}CoO_2 \cdot 1.25D_2O$ and $Na_{0.61}CoO_2$.

From XPS experiments on two Na_xCoO_2 samples with $x = 0.3$ and $x = 0.7$, the same behaviour could be observed (figure 5.4(right)). For $x = 0.3$ mainly one peak at a binding energy of ≈1070 eV exists as well as a small shoulder at ≈1071.5 eV binding energy, which can be interpreted as Na1 and Na2, respectively. With increasing sodium content ($x = 0.7$) this shoulder grows to a true peak being as strong as the one at lower binding energies which has not changed compared to the lower doping case. This behaviour is consistent with the existence of two Na sites which are filled almost successively.

The accuracy of the stoichiometry given for these samples has been checked by XPS, too, giving a surprisingly good agreement to the predictions of the crystal

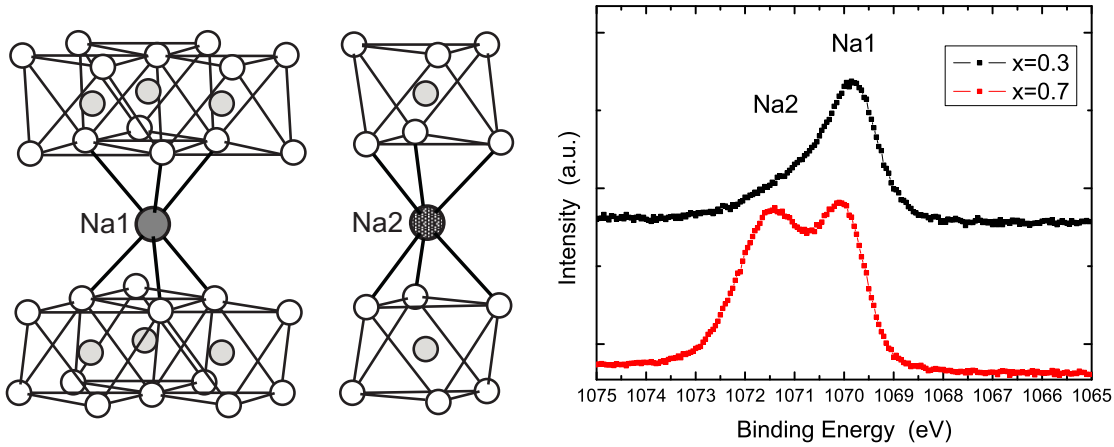

Figure 5.4: Left: Sketch of the local structure of the two different Na sites, Na1 and Na2 (figure taken from Ref. [43]). Right: Result of the XPS experiment on Na_xCoO_2 with $x = 0.3$ and $x = 0.7$. One clearly observes the change in the occupation of the two different Na sites upon doping.

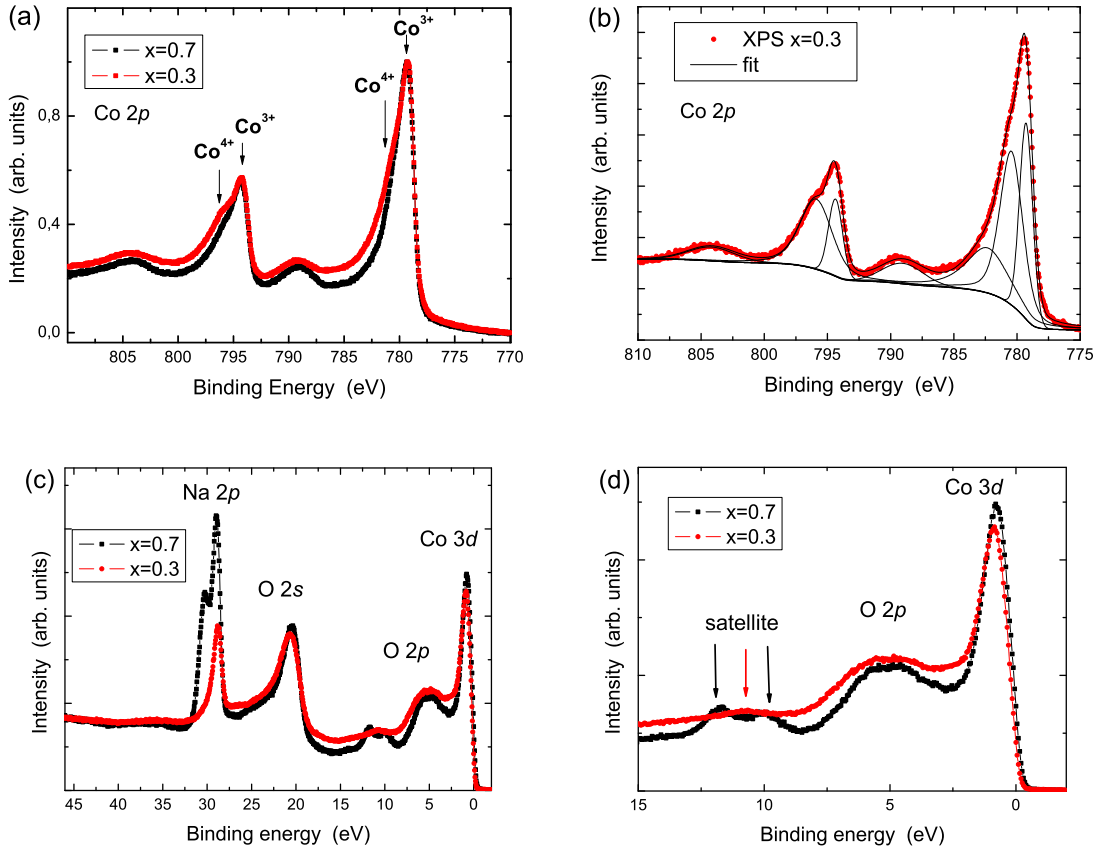

Figure 5.5: Na_xCoO_2: XPS spectra of the Co $2p$ level (a) and a fit for the $x = 0.3$ doping level (b). (c) and (b) show the low binding energy region up to 45 and 15 eV, respectively.

grower[2].

In a previous paper, Chainani *et al.* [154] presented the results of the investigation of two crystals $Na_{0.7}CoO_2$ and $Na_{0.35}CoO_2 \cdot 1.3H_2O$ using XPS. At the Co $2p$ energy level they observed two Co peaks ($2p_{1/2}$ and $2p_{3/2}$) and two satellites. Within the Co peaks they found a structure which they interpreted as belonging to Co^{3+} and Co^{4+} ions. In our own measurements, a very similar result has been found. It should be stressed that the change in spectral weight between two samples with $x = 0.3$ and $x = 0.7$ is very weak as shown in figure 5.5(a). Even though the relative Co^{3+}/Co^{4+} occupancy should have been inverted between the two doping levels, only a tendency of a spectral weight shift is observed. This result may indicate that the system is highly covalent leaving only a few "pure" Co^{4+} (i.e. d^5) ions left in the system. In figure 5.5(b) a fit of the $x = 0.3$ Co $2p$ spectra is shown. Using a Shirley background,

[2] Na_xCoO_2 turned out to be a material that is very difficult to grow in a single phase with a homogeneous Na concentration. Therefore, all stoichiometries given in literature (and in this work, too), contain a small error in x: $Na_{x\pm\delta}CoO_2$. Note, that also the oxygen content can vary slightly from its value 2.

the two satellites can be fitted by a broad, single peak, whereas the $2p_{1/2}$ peak can be nicely fitted by two peaks, and the $2p_{3/2}$ peak by two strong and one weak peak. Note that such a fitting is very rough since the spectrum is also affected by the resulting $2p$ core hole leading to a multiplet splitting [2], so that an easy picture with two peaks (Co^{3+} and Co^{4+}) of the same width is not correct. Nevertheless, there must be two main peaks connected to Co^{3+} and Co^{4+} plus a broad satellite which can be seen is this fitting. The satellites seen in the spectrum emphasise an existing hybridisation between the Co and O ions inside the CoO_6 octahedra. In the core–hole final state in the Co $2p$ XPS spectra, the core–hole potential U_{dc} lowers the $d^{n+1}\underline{L}$ and $d^{n+2}\underline{L}^2$ states by U_{dc} and $2U_{dc}$ as compared to the d^n state (here $n = 5, 6$ and $\underline{L}$ denotes a ligand hole), causing a different ordering of levels, which is the reason for the strong satellite structure [2, 12, 172] (see also chapter 1.1). Note, that the situation for the O $1s$ XPS is quite different, since the O $1s$ core–hole potential will push up further the $d^{n+1}\underline{L}$ and $d^{n+2}\underline{L}^2$ states. Therefore the lowest energy state with an O $1s$ core hole present is similar to that of the ground state and therefore little if any satellite structure is observable [12, 173].

At low binding energies (below 45 eV), the excitations from Na $2p$ appear at around 30 eV, O $2s$ at 23 eV, O $2p$ at around 5 eV, and the Co $3d$ valence band at 0.7 eV (figure 5.5(c)). In principle, the Na $2p$ states show a similar behaviour as it has been observed at the Na $1s$ states: While for $x = 0.3$ mainly one site is occupied, for $x = 0.7$ also the second Na site is partially occupied. The O $2s$ spectra remain unchanged upon doping, indicating no additional oxygen in both samples (or the same amount of additional oxygen, but that is very unlikely). At around 5 eV the O $2p$ states are localised and somewhat lower the Co $3d$ valence states at ca. 1 eV. These states are clearly separated which leads Yang *et al.* [96] to the idea that the Co-O hybridisation has to be weak. While the Co $3d$ states do not show a significant change upon doping (figure 5.5), the O $2p$ states become broader and stronger for lower x, indicating a strong hybridisation between these states. As it will be shown in the next section, the charge transfer energy $\Delta = E(d^{n+1}\underline{L}) - E(d^n)$ is actually negative for Co^{4+}. Both stoichiometries show a satellite peak around 11 eV, but interestingly they are different in shape. While for $x = 0.3$ there exists only one peak, the spectrum for $x = 0.7$ shows a double peak structure due to multiplet effects (for a detailed explanation see the next section 5.3).

An important question regarding the Na cobaltates is the sample treatment and its consequences for the electronic structure. In order to address this point, temperature dependent XPS measurements on a $x = 0.7$ crystal grown by the flux method have been performed. Since the spectrometer does not have a cryostate manipulator, the sample has been heated in the preparation chamber for an hour and transferred back into the main chamber for measuring. The results for runs between room temperature and 400°C are shown in figure 5.6. From these results, $T = 100$°C should be taken as a critical temperature. There is no difference in the spectra before and after heating at 100°C, but already after heating the sample for one hour at 150°C, the intensity at the Na $1s$ peak begins to decrease indicating a loss of Na within the probed area. This is not surprising since the Na ions are not strongly

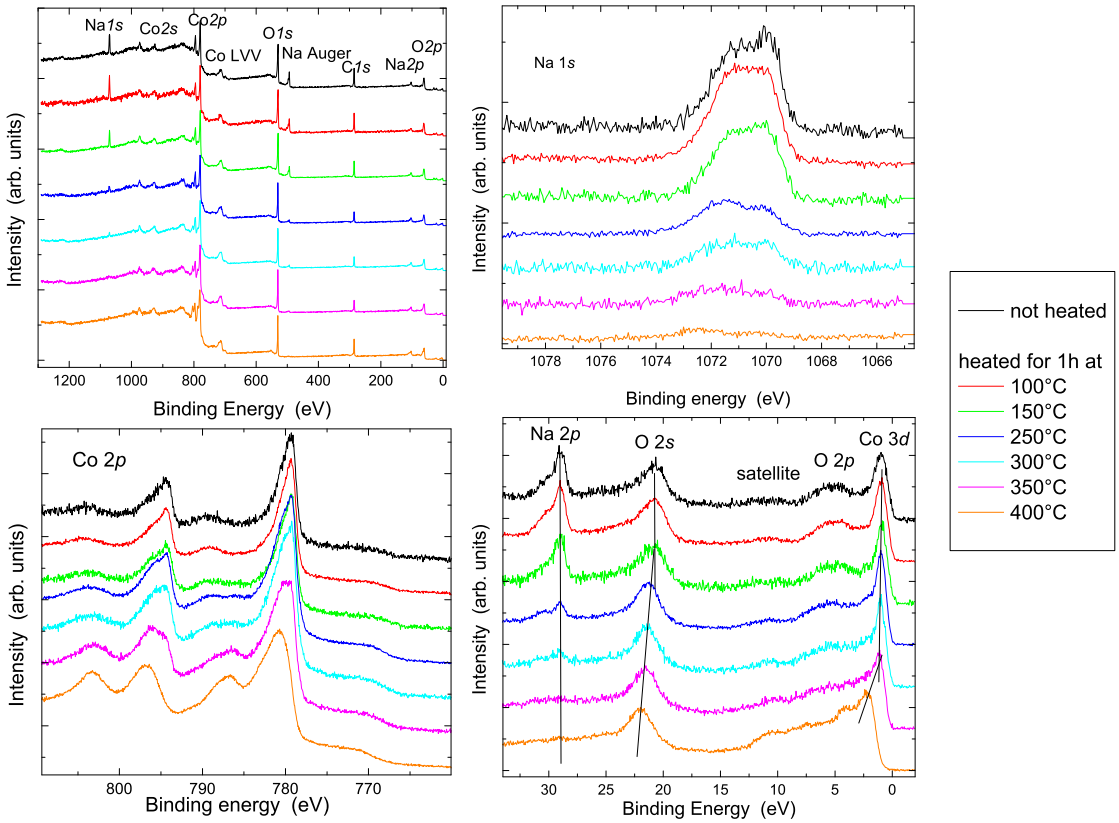

Figure 5.6: $Na_{0.7}CoO_2$: Temperature dependent XPS measurements for different binding energies.

bound within the Na layers, but are allowed to move through them. Therefore, a loss of Na with increasing temperature can be expected. When further increasing the temperature, the amount of Na constantly decreases until at 400°C no Na is left in the sample within the probed area. The position of the Na 1*s* and Na 2*p* peaks do not change with temperature, which shows that its local surrounding does not change, i.e. the CoO_6 planes do not change their structure or composition. Since the Na layer does change with temperature, a change in the peak positions for Co 2*p* and O 2*s*, as well as for the valence band is expected. Such a behaviour could indeed be observed. At temperatures above 150°C the O 2*s* peak position constantly shifts slightly towards higher binding energies, similar to the Co 2*p* peak. Interestingly, in addition to that at the Co 2*p* peak, there is a change in the spectral shape with a more pronounced charge transfer satellite with increasing temperature, consistent with an increase in the weight of the satellite at the valence band together with a broadening of the O 2*p* band. As for the satellite, mainly poorly screened multiplets of the $2p^5 3d^n$ final state (n=5,6) are responsible, whereas the main line is due to well screened $2p^5 3d^{n+1}\underline{L}$ final states, where $\underline{L}$ denotes a ligand hole at the oxygen sites surrounding the Co 2*p* core–hole site. The energy separation and the intensity ratio of these spectral features is determined by the valence–band - core–hole interaction energy U_{dc}, the effective Co 3*d* - O 2*p* hopping energy t,

and the charge transfer energy between a Co $3d$ and an O $2p$ state Δ (in Ref. [2] this relation has been shown for copper dihilates). Note that although the relative spectral weight between the main line and the satellite changes upon temperature, the peak distance remains constant. This can only be achieved if for example Δ and U_{dc} somehow depend on each other and keep their difference constant [174] (see also section 5.3). As explained above, the Co $2p$ peak shifts towards higher binding energies which is consistent with a lowering of the valence state as is expected when the Na concentration decreases. In addition to that, the intensity ratio between the main line and the satellite changes in favour of the satellite peak. Such a behaviour is also consistent with a lowering of the valence state since the charge transfer energy Δ is lower for Co^{4+} than for Co^{3+} (actually it is negative for the former, see the next section 5.3). This leads to a situation with a large amount of oxygen ligand holes already in the ground state, so that a creation of a ligand hole in the final state due to the existence of the core–hole and the resulting energy shift is not very likely to occur. Note that in this extreme case of CoO_2, containing only Co^{4+} ions with a negative charge transfer energy Δ, the description of the bands and also their classification is difficult to place into the Zaanen–Sawatzky–Allen phase diagram [155]. The resulting state could also be a charge transfer metal, rather than an insulator.

5.2.2 X–ray absorption spectroscopy

The near edge X–ray absorption fine structure (NEXAFS or short XAS) measurements of the absorption coefficient were performed at the UE52–PGM beamline at the synchrotron facility BESSY II, Berlin, analysing the drain current, and at the 8.0.1 beamline at the Advanced Light Source (ALS) synchrotron at Berkeley Labs, Berkeley, California, analysing the drain current and the fluorescence. At Bessy, the energy resolution was set to 0.09 eV and 0.16 eV for photon energies of 530 eV and 780 eV, respectively. The measurements were performed on different non–hydrated single crystals with a sodium content of nominally $x = 0.4$, $x = 0.5$, $x = 0.6$, and $x = 0.7$ at various temperatures and different polarisations of the incident synchrotron light at the sodium K, oxygen K, and cobalt $L_{2,3}$–edge. The doping levels that have been investigated belong to different and interesting regions of the phase diagram [63]: $x = 0.4$ lies in the region of a paramagnetic metal, $x = 0.5$ represents a special, insulating case, whereas $x = 0.6$ and $x \approx 0.7$ are a Curie-Weiss metal. All the crystals were of the same size with a surface area of 3mm × 3mm. The crystals were freshly cleaved *in–situ* under ultrahigh vacuum conditions (about 2×10^{-10} mbar) at 25 K, which resulted in shiny sample surfaces. Special attention has been paid to the reproducibility of the experimental data and the effects of surface contamination. The freshly cleaved surfaces turned out to be very sensitive to adsorbates. This is the reason why the fluorescence signal has not been measured, since due to setup reasons, the measurement would have downgraded the pressure inside the main chamber. Irreversible changes were observed in the O K spectra when the sample surfaces were exposed to pressures above 2×10^{-9} mbar

which can be attributed to adsorbed oxygen containing molecules at the surface. No such changes have been found for the Co absorption edges. A comparison to the temperature dependent behaviour of the Co $L_{2,3}$–edge proves that the origin of this irreversible effect is due to surface contamination and not due to a change or a transition of the whole sample, since the Co $L_{2,3}$–edge remains unchanged with temperature and pressure.

According to the dipole selection rules the O K and Co $L_{2,3}$ excitations as probed by these experiments correspond to core electron transitions into unoccupied oxygen $2p$ and cobalt $3d$ electronic states. Upon variation of the incident light polarisation, different O $2p$ and Co $3d$ orbitals can be probed [10]. For polarisation dependent measurements the samples were oriented in such a way that the direction of incident photons and the sample surface normal (i.e., the c–axis) enclose an angle of $\alpha = 70°$. The used undulator allows a rotation of the beam polarisation by 90° using the vertical and horizontal mode. This procedure avoids experimental artifacts related to the differences in the optical path and the probed area. All NEXAFS results referred to E parallel to the c–axis ($E||c$) are corrected using the formula $I_c = \frac{1}{\sin^2\alpha}(I - I_{\perp c}\cos^2\alpha)$ where $I_{\perp c}$ and I are measured NEXAFS intensities with $E \perp c$ and E in the plane defined by the c–axis and the incident photon beam, respectively. In order to compare the data, the NEXAFS spectra are normalised at higher energies where the absorption is doping independent and isotropic and the spectra for different measurements and settings should show the same intensities. The spectra are normalised at 600 eV for the O K–edge and at 810 eV for the Co $L_{2,3}$–edge.

In order to get the overall picture of the electronic structure as seen by NEXAFS measurements, two samples $x = 0.4$ and $x = 0.6$ will be discussed in the following. These two doping levels belong to the two regions around the special case $x = 0.5$. Within the phase diagram for $x < 0.75$ the main features of the electronic structure can be understood by these two representative doping levels. Therefore, it makes sense to discuss only these two cases in great detail in order to avoid confusion. Later on, more results of different doping level will be shown, underlying the results given in the next section and completing the picture.

Results and discussion

Using NEXAFS, the unoccupied energy levels close to the Fermi level can be studied by excitations from core electrons into unoccupied states. We have measured excitations from O $1s$ core levels into unoccupied O $2p$ states that are hybridised with states of primary Co and Na character, as well as excitations from Co $2p$ into Co $3d$ states. If the influence of the core hole is neglected, as is reasonable for the O $1s$ core hole excitations, a direct interpretation of the NEXAFS results in terms of the partially unoccupied density of states is possible, analogous to a one electron addition process [175, 176]. If the core hole cannot be neglected, as it is the case for Co $2p \rightarrow 3d$ excitations, the interpretation of the data requires consideration of multiplet splitting, hybridisation, and crystal field effects.

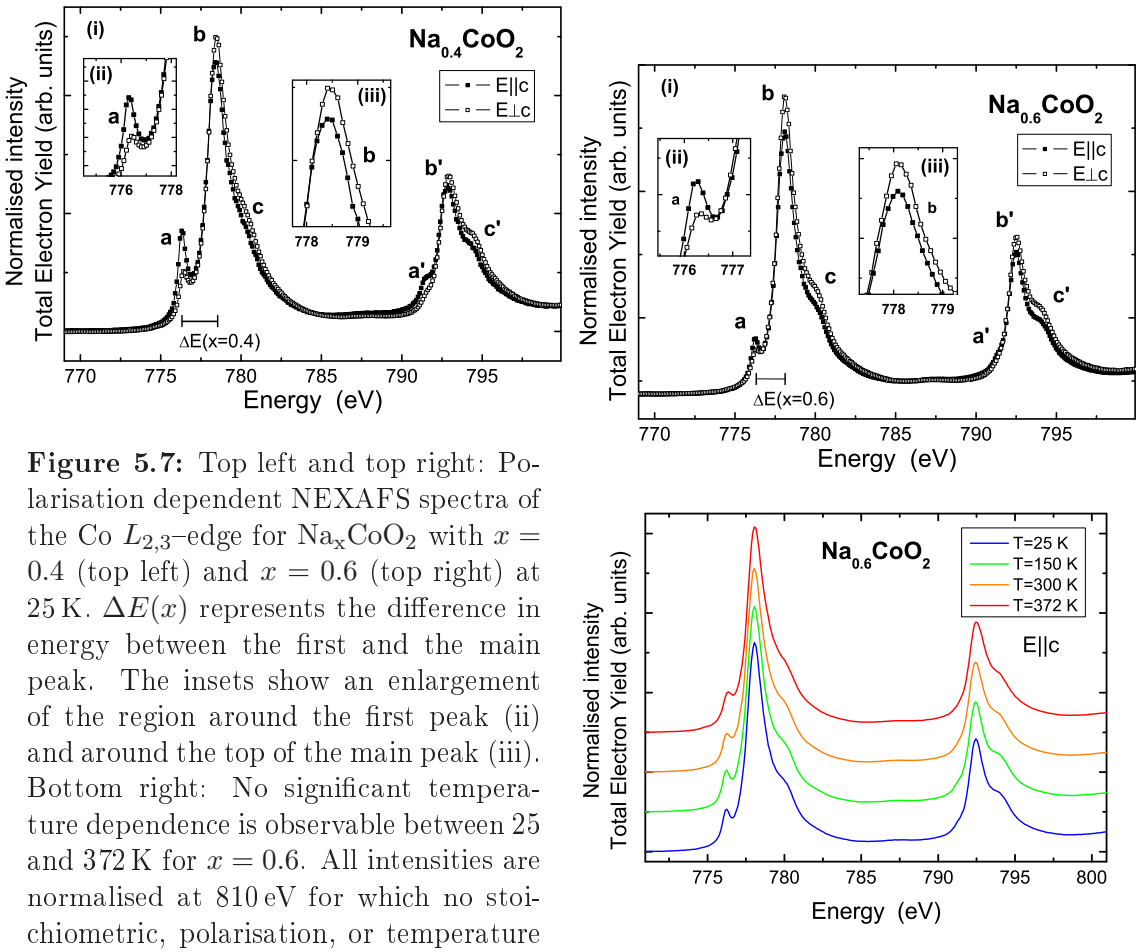

Figure 5.7: Top left and top right: Polarisation dependent NEXAFS spectra of the Co $L_{2,3}$–edge for Na_xCoO_2 with $x = 0.4$ (top left) and $x = 0.6$ (top right) at 25 K. $\Delta E(x)$ represents the difference in energy between the first and the main peak. The insets show an enlargement of the region around the first peak (ii) and around the top of the main peak (iii). Bottom right: No significant temperature dependence is observable between 25 and 372 K for $x = 0.6$. All intensities are normalised at 810 eV for which no stoichiometric, polarisation, or temperature dependence is observable.

Co L–edge

In Fig. 5.7, experimental spectra of the Co $L_{2,3}$–edges are shown, which display three main features at each edge: one strong central peak (peak b and b') with a shoulder towards higher energies (peak c and c') and a peak/shoulder towards lower energies (peak a and a'). This result can easily be compared with the similar compound $LiCoO_2$, which nominally contains only Co^{3+} ions with S=0 [177]. In the NEXAFS spectra of the Co $L_{2,3}$–edge of $LiCoO_2$ one finds only one main peak [178] different from the spectrum observed for the mixed valence system Na_xCoO_2. Especially the low energy feature (peak a and a') is absent in $LiCoO_2$. Thus this peak can be can be interpreted as a result of excitations into unoccupied $3d$ states of nominal Co^{4+} ions which are missing in $LiCoO_2$. This interpretation is also supported by the doping dependence of the Co L–edge as the low energy peak appears stronger for lower Na doping (i.e. higher Co^{4+} concentration) and weaker for higher sodium doping (i.e. lower Co^{4+} concentration), as well as by calculations as described shortly below and in great detail in the next section (5.3).

The local electronic structure around a Co atom in Na_xCoO_2 has been modelled in a cluster calculation using many–body wave functions. Within this approach, a

CoO_6 cluster containing the Co $3d$ and the O $2p$ valence electrons has been solved exactly including all interactions between $3d$ electrons in O_h symmetry with an a_{1g} like ground state for Co^{4+} as given in equation (5.2) as expected for a trigonal distortion (see also Ref. [179] and the proceeding section 5.3). For simplicity, in the following the expression Co^{4+}, referring to a CoO_6 octahedron with a formal Co^{4+} central ion containing five holes and, analogously, Co^{3+} for an octahedron containing four holes with a formal Co^{3+} central ion, will be used. From the calculations it has been found that the first peak at lower energies in the NEXAFS Co L–edge (peak a and a' in Fig. 5.7) originates from excitations into Co^{4+} final states with an A_{1g} symmetry, while the main peak (b and b') and the shoulder (c and c') are due to excitations into final states of Co^{3+} with E_g symmetry and Co^{4+} with T_{1g} and T_{2g} symmetry, respectively. Note that in order to avoid confusion we labelled the final states using capital letters (e.g. A_{1g}) while the ground state is labelled with lower case letters (e.g. a_{1g}). The ground state of the system has been found to be strongly covalent with a moderate positive charge transfer energy $\Delta_{CT} = E(d^{n+1}L) - E(d^n)$ for Co^{3+} and a negative Δ_{CT} for Co^{4+} [179].

In the experimental spectrum of the Co L–edge, it is additionally observed that the energy difference between the first peak (A_{1g}) and the largest peak (E_g) in figure 5.7 differs between the two different stoichiometries x=0.4 and x=0.6 being $\Delta E_{x=0.4} = -2.0$ eV and $\Delta E_{x=0.6} = -1.8$ eV, respectively. Theoretically, this behaviour can be best explained by a change of the energy splitting between the t_{2g} and the e_g states (10Dq). An explanation for a lower 10Dq for higher Na content can be found from neutron powder diffraction by Huang *et al.* An increasing Co–O distance with increasing Na content is found [60] which guides a lower influence of the crystal field and charge transfer, i.e. a lower 10Dq.

The a_{1g} orbital of the ground state in trigonal symmetry points along the (1 1 1) direction of the distorted CoO_6 octahedra, i.e. parallel to the crystallographic c–axis, while the two e_g^π orbitals point perpendicular to it. From polarisation dependent measurements with the **E** vector of photons parallel and 70° to the crystallographic c–axis, one observes the a_{1g} peak of Co^{4+} to be stronger for **E**||c as compared to **E** $\perp$ c. This behaviour is expected for a local trigonal distortion, where the t_{2g} ground states split into states with a_{1g} and e_g^π symmetry, whereas the e_g^σ states remain untouched (c.f. figure 5.1) and therefore should not show a strong polarisation dependence. Different from that, the intensity of the Co^{3+} central peak is significantly larger for **E** $\perp$ c compared to **E**||c (figure 5.7), which is unexpected from symmetry arguments and also from performed calculations. This effect points to an additional distortion that splits the e_g^σ levels.

Such a splitting may be caused by two mechanisms: First, from spectral ellipsometry on a $Na_{0.82}CoO_2$ sample, Bernhard *et al.* [138] found a transition at 280 K which they explained by the formation of magnetopolarons using the idea of a spin–state transition, similar to the related compound $La_{1-y}Sr_yCoO_3$ [139–141, 143]. In Na_xCoO_2, this mechanism would be driven by a displacement of the neighbouring oxygen ligands towards the central Co^{4+} ion, which may favour an intermediate–spin

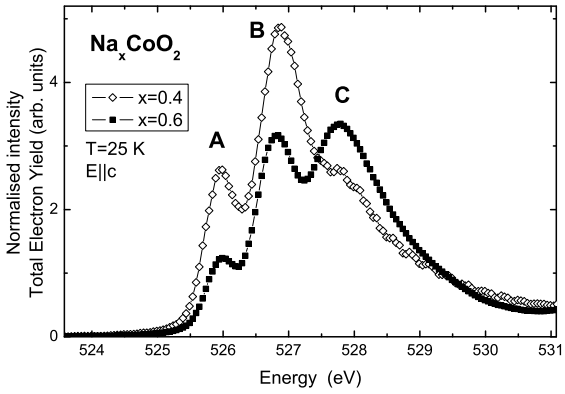

Figure 5.8: Stoichiometric dependence of the spectrum of Na_xCoO_2 at the oxygen K–edge. A, B, and C represent the positions of the three main peaks. The intensities are normalised at 600 eV.

(IS) state with S=1 over a low–spin (LS) state with S=0 of the Co^{3+} ions [138]. This displacement would result in a splitting of the e_g^σ levels. As a second possibility, an additional distortion could arise from the effect of sodium ordering at special doping levels [60, 76, 115, 125]. It is assumed that this results in orthorhombic symmetry which may lead to a perturbation of the trigonal distortion of the octahedra. Both possible contributions are related to a corresponding ordering temperature. The formation of magnetopolarons was observed at 280 K, whereas the Na ordering appears at temperatures below 350 K for x=0.75. However, no significant temperature dependence for $Na_{0.6}CoO_2$ has been found between 25 K and 370 K in the present NEXAFS studies. This implies that the spin–state of Co as well as the electronic structure in this energy range as seen by NEXAFS is not affected by temperature neither by a spin state transition nor by a structural transition involving Na ordering (figure 5.7 bottom right). A temperature independent distortion would be expected if the non–trigonal distortion is purely structural.

O K-edge

In Figure 5.8, the results for the O K absorption edge of $Na_{0.4}CoO_2$ and $Na_{0.6}CoO_2$ measured with light polarised parallel to the crystallographic c–axis are presented. For both stoichiometries three pronounced features A, B and C above the absorption threshold have been observed, showing a significant doping dependence. Features A and B increase for smaller x, while feature C decreases, i.e. features A and B increase with an increasing hole doping. In the related compound $LiCoO_2$ the situation is very similar to Na_1CoO_2, since both systems are assumed to have a low–spin state meaning that all six t_{2g} states are occupied by electrons while the four e_g states are empty. The resulting absorption spectrum shows only one peak due to O $2p$ orbitals hybridised with the Co $3d$ orbitals with e_g symmetry [178]. In Na_xCoO_2, excitations into unoccupied Co^{3+} states should therefore only be responsible for a single peak in the whole O K absorption edge spectra of Na_xCoO_2. Therefore, the first two features A and B in figure 5.8 can be attributed to doping induced states related to the formation of Co^{4+} sites and feature C to the formation of Co^{3+} sites, surrounded by oxygen octahedra. It has been shown previously that the pre–edge peaks in the O K NEXAFS spectra of the late transition–metal (TM)

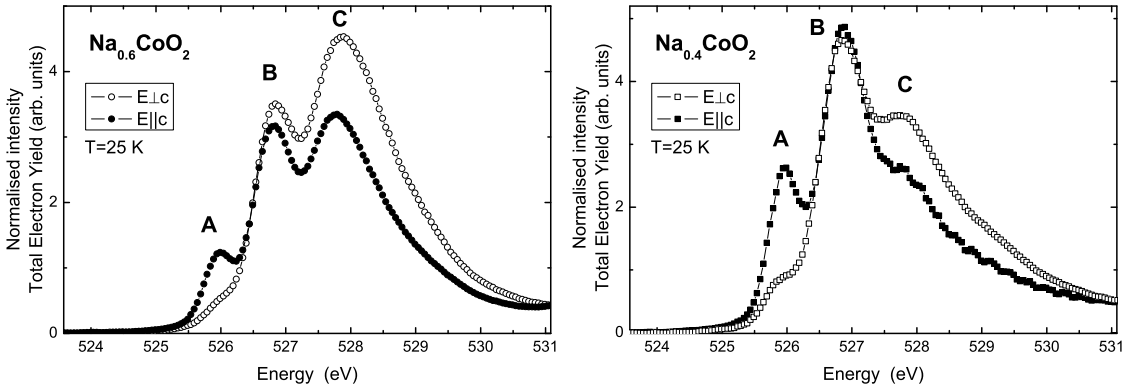

Figure 5.9: NEXAFS polarisation dependence of the oxygen K–edge of Na_xCoO_2 for $x = 0.6$ (top) and $x = 0.4$ (bottom). Polarisation $E||c$ is indicated by filled symbols, $E||c$ is indicated by open symbols. The intensities are normalised at 600 eV where the spectrum is isotropic.

oxides are shifted by about 1 eV to lower energies when the TM valence increases by 1 [180]; therefore, spectral features from two different valence states can be well resolved. The energetic downshift can be explained by a decrease of the energy between the partially filled Co $3d$ states; the valence electrons will be screened by an additional 1 eV with every added valence electron, resulting in a situation that for late transition metals a higher valency corresponds to a lower excitation energy. Upon hole addition (decreasing x), the increase of features A and B, and the decrease of feature C indicate that both are related to the doping process and it is natural to ascribe them to excitations into unoccupied O $2p$ states hybridised with Co^{3+} e_g^σ states (feature C) and, about 1 eV lower in energy, to excitations into unoccupied O $2p$ states hybridised with Co^{4+} e_g^σ states (feature B) and those hybridised with Co^{4+} a_{1g} states (feature A). Additionally, these results show that the holes in Na_xCoO_2 have a significant oxygen character, which is in good agreement with other cobalt based compounds [141, 178, 181].

Next we turn to the polarisation dependence of the O K absorption edges as shown in figure 5.9. From polarisation dependent absorption measurements, information about the orientation of the corresponding orbitals can be obtained. The data signal that the doping induced absorption feature A is strong for E||c, but substantially weaker for E $\perp$ c. Consequently, from the orientation of the a_{1g}–orbital and the attribution of the three peaks as described above, the holes doped into the CoO_2 layers of Na_xCoO_2 have a predominant a_{1g} character similar to the result found by Wu *et al.* also using X–ray absorption spectroscopy [165]. Band structure calculations revealed that although the a_{1g} and e_g^π states overlap and mix to some extent, the centers of these states are energetically separated, with those closer to ϵ_F having dominant a_{1g} character [57], in good agreement with our results. In addition, while feature B is not or only slightly polarisation dependent, the intensity of peak C (Co^{3+}) is significantly stronger for $\mathbf{E} \perp c$ than for $\mathbf{E}||c$. The same result has already been observed at the Co L–edge, but because of the large central peak no quantitative analysis of the polarisation dependence of the Co^{4+} shoulder could be made.

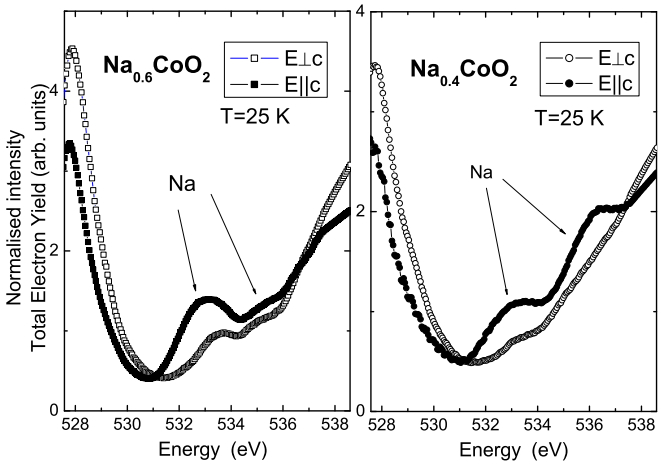

Figure 5.10: Dependence on stoichiometry and polarisation of the NEXAFS spectra of Na_xCoO_2 at the oxygen K–edge. The energy range right above the oxygen threshold is shown where the the hybridisation between O and Na can be monitored. All curves are normalised at 600 eV.

At the oxygen K–edge these two peaks are well separated and a difference in the response due to different polarisations is observable. From this, one can conclude that the trigonal symmetry has a larger effect in the octahedra containing a Co^{4+} central ion, whereas in octahedra containing a Co^{3+} central ion an additional distortion has to be present. Such a situation has already been suggested by Bernhard and co–workers as an origin of magnetopolarons [138]. As already mentioned in the previous paragraph, the underlying idea for such an effect is a lowering of the local symmetry around the Co^{3+}. Thus, also the e_g^σ doublet splits and becomes polarisation dependent. The effect may be stronger at temperatures below 20 K, which is also the critical temperature for a magnetic transition to a bulk antiferromagnetic ordered state for $x = 0.82$ [62,63]. At temperatures lower than 20 K, the mobility of the magnetopolarons is assumed to be lower due to an increased self–trapping energy in the antiferromagnetic state [138]. Such a reduction of the symmetry around one of the two Co ions has only been seen by X–ray absorption spectroscopy (and, notably, not by X–ray diffraction), indicating that it is not a static but a dynamic effect. Since Na_xCoO_2 shows metallic behaviour for all x except $x = 0.5$ and the electronic transport works via Co^{3+} and Co^{4+} ions, the charge carriers must have polaronic character.

Somewhat higher in energy at E $\approx$ 535 eV, one finds excitations into unoccupied O levels which are hybridised with Na orbitals [165]. As expected, the resulting peaks increase in intensity with increasing Na intercalation. In addition to that, they are strongly polarisation dependent. As shown in figure 5.10, the intensity for $\vec{E}||c$ is stronger than for $\vec{E} \perp c$. This leads to a finite Na–O hybridisation along c. A consequence of this hybridisation could be a three–dimensional magnetism as has been proposed by Johannes *et al.* [145]. From this data, it becomes clear that the inter–planar binding is more likely to have a covalent rather than an ionic character, so that a 3D magnetism is reasonable.

Na K–edge

When looking at the Na K edges at around 1072 eV, a quantitative interpretation is very difficult or almost impossible since in such a process an electron is excited from a $1s$ core level state into an unoccupied $3p$ state. The electronic configuration of a Na atom is [Ne].$3s^1$, leaving the Na^{+1} ion with the electronic configuration of Ne. Therefore, an excitation into unoccupied $2p$ states (as in oxygen) is impossible. Due to the dipole selection rule $\Delta l = \pm 1$ only a transition into p states is allowed, leaving $3p$ as the most likely excitation partner. Moreover, the energy separation between the unoccupied Na $3s$ and $3p$ states in Na_xCoO_2 has been found to be rather small, in fact smaller than the corresponding bandwidth. This allows the s and $p_{x,y}$ orbitals of a Na atom, sitting inside an O_6 prism, to combine and form bands that may be described as resulting from sp_2 hybrid orbitals. These are asymmetric, orthonormal, and directed to the midpoints of the O prism edges [145]. For these states, there are various hybridisation paths which make a good interpretation very challenging. In figure 5.11, the NEXAFS spectra of the Na K–edge for various doping levels are shown, where a clear polarisation dependence is observable. For $E||c$ a broad region around 1080 eV dominates the spectra of all stoichiometries. This changes with a change in polarisation to $E \perp c$, for which the strongest part in the spectra is a relatively sharp peak at 1073.3 eV. As one can see in figure 5.11, the relative spectral weight between these two prominent features depends on the doping level x. It is clear from the crystal structure and the Na sp_2 hybridisation that there are many exchange path possible along c, leading to a broad peak structure, different to a polarisation perpendicular to c. Interestingly, these states are higher in energy than the ones perpendicular to c. This may be due to Coulomb repulsion since the lobes of the corresponding orbitals are pointing towards each other which lifts these states (similar to the energy splitting due to the crystal field for the $3d$ states). In both stoichiometries, the same peaks are present at the same energies, however, with a different spectral weight. In the Na–rich cases $x = 0.7$ and $x = 0.65$, a stronger polarisation dependence is observable compared to the other cases $x = 0.5$ and $x = 0.4$. This is somewhat surprising since the crystallographic c–axis shrinks with increasing x so that the hybridisation along the c–axis should be weaker for higher x and the polarisation dependence should be the other way around. Note that the results for $x = 0.6$ and $x = 0.7$ look very similar, but change dramatically when crossing the special case $x = 0.5$ in the phase diagram.

Dependence of the O K– and Co $L_{2,3}$–edge on stoichiometry ($0.4 \leq x \leq 0.7$)

Different from what has been observed at the Na K–edge, there is a smooth crossing of the phase separation line $x = 0.5$ in both the O K and the Co $L_{2,3}$–edge as shown in figure 5.12 for incoming light polarised parallel and perpendicular to the crystallographic c–axis. From a comparison of all crystals that have been measured and a careful determination of the actual stoichiometry of the measured crystals (3), (5), and (7), it turns out that the stoichiometry $x = 0.6$ of crystal (6) as given

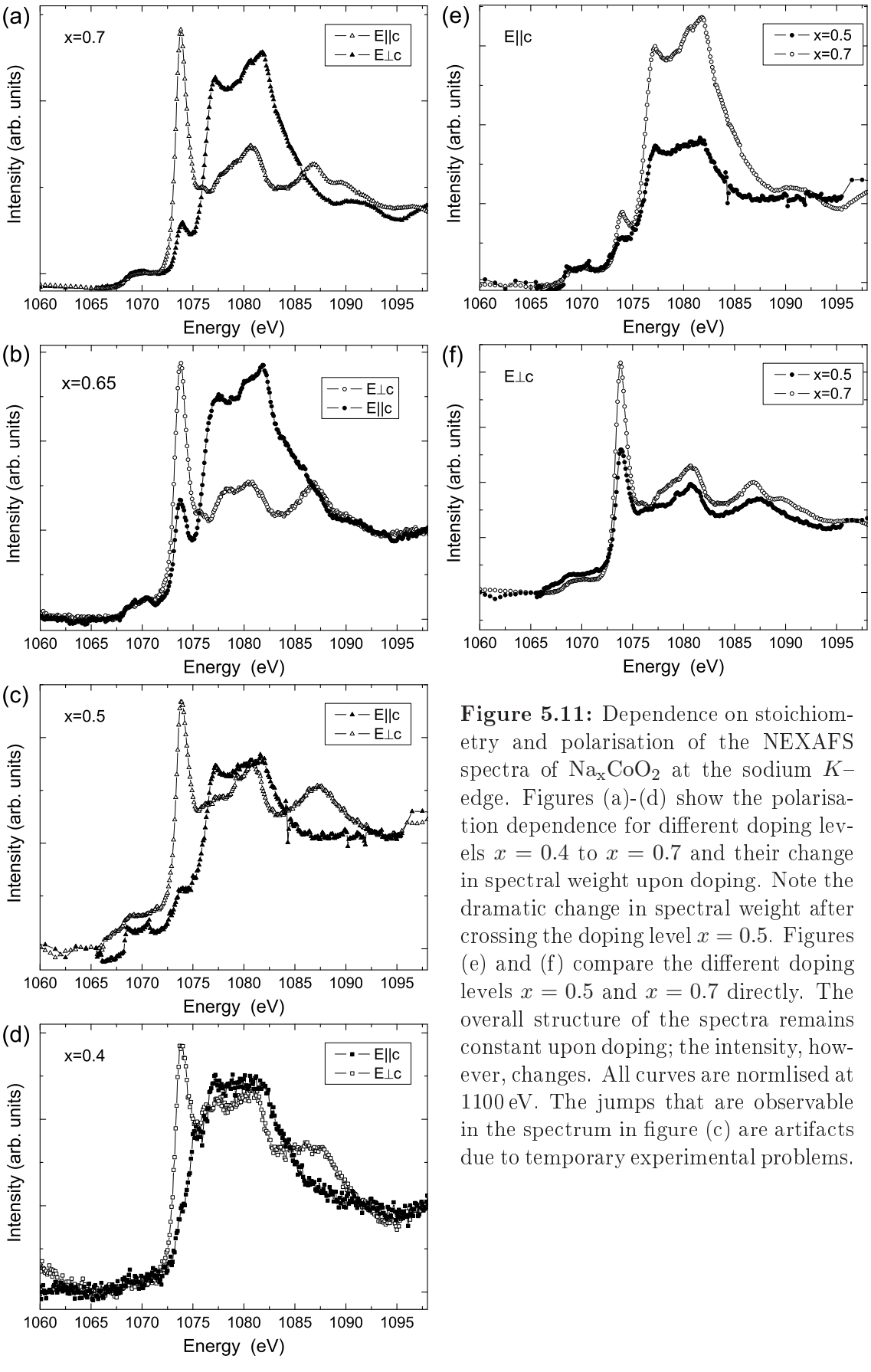

Figure 5.11: Dependence on stoichiometry and polarisation of the NEXAFS spectra of Na_xCoO_2 at the sodium K–edge. Figures (a)-(d) show the polarisation dependence for different doping levels $x = 0.4$ to $x = 0.7$ and their change in spectral weight upon doping. Note the dramatic change in spectral weight after crossing the doping level $x = 0.5$. Figures (e) and (f) compare the different doping levels $x = 0.5$ and $x = 0.7$ directly. The overall structure of the spectra remains constant upon doping; the intensity, however, changes. All curves are normlised at 1100 eV. The jumps that are observable in the spectrum in figure (c) are artifacts due to temporary experimental problems.

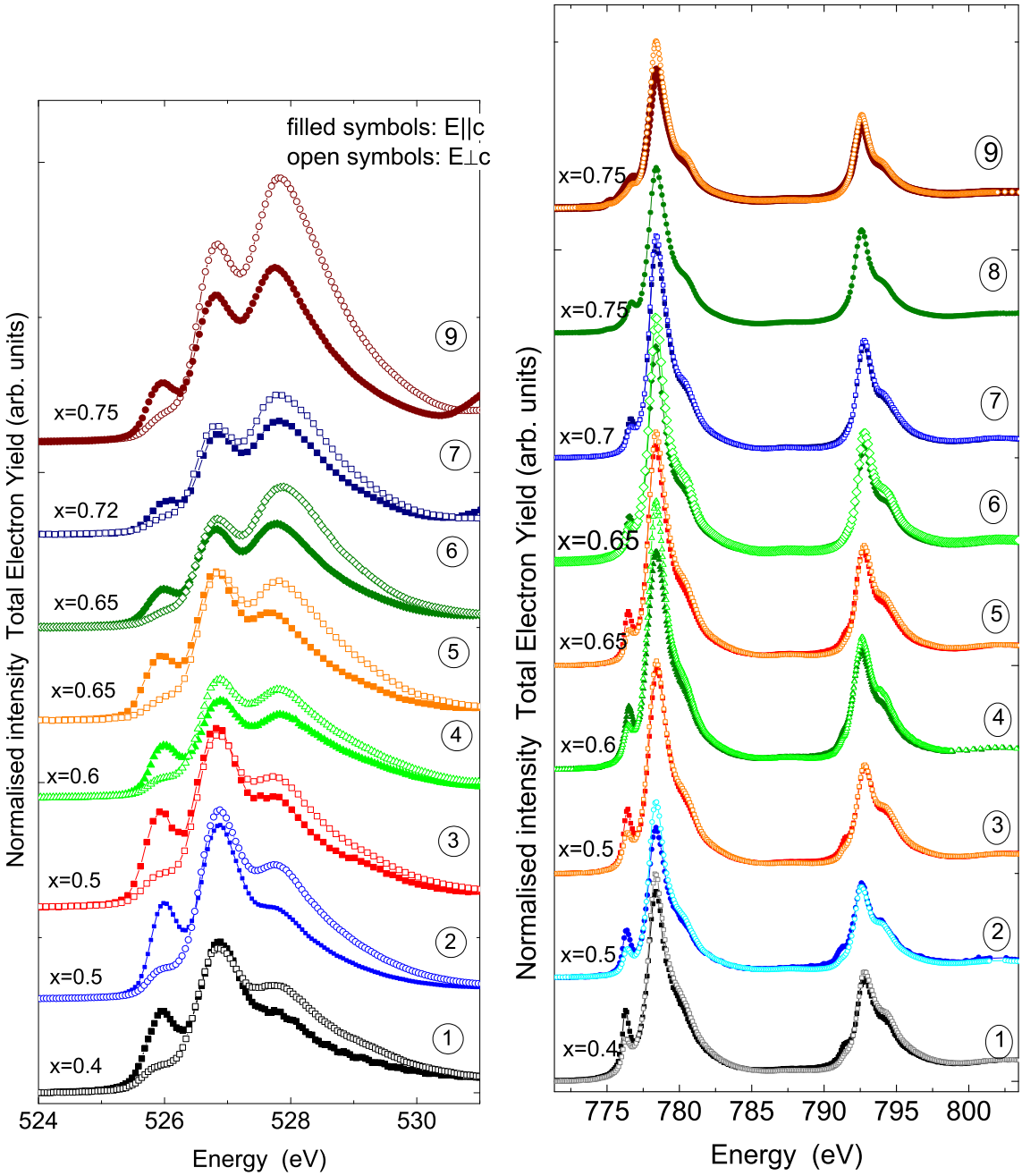

Figure 5.12: Na_xCoO_2: NEXAFS O K and Co $L_{2,3}$–edges for $E||c$ and $E \perp c$ at various doping levels. All spectra are normalised at 810 eV. Open symbols represent a polarisation of the incoming light perpendicular to the crystallographic c–axis, whereas filled symbols denote a polarisation parallel to c.

in Ref. [148] has to be revised to $x = 0.65$. Regrettably, due to technical problems for crystal (8) only a good spectrum of the Co $L_{2,3}$–edge with $E||c$ is available and therefore only this one is shown in figure 5.12.

A deviation from the trigonal distortion as it is explained above is observable in all samples indicated by a polarisation dependence of the Co^{3+} peak that should only

be very weak at pure trigonal symmetry for both the Co $L_{2,3}$ and the O K–edge. The low energy peak in the O K spectra, which could be assigned to states that are hybridised with the Co $3d$ a_{1g} states, decreases systematically with increasing Na intercalation. From a first look, it seems that the ratio of the a_{1g} intensity for $E||c$ and $E \perp c$ varies with doping in such a way that $I^{||}_{a_{1g}}/I^{\perp}_{a_{1g}}$ at the O K–edge decreases with increasing x. Mizokawa *et al.* [182] fitted the O $1s$ NEXAFS spectra using two Gaussians for the first two lower lying structures (named A and B in figure 5.8), and the tail of another Gaussian to represent the tail of the higher energy structure (named C in figure 5.8). From an analysis of the angular dependence they found that the ratio $n_{a_{1g}}/n_{e_g}$ is $\sim$1.5, where $n_{a_{1g}}$ and n_{e_g} are the number of holes in the a_{1g} and e^{π}_g states, respectively [182]. At this point, the author of this thesis has abstained from following this procedure and refused to estimate a doping dependent hole occupation ratio from the NEXAFS O K–edge since the uncertainty of the fit, especially from the tail of the higher energy structure, is uncontrollable. Therefore, conclusions from such a procedure should be drawn with great care. Note that the O K spectra of Na_xCoO_2 for $x = 0.5 - 0.6$ as presented by Mizokawa *et al.* [182] show only a weak polarisation dependence in the whole spectra, very different from what has been published in Ref. [165] and Ref. [148], and also from the (unpublished) data shown in this work. It should be emphasised that these results have been obtained by different experimentalists on various crystals with different x which have been grown by different crystal growers using different methods. All this makes these results very reliable.

From the polarisation dependent measurements over a wide doping range $0.4 \leq x \leq 0.75$, it becomes clear that the trigonal symmetry is always present around Co^{4+}, but distorted around Co^{3+}. The only exception is found in a crystal with $x = 0.75$ (number (9)), where also a polarisation dependence at the Co^{4+} e^{σ}_g peak could be observed. This crystal has been grown in the group of R.J. Cava at Princeton University, USA, by a travelling floating zone method. Beside the fact that these crystals are something special as will become clear in the measurements of the Co $L_{2,3}$–edge, it should be noted that they have been measured at the ALS synchrotron at Berkeley, USA, where the polarisation of the incoming beam cannot be changed. Therefore, the whole crystal had to be rotated in order to change the polarisation of the light with respect to the crystal. Naturally, the investigated crystal portion has changed after a rotation and also the penetration depth changed. In summary, it is not clear if this polarisation dependence is intrinsic or due to a different setup. Note that also the sample with $x = 0.5$ shows a deviation of the trigonal symmetry and that there exists no charge ordering pattern which balances this additional effect.

At the Co $L_{2,3}$–edge, there is a systematic decrease of the intensity of the low energy a_{1g} peak corresponding to a change in the Co^{3+}/Co^{4+} ratio. In addition to that, the low energy a_{1g} peak shifts towards the middle peak that corresponds to Co^{3+}, indicating a decrease of the crystal field splitting with increasing x [179]. Note that the energy of the central peak (Co^{3+}) and its high energy shoulder (Co^{4+}) does not depend on the crystal field, but only the low energy a_{1g} peak does. Therefore,

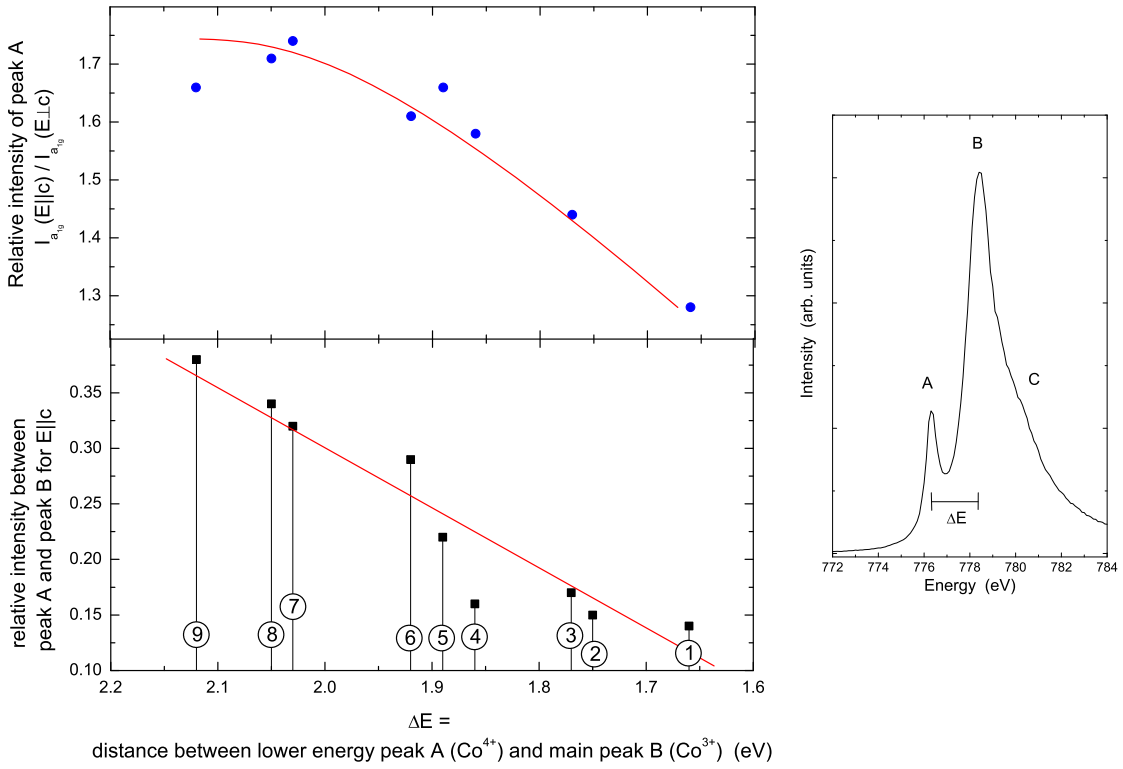

Figure 5.13: Na_xCoO_2: Behaviour of the Co^{4+} a_{1g} peak for different doping levels (the corresponding x of crystal (1) to (9) is given in the previous figure). In the horizontal axis the distance between peaks A and B is represented. The bottom panel shows the intensity of the a_{1g} peak compared to the e_g peak for $E||c$, and the top panel gives the ratio of the a_{1g} peak for polarisation parallel and perpendicular to c. The red lines may act as a guide to the eye. In the right figure the peaks A, B, and C are shown again.

the conclusion mentioned above about the change in crystal field symmetry can be drawn from a comparison of the energy difference between the a_{1g} peak of Co^{4+} and the e_g peak of Co^{3+}. Further details will be explained in the following chapter. Huang *et al.* [60] observed from X–ray diffraction experiments an increase of the Co–O bond length with increasing doping which corresponds to the NEXAFS results and a decrease of the crystal field effect.

A special case in the series shown in figure 5.12 are the results from crystals with $x = 0.75$. As already mentioned above, these crystals have been grown in the group of R.J. Cava. They were labelled as $x = 0.7$, but from a comparison with all other crystals the stoichiometry of the investigated portion of the sample should be about $x = 0.75$. This is remarkably close to the region $x > 0.75$ where a magnetic phase transition occurs below $\approx 20\,\mathrm{K}$. And indeed, these crystals show an additional feature at energies below the Co^{4+} a_{1g} peak. Kubota *et al.* [183] mention the possibility of Co^{2+} impurities in their samples, and from X–MCD measurements experimental proof has been found for the existence of Co^{2+} impurities in investigated $Na_{0.75}CoO_2$ samples, which leads to a peak at energies lower than the a_{1g} peak in X–ray absorp-

tion [184]. Recently, this additional peak in the NEXAFS spectrum has also been found in higher doped crystals (grown by the same group) [185]. As a possible explanation of this weak peak a transition to a high spin state in Co^{4+} is discussed; in a high spin state also excitations into the lower lying e_g^π states would be possible, leading to an additional lower lying peak. Such a transition is well possible since the energy splitting between the t_{2g} and e_g states is about 3-3.5 eV, which is in the vicinity of a spin state transition for Co^{4+}. Here, two arguments can be given against this interpretation. First, the energy difference between the a_{1g} and the additional peak is about 1.5 eV which is too large for the splitting of the t_{2g} states and cannot be explained by multiplet effects easily. Second, pure Co^{4+} d^5 multiplet calculations including the full multiplet in D_{3d} symmetry show a clear cut–off a_{1g} peak at low energies for a low–spin situation, but a spectrum being smeared out at lower energies for a high–spin situation without showing clear peaks as seen in the experimental spectrum. These arguments may lead to Co^{2+} impurities as the origin of the additional low energy peak in the NEXAFS spectra for $Na_{0.75}CoO_2$ presented here. Note, that these arguments do not exclude the possibility of an actual high–spin state for Co^{4+} at higher doping levels.

In figure 5.13, the results of the Co $L_{2,3}$–edge are summarised. The spectrum on the right shall help the reader to interpret the main figure. In the left figure, the results of the crystals (1)–(9) are shown, on the horizontal axis the distance between the lower energy peak A (Co^{4+} a_{1g}) and the middle peak B (Co^{3+} e_g) is shown for all crystals. The vertical axis is divided into two parts, the lower part displays the intensity of the Co^{4+} a_{1g} peak in relation to the central Co^{3+} e_g peak for $E||c$, whereas in the vertical axis of the top panel the intensity ratio of the a_{1g} peak for light polarised parallel and perpendicular to the c–axis is plotted. The red curves in both panels may work as guides to the eye. Therefore, this figure contains three important information about the system Na_xCoO_2:

- The distance between the lower lying Co^{4+} a_{1g} peak A and the middle Co^{3+} e_g peak B decreases monotonically with increasing doping. Since such a behaviour can be explained by a decrease of the crystal field [179], one could speculate about a spin state transition of the Co^{4+} ion as a possible origin of the onset of the magnetic region.

- In relation to the middle Co^{3+} e_g peak the intensity of the Co^{4+} a_{1g} peak decreases linearly with increasing x due to the loss of Co^{4+} ions.

- The ratio of the intensity of the Co^{4+} a_{1g} peak for incoming light polarised parallel and perpendicular to the crystallographic c–axis decreases non linearly with increasing x, emphasising a different occupation relation of the holes in the a_{1g} and the e_g^π levels.

5.3 The electronic structure derived from cluster calculations

Naturally, a deeper understanding of the experimental spectra cannot be achieved just by looking at them, but theoretical work plays an important role in the understanding of the experimental results. Therefore, cluster calculations on the sodium cobaltates Na_xCoO_2 have been performed. In this work, a cluster composed of a Co atom and its six nearest–neighbour O atoms for the geometry and oxidations states relevant to Na_xCoO_2 has be solved exactly. The aim is to learn more about the electronic structure of the system at an intermediate energy scale by comparison with experimental results on the polarisation dependence of NEXAFS spectra [148]. It will be seen that previous results concerning the highly covalent Co–O bond and the low spin state of Co [148, 165] can be confirmed. Furthermore, the scenario suggested by Koshibae and Maekawa [159] that the effective Co–Co hopping through the intermediate O sites is an essential part of the low energy physics will be supported. Additionally, it will be shown that due to the strong covalency of the Co–O bond a large amount of holes reside at the oxygen sites. Finally, with the help of the cluster perturbation method an estimate of the hopping parameter t is presented, which describes the indirect hopping of a hole (or an electron) from a cobalt site via oxygen to the neighbouring cobalt site.

These calculations were mainly done at the Centro Atomico Bariloche, Bariloche, Argentina, under the supervision of Armando A. Aligia, as well as at the University of British Columbia, Vancouver, Canada, under the supervision of George A. Sawatzky. To some part the following discussion has already been published in Physical Review B, **74**, 114124 (2006).

Ideally, from the knowledge of important parameters such as the d–d Coulomb interaction which includes the exchange energy, the different hopping terms, and the charge–transfer energy, one directly gains information about the band gap and the character of the electronic structure, as explained in the classification scheme of Zaanen, Sawatzky, and Allen [155]. Additionally, knowing important orbitals and interactions at an intermediate energy scale accessible to optical experiments, like the three–band Hubbard model in the case of cuprates [186], one could derive an effective low–energy model (like the $t - J$ model based on Zhang–Rice singlets [187–191] for the cuprates) which describes the relevant low–energy physics. As an example, interesting phenomena have been explained by the formation of the Zhang–Rice singlets, such as the unusual magnetic and transport properties in $(La, Ca)_xSr_{14-x}Cu_{24}O_{41}$ [192] and other cuprates. Similarly, low–energy reduction procedures have been followed in the case of the nickelates [193] and magnetic double perovskites [194]. However, a systematic low–energy reduction has not been carried out for Na_xCoO_2, and it appears that no consensus exists on the low–energy effective theory, in spite of the experimental and theoretical effort concerning the electronic structure of the system. At energy scales of 1 eV or larger, valuable information on this electronic structure is provided by local spectroscopic probes, like

X–ray absorption spectroscopy (XAS or NEXAFS) [148, 165], and X–ray photoemission (XPS) [154], while angle resolved photoemission (ARPES) [95–97] provides information on the dispersion relation just below the Fermi energy. In particular, NEXAFS, including a recent study of its dependence on the polarisation of the incident light [148, 165], indicates that Na_xCoO_2 exhibits the character of a doped charge–transfer insulator [155] rather than a doped Mott–Hubbard insulator, and the ground state contains a significant O $2p$ contribution. Several calculations of the band structure use a single band effective model [57, 83, 87, 93, 168]. These descriptions can be justified if the lattice distortion (or crystal field) breaks the degeneracy of the $3d$ t_{2g} orbitals which are otherwise degenerate in a cubic environment, and if the O degrees of freedom can be integrated out in a similar way as in the cuprates. However, Koshibae and Maekawa proposed an alternative scenario, based on an estimate of the effects of the above mentioned lattice distortion, and simple geometrical arguments, with four interpenetrating Kagomé sublattices hidden in the CoO_2 layer [159]. This scenario has been supported by Indergand *et al.* who derived the different hopping elements and interactions in the ensuing multi–band model [166]. Starting from this picture, Khalliulin *et al.* argued that the spin–orbit coupling of the correlated electrons on the t_{2g} level, although relatively small ($\sim 80\,\mathrm{meV}$ [195]) strongly influences the coherent part of the wave functions and the Fermi surface topology at low doping and favours triplet superconductivity, in marked contrast to the cuprates [196].

The following section is divided into two parts. First, the model with its formalism and relevant equations is introduced (section 5.3.1). Then, the results will be presented and compared with the experiments (section 5.3.2).

5.3.1 Method

The model

An adequate starting point for the description of the electronic structure of Na_xCoO_2 is a multiband Hubbard model including all Co $3d$ orbitals and O $2p$ orbitals and their interactions (like the three–band Hubbard model for the cuprates [186]). This model cannot be solved exactly, but one has to resort to some approximation. Calculations starting from first principles approximate the interactions and are known to lead to wrong results when the on–site Coulomb repulsion U_d between transition–metal $3d$ electrons is important. For example, they predict that $LaCuO_4$ is a paramagnetic metal, whereas the experiment shows that it is an antiferromagnetic insulator. In this work we take the opposite approach and retain exactly all $3d$-$3d$ interactions at the price of considering only one Co atom together with its six nearest–neighbour O atoms, with octahedral O_h symmetry. Distortions effects are discussed later. Some additional approximations are also made which are not essential but reduce the size of the matrices of the Hamiltonian in each symmetry sector. This provides a calculational tool flexible enough to allow a fit of the NEXAFS spectra in a reasonable amount of computer time. For example, the interactions between

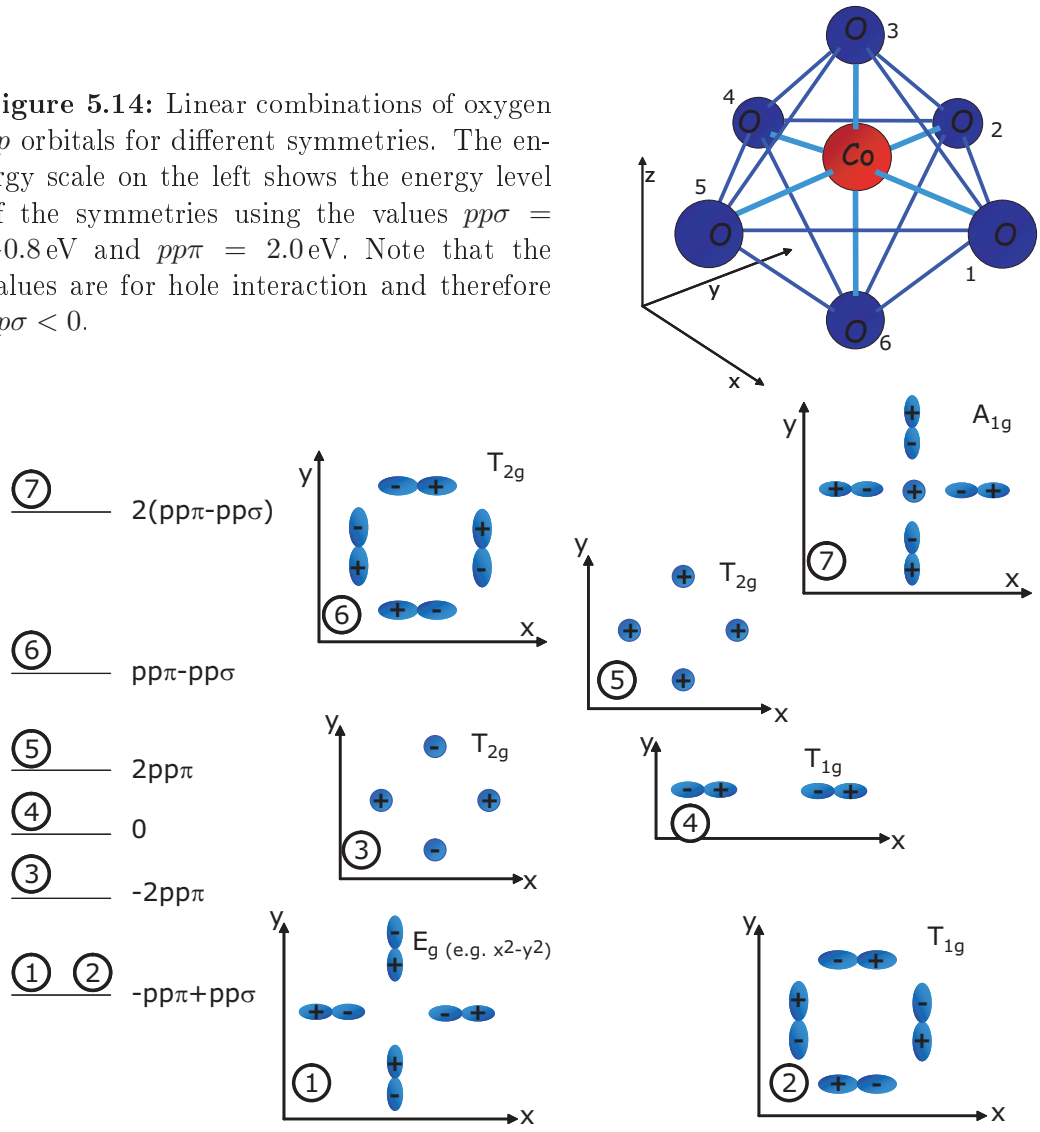

Figure 5.14: Linear combinations of oxygen $2p$ orbitals for different symmetries. The energy scale on the left shows the energy level of the symmetries using the values $pp\sigma = -0.8\,\text{eV}$ and $pp\pi = 2.0\,\text{eV}$. Note that the values are for hole interaction and therefore $pp\sigma < 0$.

O $2p$ holes are neglected and this allows us to take advantage of a restricted basis for these orbitals which has the same symmetry as the $3d$ t_{2g} and e_g orbitals. The other O $2p$ orbitals become irrelevant in the absence of O–O interactions.

A great part of the work is devoted to the determination of the basis functions of both, the initial and final states in all symmetry sectors before and after X–ray excitation. In the procedure of finding the basis functions, group theory plays a major role. An introduction to group theory has been given in chapter 2.2.

An important role in Na_xCoO_2 is played by the six oxygen ions located at the corners of an undistorted octahedron (cubic O_h symmetry) surrounding a central cobalt ion. Since there are six oxygen sites with three $2p$ orbitals each, there are $3 \times 6 = 18$ linear combinations of O $2p$ orbitals that act as basis functions in O_h symmetry. In figure 5.14 one octahedron with six oxygen ions at sites 1...6 is shown.

Using the projector operator and the relation $\mathcal{P}^{\alpha}_{mn}\psi^{\beta}_{j} = \delta_{\alpha\beta}\delta_{nj}\psi^{\alpha}_{m}$ (see also equation (2.27) in chapter 2.2), where α and β denote two irreducible representations and ψ^{β}_{j} are basis functions transforming as the unitary irreducible representation Γ^{β} of the group G, together with a notation where a hole in a $2p_x$ orbital at site 1 is represented as $p^{+}_{1x}|0\rangle$, where $p^{+}_{i\alpha}$ creates a p hole at site i and orbital p_x and $|0\rangle$ denotes the vacuum, the 18 basis functions are:

$$
\begin{aligned}
|1\rangle_{t_{2g}} &= \tfrac{1}{2}\big(p^{+}_{2x} - p^{+}_{5x} + p^{+}_{1y} - p^{+}_{4y}\big)|0\rangle &&= p^{+}_{xy}|0\rangle\\
|2\rangle_{t_{2g}} &= \tfrac{1}{2}\big(p^{+}_{3y} - p^{+}_{6y} + p^{+}_{2z} - p^{+}_{5z}\big)|0\rangle &&= p^{+}_{yz}|0\rangle\\
|3\rangle_{t_{2g}} &= \tfrac{1}{2}\big(p^{+}_{3x} - p^{+}_{6x} + p^{+}_{1z} - p^{+}_{4z}\big)|0\rangle &&= p^{+}_{zx}|0\rangle\\
|4\rangle_{t_{2g}} &= \tfrac{1}{2}\big(p^{+}_{1z} + p^{+}_{4z} - p^{+}_{2z} - p^{+}_{5z}\big)|0\rangle\\
|5\rangle_{t_{2g}} &= \tfrac{1}{2}\big(p^{+}_{3x} + p^{+}_{6x} - p^{+}_{2x} - p^{+}_{5x}\big)|0\rangle\\
|6\rangle_{t_{2g}} &= \tfrac{1}{2}\big(p^{+}_{3y} + p^{+}_{6y} - p^{+}_{1y} - p^{+}_{4y}\big)|0\rangle\\
|7\rangle_{t_{2g}} &= \tfrac{1}{2}\big(p^{+}_{3x} + p^{+}_{6x} + p^{+}_{2x} + p^{+}_{5x}\big)|0\rangle\\
|8\rangle_{t_{2g}} &= \tfrac{1}{2}\big(p^{+}_{3y} + p^{+}_{6y} + p^{+}_{1y} + p^{+}_{4y}\big)|0\rangle\\
|9\rangle_{t_{2g}} &= \tfrac{1}{2}\big(p^{+}_{1z} - p^{+}_{4z} + p^{+}_{2z} + p^{+}_{5z}\big)|0\rangle\\
|10\rangle_{t_{1g}} &= \tfrac{1}{\sqrt{2}}\big(p^{+}_{1x} + p^{+}_{4x}\big)|0\rangle\\
|11\rangle_{t_{1g}} &= \tfrac{1}{\sqrt{2}}\big(p^{+}_{2y} + p^{+}_{5y}\big)|0\rangle\\
|12\rangle_{t_{1g}} &= \tfrac{1}{\sqrt{2}}\big(p^{+}_{3z} + p^{+}_{6z}\big)|0\rangle\\
|13\rangle_{t_{1g}} &= \tfrac{1}{2}\big(p^{+}_{3y} - p^{+}_{6y} - p^{+}_{2z} + p^{+}_{5z}\big)|0\rangle\\
|14\rangle_{t_{1g}} &= \tfrac{1}{2}\big(p^{+}_{1z} - p^{+}_{4z} - p^{+}_{3x} + p^{+}_{5x}\big)|0\rangle\\
|15\rangle_{t_{1g}} &= \tfrac{1}{2}\big(p^{+}_{2x} - p^{+}_{5x} - p^{+}_{1y} + p^{+}_{4y}\big)|0\rangle\\
|16\rangle_{e_g} &= \tfrac{1}{2}\big(p^{+}_{1x} - p^{+}_{4x} - p^{+}_{2y} + p^{+}_{5y}\big)|0\rangle &&= p^{+}_{x^2-y^2}|0\rangle\\
|17\rangle_{t_{2g}} &= \tfrac{1}{2\sqrt{3}}\big(2p^{+}_{3z} - 2p^{+}_{6z} - p^{+}_{1x} + p^{+}_{4x} + p^{+}_{2y} - p^{+}_{5y}\big)|0\rangle &&= p^{+}_{3z^2-r^2}|0\rangle\\
|18\rangle_{a_{1g}} &= \tfrac{1}{\sqrt{6}}\big(p^{+}_{1x} - p^{+}_{4x} + p^{+}_{2y} - p^{+}_{5y} + p^{+}_{3z} - p^{+}_{6z}\big)|0\rangle
\end{aligned}
\tag{5.6}
$$

These functions are partially illustrated in figure 5.14 together with their energies. In an undistorted octahedron without O–O interactions, only five of the linear combinations can hybridise with the $3d$ t_{2g} and e_g orbitals, namely those combinations which have the same symmetry. All the other $p-d$ hoppings are zero because of symmetry reasons. This reduces the problem to a two site problem with one Co site having five d orbitals and one O site with five linear combinations of p orbitals $|1\rangle$, $|2\rangle$, $|3\rangle$, $|16\rangle$, and $|17\rangle$, respectively. Treating the problem of one hole in an undistorted octahedron (including the central $3d$ ion) with a Hamiltonian that includes only $d-p$ and $p-p$ hopping, the Hamiltonian reads

$$
\mathcal{H}_{hop} = \sum_{\alpha\beta\sigma} t^{\alpha\beta}\big(p^{+}_{\alpha\sigma}d_{\beta\sigma} + \text{H.c.}\big) + \sum_{\alpha\beta\sigma}\tau^{\alpha\beta}p^{+}_{\alpha\sigma}p_{\beta\sigma}, \tag{5.7}
$$

where $p^+_{i\alpha\sigma}$ creates a hole on the O $2p$ orbital α at site i with spin σ whereas $p_{i\alpha\sigma}$ annihilates one. The operator $d_{\alpha\sigma}$ has an analogous meaning for the Co $3d$ orbitals. From this Hamiltonian, one gets the relevant hopping parameters $t^{\alpha\beta}$ and $\tau^{\alpha\beta}$. Using the Slater–Koster symmetry factors [197,198] (see appendix A.2), one finds for holes $t^{xy,xy} = t^{yz,yz} = t^{zx,zx} = -2pd\pi$ and $t^{x^2-y^2,x^2-y^2} = t^{3z^2-r^2,3z^2-r^2} = -\sqrt{3}pd\sigma$ for the d-p hopping, and $\tau^{xy,xy} = \tau^{yz,yz} = \tau^{zx,zx} = pp\pi - pp\sigma$ and $\tau^{x^2-y^2,x^2y^2} = \tau^{3z^2-r^2,3z^2-r^2} = -pp\pi + pp\sigma$ for the p-p hopping. $pd\pi$ and $pd\sigma$ are related via $pp\sigma = -\frac{0.81}{3.24}pp\pi$, and $pd\pi$ and $pd\sigma$ are related via $pd\pi = -\frac{\sqrt{3}}{4}pd\sigma$ [30], which leads to a ratio $t^{e_g,e_g} = 2t^{t_{2g},t_{2g}}$. This is also valid for many–particle problems.

In order to find the basis functions for the whole CoO_6 octahedron with 4 holes (Co^{3+}) or 5 holes (Co^{4+}) in the O_h symmetry group, again group theory will be important. The procedure of finding the basis functions will be explained with the help of Co^{3+} (4 holes) because in that case the number of basis functions is smaller and the functions are a lot easier to construct.

Na_xCoO_2 is assumed to be in a low spin state, i.e. $S = 0$ for 4 holes, which is realised in a situation where all six t_{2g} states are occupied by electrons, so that the four holes occupy the four e_g states. Configurations such as three e_g holes and one t_{2g} hole were neglected due to the large crystal field splitting compared to the interaction term. The basis function for a system with four d holes can be written as

$$|1\rangle_i = d^+_{x^2-y^2\uparrow} d^+_{x^2-y^2\downarrow} d^+_{3z^2-r^2\uparrow} d^+_{3z^2-r^2\downarrow} |0\rangle, \tag{5.8}$$

where the subscript i denotes initial states. The symmetry of such a configuration is A_{1g}. For the sake of clarity, capital letters will be used in the following to denote the irreducible representations of many–body states. In the case of one oxygen p hole in the ground state, one finds one possible basis function with A_{1g} symmetry:

$$\begin{aligned} |2\rangle_i \;=\; & \frac{1}{2}\big(d^+_{x^2-y^2\uparrow} d^+_{x^2-y^2\downarrow} (d^+_{3z^2-r^2\uparrow} p^+_{3z^2-r^2\downarrow} - d^+_{3z^2-r^2\downarrow} p^+_{3z^2-r^2\uparrow}) + \\ & (d^+_{x^2-y^2\uparrow} p^+_{x^2-y^2\downarrow} - d^+_{x^2-y^2\downarrow} p^+_{x^2-y^2\uparrow}) d^+_{3z^2-r^2\uparrow} d^+_{3z^2-r^2\downarrow}\big)|0\rangle. \end{aligned} \tag{5.9}$$

For two oxygen p holes and two cobalt d holes the situation becomes a bit more

complicated. In this case one finds three additional basis functions:

$$\begin{aligned}
|3\rangle_i &= \frac{1}{2}\big(d^+_{x^2-y^2\uparrow}d^+_{x^2-y^2\downarrow}(p^+_{x^2-y^2\uparrow}p^+_{x^2-y^2\downarrow}+p^+_{3z^2-r^2\uparrow}p^+_{3z^2-r^2\downarrow})+\\
&\quad d^+_{3z^2-r^2\uparrow}d^+_{3z^2-r^2\downarrow}(p^+_{x^2-y^2\uparrow}p^+_{x^2-y^2\downarrow}+p^+_{3z^2-r^2\uparrow}p^+_{3z^2-r^2\downarrow})\big)|0\rangle\\
|4\rangle_i &= \frac{1}{\sqrt{8}}\big(d^+_{x^2-y^2\uparrow}d^+_{x^2-y^2\downarrow}(p^+_{x^2-y^2\uparrow}p^+_{x^2-y^2\downarrow}-p^+_{3z^2-r^2\uparrow}p^+_{3z^2-r^2\downarrow})+\\
&\quad (d^+_{x^2-y^2\uparrow}d^+_{3z^2-r^2\downarrow}-d^+_{x^2-y^2\downarrow}d^+_{3z^2-r^2\uparrow})(p^+_{x^2-y^2\uparrow}p^+_{3z^2-r^2\downarrow}-p^+_{x^2-y^2\downarrow}p^+_{3z^2-r^2\uparrow})+\\
&\quad d^+_{3z^2-r^2\uparrow}d^+_{3z^2-r^2\downarrow}(p^+_{x^2-y^2\uparrow}p^+_{x^2-y^2\downarrow}+p^+_{3z^2-r^2\uparrow}p^+_{3z^2-r^2\downarrow})\big)|0\rangle\\
|5\rangle_i &= \frac{1}{\sqrt{3}}\big(d^+_{x^2-y^2\uparrow}d^+_{3z^2-r^2\uparrow}p^+_{x^2-y^2\downarrow}p^+_{3z^2-r^2\downarrow}+d^+_{x^2-y^2\downarrow}d^+_{3z^2-r^2\downarrow}p^+_{x^2-y^2\uparrow}p^+_{3z^2-r^2\uparrow}-\\
&\quad \frac{1}{2}(d^+_{x^2-y^2\uparrow}d^+_{3z^2-r^2\downarrow}+d^+_{x^2-y^2\downarrow}d^+_{3z^2-r^2\uparrow})(p^+_{x^2-y^2\uparrow}p^+_{3z^2-r^2\downarrow}+p^+_{x^2-y^2\downarrow}p^+_{3z^2-r^2\uparrow})\big)|0\rangle.
\end{aligned} \tag{5.10}$$

Especially for functions $|4\rangle$ and $|5\rangle$ the use of the projector $\mathcal{P}$ is very helpful. If two functions $|i\rangle$ and $|j\rangle$ are not orthonormal, a function $|k\rangle$ can be found in such a way that $|i\rangle$ and $|k\rangle$ become orthonormal: If $|k\rangle = |j\rangle - \langle i|j\rangle|i\rangle$, then $\langle i|k\rangle = 0$. This relation has been used to orthonormalise non orthogonal functions. The last two missing basis functions for (a) a situation with three p holes and only one d hole left and for (b) a situation with four p holes are easily obtained by simply interchanging p and d in the basis functions $|2\rangle$ and $|1\rangle$:

$$\begin{aligned}
|6\rangle_i &= \frac{1}{2}\big(p^+_{x^2-y^2\uparrow}p^+_{x^2-y^2\downarrow}(d^+_{3z^2-r^2\uparrow}p^+_{3z^2-r^2\downarrow}-d^+_{3z^2-r^2\downarrow}p^+_{3z^2-r^2\uparrow})+\\
&\quad (d^+_{x^2-y^2\uparrow}p^+_{x^2-y^2\downarrow}-d^+_{x^2-y^2\downarrow}p^+_{x^2-y^2\uparrow})p^+_{3z^2-r^2\uparrow}p^+_{3z^2-r^2\downarrow}\big)|0\rangle\\
|7\rangle_i &= p^+_{x^2-y^2\uparrow}p^+_{x^2-y^2\downarrow}p^+_{3z^2-r^2\uparrow}p^+_{3z^2-r^2\downarrow}|0\rangle.
\end{aligned} \tag{5.11}$$

Finally, there are seven basis functions for the ground state with A_{1g} symmetry for a CoO_6 octahedron with a nominally Co^{3+} central ion.

In the NEXAFS exited state a $2p$ core electron has been lifted up into a $3d$ state, reducing the number of holes in the octahedron to three. Because of total spin conservation, the spin state of the three holes (neglecting the core–hole) is $S = 1/2$ with $S_z = \pm 1/2$. The only energy level which the excited electron can go to is a d_{e_g} level, i.e. the destroyed hole has e_g symmetry. Since $A_{1g} \otimes e_g = E_g$[3], the excited states have to have E_g symmetry. In order to find all basis functions of the excited state for E_g symmetry of Co^{3+} (three holes), one has to check all possible combinations of orbitals and spin, and construct the basis functions. Finally for Co^{3+} there are eight basis functions for the excited state for each subspace (E_g has dimension two, i.e. two subspaces for a given spin). Only one subspace is given with $S_z = 1/2$, and wave functions transforming like the first basis state of E_g. The basis functions of the other wave functions can be found by a rotation of the basis

[3] see also the multiplication table 2.5 in chapter 2.2

functions or with the help of the projector $\mathcal{P}$:

$$\begin{aligned}
|1\rangle_e &= d^+_{x^2-y^2\uparrow} d^+_{3z^2-r^2\uparrow} d^+_{3z^2-r^2\downarrow} |0\rangle \\
|2\rangle_e &= \frac{1}{\sqrt{2}} \big(d^+_{x^2-y^2\uparrow} d^+_{x^2-y^2\downarrow} p^+_{x^2-y^2\uparrow} + d^+_{3z^2-r^2\uparrow} d^+_{3z^2-r^2\downarrow} p^+_{x^2-y^2\uparrow} \big) |0\rangle \\
|3\rangle_e &= \frac{1}{\sqrt{6}} \big(d^+_{x^2-y^2\downarrow} d^+_{3z^2-r^2\uparrow} p^+_{3z^2-r^2\uparrow} + d^+_{x^2-y^2\uparrow} d^+_{3z^2-r^2\downarrow} p^+_{3z^2-r^2\uparrow} - \\
&\qquad 2 d^+_{x^2-y^2\uparrow} d^+_{3z^2-r^2\uparrow} p^+_{3z^2-r^2\downarrow} \big) |0\rangle \\
|4\rangle_e &= \frac{1}{2} \big(d^+_{x^2-y^2\uparrow} d^+_{x^2-y^2\downarrow} p^+_{x^2-y^2\uparrow} - d^+_{x^2-y^2\downarrow} d^+_{3z^2-r^2\uparrow} p^+_{3z^2-r^2\uparrow} + \\
&\quad d^+_{x^2-y^2\uparrow} d^+_{3z^2-r^2\downarrow} p^+_{3z^2-r^2\uparrow} - p^+_{x^2-y^2\uparrow} d^+_{3z^2-r^2\uparrow} d^+_{3z^2-r^2\downarrow} \big) |0\rangle \\
|5\rangle_e &= \frac{1}{\sqrt{2}} \big(d^+_{x^2-y^2\uparrow} p^+_{x^2-y^2\uparrow} p^+_{x^2-y^2\downarrow} + d^+_{x^2-y^2\uparrow} p^+_{3z^2-r^2\uparrow} p^+_{3z^2-r^2\downarrow} \big) |0\rangle \\
|6\rangle_e &= \frac{1}{\sqrt{6}} \big(p^+_{x^2-y^2\downarrow} d^+_{3z^2-r^2\uparrow} p^+_{3z^2-r^2\uparrow} - 2 p^+_{x^2-y^2\uparrow} d^+_{3z^2-r^2\downarrow} p^+_{3z^2-r^2\uparrow} + \\
&\qquad p^+_{x^2-y^2\uparrow} d^+_{3z^2-r^2\uparrow} p^+_{3z^2-r^2\downarrow} \big) |0\rangle \\
|7\rangle_e &= \frac{1}{\sqrt{6}} \big(d^+_{x^2-y^2\uparrow} d^+_{x^2-y^2\downarrow} p^+_{x^2-y^2\uparrow} - d^+_{x^2-y^2\downarrow} d^+_{3z^2-r^2\uparrow} p^+_{3z^2-r^2\uparrow} + \\
&\quad d^+_{x^2-y^2\uparrow} d^+_{3z^2-r^2\downarrow} p^+_{3z^2-r^2\uparrow} - p^+_{x^2-y^2\uparrow} d^+_{3z^2-r^2\uparrow} d^+_{3z^2-r^2\downarrow} \big) |0\rangle \\
|8\rangle_e &= p^+_{x^2-y^2\uparrow} p^+_{3z^2-r^2\uparrow} p^+_{3z^2-r^2\downarrow} |0\rangle . \qquad (5.12)
\end{aligned}$$

In a very similar way one can find all basis functions for a CoO_6 octahedron with a nominal Co^{4+} (5 holes) central ion. In the ground state the spin state is assumed to be low spin, i.e. $S = 1/2$ and $S_z = \pm 1/2$. The t_{2g} states are not completely filled by electrons as in the Co^{3+} case, but there is one t_{2g} hole. As expected, it turns out that the ground state of a system with five holes and $S = 1/2$ has T_{2g} symmetry. The process of finding the corresponding basis functions is a lot more complicated. Therefore, only a sketch will be given. The easiest basis function that can be written down directly is the one for five d holes (here for the xy subspace and $S_z = 1/2$):

$$|1\rangle_{i,t2g} = d^+_{xy\uparrow} d^+_{x^2-y^2\uparrow} d^+_{x^2-y^2\downarrow} d^+_{3z^2-r^2\uparrow} d^+_{3z^2-r^2\downarrow} |0\rangle . \qquad (5.13)$$

In principle, all permutations and occupations of d and p holes are possible. In order to find the correct combinations which are orthonormal to each other and belong to the same irreducible representation, one can use once again the projector $\mathcal{P}$, the orthonormalisation relation mentioned above and the Clebsch–Gordon coefficients as they are given in appendix A.4. After all basis functions of one subspace of the irreducible representation T_{2g} are found, the two missing subspaces can be built with the projector $\mathcal{P}$ since $\mathcal{P}^{T_{2g}}_{11} \psi^{T_{2g}}_1 = \psi^{T_{2g}}_1$, $\mathcal{P}^{T_{2g}}_{21} \psi^{T_{2g}}_1 = \psi^{T_{2g}}_2$, and $\mathcal{P}^{T_{2g}}_{31} \psi^{T_{2g}}_1 = \psi^{T_{2g}}_3$ with $\psi^{T_{2g}}_1 = \psi^{T_{2g}}_{xy}$, $\psi^{T_{2g}}_2 = \psi^{T_{2g}}_{yz}$, and $\psi^{T_{2g}}_3 = \psi^{T_{2g}}_{zx}$. It turns out that the basis functions for five holes in a low spin state have either T_{1g} or T_{2g} symmetry, with the latter one being lower in energy. For the T_{2g} symmetry ground state, 38 basis functions for each of the six subspaces (xy, yz, and zx with $S_z = \pm 1/2$) have been found.

In the excited or final state, a $2p$ electron can be excited either into a t_{2g} orbital or into an e_g orbital. In the first case it is $T_{2g} \otimes t_{2g} = A_{1g} + E_g + T_{2g} + T_{1g}$ and in the latter one we have $T_{2g} \otimes e_g = T_{2g} + T_{1g}$. If an electron is excited into a t_{2g} orbital (i.e. a hole in the t_{2g} orbital is destroyed), one ends up in the same situation as for the Co^{3+} ground state with $S = 0$ and A_{1g} symmetry. If a hole in an e_g orbital is destroyed, different spin states $S = 0$ and $S = 1$ are allowed. Summarising, for final states with a T_{1g} or T_{2g} symmetry, there are 3×20 basis functions each for $S = 0, S_z = 0$ and also 3×20 basis functions for $S = 1, S_z = 0, \pm 1$.

The Hamiltonian that describes the dynamics of holes inside the CoO_6 cluster includes all $d - d$ interactions as well as pd and pp hopping terms:

$$\begin{aligned} H &= \sum_{\alpha \in t_{2g},\sigma} \epsilon_{t_{2g}} d^+_{\alpha\sigma} d_{\alpha\sigma} + \sum_{\alpha \in e_g,\sigma} \epsilon_{e_g} d^+_{\alpha\sigma} d_{\alpha\sigma} + \sum_{jm} \epsilon_j c^+_{jm} c_{jm} \\ &\quad + \sum_{i\alpha\sigma} \epsilon_{\mathrm{O}} p^+_{i\alpha\sigma} p_{i\alpha\sigma} + \sum_{i \neq j \alpha\beta\sigma} t_i^{\alpha\beta} (p^+_{i\alpha\sigma} d_{\beta\sigma} + \mathrm{H.c.}) \\ &\quad + \sum_{i \neq k \alpha\beta\sigma} \tau_{ik}^{\alpha\beta} p^+_{i\alpha\sigma} p_{k\beta\sigma} + \frac{1}{2} \sum_{\lambda\mu\nu\rho} V_{\lambda\mu\nu\rho} d^+_\lambda d^+_\mu d_\rho d_\nu \\ &\quad + U_{cd} \sum_{jm\alpha\sigma} c^+_{jm} c_{jm} d^+_{\alpha\sigma} d_{\alpha\sigma}. \end{aligned} \tag{5.14}$$

Here, $p^+_{i\alpha\sigma}$ creates a hole on the O 2p orbital α at site i with spin σ. The operator $d^+_{\alpha\sigma}$ has an analogous meaning for the Co 3d orbitals. Similarly, c^+_{jm} creates a Co 2p core hole with angular momentum j and projection m.

The first two terms of Eq. (5.14) describe the energy of the t_{2g} and e_g Co $3d$ orbitals, split by a crystal field $\epsilon_{t_{2g}} - \epsilon_{e_g} = 10Dq$. Note that this difference can be called the "ionic" contribution to the crystal field splitting, since after hybridisation with the O orbitals the difference between mixed t_{2g} and e_g orbitals is much larger due to what is called the ligand field contributions. The third term describes the energy of the Co core hole, with a splitting $\epsilon_{3/2} - \epsilon_{1/2} \sim 15\,\mathrm{eV}$. The fourth term corresponds to the energy of the O $2p$ orbitals. The next two terms represent the Co–O and O–O hopping, parameterised as usual, in terms of the Slater–Koster parameters [197]. The term before the last one includes all interactions between $3d$ orbitals originated by the Coulomb repulsion of electrons in the $3d$ shell. For the description of the Co L–edge NEXAFS spectra one also needs to include in the Hamiltonian the energy of the Co $2p$ core hole and its repulsion with the Co $3d$ holes [2,186,199]. The last term describes the repulsion between the Co $3d$ holes and a Co $2p$ core hole if present. The exchange and higher multipole Coulomb interactions between these orbitals have been neglected. Their effects will be discussed later. Spin–orbit coupling of the $3d$ electrons is negligible compared with the other energies in the problem ($\sim 80\,\mathrm{meV}$ [195]) and was also neglected.

The matrix elements of the interactions inside the $3d$ shell are given by [200]

$$V_{\lambda\mu\nu\rho} = \int d\mathbf{r}_1 d\mathbf{r}_2 \bar{\varphi}_\lambda(\mathbf{r}_1)\bar{\varphi}_\mu(\mathbf{r}_2)\frac{e^2}{|\mathbf{r}_1 - \mathbf{r}_2|}\varphi_\nu(\mathbf{r}_1)\varphi_\rho(\mathbf{r}_2), \tag{5.15}$$

where $\varphi_\lambda(\mathbf{r}_1)$ is the wave function of the spin–orbital λ. All these integrals have been calculated in terms of the Slater parameters F_0, F_2, and F_4 using known methods of atomic physics [29,31]. The resulting form of this interaction term is long and is not reproduced here. A complete list of the integrals is given in appendix A.1. In appendix A.3, the full Hamiltonian concerning $d-d$ interactions is written down. The terms including only t_{2g} orbitals are also described in Ref [201], and those involving e_g ones are described for example in Ref. [193]; some of the remaining terms are listed in Ref. [31]. In particular, the value of the Coulomb repulsion between electrons of opposite spin at the same orbital is $U_d = F_0 + 4F_2 + 36F_4$, and the spin–spin interaction between $3d$ orbitals of the same irreducible representation is $J_{t_{2g}} = 3F_2 - 20F_4$, and $J_{e_g} = 4F_2 + 15F_4$.

The overlap between the wave functions of different CoO_6 clusters has been neglected because of the small O occupancy. Two neighbouring CoO_6 clusters share an edge with two common O atoms. The cluster with the larger O occupancy is the Co^{4+} cluster with an average of 1.44 O holes (see below). This means that each O site has an average of 0.12 holes with a given spin. Therefore one expects a small overlap, which should not substantially affect the conclusions presented in the following. The most important O–O interaction is the on–site one, which in the cuprates was estimated as $U_p \sim 4\,\mathrm{eV}$ [202–204]. According to the average occupation of O spin–orbitals, a mean–field estimate of this energy in the worst case is $6U_p n_\uparrow n_\downarrow \sim 6*4*0.12^2 = 0.35\,\mathrm{eV}$. This is actually an upper bound since correlations should decrease this quantity. In any case it is much lower than the effective hybridisation between the different configurations and therefore does not modify the main results. This justifies the restriction to one CoO_6 octahedron.

In Na_xCoO_2, the formal oxidation state of the O ions is -2, and that of Co depends on the Na content x, being Co^{3+} for $x = 1$, and Co^{4+} for $x = 0$. This means that the cluster has to be solved for a total of four holes (configurations d^6L^0, d^7L^1, d^8L^2, etc.) in the former case and five holes (configurations d^5L^0, d^6L^1, etc.) in the latter one. The respective probabilities are assumed to be x and $1-x$. For simplicity, these two cases will be labelled as Co^{3+} and Co^{4+}, respectively, although as we shall see there is a significant degree of covalency and the true Co oxidation states are smaller.

The X–ray absorption intensity

The ground state of the cluster in both above mentioned cases (for Co^{3+} and Co^{4+}) does not contain any Co $2p$ core hole. The excitation with light promotes a Co $2p$ electron to the Co $3d$ shell, or in other words, it creates a core hole and destroys a $3d$ hole. In the dipolar approximation, the effect of light is calculated in time–dependent perturbation theory from the addition of the term $\mathcal{H}_L = \mathbf{p}\cdot\mathbf{A}$ to the Hamiltonian,

where $\mathbf{p}$ is the momentum operator and $\mathbf{A} = (A_x, A_y, A_z)$ is the vector potential. Except for an unimportant prefactor, the relevant part of $\mathcal{H}_L$ can be deduced from symmetry arguments and general physical considerations: it should be rotationally invariant, spin independent, and should contain terms that destroy a $3d$ hole and create a core hole. This leads to the operator

$$\mathcal{H}_L = \sum_{l_z\sigma} (O^+_{2l_z\sigma} d_{2l_z\sigma} + \text{H.c.}). \tag{5.16}$$

Here the destruction operators of the $3d$ holes $d_{2l_z\sigma}$ are expressed in terms of l_z, the orbital angular momentum projection. $O^+_{2l_z\sigma}$ is an irreducible operator that transforms like an angular momentum $L = 2$ with projection l_z, constructed from the combination of the components of $\mathbf{A}$ in spherical harmonics (A_{1l_z}) with the core hole operators $c^+_{1l_z\sigma}$ that create a Co $2p$ hole with angular momentum projection l_z and spin σ. The expression of the five components of $O^+_{2l_z\sigma}$ ($l_z = -2$ to 2) is derived using Clebsch–Gordan coefficients. It is

$$\begin{aligned}
O^+_{22\sigma} &= p^+_{11\sigma} A_+, \qquad & O^+_{21\sigma} &= \frac{1}{\sqrt{2}}(p^+_{10\sigma} A_+ + p^+_{10\sigma} A_0) \\
& & O^+_{20\sigma} &= \frac{1}{\sqrt{6}}(p^+_{11\sigma} A_- + p^+_{1-1\sigma} A_+ + 2p^+_{10\sigma} A_0) \\
O^+_{2-1\sigma} &= \frac{1}{\sqrt{2}}(p^+_{10\sigma} A_- + p^+_{1-1\sigma} A_0), \qquad & O^+_{2-2\sigma} &= p^+_{1-1\sigma} A_0
\end{aligned}$$

with

$$\begin{aligned}
A_+ &= -\frac{1}{\sqrt{2}}(A_x + iA_y), \quad A_0 = A_z, \quad A_- = \frac{1}{\sqrt{2}}(A_x - iA_y) \quad \text{and} \\
p^+_{11\sigma} &= -\frac{1}{\sqrt{2}}(p^+_{x\sigma} + ip^+_{y\sigma}), \quad p^+_{10\sigma} = p^+_{z\sigma}, \quad p^+_{1-1\sigma} = \frac{1}{\sqrt{2}}(p^+_{x\sigma} - ip^+_{y\sigma})
\end{aligned}$$

Using the Clebsch–Gordan coefficients one can relate the operators of the core hole in the jm bases to those in the $l\sigma$ one:

$$\begin{aligned}
p^+_{3/2,3/2} &= p^+_{11\uparrow}, \qquad & p^+_{3/2,-3/2} &= p^+_{1-1\downarrow} \\
p^+_{3/2,1/2} &= \frac{1}{\sqrt{3}} p^+_{11\downarrow} + \frac{2}{\sqrt{3}} p^+_{10\uparrow}, \qquad & p^+_{1/2,1/2} &= \frac{2}{\sqrt{3}} p^+_{11\downarrow} - \frac{1}{\sqrt{3}} p^+_{10\uparrow} \\
p^+_{3/2,-1/2} &= \frac{2}{\sqrt{3}} p^+_{10\downarrow} + \frac{1}{\sqrt{3}} p^+_{1-1\uparrow}, \qquad & p^+_{1/2,-1/2} &= \frac{1}{\sqrt{3}} p^+_{10\downarrow} - \frac{2}{\sqrt{3}} p^+_{1-1\uparrow}.
\end{aligned}$$

The two bottom lines can be rewritten as

$$\begin{aligned}
p^+_{1,1,\downarrow} &= \frac{1}{\sqrt{3}} p^+_{3/2,1/2} + \frac{2}{\sqrt{3}} p^+_{1/2,1/2}, \qquad & p^+_{1,0,\uparrow} &= \frac{2}{\sqrt{3}} p^+_{3/2,1/2} - \frac{1}{\sqrt{3}} p^+_{1/2,1/2} \\
p^+_{1,0,\downarrow} &= \frac{2}{\sqrt{3}} p^+_{3/2,-1/2} + \frac{1}{\sqrt{3}} p^+_{1/2,-1/2}, \qquad & p^+_{1,-1,\uparrow} &= \frac{1}{\sqrt{3}} p^+_{3/2,-1/2} - \frac{2}{\sqrt{3}} p^+_{1/2,-1/2}.
\end{aligned}$$

Together with the relations

$$d^+_{2,2,\sigma} = \frac{1}{\sqrt{2}}(d^+_{x^2-y^2,\sigma} - id^+_{xy,\sigma}), \qquad d^+_{2,1,\sigma} = \frac{1}{\sqrt{2}}(-d^+_{zx,\sigma} + id^+_{yz,\sigma})$$
$$d^+_{2,-2,\sigma} = \frac{1}{\sqrt{2}}(d^+_{x^2-y^2,\sigma} + id^+_{xy,\sigma}), \qquad d^+_{2,-1,\sigma} = \frac{1}{\sqrt{2}}(d^+_{zx,\sigma} + id^+_{yz,\sigma})$$
$$d^+_{2,0,\sigma} = d^+_{3z^2-r^2,\sigma},$$

it is easy to express the light operator $\mathcal{H}_L$ in terms of the basis for the orbitals p_{jm} ($j = 1/2,\ 3/2$) used in the Hamiltonian (equation (5.14)) and Cartesian coordinates of $\mathbf{A}$.

$$\mathcal{H}_L = \sum_{\beta jm\alpha\sigma} a_{\beta jm\alpha\sigma} A_\beta p^+_{jm} d_{\alpha\sigma} + \text{H.c.} \tag{5.17}$$

This is the most convenient form for our purposes[4].

Using Fermi's golden rule and neglecting an unimportant prefactor, the NEXAFS intensity becomes

$$I = \sum_{if} p_i |\langle f|\mathcal{H}_L|i\rangle|^2 \delta(E_f - E_i - \hbar\omega). \tag{5.18}$$

Here, $|i\rangle$ is one of the two possible initial states (ground state for Co^{3+} or Co^{4+}), p_i is its probability that depends on the Na content, and E_i its energy. Similarly, f labels the final states. $\hbar\omega$ is the energy of the incoming light represented by the vector potential $\mathbf{A}$.

In order to simulate the measured spectra, the delta functions appearing in equation (5.18) have been broadened replacing them by a Lorentzian line shape with a full width of 0.5 eV at half maximum (FWHM) at the L_3–edge and 0.7 eV at the L_2–edge due to different life time broadening effects.

The X–ray photoemission intensity

In a X–ray photoemission spectroscopy (XPS) experiment incoming light excites some electrons of a system into the vacuum, i.e. it creates a hole at a particular ion. With the formulism as it is described above, such a process for a Co $3d$ electron can

[4]For the sake of completeness and usefulness for other applications, expressions for the p and d orbitals using l and m_l as a basis are stated here:

$$p^+_x = \frac{-1}{\sqrt{2}}[p^+_{11} - p^+_{1-1}],\ p^+_y = \frac{-1}{i\sqrt{2}}[p^+_{11} + p^+_{1-1}],\ p^+_z = p^+_{10}$$
$$d_{xy} = \frac{1}{i\sqrt{2}}[d_{22} - d_{2-2}],\ d_{yz} = \frac{-1}{i\sqrt{2}}[d_{21} + d_{2-1}],\ d_{zx} = \frac{-1}{\sqrt{2}}[d_{21} - d_{2-1}],$$
$$d_{x^2-y^2} = \frac{1}{\sqrt{2}}[d_{22} + d_{2-2}],\ d_{3z^2-r^2} = d_{20}$$

be described easily. In this case the Hamiltonian of the light consists simply of the creation operator for a d hole:

$$\mathcal{H}_{L,XPS} = \sum_{\alpha\sigma} d^+_{\alpha\sigma} \tag{5.19}$$

where α represents one of the five d orbitals and σ the spin. In the case of a Co^{3+} ion (four holes) this means that the final state contains five holes. The ground (initial) state has A_{1g} symmetry so that the final state can only have T_{2g} symmetry in case of a creation of a t_{2g} hole, or the final state has E_g symmetry in case of the creation of an e_g hole. In the former case, the basis functions are already known since they match the basis functions of Co^{4+} with T_{2g} symmetry.

Using again Fermi's golden rule and neglecting an unimportant prefactor, the XPS intensity becomes

$$I_{XPS} = \sum_f |\langle f|\mathcal{H}_{L,XPS}|i\rangle|^2 \delta(E_f - E_i - \hbar\omega) \tag{5.20}$$

Similar to the NEXAFS intensities, the XPS intensities have been broadened replacing them by a Lorentzian line shape with a full width of 0.5 eV at half maximum (FWHM).

5.3.2 Results

The structure of the ground state

There are already indications that the Co ions in Na_xCoO_2 are in a low spin state [64, 205], also supported by the interpretation of NEXAFS measurements using polarised light [148, 165]. This means that crystal field effects dominate over the exchange terms. In fact, from the parameters that best fit the experiment (see Table 5.2), one sees that $10Dq^i = 1.2\,\text{eV}$. As mentioned in the previous section, this corresponds to the "ionic" part of the crystal field. Therefore, the superscript i is used. The actual splitting is much larger due to the strong covalency effects. In table 5.1 an overview of the configurations is presented in the ground state for clusters with nominal oxidation state Co^{3+} and Co^{4+}.

The ground state for Co^{3+} is a singlet with A_{1g} symmetry. For the cluster representing nominal Co^{3+} and parameters that fit the NEXAFS spectra, important configurations in the ground state are d^6 (30%) and d^7L^1 (47%), indicating a very strong covalency in the system. Note that the d^6 population is smaller than the d^7L population and considerably less than 50% of the total population. Such a behaviour can only be explained if one takes more than one ligand hole into account. In a configuration containing only d^6 and d^7L with a positive charge transfer gap $\Delta_{CT} = E(d^{n+1}L) - E(d^n)$, the d^6 population will always be larger than d^7L for realistic values. Things change if one includes also configurations containing two ligand holes d^8L^2 with sufficiently large hopping terms. In this case the relative

Co^{3+} Groundstate	
d^6	0.30
d^7L^1	0.47
d^8L^2	0.20
d^9L^3	0.03
$d^{10}L^4$	0.00

Co^{4+} Groundstate	
d^5	0.14
d^6L^1	0.40
d^7L^2	0.35
d^8L^3	0.10
d^9L^4	0.01
$d^{10}L^5$	0.00

Co^{4+} (five holes) Ground state	
d^5	0.14
$d^6L^1_{e_g^1}$	0.37
$d^7L^2_{e_g^2}$	0.28
$d^6L^1_{t_{2g}^1}$	0.03
$d^7L^2_{e_g^1 t_{2g}^1}$	0.07

Table 5.1: Left: Overview of the hole distribution for the ground states of Co^{3+} and Co^{4+}. Right: Detailed hole distribution for the ground state of the Co^{4+} cluster for the important configurations, including information on symmetry up to configurations with two ligand holes. The numbers give the hole distribution in percent.

hole population changes towards the d^7L configuration, so that even for a positive charge transfer gap Δ_{CT} the dominant configuration can include a ligand hole. This is a rather important result since it demonstrates that the hybridisation between all those states involving one or more ligand holes is large enough to produce a low energy state which in fact is lower than that of the starting d^6 configuration containing no ligand holes. The d^6 configuration corresponds to t_{2g}^6 (all holes with e_g symmetry occupied). For simplicity, the configurations $t_{2g}^5 e_g^1$ have been neglected, thereby reducing the size of the matrices in the fitting procedure. This is justified by the fact that the interaction term which mixes the $3d$ configurations t_{2g}^6 and $t_{2g}^5 e_g^1$ is $\lambda = \sqrt{3}(F_2 - 5F_4) \simeq 0.3\,\mathrm{eV}$ (see Table 5.2), is much smaller than the effective crystal–field splitting $\sim 3\,\mathrm{eV}$. The amount of $t_{2g}^5 e_g^1$ $3d$ configurations can be calculated by perturbation theory. At most, however, its influence on the NEXAFS spectra is of the order of 1%. Similarly, for Co^{4+}, states with more than one 3d t_{2g} hole are neglected.

With these simplifications and because of the neglect of interactions between electrons at the O sites, the number of relevant states in the subspace of the ground state for Co^{3+}, is reduced to 7 singlets with A_{1g} symmetry. Similarly, the ground state for Co^{4+} is obtained from six identical 38x38 matrices and corresponds to a spin doublet with T_{2g} symmetry (this means three-fold orbital degeneracy). When the O_h symmetry is broken, the E_g singlets mix with the ground state (see next subsection).

Due to the symmetry of the cluster (O_h), the $3d$ holes conserve its symmetry when they hop to the O $2p$ states. Neglecting the small amount of $3d$ $t_{2g}^5 e_g^1$ states in Co^{3+}, the only possibility for a ligand hole is then a linear combination of oxygen orbitals with e_g symmetry giving the configuration $d^7_{t_{2g}^6 e_g^1} L^1_{e_g^1}$.

A more complicated picture is expected for the cluster corresponding to Co^{4+}. Since Co^{4+} contains five holes meaning that there will be one hole with t_{2g} symmetry in the system (either at the Co site or distributed among the O ions). For the parameters that fit the experiment, the ground state of this cluster is a spin doublet with orbital symmetry T_{2g}. This three–fold degeneracy in the point group

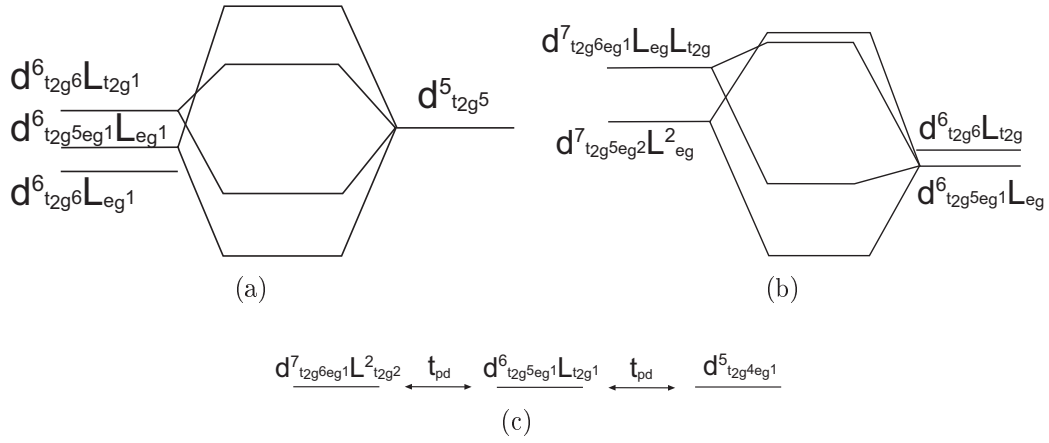

Figure 5.15: Sketches of the energy scheme for different hole configurations of Co^{4+}. (a): Hybridisation between states with none and one ligand hole, (b) and (c): Hybridisation between states with one and two ligand holes.

O_h is split by the rhombohedral distortion as discussed in the next subsection. An overview of the structure of the ground state is given in table 5.1 (left). The distribution among different possible configurations up to two ligand holes for the ground state of the Co^{4+} octahedra is shown in table 5.1 (right). Note that states with one and two ligand holes dominate the composition of the ground state. The d^5 configuration is very simple. It consists of four $3d_{e_g}$ holes and one $3d_{t_{2g}}$ hole, or equivalently it consists of five $3d_{t_{2g}}$ electrons ($d^5_{t^5_{2g}}$). The configurations with one ligand hole with the same symmetry are $d^6_{t^5_{2g}e^1_g}L_{e^1_g}$, and $d^6_{t^6_{2g}}L_{t^1_{2g}}$. The former has a larger hybridisation with the d^5 configuration because the hopping between $3d$ and $2p$ e_g or t_{2g} electrons involves the Slater–Koster parameter $(pd\sigma)$ or $(pd\pi)$ with the former having a larger magnitude. For configurations with two ligand holes there are two configurations with T_{2g} symmetry: $d^7_{t^6_{2g}e^1_g}L_{e^1_g}L_{t^1_{2g}}$ and $d^7_{t^5_{2g}e^2_g}L_{e^2_g}$. They both hybridise with the dominant one–hole state $d^6_{t^5_{2g}e^1_g}L_{e^1_g}$. The only difference is that the first configuration couples via $t_{t_{2g}}$ hopping to the one–hole state while the second configuration couples via a t_{e_g} hopping which is larger and results in a stronger occupation of this state (see table 5.1 (right)). Although it is allowed by symmetry, the above mentioned states with two ligand holes do not hybridise with the state $d^6_{t^6_{2g}}L_{t_{2g}}$ due to the particular structure of the wave functions.

From the above described distribution of holes in the Co^{3+} and Co^{4+} clusters, it turns out that the true Co valence for each cluster is 2.04 and 2.56 respectively, emphasising again the very strong degree of covalency in these systems.

Breaking the octahedral symmetry

The edge–sharing CoO_6 octahedra in a CoO_2 layer of Na_xCoO_2 are compressed along the c–axis (oriented parallel to the (1 1 1) direction of one octahedron, see

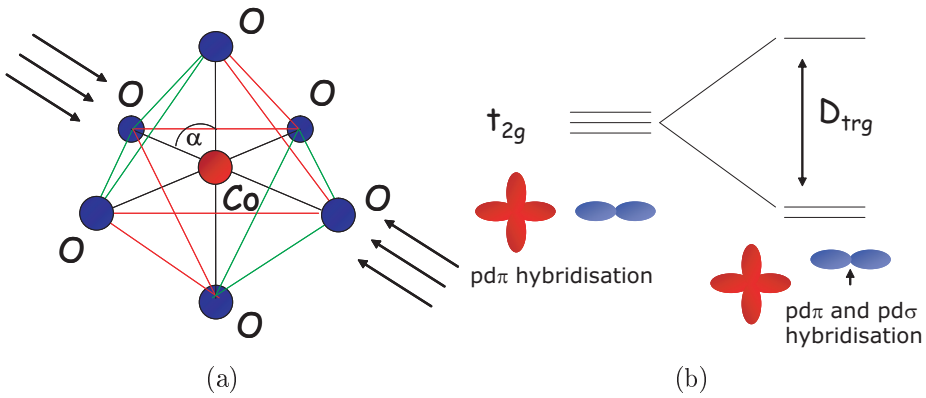

Figure 5.16: (a): Distortion of the octahedra. (b): Splitting of the t_{2g} states in a trigonal crystal field.

figure 5.16(a)). This distortion reduces the point group symmetry of the cluster to D_{3d}. As explained above, the ground state of the Co^{4+} cluster belongs to the T_{2g} representation of O_h. This representation is split in D_{3d} as $T_{2g} = A'_{1g} + E'_g$, where to avoid confusion, the representations of D_{3d} are primed. Labelling the basis functions of the representation T_{2g} as $|xy\rangle$, $|yz\rangle$, and $|zx\rangle$ (which in this case correspond to the many–body wave functions of the Co^{4+} cluster), the basis functions that transform irreducibly in D_{3d} can be written as

$$|A'_{1g}\rangle = \frac{1}{\sqrt{3}}(|xy\rangle + |yz\rangle + |zx\rangle) \tag{5.21}$$

for the state invariant under operations in D_{3d} and

$$|E'_g\pm\rangle = \frac{1}{\sqrt{3}}(|xy\rangle + e^{\pm i\frac{2\pi}{3}}|yz\rangle + e^{\pm i\frac{4\pi}{3}}|zx\rangle) \tag{5.22}$$

for the doubly degenerate states that transform like E'_g. A $3d$ orbital with the symmetry A'_{1g} looks like a $3z^2 - r^2$ orbital and points into the direction of the crystallographic c–axis. In a one–electron picture, for an adequate ordering of the energy of the orbitals, the Co^{4+} cluster would correspond to e'_g orbitals completely filled with 4 electrons and a half filled a'_{1g} orbital [62].

The rhombohedral distortion of the CoO_6 octahedra is estimated by the deviation of the Co-O-Co bond angle from 90°. For example, for $x \approx 0.7$ Huang *et al.* find an angle $\alpha \approx 96°$ [61] which leads to a change of the thickness of one octahedron by 10%, assuming that the Co–O bond distance remains constant during distortion.

From the fit of unpolarised NEXAFS spectra [165], Wu *et al.* estimated $D_{trg} = 1\,\text{eV}$ for the splitting $D_{trg} = \langle E'_g\pm|\mathcal{H}|E'_g\pm\rangle - \langle A'_{1g}|\mathcal{H}|A'_{1g}\rangle$ between the many–body ground state A'_{1g} and the excited states $|E'_g\pm\rangle$. By contrast, Koshibae and Maekawa using a point charge model obtained a negligible splitting and suggested that the band splitting at the zone center obtained in band structure calculations is dominated by the effective Co-Co hopping mediated by intermediate O atoms [159]. However,

one expects that the splitting is dominated by covalency effects and that the ionic contribution only plays a minor role.

In order to estimate the energy splitting between A'_{1g} and E'_g due to the trigonal distortion, further calculations have been done. As already explained, the A'_{1g} states can be written as $A'_{1g} = \frac{1}{\sqrt{3}}(|xy\rangle+|yz\rangle+|zx\rangle)$, the E'_g states as $E'_{g,1} = \frac{1}{\sqrt{2}}(|yz\rangle-|zx\rangle)$ and $E'_{g,2} = \frac{1}{\sqrt{6}}(|xy\rangle - |yz\rangle - |zx\rangle)$. The only part of the Hamiltonian where the trigonal distortion comes into play is a change in the hopping part through changes in relative orientations of the orbitals and the O-O distances. In addition, an r^{-3} distance dependence for the hopping between p orbitals [30] has been assumed. For the parameters determined as explained below a negative value of $D_{trg} = E(E'_g) - E(A'_{1g}) =\sim -0.1\,\text{eV}$ has been obtained. However, the sign is sensitive to the relative values of Co-O and O-O hybridisation. In this sense, there is a competition between t_{pp} and t_{pd}. Here, t_{pp} shifts the A_{1g} states to lower energies and increases the values of D_{trg} until, at a critical ratio t_{pd}/t_{pp}, D_{trg} changes sign. This calculation is only a first order approximation, since only the positions of the corresponding atoms have been changed under a trigonal distortion, but not the orientation of their orbitals, which can lead to second order effects since only the orbitals are included that hybridise in the undistorted case. In order to address this point, calculations with only one hole but all possible oxygen states (see equation (5.6) have been carried out, which led to the result that effects beyond first order perturbation are important. Therefore, while a realistic calculation of D_{trg} seems to require a full diagonalisation in the D_{3d} group (which is beyond the scope of this work) these results suggest a small value of $|D_{trg}|$.

Very recently, $D_{trg} = 0.315$eV has been obtained by an ab–initio quantum chemical configuration interaction method in a CoO_6 cluster [206]. In fact, this is the most reliable result. The method used is known to provide accurate results for charge conserving excitations and has been used successfully in a large family of strongly correlated systems [206].

To check wether the distortion affects the results for cubic symmetry, the matrix element $Q_{mix} = \langle E'_g \pm |\mathcal{H}|E'_g\pm, 2\rangle$ between the E'_g states and the lowest exited states $|E'_g\pm, 2\rangle$ of the same symmetry has been estimated. These excited states belong to the irreducible representation E_g of O_h and therefore do not hybridise with the ground state in cubic symmetry. With a pure hopping Hamiltonian as explained above and an assumed r^{-3} distance dependence for the hopping between p orbitals [30], a $Q_{mix} = -0.09\,\text{eV}$ was found. Since $|Q_{mix}|$ is very small compared to the other energies of the model, in particular $10Dq$ and the separation between T_{2g} and E_g levels, one can safely use the states obtained in cubic symmetry for the calculation of the NEXAFS spectra.

A ground state with E'_g symmetry is incompatible with the NEXAFS data. Therefore only a positive D_{trg} is consistent with experiment. The value $D_{trg} = 0.315\,\text{eV}$ is smaller but of the order of magnitude of the band width reported in ab–initio calculations. A small value of D_{trg} would be consistent with the proposal of Koshibae and Maekawa [159] that the energy splitting does not originate in the crystal field, but

is determined by the kinetic energy of the electrons. Within this picture, translated to the many–body states and neglecting D_{trg}, the ground state for one Co^{4+} cluster moving in a lattice of Co^{3+} is a Bloch state with total wave vector $K = 0$ in an effective Kagomé sublattice with point symmetry $A_{1g}^{'}$. To keep it simple, restricting the wave function to only three sites and one of the four Kagomé sublattices, the ground state would be

$$|g\rangle = \frac{1}{\sqrt{3}}(|1, xy\rangle + |2, yz\rangle + |3, zx\rangle), \tag{5.23}$$

where $|i, \alpha\rangle$ denotes a state composed of the ground state of one Co^{4+} cluster with symmetry α at site i and the (invariant A_{1g}) ground state of the Co^{3+} cluster at the other two sites. However, the effective tight–binding Hamiltonian, considering only the most important hopping term and neglecting D_{trg}, has a U(4) symmetry due to the equivalence between the four Kagomé sublattices. The different possibilities of breaking this symmetry leads to several scenarios for the ground state [166].

The difference between equations (5.21) and (5.23) for the polarisation dependence of the intensity in the NEXAFS spectra can be easily illustrated for the hypothetical case in which the final states $|f_\alpha\rangle$ in equation (5.18) for a Co^{4+} cluster have a core hole $2p_\alpha$ ($\alpha = x$, y, or z) with given spin and the rest of the state (the holes of the 3d shell) belongs to the A_{1g} irreducible representation. This intensity with a factor two of resulting from the spin corresponds to the sum of the intensities of the peak A in figure 5.17 (for a total momentum $j = 3/2$ of the core hole) and the corresponding peak at higher energies and lower intensity for $j = 1/2$ (A' in figure 5.17). For incoming light in the direction β, $\mathcal{H}_L$ is proportional to the momentum operator in this direction $\hat{p}_\beta$. Then by symmetry, all matrix elements $\langle f|\mathcal{H}_L|i\rangle$ entering equation (5.18) can be related to $\gamma = \langle f_x|\hat{p}_y|xy\rangle$.

With this, the polarisation dependence can be calculated. The crystallographic c–axis is represented by $\frac{1}{\sqrt{3}}(x + y + z)$ and the a and b–axes by $\frac{1}{\sqrt{2}}(x - y)$ and $\frac{1}{\sqrt{6}}(2z - x - y)$, respectively. Using equation (5.21), the contribution of these states (summed over α) to the intensity in the one-cluster picture can be calculated. For **A** being parallel and perpendicular to the c–axis, respectively, becomes

$$I_{\parallel}^{1} = 4|\gamma|^2/3,\ I_{\perp}^{1} = |\gamma|^2/3. \tag{5.24}$$

In the extended picture (equation (5.23)) the light operator is a sum over all sites as it is already described. Taking again only three sites for simplicity, there are three possible final states for each core hole orbital $2p_\alpha$ $|i, f_\alpha\rangle$ depending on which site i was excited by the core hole. Adding these contributions one finds from equation (5.18)

$$I_{\parallel}^{ext} = I_{\perp}^{ext} = 2|\gamma|^2/3. \tag{5.25}$$

Thus, when the hole is distributed over one Kagomé lattice so that coherence is lost, then there is a drop in intensity by a factor of two for **A** parallel to c in the

$F_0 = 3.5$	$pd\sigma = 2.35$	$10Dq^i = 1.2$
$F_2 = 0.2$	$pd\pi = -1.0$	$\epsilon_O = 13$
$F_4 = 0.006$	$pp\sigma = 0.8$	$\Delta_{CT}(\mathrm{Co}^{3+}) = 2.9$
$U_{dd} = 4.52$	$pp\pi = -0.2$	$\Delta_{CT}(\mathrm{Co}^{4+}) = -1.1$

Table 5.2: Best fit parameters, all parameters given in eV. The superscript i in $10Dq^i$ denotes the "ionic" part of the energy splitting.

NEXAFS spectra for the sum of the contributions of peaks A and A' (see figure 5.17). This factor is large enough to be detected in the experiment. In this case where a hole is distributed over one Kagomé lattice, the result is the same as for a ground state composed of a statistical average of the three T_{2g} states and has no polarisation dependence. The situation is different if the breaking of the above mentioned U(4) symmetry leads to some coherence between T_{2g} states at the same site. Note that the intensity is redistributed among the different directions but keeps the same angular average. This is due to the local character of the transition and the fact that only one irreducible representation is involved in the initial state, in the final state and the operator.

We shall show that our results point to an intermediate situation, but with dominance of the lattice effects over the on-site distortion.

The NEXAFS intensity

As mentioned above, the ground state for a Co^{3+} cluster is invariant under the symmetry operations of O_h and as a consequence, the corresponding NEXAFS intensity is independent of the polarisation of the incident light. Also, for Co^{4+}, the NEXAFS intensity for a statistical average of the three states of the irreducible representation T_{2g} ($|xy\rangle$, $|yz\rangle$ and $|zx\rangle$) (which would correspond to a ground state like equation (5.23)) leads to the same intensity for $\mathbf{A}||c$ and $\mathbf{A}\perp c$.

Instead, using equation (5.21) for the ground state of Co^{4+}, one obtains a polarisation dependence similar to the experiment, but more pronounced: The ratio of the intensities for excitations to a state with A_{1g} symmetry plus a core hole is $I^1_{||}/I^1_{\perp} = 4$ (see equation (5.24)) whereas the experimental ratio has been found to be $I^{exp}_{||}/I^{exp}_{\perp} \approx 1.8$. The experiment, therefore, suggests an intermediate situation between the ground states (5.21) and (5.23). The actual many–body ground state of the system is out of the scope of these cluster calculations. In order to simulate this situation, the spectrum has been calculated as a weighted average of equations (5.24) and (5.25) :

$$I_{total} = (1-\xi)I^1_f + \xi I^{ext}_f \tag{5.26}$$

with $0 \leq \xi \leq 1$. In order to optain the observed experimental ratio for the A_{1g} peak ξ has to be approximately equal to 0.73.

In figure 5.17 the results for the NEXAFS intensity for the parameters indicated in Table 5.2 that best fit the experiment are shown. As adjustable parameters,

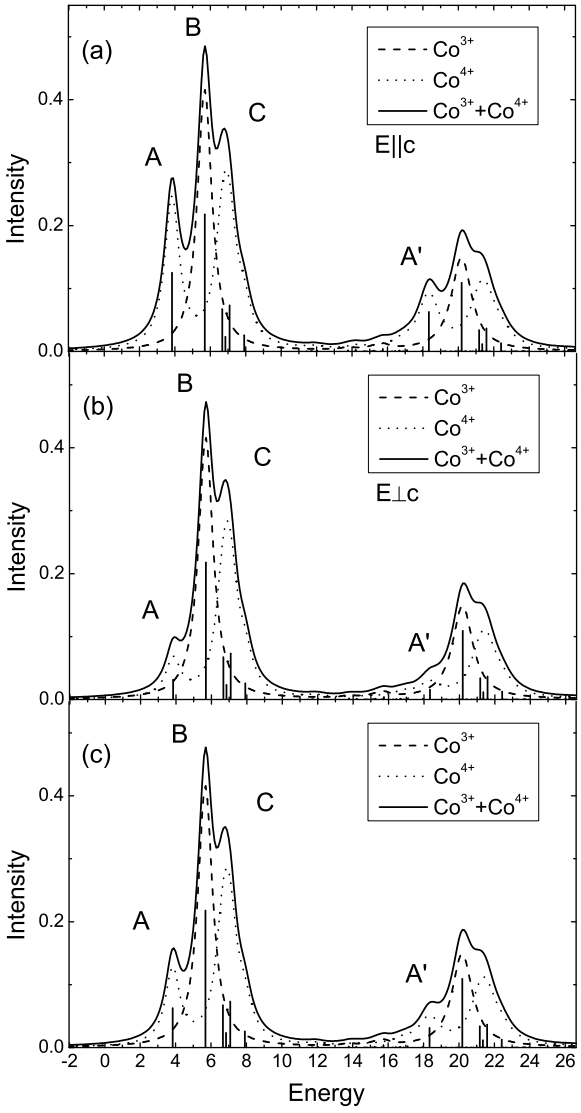

Figure 5.17: NEXAFS spectra of $Na_{0.5}CoO_2$ for different polarisations: (a) $E||c$ and (b) $E \perp c$. In (a) and (b) equation (5.21) was used to calculate the ground state of the Co^{4+} cluster, while (c) corresponds to equation (5.21) yielding a polarisation independent result. Contributions due to the Co^{3+} cluster are shown by dashed drawn curves, those of the Co^{4+} cluster are indicated by dotted curves. The fully drawn curves represent their sum.

F_0 (or $U_d = F_0 + 4F_2 + 36F_4$), ϵ_O (or $\Delta_{CT}(Co^{n+}) = E(d^{n+1}L) - E(d^n)$), $10Dq$, $(pd\sigma)$, and $(pp\sigma)$ are used with $U_{dc} = U_d + 0.15\,\text{eV}$. F_2 and F_4 were taken from values that approximately fit the energy separation between different terms in atomic spectra [207]. For the hopping process, the relations $(pd\pi) = -\sqrt{3}(pd\sigma)/4$, and $(pp\pi) = -0.81(pd\sigma)/3.24$ [30] have been assumed.

In terms of more fundamental parameters one has:

$$\begin{aligned} \Delta(Co^{3+}) &= \epsilon_O - \epsilon_{e_g} - 3F_0 + 8F_2 - 33F_4 - pp\sigma + pp\pi \\ \Delta(Co^{4+}) &= \epsilon_O - \epsilon_{e_g} - 4F_0 + 4F_2 - 37F_4/2 - pp\sigma + pp\pi, \end{aligned} \tag{5.27}$$

which correspond to the minimum energy necessary to promote a Co $3d$ hole to a linear combination of O $2p$ states in absence of Co-O hopping. If the O $2p$ hole is

localised at one site, $pp\sigma$ and $pp\pi$ are absent in these equations and both $\Delta(Co^{3+})$ increase by 1.0 eV.

The observed electronic structures can only be understood when it is assumed that several electronic configurations with a considerable amount of ligand holes (as described above) is present in the ground state. This implies large covalency, and this in turn points to high hybridisation, a low charge transfer gap Δ_{CT} and low U_d in comparison with other transition metal oxides. Also, the relative positions and the structures of the peaks of Co^{3+} and Co^{4+} point to a relatively large $10Dq$ and a low spin configurations. This is a rough explanation of the resulting parameters in Table 5.2.

The Co^{3+} cluster (dashed drawn curve in figure 5.17) shows only one main peak at the $L_{3,2}$ edge (peak (B)) which results from an excitation from the ground state with A_{1g} symmetry to an excited state with E_g symmetry. The peak is polarisation independent. In the similar system $LiCoO_2$ which nominally contains only octahedra with four holes (i.e. a Co^{3+}–central ion) [178] one observes a weak structure on the high energy side of the e_g peak which is missing here because of the missing $2p$–$3d$ core hole exchange interaction. The Co^{4+} cluster shows two main structures at both edges. The lower energy peak structure (A) contains a single peak and results from excitations into states with A_{1g} symmetry, while the higher energy peak structure (C) originates from many excitations of low intensity to final states with T_{1g} and T_{2g} symmetry. Only peak (A) shows a polarisation dependence and is strong when light is polarised along the (1 1 1) direction (crystallographic c–axis), but weak for polarisation perpendicular to the (1 1 1) direction (in–plane polarisation). The main conclusions regarding the electronic structure have been drawn from the polarisation dependence of the A_{1g} peaks, for which the $3d$ shell is in a singlet spin state after the excitation. Therefore, the effect of the $2p$–$3d$ exchange vanishes in first order.

In figure 5.18 the theoretical results are compared with experimental data for the stoichiometries $Na_{0.4}CoO_2$ and $Na_{0.6}CoO_2$ as well as for polarisation perpendicular and parallel to the crystallographic c–axis. In the theoretical curve at the bottom, the weighted average equation (5.26) with $\xi = 0.73$ which best fits the polarisation dependence of peaks A and A' has been used. As explained above, this average redistributes the spectral weight among the different polarisations but does not affect the total intensity resulting from a Co^{4+} cluster. However, when comparing the bottom and top curves in figure 5.18, the above mentioned average is not sufficient to produce a quantitative agreement with the experiment: there is still a disagreement in the intensity ratio between that resulting from a Co^{4+} cluster and that originating from a Co^{3+} cluster. For $x = 0.4$, the theoretical contribution of Co^{4+} seems to be two times larger than observed in the experiment (the ratio is a bit smaller than two for x=0.6). Wet chemical redox analysis points to an oxygen non–stoichiometry $Na_xCoO_{2-\delta}$ for $x \leq 0.7$, leading to a proportion of Co^{+4} smaller than that corresponding to the nominal Na content. Actually, upon Na de–intercalation, the Co valence first increases as expected, but does not exceed the value of 3.5 [208]. This can explain part of the discrepancy. Another possible explanation is the redistribu-

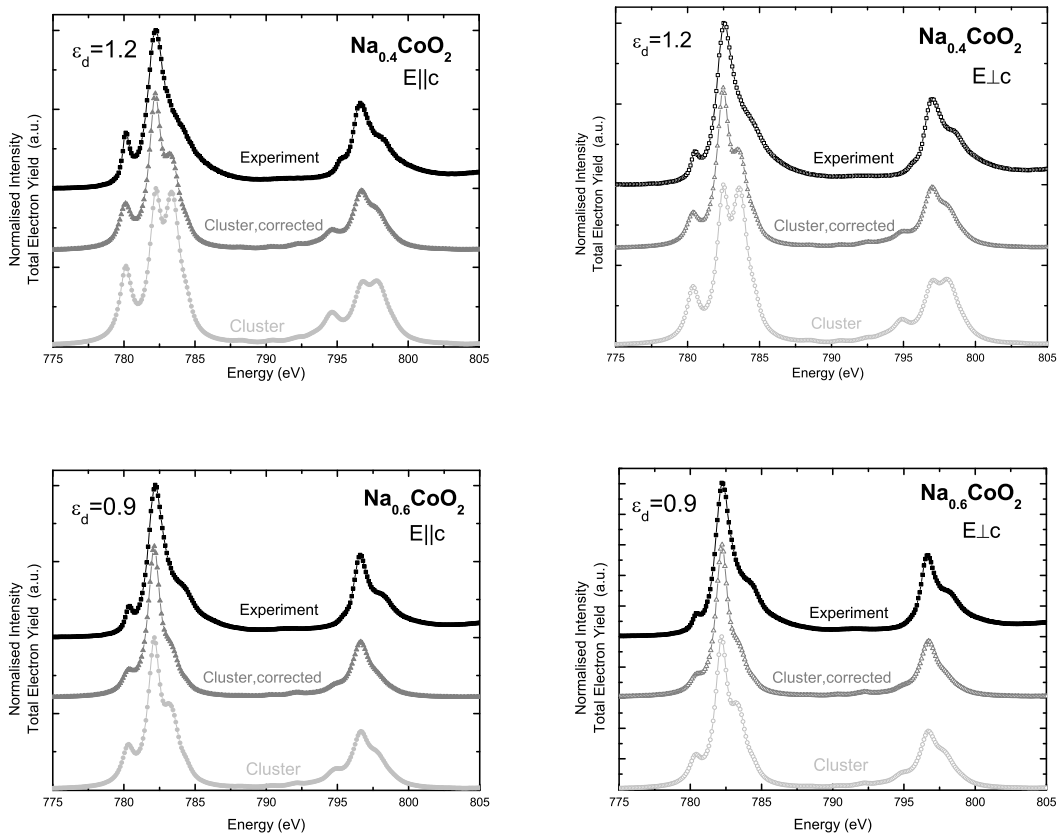

Figure 5.18: Comparison of the theoretical results (bottom) with experimental data (top) for x=0.4 and x=0.6 for polarisations indicated inside each figure. In the middle curve the results are manipulated in such a way, that the intensity of the Co^{4+} cluster is decreased by a factor 2.0.

tion of spectral weight due to itineracy of the final states. The effects of the hopping in a model of two sites has been studied by G.A. Sawatzky and A. Lenselink [209]. In principle, this is possible to calculate when the knowledge of the local transition matrix elements is combined with an effective Hamiltonian for the motion of the holes through the lattice. This approach has been followed to calculate different optical properties of the cuprates [186, 191, 210–213]. However, in this system this task is more difficult and is beyond the scope of the present work. In addition, in the present case, these effects seem to be of minor importance for the peak A, because the expected magnitude of the hopping $\sim 0.1\,\mathrm{eV}$ [159] is much smaller than the energy difference between excited states (~ 1.9 eV). However, they are certainly important for the higher energy multiplets.

Note that the neglect of the exchange interaction between the core hole and the $3d$ holes leads to a slight change in the shape of the curves, but does not affect the total intensities for both clusters.

Spin–orbit coupling inside the $3d$ shell, which has been neglected, might also lead to a reduction of the intensity of the low energy peak at the L_2–edge that corresponds to peak A as an effect of selection rules [214]. However, in this case, the effect of spin–orbit coupling is small compared to the intersite hopping terms $t \sim 0.1$ eV [159]. Therefore, the approach of considering a sixfold degenerate ground state for Co^{4+} instead of a split doublet and quartet states is justified. Therefore, it can be expected that the reduction of intensity due to spin–orbit coupling inside the $3d$ shell is small.

The relative peak positions do not change upon doping, except for the A_{1g} peak. The distance between the main (E_g) peak and the A_{1g} peak becomes smaller with increasing x (decreasing amount of Co^{4+} ions) [148]. This change is best simulated by a variation of the ionic crystal field $10Dq^i$ from 1.2 eV (x=0.4) to 0.9 eV (x=0.6). A decreasing value of $10Dq$ is also supported by Huang *et al.* who performed neutron diffraction experiments on powder samples and found an increasing Co–O bond length with increasing doping [61]. This would change the total crystal field splitting (the ionic term $10Dq$ plus the effects of hopping), but a slight change in the hopping parameters does not change the relative peak positions.

The XPS intensity

In addition to the calculations of the NEXAFS experiments, polarisation independent calculations of the Co $3d$ XPS intensity at the valence band for Co^{3+} have been performed, too. Different from NEXAFS which is mostly sensitive to crystal field effects, XPS is very sensitive to charge transfer effects. As it will be shown, the position of the Co $3d$ satellite peak depends strongly on the size of the pd hopping integral. Note that no core hole is involved in such a process. In addition, the spectra are multiplied by a Fermi distribution function in order to get the correct shape at low binding energies. Since the XPS spectra have been calculated only for an octahedron with a Co^{3+} central ion, it is most useful to compare the theoretical data with the experimental data for the highest Na content, in this case $x = 0.7$. Calculations for Co^{4+} have not been done since there the matrices become very large due to a large number of possible configurations. In figure 5.19 (a) a comparison of the result of the Co^{3+} cluster using the parameters that best fit the NEXAFS experiment (see Table 5.2) with experimental data for $x = 0.3$ and $x = 0.7$. The theoretical result fits the experiment pretty well; note that even the double peak structure at the satellite at ≈11 eV is reproduced. The spectra are essentially composed of three parts: A strong peak at ≈0.7 eV and a satellite double peak structure at around 11 eV that both originate from excitations with the final states having T_{2g} symmetry. A third peak in between these two at around 6 eV consists of a mix of excited states with T_{2g} and E_g symmetry. In the true spectra of this region also the oxygen $2p$ states are present which are missing in the calculation since we consider only the ejection of $3d$ electrons. It is worth noting that the peak at 11.4 eV binding energy originates from excitations into final states that contain a sizeable amount (20%) of a d^8L^3 configuration. Note that the connected ground state configuration d^9L^3 plays a minor role in the electronic structure (Table 5.1). Therefore, these

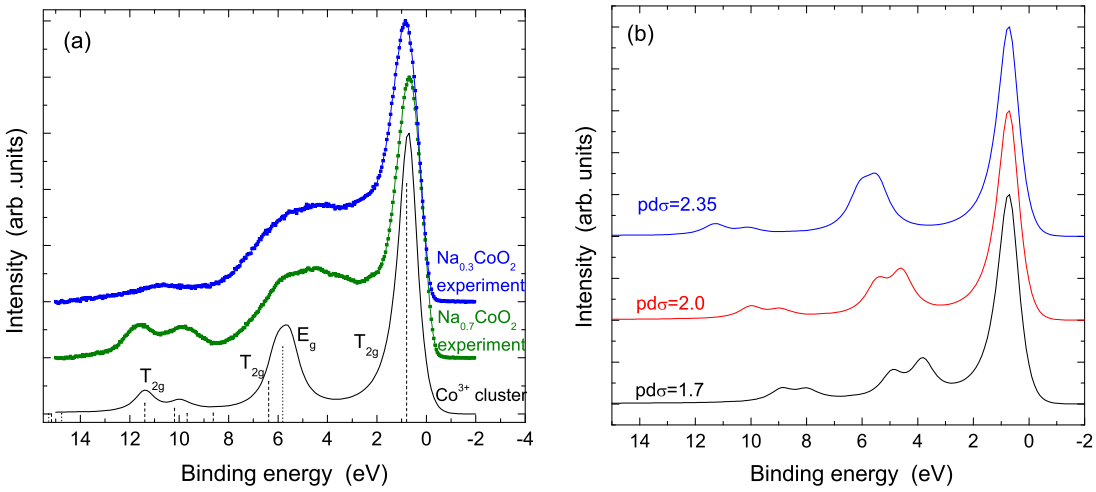

Figure 5.19: (a) Comparison of the theoretical results for Co^{3+} (black) with experimental data for x=0.3 (blue) and x=0.7 (dark green) for unpolarised light. The dashed vertical lines represent the intensity for excitations into final states with T_{2g} symmetry, whereas dotted lines represent excitations into final states with E_g symmetry. (b) Comparison of the effect of different $pd\sigma$ values on the results of calculations for Co^{3+} using the parameters as in table 5.2.

states can only appear after a charge redistribution in the final state due to the strong hybridisation in the CoO_6 octahedron. The main parameters that change the spectrum are the pd intersite hopping t_{pd} as well as the on–site energy E_p of the oxygen ligands. In figure 5.19 (b) the dependence of the spectral shape for different values of $pd\sigma$ is shown. It is seen that the satellite peak structure around 11 eV binding energy shifts to higher energies with increasing $pd\sigma$ due to increasing hybridisation. The fits lead to $pd\sigma = 2.35\,\text{eV}$, a value also used in the NEXAFS calculation. A similar behaviour of the center peak at around 4-6 eV was observed for different O $2p$ on–site energies.

Indirect d-d hopping - an approach by cluster perturbation method

In the results presented above always only one CoO_6 octahedron has been used, which, of course, makes a Co–Co hopping impossible. From what has been shown by Koshibae and Maekawa [159] the main hopping path from one Co site to a neighbouring Co site is via an intermediate O site which leads to a picture of a Kagomé lattice. In figure 5.20 (left) a part of a Kagomé lattice is shown without any distortion. One finds that hopping is only reasonable from a t_{2g} orbital to another t_{2g} orbital since the e_g orbitals are too high in energy. The calculations presented above give all values necessary to calculate an effective dd hopping using a cluster perturbation approach.

To explain the idea, it will be illustrated with a simple model that consists of two

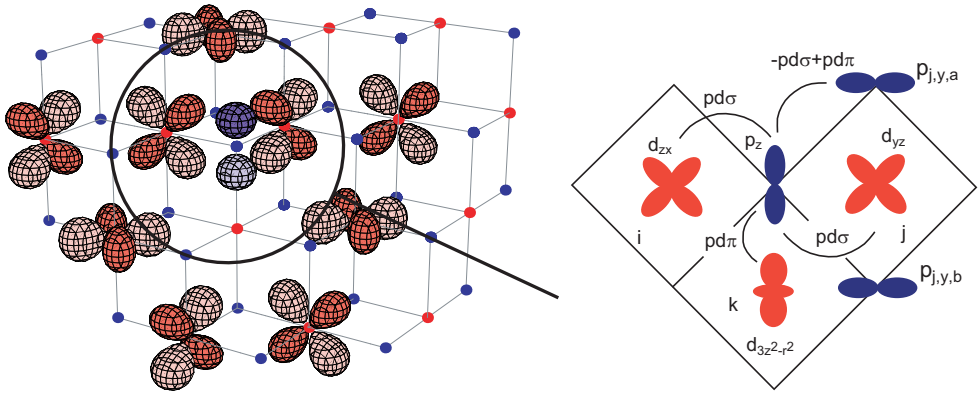

Figure 5.20: Illustration of a possible hopping path. On the left a part of a CoO_2 plane is shown with the d orbitals that may contribute to the transport. For the sake of a clearer view only one oxygen orbital is depicted. Cobalt sites are indicated by red colour, oxygen sites by blue colour. On the right an enlargement is shown with three Co sites and important O orbitals that illustrates a hopping from one cobalt site (i) to another Co site (j) via an intermediate O site.

d sites 1 and 2 with an O site in the middle in a linear arrangement containing only one hole. Without loss of generality one can consider the Co site 1 and the O site as one cluster that contains the hole with the ground state $|g_1(1)\rangle = d_1^+|0\rangle - \frac{t_{pd}}{\Delta}p^+|0\rangle$ for $t_{pd} << \Delta$, where the subscript denotes the site and the number in parentheses denotes the number of holes. d_i^+ creates a hole on the d site i; similarly for p^+ at the oxygen site. Consequently, the second Co site has the basis function $|g_2(0)\rangle$. In first order, the hopping t_{dd} of the hole from site 1 ($|g_1(1)g_2(0)\rangle$) to site 2 ($|g_1(0)g_2(1)\rangle$) is described by

$$\begin{aligned}\langle g_1(0)g_2(1)| + t_{pd}d_2^+p|g_1(1)g_2(0)\rangle &= t_{pd}\langle g_1(0)|p|g_1(1)\rangle\langle g_2(1)|d_2^+|g_2(0)\rangle \\ &= -\frac{t_{pd}^2}{\Delta}\langle g_2(1)|d_2^+|g_2(0)\rangle, \qquad (5.28)\end{aligned}$$

as we know from second-order perturbation theory. The situation in Na_xCoO_2 is different because of the importance of covalency and the smaller overlap between cluster states. In figure 5.20 (right) a sketch of the hopping possibilities of a hole from site i to site j and also to site k are shown. Note that the only possibility for a hole to hop from a t_{2g} orbital at site i to site k is into an e_g orbital. Such an effective hopping involves states higher in energy and is disregarded. The only hopping processes that have been taken into account are from a Co^{4+} site (5 holes) to a Co^{3+} site (4 holes). From energetic reasons, all other possibilities are less likely. As it can be seen in figure 5.20 (right) a hole that sits on the intermediate oxygen site p_y has three possibilities to hop on: Either to the Co site $d_{j,yz}$ or to one of the two O sites above $p_{j,y,a}$ and below $p_{j,y,b}$ the Co site. This scenario leads to the

intersite hopping parameter t_{dd}:

$$\begin{aligned} t_{dd} &= \langle g_i(4)g_j(5)|(t_{pd}d^+_{j,yz} + t_{pp}(p^+_{j,y,a} - p^+_{j,y,b}))p_z|g_i(5)g_j(4)\rangle \\ &= \langle g_i(4)|p_z|g_i(5)\rangle\langle g_j(5)| - t_{pd}d^+_{j,yz} - t_{pp}(p^+_{j,y,a} - p^+_{j,y,b})|g_j(4)\rangle \\ &= \langle g_i(4)|\frac{1}{2}p_{yz}|g_i(5)\rangle\langle g_j(5)| - t_{pd}d^+_{j,yz} - t_{pp}p^+_{j,yz}|g_j(4)\rangle \\ &= -\frac{1}{2}\langle g_i(4)|p_{yz}|g_i(5)\rangle\langle g_j(5)|t_{pd}d^+_{j,yz} + t_{pp}p^+_{j,yz}|g_j(4)\rangle. \end{aligned} \tag{5.29}$$

With the parameters found from a fit of the experimental NEXAFS and XPS data (see Table 5.2) the *dd* hopping via an intermediate oxygen site has been found to be $t_{dd} = 101\,\text{meV}$, which is in a good agreement to the value $t = 0.1\,\text{eV}$ as it has been estimated by Khalliulin *et al.* [196] from the free–electron bandwidth $\sim$1 eV [57]. Naturally, t_{dd} is sensitive to the value of $pd\sigma$ and $pd\pi$.

5.4 Electronic structure and Fermi surface topology of Na_xCoO_2

Despite all efforts, a discrepancy between the experimental results of the shape of the Fermi surface (FS) and its theoretical explanations remains. As explained above, angle–resolved photoemission (ARPES) revealed only a single hole like FS around Γ and no hole pockets [95–97, 127]. Theoretically, local–density approximation (LDA) calculations predict a Fermi surface with a large portion around the Γ point of the Brillouin zone in agreement with the experiment, and six pockets near the K points [57, 112] in disagreement with the experimental data. Since the associated e'_g band fails to cross the Fermi level for a wide range of sodium doping concentration x these pockets cannot be observed at the Fermi surface.

In the following, the reason for this discrepancy will be explained and a solution for the correct theoretical treatment will be shown. Most of the following section has been accepted for publication in Physica C (see also cond-mat/0610173) [160]. There, a detailed description of the formalism and further arguments can be found.

In general, LDA is a procedure for calculating the energy of the system in terms of the local electronic density, approximating exchange and correlation in mean field. The density is expressed in terms of (fictitious) eigenstates of a suitable chosen one–particle problem. It is known that LDA fails to reproduce the band structure of highly correlated systems. However, when using exact diagonalisation or the self–consistent Born approximation applied to generalised effective Hubbard or t–J models, the dispersion was successfully explained, for example, in the case of Sr oxychlorides or underdoped cuprates [212, 213, 215–217]. LDA is also known to fail in low dimensional materials, like layered systems or two-dimensional electron gases, for which new techniques like exact exchange have been developed [218].

In particular, one effect of the correlations is to narrow the bands predicted by LDA. When there are several bands crossing the Fermi energy, the narrowing of each band may be different and leads to distortion of the Fermi surface. It has been suggested that the discrepancy between the LDA calculations and the Fermi surface measured by ARPES can be explained as an effect of the correlations [219], which are absent in LDA and LDA+U approaches, even in the most sophisticated treatments [157]. However, the effective Hamiltonian used is unjustified and differs from the one that will be introduced below. Moreover, the dispersion relation along Γ–K differs from the experimentally observed one, and the results contradict those obtained using dynamical mean field theory, which actually obtain an enhancement of the hole pockets [220]. Another recently proposed explanation is a localisation of the hole pockets by disorder [221]. However, this localisation is not expected to alter the small volume enclosed by the main portion of the LDA Fermi surface around Γ, while according to the more recent ARPES experiments, this portion contains all holes in a way consistent with the Luttinger theorem [97].

Another reason for the observed discrepancy is the large value $3D \sim 0.3\,\mathrm{eV}$ of the T_{2g} splitting in the effective three–band model for the cobaltates. This value has been obtained by quantum chemical methods [206], which are the most reliable for this type of calculations, because they properly include the effects of correlations and covalency. The effects of correlations in the original multiband Hamiltonian (including Co and O orbitals) that have an effect in "tuning" the Co–O charge transfer energy are crucial. These effects are neglected in LDA.

Therefore, a good starting point should account for the strong Co–O covalency. In Ref. [160] A. Bourgeois *et al.* start from the exact solution of the appropriate multiband Hamiltonian for Co $3d$ and O $2p$ holes in the basic CoO_6 octahedron. The parameters of the multiband model were fixed by a previous fitting of the polarisation dependent NEXAFS spectra (see the previous section and Ref. [179]). The effective model has been solved in a slave–boson mean–field approximation [222, 223]. The most important effective hopping is the one mediated by O orbitals, described by the hopping parameter $t = 0.1\,\mathrm{eV}$ (see previous section). While t is the more important hopping process [166], the direct hopping t' between d electrons might be important for a realistic description of the band structure [159]. For the direct hopping Bourgeois *et al.* find $t' = 50\,\mathrm{meV}$ [160]. The energy splitting of the t_{2g} states due to the trigonal distortion is an essential parameter of the effective model. Its large value compared to estimations using a point charge model [159] is due to the effects of the Co–O hybridisation. Therefore, the effect of the distortion of the CoO_6 octahedra is stronger than in previous multiband approaches, but not so strong as to justify a one–band model based on localised a'_{1g} bands [160].

In figure 5.21 the resulting dispersion relation for electrons for three different values of x and the corresponding FS are shown. As a consequence of the relatively strong trigonal splitting due to the large Co–O covalency and the band renormalisation, the hole pockets near the Brillouin zone boundary disappear. Note that if only one of these effects were present, these pockets would remain [160]. The results agree

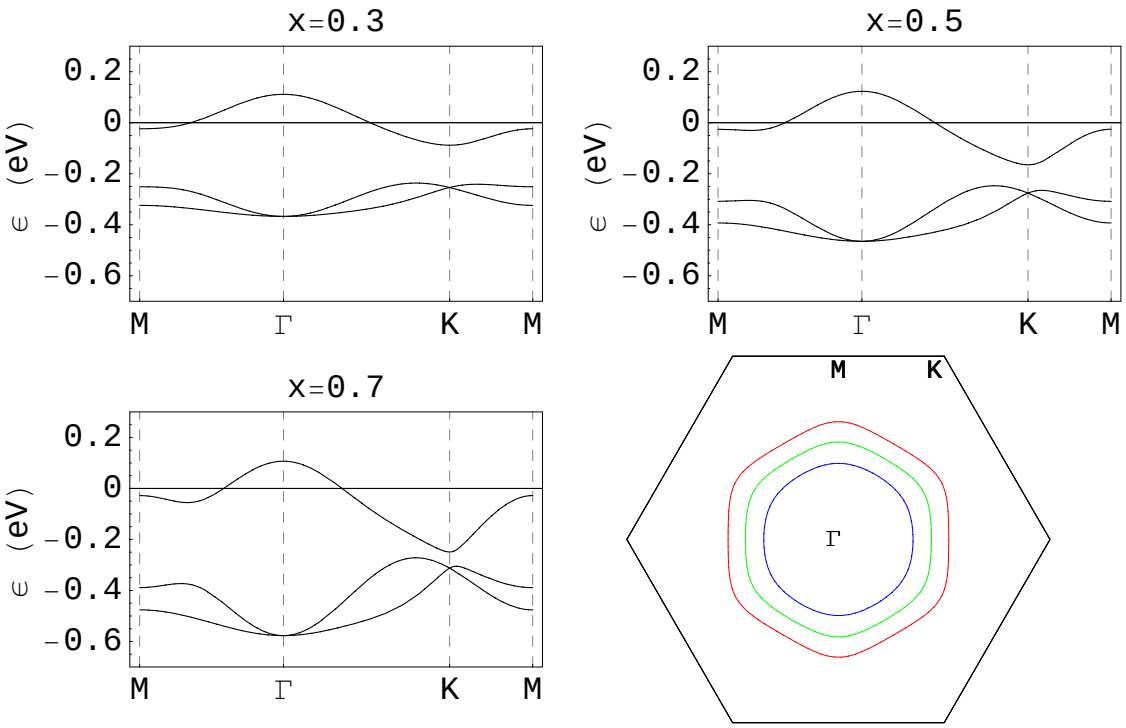

Figure 5.21: Renormalised band–structures for doping $x = 0.3,\ 0.5,\ 0.7$ and corresponding FS in red, green, blue respectively. Larger FS corresponds to lower doping x. The figures are taken from Ref. [160].

with the most recent ARPES measurements [97], the Fermi surface shows only a central lobe with a hexagonal shape, which is more pronounced for a lower doping level. The feature that would give rise to the hole pockets near the K points remains under ϵ_F with almost no doping dependence. The a'_{1g} character has been found to be minimal in the Γ-K direction and maximal in the Γ-M direction, which indicates that although only one band crosses the ϵ_F, its character is strongly mixed and cannot be derived from states of a'_{1g} symmetry only [160]. Also, the dispersion relation in the Γ-K direction has the form of a hysteresis loop, in agreement with experiment.

Summary

In this work, the electronic structure of Na_xCoO_2 has been investigated using experimental and theoretical methods. As experimental tools, mainly X–ray absorption and photoemission spectroscopy have been employed, but also magnetisation and X–ray diffraction experiments have been performed. For the theoretical description of the absorption data, cluster calculations have been done which are able to explain the experimental results and help to improve the fundamental understanding of the system.

The phase diagram of Na_xCoO_2 shows three important regions including the special case $x = 0.5$. At this composition an insulating behaviour has been found, different from all other doping levels. In this case, Na ordering as well as charge ordering are expected. Using high energy X–ray diffraction, Na ordering could be confirmed at low temperatures at which the reflection pattern in the reciprocal space showed reflections of half and quarter integers, implying an enlarged unit cell due to ordering. Resonant X–ray scattering at the Co K–edge of an electrochemically de–intercalated $Na_{0.66}CoO_2$ sample showed evidence for two different cobalt sites which can be explained by lattice independent charge ordering, but also lattice distortion effects or orbital ordering can not be ruled out. As a function of temperature, the resonance peak in the $\sigma\sigma$–channel decreases non linearly with increasing temperatures. Such a behaviour may be caused by a loss of order which in turn may be connected to the electronic and thermal transport properties.

Magnetisation measurements on a $Na_{0.82}CoO_2$ single crystal confirmed at $T = 4.2\,\mathrm{K}$ a spin–flop transition for fields parallel to the crystallographic c–axis at $\approx 8.5\,\mathrm{T}$. For a higher doping $x = 0.9$ a stronger signature of uncoupled spins has been found, consistent with a low spin picture at least for the Co^{3+} ions and a decrease of Co^{4+} ions with increasing x.

In order to learn more about the electronic structure of non–hydrated Na_xCoO_2, X–ray absorption and photoemission spectroscopy experiments have been performed on a wide doping range. Since both methods are surface sensitive, the crystals have been cleaved *in–situ* in order to gain information of the bulk properties. Core–level photoemission results show two different Na sites which are occupied differently for doping levels $x = 0.3$ and $x = 0.7$ in such a way that at $x = 0.3$ mainly just one site is occupied, whereas at $x = 0.7$ both sites are almost equally occupied. Such a behaviour can be understood in terms of two different Coulomb energies due to different Na–Co distances. From temperature dependent measurements a change in

the electronic structure at temperatures larger than 100°C has been observed and a loss of Na at temperatures larger than 150°C. After heating the sample at 400°C for one hour, Na could no longer be detected in the photoemission experiment.

Furthermore, X–ray absorption spectroscopy experiments at the Co $L_{2,3}$–edge, the O K–edge, and the Na K–edge have been performed at different temperatures choosing polarised light perpendicular to the crystallographic c–axis and at a grazing incident of 70° with respect to c. It turned out that the surface of Na_xCoO_2 single crystals is very sensitive to adsorbates, so that the samples had to be cleaved *in–situ* at low temperatures under ultra–high vacuum conditions. These adsorbates usually contain oxygen which makes the temperature dependent measurement of the O K–edge unreliable. The adsorbates, however, do not exert any influence at the Co $L_{2,3}$–edge which did not exhibit any significant variation between 25 and 372 K. The study of single crystals with a stoichiometry between $x = 0.4$ and $x = 0.75$ revealed polarisation dependencies that cannot be explained by a simple trigonal distortion of the CoO_6 octahedra. Taking into account the results of both the Co $L_{2,3}$–edge and the O K–edge, it follows that an additional distortion must be present which is stronger for octahedra with a formal Co^{3+} central ion than for octahedra with a formal Co^{4+} central ion. A possible explanation for such a phenomenon has been given by Bernhard *et al.* who found magnetopolarons in $Na_{0.82}CoO_2$ due to a lowering of the local symmetry. Furthermore, doping dependent relative peak positions at the Co $L_{2,3}$–edge have been detected which can be explained by a doping dependent splitting of the t_{2g}–e_g levels (10 Dq) in agreement with cluster calculations. An explanation of the doping dependent splitting is the variation of the Co-O bond lengths which themselves vary with the amount of doping. At the O K–edge strongly polarisation dependent excitations into unoccupied O levels occur. These levels which are hybridised with Na orbitals emphasising the covalent character of the interplanar binding of the CoO_2 and Na planes.

For a further understanding, the local electronic structure around a Co atom in Na_xCoO_2 has been investigated by solving exactly a CoO_6 cluster (a basic octahedron of the system) containing the Co $3d$ and O $2p$ valence electrons and given the appropriate charge according to the Na doping. All interactions between $3d$ electrons in the cluster have been included. For the calculation of the polarisation dependence of the X–ray absorption spectrum, the energy of the Co $2p$ core hole with its spin–orbit coupling $\Delta_{SO} \sim 15\,\mathrm{eV}$ and its repulsion with the Co $3d$ holes has been included. The exchange interaction between Co $2p$ and $3d$ holes has been neglected for simplicity. Due to a comparatively large magnitude of Δ_{SO} as well as crystal–field effects and covalency the influence of this term is expected to be small compared to lighter $3d$ transition metals.

Furthermore, the main conclusions regarding the electronic structure have been drawn from the polarisation dependence of the A_{1g} peaks, for which the $3d$ shell is in a singlet spin state after the excitation. Therefore, the effect of the $2p$–$3d$ exchange vanishes in first order.

Within a purely local picture, assuming an A'_{1g} ground state and disregarding for

the moment the total intensity of the Co^{4+} contribution, it is possible to reproduce the essential features of the polarisation dependent NEXAFS experiments fairly well. Slight differences at the shoulders of the largest peaks originate from the neglect of the Co $2p$-$3d$ exchange interaction which would add an additional weak structure in this region, as shown by comparison with $LiCoO_2$.

Quantitatively, a fully coherent A'_{1g} ground state leads to too a large intensity ratio for the low energy peak of the Co^{+4} contribution between light polarised parallel or perpendicular to the trigonal axis. This indicates that a purely local picture is not fully consistent with experiment. In fact, the best fit corresponds to a $\approx 70\%$ loss of coherence produced by delocalisation. This redistribution of intensity among the different polarisations is consistent with a picture of itinerant electrons based on four Kagomé sublattices hidden in the CoO_2 layer as a first approximation for the electronic structure.

The above mentioned redistribution is not sufficient to explain the large total amount of the Co^{+4} contribution to the intensity. To some degree this discrepancy might be due to a proportion of Co^{+4} that is smaller than suggested by the nominal Na content. A more quantitative calculation of the X–ray absorption spectrum requires that the itineracy of holes in the ground state and the excited states after the creation of the core hole is taken into account, which leads to spectral weight transfer between Co^{+4} and Co^{+3} contributions. Using the cell perturbation method, the indirect Co–Co hopping t via an intermediate O site could be determined to be 100 meV for the values that best fit the experimental spectra.

Finally, an effective Hamiltonian for the motion of the highly correlated t_{2g} states in Na_xCoO_2 has been constructed in a three-band model. It includes the indirect Co-O-Co hopping $t = 100\,\text{meV}$ and the crystal field splitting. In this model, without any additional hypothesis or new adjustable parameters, the dispersion of the bands near the Fermi energy and Fermi surface topology agrees with angle–resolved photoemission experiments, in contrast to predictions using the local-density approximation.

Appendix A

Theoretical tools

A.1 The d-d interaction matrix elements

A complete list of all $\langle ab|\frac{1}{r_{12}}|cd\rangle$ matrix elements for d–d electrons (holes):

(I) Matrix elements for operators that leave the number of occupied states within the t_{2g} and e_g levels unchanged:

	a	b	c	d	$\langle ab\|1/r_{12}\|cd\rangle$
$J(z^2, z^2)$	z^2	z^2	z^2	z^2	$F_0 + 4F_2 + 36F_4 = U_{dd}$
$J(x^2-y^2, x^2-y^2)$	x^2-y^2	x^2-y^2	x^2-y^2	x^2-y^2	$F_0 + 4F_2 + 36F_4 = U_{dd}$
$J(xy, xy)$	xy	xy	xy	xy	$F_0 + 4F_2 + 36F_4 = U_{dd}$
$J(zx, zx)$	zx	zx	zx	zx	$F_0 + 4F_2 + 36F_4 = U_{dd}$
$J(yz, yz)$	yz	yz	yz	yz	$F_0 + 4F_2 + 36F_4 = U_{dd}$
$J(x^2-y^2, zx)$	x^2-y^2	zx	x^2-y^2	zx	$F_0 - 2F_2 - 4F_4$
$J(x^2-y^2, yz)$	x^2-y^2	yz	x^2-y^2	yz	$F_0 - 2F_2 - 4F_4$
$J(xy, yz)$	xy	yz	xy	yz	$F_0 - 2F_2 - 4F_4$ $= U_{dd} - 2J_H(t_{2g})$
$J(xy, zx)$	xy	zx	xy	zx	$F_0 - 2F_2 - 4F_4$ $= U_{dd} - 2J_H(t_{2g})$
$J(zx, yz)$	zx	yz	zx	yz	$F_0 - 2F_2 - 4F_4$ $= U_{dd} - 2J_H(t_{2g})$
$J(z^2, zx)$	z^2	zx	z^2	zx	$F_0 + 2F_2 - 24F_4$
$J(z^2, yz)$	z^2	yz	z^2	yz	$F_0 + 2F_2 - 24F_4$
$J(z^2, xy)$	z^2	xy	z^2	xy	$F_0 - 4F_2 + 6F_4$
$J(z^2, x^2-y^2)$	z^2	x^2-y^2	z^2	x^2-y^2	$F_0 - 4F_2 + 6F_4$ $= U_{dd} - 2J_H(e_g)$
$J(x^2-y^2, xy)$	x^2-y^2	xy	x^2-y^2	xy	$F_0 + 4F_2 - 34F_4$
$K(xy, yz)$	xy	yz	yz	xy	$3F_2 + 20F_4 = J_H(t_{2g})$
$K(xy, zx)$	xy	zx	zx	xy	$3F_2 + 20F_4 = J_H(t_{2g})$
$K(zx, yz)$	zx	yz	yz	zx	$3F_2 + 20F_4 = J_H(t_{2g})$
	xy	xy	yz	yz	$3F_2 + 20F_4 = J_H(t_{2g})$
	yz	yz	zx	zx	$3F_2 + 20F_4 = J_H(t_{2g})$

	zx	zx	xy	xy	$3F_2 + 20F_4 = J_H(t_{2g})$
$K(x^2-y^2, zx)$	x^2-y^2	zx	zx	x^2-y^2	$3F_2 + 20F_4$
$K(x^2-y^2, yz)$	x^2-y^2	yz	yz	x^2-y^2	$3F_2 + 20F_4$
$K(z^2, x^2-y^2)$	z^2	x^2-y^2	x^2-y^2	z^2	$4F_2 + 15F_4 = J_H(e_g)$
	x^2-y^2	x^2-y^2	z^2	z^2	$4F_2 + 15F_4 = J_H(e_g)$
$K(z^2, xy)$	z^2	xy	xy	z^2	$4F_2 + 15F_4$
$K(z^2, zx)$	z^2	zx	zx	z^2	$F_2 + 30F_4$
$K(z^2, yz)$	z^2	yz	yz	z^2	$F_2 + 30F_4$
$K(x^2-y^2, xy)$	x^2-y^2	xy	xy	x^2-y^2	$35F_4$
	zx	z^2	zx	x^2-y^2	$-2\sqrt{3}F_2 + 10\sqrt{3}F_4$
	yz	z^2	yz	x^2-y^2	$2\sqrt{3}F_2 - 10\sqrt{3}F_4$
	zx	zx	z^2	x^2-y^2	$\sqrt{3}F_2 - 5\sqrt{3}F_4$
	yz	yz	z^2	x^2-y^2	$-\sqrt{3}F_2 + 5\sqrt{3}F_4$
	z^2	zx	zx	x^2-y^2	$\sqrt{3}F_2 - 5\sqrt{3}F_4$
	x^2-y^2	xy	yz	zx	$-\sqrt{3}F_2 + 5\sqrt{3}F_4$

(II) Matrix elements for operators that change the number of occupied states within the t_{2g} and e_g levels by one:

a	b	c	d	$\langle ab\|1/r_{12}\|cd\rangle$
z^2	xy	zx	yz	$\sqrt{3}F_2 - 5\sqrt{3}F_4$
z^2	xy	yz	zx	$\sqrt{3}F_2 - 5\sqrt{3}F_4$
z^2	zx	xy	yz	$-2\sqrt{3}F_2 + 10\sqrt{3}F_4$
z^2	yz	zx	xy	$\sqrt{3}F_2 - 5\sqrt{3}F_4$
z^2	zx	yz	xy	$\sqrt{3}F_2 - 5\sqrt{3}F_4$
z^2	yz	xy	zx	$-2\sqrt{3}F_2 + 10\sqrt{3}F_4$
x^2-y^2	xy	zx	yz	$3F_2 - 15F_4$
x^2-y^2	xy	yz	zx	$-3F_2 + 15F_4$
x^2-y^2	yz	zx	xy	$3F_2 - 15F_4$
x^2-y^2	zx	yz	xy	$-3F_2 + 15F_4$

(III) Matrix elements for operators that change the number of occupied states within the t_{2g} and e_g levels by two:

a	b	c	d	$\langle ab\|1/r_{12}\|cd\rangle$
zx	zx	z^2	x^2-y^2	$\sqrt{3}F_2 - 5\sqrt{3}F_4$
zx	zx	x^2-y^2	z^2	$-\sqrt{3}F_2 + 5\sqrt{3}F_4$
yz	yz	z^2	x^2-y^2	$\sqrt{3}F_2 - 5\sqrt{3}F_4$
yz	yz	x^2-y^2	z^2	$-\sqrt{3}F_2 + 5\sqrt{3}F_4$
x^2-y^2	x^2-y^2	zx	zx	$2F_2 + 20F_4$
x^2-y^2	x^2-y^2	yz	yz	$2F_2 + 20F_4$
x^2-y^2	x^2-y^2	xy	xy	$35F_4$
z^2	z^2	zx	zx	$F_2 + 30F_4$
z^2	z^2	yz	yz	$F_2 + 30F_4$
z^2	z^2	xyz	xy	$4F_2 + 15F_4$

A.2 The hopping integrals

Hopping integrals for ss-, sp-, sd-, pd-, and dd-hopping using the Slater–Koster parameters [197]:

$E_{s,s}$	$(ss\sigma)$
$E_{s,x}$	$l(sp\sigma)$
$E_{x,x}$	$l^2(pp\sigma) + (1-l^2)(pp\pi)$
$E_{x,y}$	$lm(pp\sigma) - lm(pp\pi)$
$E_{x,z}$	$ln(pp\sigma) - ln(pp\pi)$
$E_{s,xy}$	$\sqrt{3}(sd\sigma)$
E_{s,x^2-y^2}	$\frac{1}{2}\sqrt{3}(l^2-m^2)(sd\sigma)$
$E_{s,3z^2-r^2}$	$[n^2 - \frac{1}{2}(l^2+m^2)](sd\sigma)$
$E_{x,xy}$	$\sqrt{3}l^2m(pd\sigma) + m(1-2l^2)(pd\pi)$
$E_{x,yz}$	$\sqrt{3}lmn(pd\sigma) - 2lmn(pd\pi)$
$E_{x,zx}$	$\sqrt{3}l^2n(pd\sigma) + n(1-2l^2)(pd\pi)$
E_{x,x^2-y^2}	$\frac{1}{2}\sqrt{3}l(l^2-m^2)(pd\sigma) + l(1-l^2-m^2)(pd\pi)$
E_{y,x^2-y^2}	$\frac{1}{2}\sqrt{3}m(l^2-m^2)(pd\sigma) - m(1+l^2-m^2)(pd\pi)$
E_{z,x^2-y^2}	$\frac{1}{2}\sqrt{3}n(l^2-m^2)(pd\sigma) - n(l^2-m^2)(pd\pi)$
$E_{x,3z^2-r^2}$	$l[n^2 - \frac{1}{2}(l^2+m^2)](pd\sigma) - \sqrt{3}ln^2(pd\pi)$
$E_{y,3z^2-r^2}$	$m[n^2 - \frac{1}{2}(l^2+m^2)](pd\sigma) - \sqrt{3}mn^2(pd\pi)$
$E_{z,3z^2-r^2}$	$n[n^2 - \frac{1}{2}(l^2+m^2)](pd\sigma) + \sqrt{3}n(l^2+m^2)(pd\pi)$
$E_{xy,xy}$	$3l^2m^2(dd\sigma) + (l^2+m^2-4l^2m^2)(dd\pi) + (n^2+l^2m^2)(dd\delta)$
$E_{xy,yz}$	$3lm^2n(dd\sigma) + ln(1-4m^2)(dd\pi) + ln(m^2-1)(dd\delta)$
$E_{xy,zx}$	$3l^2mn(dd\sigma) + mn(1-4l^2)(dd\pi) + mn(l^2-1)(dd\delta)$
E_{xy,x^2-y^2}	$\frac{3}{2}lm(l^2-m^2)(dd\sigma) + 2lm(m^2-l^2)(dd\pi) + \frac{1}{2}lm(l^2-m^2)(dd\delta)$
E_{yz,x^2-y^2}	$\frac{3}{2}mn(l^2-m^2)(dd\sigma) - mn[1+2(l^2-m^2)](dd\pi) + mn[1+\frac{1}{2}(l^2-m^2)](dd\delta)$
E_{zx,x^2-y^2}	$\frac{3}{2}nl(l^2-m^2)(dd\sigma) + nl[1-2(l^2-m^2)](dd\pi) - nl[1-\frac{1}{2}(l^2-m^2)](dd\delta)$
$E_{xy,3z^2-r^2}$	$\sqrt{3}lm[n^2-\frac{1}{2}(l^2+m^2)](dd\sigma) - 2\sqrt{3}lmn^2(dd\pi) + \frac{1}{2}\sqrt{3}lm(1+n^2)](dd\delta)$
$E_{yz,3z^2-r^2}$	$\sqrt{3}mn[n^2 - \frac{1}{2}(l^2+m^2)](dd\sigma) + \sqrt{3}mn(l^2+m^2-n^2)(dd\pi) - \frac{1}{2}\sqrt{3}mn(l^2+n^2)](dd\delta)$
$E_{zx,3z^2-r^2}$	$\sqrt{3}ln[n^2-\frac{1}{2}(l^2+m^2)](dd\sigma) + \sqrt{3}ln(l^2+m^2-n^2)(dd\pi) - \frac{1}{2}\sqrt{3}ln(l^2+n^2)](dd\delta)$
$E_{x^2-y^2,x^2-y^2}$	$\frac{3}{4}(l^2-m^2)^2(dd\sigma) + [l^2+m^2-(l^2-m^2)^2](dd\pi) + [n^2+\frac{1}{4}(l^2-m^2)^2](dd\delta)$
$E_{x^2-y^2,3z^2-r^2}$	$\frac{1}{2}\sqrt{3}(l^2-m^2)[n^2-\frac{1}{2}(l^2+m^2)](dd\sigma) + \sqrt{3}n^2(m^2-l^2)(dd\pi) + \frac{1}{4}\sqrt{3}(1+n^2)(l^2-m^2)](dd\delta)$
$E_{3z^2-r^2,3z^2-r^2}$	$[n^2 - \frac{1}{2}(l^2+m^2)]^2(dd\sigma) + 3n^2(l^2+m^2)(dd\pi) + \frac{3}{4}(l^2+m^2)^2(dd\delta)$

A.3 The Hamiltonian concerning d-d interaction

The complete Hamiltonian concerning the $d-d$ interactions. It is $U_d = F_0 + 4F_2 + 36F_4$, $J_{H,t_{2g}} = 3F_2 - 20F_4$, $J_{H,e_g} = 4F_2 + 15F_4$, $\lambda_1 = \sqrt{3}(F_2 - 5F_4)$, $\lambda_2 = F_0 - 2F_2 - 4F_4)$, $\lambda_3 = F_0 + 4F_2 - 34F_4$, $\lambda_4 = F_0 + 2F_2 - 24F_4$, $\lambda_5 = F_0 - 4F_2 + 6F_4$, $\lambda_6 = 3F_2 + 20F_4$, $\lambda_7 = 35F_4$, $\lambda_8 = F_2 + 30F_4$, and $\lambda_9 = 4F_2 + 15F_4$.

$$
\begin{aligned}
\mathcal{H}_{dd} \;=\; & \\
& U_d\big(n_{xy,\uparrow}n_{xy,\downarrow} + n_{yz,\uparrow}n_{yz,\downarrow} + n_{zx,\uparrow}n_{zx,\downarrow} + n_{x^2-y^2,\uparrow}n_{x^2-y^2,\downarrow} + n_{3z^2-r^2,\uparrow}n_{3z^2-r^2,\downarrow}\big) + \\
& (U_d - 2J_{H,e_g}) \sum_{\sigma_1}\sum_{\sigma_2} n_{x^2-y^2,\sigma_1}n_{3z^2-r^2,\sigma_2} + \\
& \frac{J_{H,e_g}}{2} \sum_{\sigma_1}\sum_{\sigma_2} \big(d^+_{x^2-y^2,\sigma_1}d^+_{3z^2-r^2,\sigma_2}d_{x^2-y^2,\sigma_2}d_{3z^2-r^2,\sigma_1} + h.c.\big) + \\
& J_{H,e_g}\big(d^+_{x^2-y^2,\uparrow}d^+_{x^2-y^2,\downarrow}d_{3z^2-r^2,\downarrow}d_{3z^2-r^2,\uparrow} + h.c.\big) + \\
& (U_d - 2J_{H,t_{2g}}) \sum_{\sigma_1}\sum_{\sigma_2} \big(n_{xy,\sigma_1}n_{yz,\sigma_2} + n_{xy,\sigma_1}n_{zx,\sigma_2} + n_{yz,\sigma_1}n_{zx,\sigma_2}\big) + \\
& \frac{J_{H,t_{2g}}}{2}\big(d^+_{xy,\sigma_1}d^+_{yz,\sigma_2}d_{xy,\sigma_2}d_{yz,\sigma_1} + d^+_{yz,\sigma_1}d^+_{zx,\sigma_2}d_{yz,\sigma_2}d_{zx,\sigma_1} + \\
& \qquad d^+_{xy,\sigma_1}d^+_{zx,\sigma_2}d_{xy,\sigma_2}d_{zx,\sigma_1} + h.c.\big) + \\
& J_{H,t_{2g}}\big(d^+_{xy,\uparrow}d^+_{xy,\downarrow}d_{yz,\downarrow}d_{yz,\uparrow} + d^+_{yz,\uparrow}d^+_{yz,\downarrow}d_{zx,\downarrow}d_{zx,\uparrow} + d^+_{zx,\uparrow}d^+_{zx,\downarrow}d_{yz,\downarrow}d_{yz,\uparrow} + h.c.\big) - \\
& 2\lambda_1 \sum_{\sigma_1}\sum_{\sigma_2} \big(n_{zx,\sigma_1} - n_{yz,\sigma_1}\big)\big(d^+_{3z^2-r^2,\sigma_2}d_{x^2-y^2,\sigma_2} + d^+_{x^2-y^2,\sigma_2}d_{3z^2-r^2,\sigma_2}\big) + \\
& \lambda_2 \sum_{\sigma_1}\sum_{\sigma_2} \big(n_{x^2-y^2,\sigma_1}(n_{zx,\sigma_2} + n_{yz,\sigma_2})\big) + \lambda_3 \sum_{\sigma_1}\sum_{\sigma_2} \big(n_{x^2-y^2,\sigma_1}n_{xy,\sigma_2}\big) + \\
& \lambda_4 \sum_{\sigma_1}\sum_{\sigma_2} \big(n_{3z^2-r^2,\sigma_1}(n_{zx,\sigma_2} + n_{yz,\sigma_2})\big) + \lambda_5 \sum_{\sigma_1}\sum_{\sigma_2} \big(n_{3z^2-r^2,\sigma_1}n_{xy,\sigma_2}\big) + \\
& \lambda_6 \sum_{\sigma_1}\sum_{\sigma_2} \big(d^+_{x^2-y^2,\sigma_1}d^+_{zx,\sigma_2}d_{x^2-y^2,\sigma_2}d_{zx,\sigma_1} + d^+_{x^2-y^2,\sigma_1}d^+_{yz,\sigma_2}d_{x^2-y^2,\sigma_2}d_{yz,\sigma_1}\big) + \\
& \lambda_7 \sum_{\sigma_1}\sum_{\sigma_2} \big(d^+_{x^2-y^2,\sigma_1}d^+_{xy,\sigma_2}d_{x^2-y^2,\sigma_2}d_{xy,\sigma_1}\big) + \\
& \lambda_8 \sum_{\sigma_1}\sum_{\sigma_2} \big(d^+_{3z^2-r^2,\sigma_1}d^+_{zx,\sigma_2}d_{3z^2-r^2,\sigma_2}d_{zx,\sigma_1} + d^+_{3z^2-r^2,\sigma_1}d^+_{yz,\sigma_2}d_{3z^2-r^2,\sigma_2}d_{yz,\sigma_1}\big) + \\
& \lambda_9 \sum_{\sigma_1}\sum_{\sigma_2} \big(d^+_{3z^2-r^2,\sigma_1}d^+_{xy,\sigma_2}d_{3z^2-r^2,\sigma_2}d_{xy,\sigma_1}\big) +
\end{aligned}
$$

$$
\begin{aligned}
&\lambda_1 \sum_{\sigma_1}\sum_{\sigma_2} \big(d^+_{3z^2-r^2,\sigma_1} d^+_{zx,\sigma_2} d_{x^2-y^2,\sigma_2} d_{zx,\sigma_1} + d^+_{x^2-y^2,\sigma_1} d^+_{zx,\sigma_2} d_{3z^2-r^2,\sigma_2} d_{zx,\sigma_1} - \\
&\qquad\qquad d^+_{3z^2-r^2,\sigma_1} d^+_{yz,\sigma_2} d_{x^2-y^2,\sigma_2} d_{yz,\sigma_1} - d^+_{x^2-y^2,\sigma_1} d^+_{yz,\sigma_2} d_{3z^2-r^2,\sigma_2} d_{yz,\sigma_1}\big) + \\
&\lambda_1\big((d^+_{zx,\uparrow} d^+_{zx,\downarrow} - d^+_{yz,\uparrow} d^+_{yz,\downarrow})(d_{x^2-y^2,\downarrow} d_{3z^2-r^2,\uparrow} - d_{x^2-y^2,\uparrow} d_{3z^2-r^2,\downarrow}) + \\
&(d^+_{3z^2-r^2,\uparrow} d^+_{x^2-y^2,\downarrow} - d_{3z^2-r^2,\downarrow} d_{x^2-y^2,\uparrow})(d_{zx,\downarrow} d^+_{zx,\uparrow} - d_{yz,\downarrow} d^+_{yz,\uparrow})\big) + \\
&\lambda_6\big(d^+_{x^2-y^2,\uparrow} d^+_{x^2-y^2,\downarrow}(d_{zx,\downarrow} d_{zx,\uparrow} + d_{yz,\downarrow} d_{yz,\uparrow}) + (d^+_{zx,\uparrow} d^+_{zx,\downarrow} + d^+_{yz,\uparrow} d^+_{yz,\downarrow}) d_{x^2-y^2,\downarrow} d_{x^2-y^2,\uparrow}\big) + \\
&\lambda_8\big(d^+_{3z^2-r^2,\uparrow} d^+_{3z^2-r^2,\downarrow}(d_{zx,\downarrow} d_{zx,\uparrow} + d_{yz,\downarrow} d_{yz,\uparrow}) + (d^+_{zx,\uparrow} d^+_{zx,\downarrow} + d^+_{yz,\uparrow} d^+_{yz,\downarrow}) d_{3z^2-r^2,\downarrow} d_{3z^2-r^2,\uparrow}\big) + \\
&\lambda_7\big(d^+_{xy,\uparrow} d^+_{xy,\downarrow} d_{x^2-y^2,\downarrow} d_{x^2-y^2,\uparrow} + h.c.\big) + \\
&\lambda_9\big(d^+_{xy,\uparrow} d^+_{xy,\downarrow} d_{3z^2-r^2,\downarrow} d_{3z^2-r^2,\uparrow} + h.c.\big) + \\
&\lambda_1 \sum_{\sigma_1}\sum_{\sigma_2} \big(d^+_{3z^2-r^2,\sigma_1} d^+_{xy,\sigma_2}(d_{yz,\sigma_2} d_{zx,\sigma_1} + d_{zx,\sigma_2} d_{yz,\sigma_1}) + \\
&d^+_{3z^2-r^2,\sigma_1} d^+_{yz,\sigma_2} d_{xy,\sigma_2} d_{zx,\sigma_1} + d^+_{3z^2-r^2,\sigma_1} d^+_{zx,\sigma_2} d_{xy,\sigma_2} d_{yz,\sigma_1} + h.c.\big) - \\
&2\lambda_1 \sum_{\sigma_1}\sum_{\sigma_2} \big(d^+_{3z^2-r^2,\sigma_1} d^+_{zx,\sigma_2} d_{yz,\sigma_2} d_{xy,\sigma_1} - d^+_{3z^2-r^2,\sigma_1} d^+_{yz,\sigma_2} d_{zx,\sigma_2} d_{xy,\sigma_1} + h.c.\big) - \\
&\sqrt{3}\lambda_1 \sum_{\sigma_1}\sum_{\sigma_2} \big(d^+_{x^2-y^2,\sigma_1} d^+_{xy,\sigma_2}(d_{zx,\sigma_2} d_{yz,\sigma_1} - d_{yz,\sigma_2} d_{zx,\sigma_1}) + \\
&d^+_{x^2-y^2,\sigma_1} d^+_{yz,\sigma_2} d_{xy,\sigma_2} d_{zx,\sigma_1} - d^+_{x^2-y^2,\sigma_1} d^+_{zx,\sigma_2} d_{xy,\sigma_2} d_{yz,\sigma_1} + h.c.\big)
\end{aligned}
$$

A.4 Clebsch-Gordon coefficiants

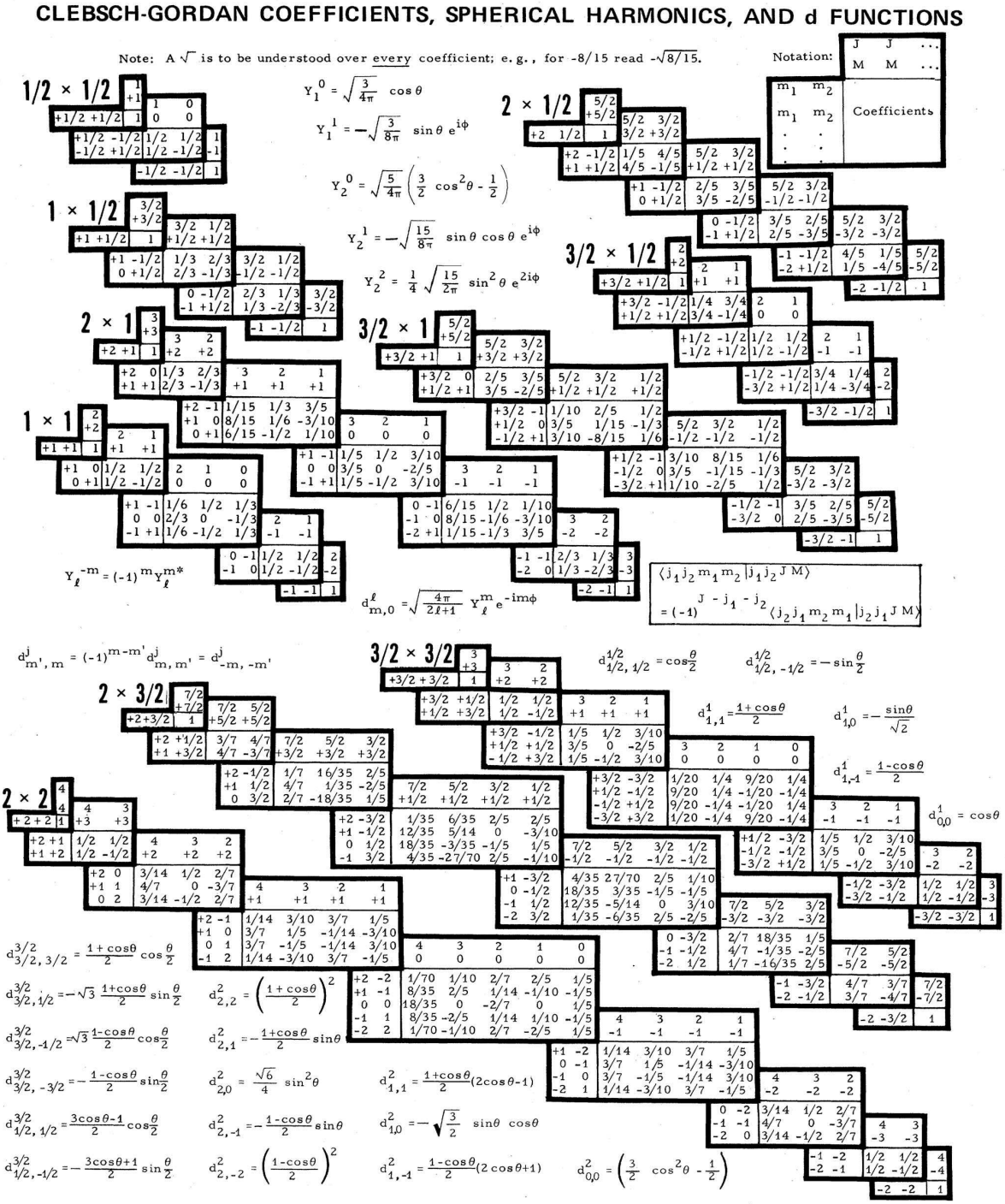

Figure A.1: Taken from T.G. Trippe *et al.*, Reviews of Modern Physics **84** S1 (1976), "Review of particle properties (Particle Data Group)", page S36 [224]

Bibliography

[1] B.T. Thole, R.D. Cowan, G.A. Sawatzky, J. Fink, and J.C. Fuggle. *Phys. Rev. B* **31**, 6856 (1985).

[2] G. van der Laan, C. Westra, C.Haas, and G.A. Sawatzky. *Phys. Rev. B* **23**, 4369 (1981).

[3] G. v.d. Laan, B.T. Thole, G.A. Sawatzky, and M. Verdaguer. *Phys. Rev. B* **37**, 6587 (1988).

[4] P. Kuiper, G. Kruizinga, J. Ghijsen, G.A. Sawatzky, and H. Verweij. *Phys. Rev. Lett.* **62**, 221 (1989).

[5] H. Eskes, M.B.J. Meinders, and G.A. Sawatzky. *Phys. Rev. Lett.* **67**, 1035 (1991).

[6] R.H. Potze, G.A. Sawatzky, and M. Abbate. *Phys. Rev. B* **51**, 11501 (1995).

[7] M. Abbate, J.C. Fuggle, A. Fujimori, L.H. Tjeng, C.T. Chen, R. Potze, G.A. Sawatzky, H. Eisaki, and S. Uchida. *Phys. Rev. B* **47**, 16124 (1993).

[8] M. Abbate, R.H. Potze, G.A. Sawatzky, and A. Fujimori. *Phys. Rev. B* **49**, 7210 (1994).

[9] J. Stöhr. *NEXAFS Spectroscopy.* Springer Series in Surface Science, Vol. 25, Springer Berlin. 1992.

[10] J. Fink, N. Nücker, E. Pellegrin, H. Romberg, M. Alexander, and M. Knupfer. *J. Electron Spectrosc. Relat. Phenom.* **6**, 395 (1994).

[11] M. Kielwein. Dissertation, TU Desden 2000.

[12] J. van Elp, J.L. Wieland, H. Eskes, P. Kuiper, G.A. Sawatzky, F.M.F. de Groot, and T.S. Turner. *Phys. Rev. B* **44**, 6090 (1991).

[13] J. Zaanen, G.A. Sawatzky, J. Fink, W. Speier, and J.C. Fuggle. *Phys. Rev. B* **32**, 4905 (1985).

[14] T. Thole, and G. van der Laan. *Phys. Rev. B* **38**, 3158 (1988).

[15] S. Gasiorowicz. *Quantum Physics.* John Wiley and Sons. 1987.

[16] C. Cohen-Tannoudji, B. Diu, and F. Laloë. *Quantum Mechanics.* Wiley-Interscience publication, New York. 1977.

[17] J. Zaanen, C. Westra, and G.A. Sawatzky. *Phys. Rev. B* **33**, 8060 (1986).

[18] F.M.F. de Groot, J.C. Fuggle, B.T. Thole, and G.A. Sawazky. *Phys. Rev. B* **42**, 5459 (1990).

[19] C.T. Chen, L-H. Tjeng, J. Kwo, H.L. Kao, P. Rudolf, F. Sette, and R.M. Flemming. *Phys. Rev. Lett.* **68**, 2543 (1992).

[20] M. Hücker. Dissertation, Universität zu Köln 1999.

[21] R. Klingeler. Dissertation, RWTH Aachen 2003.

[22] T. Kroll. Diploma thesis, RWTH Aachen 2003.

[23] R. Bouchard. *Synchrotron Radiation News* **5**, 90 (1998).

[24] C. Giacovazzo, H.L. Monaco, D. Viterbo, F. Scordari, G. Gilli, G. Zanotti, and M. Catti. *Fundamentals of Cristallography.* International Union of Crystallography, Oxford University Press. 1998.

[25] J.J. Sakurai. *Advanced Quantum Mechanics.* Series in Advanced, Addison-Wesley. 1967.

[26] S.W. Lovesey, and S.P. Collins. *X-ray scattering and Absorption by Magnetic Materials.* Oxford Series and Synchrotron Radiation, Clarendon Press-Oxford. 1996.

[27] J. Geck. Dissertation, RWTH Aachen 2004.

[28] S. Kiele. Dissertation, TU Desden 2006.

[29] U.E. Condon, and G.H. Shortley. *Theory of Atomic Spectra.* Cambridge University Press, Cambridge and New York. 1935.

[30] W.A. Harrison. *Electron Structure and the Properties of Solids.* Freeman, San Francisco. 1980.

[31] C.L. Ballhausen. *Introduction to Ligand Field Theory.* McGraw-Hill Series in Advanced Chemistry. 1962.

[32] J.W. Negele, and H. Orland. *Quantum Many-Particle Systems.* Addison-Wesley, New York. 1988.

[33] J.C. Slater. *Quantum Theory of Matter.* McGraw-Hill Book Company. 1951.

[34] L.D. Landau, and E.M. Lifshitz. *Quantum Mechanics.* Butterworth-Heinemann. 1958.

[35] J.F. Cornwell. *Group theory in physics.* Academic Press, London. 1984.

[36] M. Tinkham. *Group Theory and Quantum Mechanics.* McGraw-Hill. 1964.

[37] I. Terasaki, Y. Sasago, and K. Uchinokura. *Phys. Rev. B* **56**, 12685 (1997).

[38] I. Terasaki, I. Tsukada, and Y. Iguchi. *Phys. Rev. B* **65**, 195106 (2002).

[39] M. Mikami, M. Yoshimura, Y. Mori, T. Sasaki, R. Funahashi, and M. Shikano. *Jpn. J. Appl. Phys.* **42**, 7383 (2003).

[40] K. Takada, H. Sakurai, E. Takayama-Muromachi, F. Izumi, R. Dilanian, and T. Sasaki. *Nature* **422**, 53 (2003).

[41] M. von Jansen, and R. Hoppe. *Z. Anorg. Allg. Chem.* **408**, 104 (1974).

[42] J.W. Lynn, Q. Huang, C.M. Brown, V.L. Miller, M.L. Foo, R.E. Schaak, C.Y. Jones, E.A. Mackey, and R.J. Cava. *Phys. Rev. B* **68**, 214516 (2003).

[43] J.D. Jorgensen, M. Avdeev, D.G. Hinks, J.C. Burley, and S. Short. *Phys. Rev. B* **68**, 214517 (2003).

[44] D.P. Chen, H.C. Chen, A. Maljuk, A. Kulakov, H. Zhang, P. Lemmens, and C.T. Lin. *Phys. Rev. B* **70**, 024506 (2004).

[45] T. Motohashi, E. Naujalis, R. Ueda, K. Isawa, M. Karppinen, and H. Yamauchi. *Appl. Phys. Lett.* **79**, 1480 (2001).

[46] T. Tanaka, S. Nakamura, and S. Iida. *Jpn. J. Appl. Phys.* **33**, L581–L582 (1994).

[47] R. Funahashi, I. Matsubara, H. Ikuta, T. Takeuchi, U. Mizutani, and S. Sodeoka. *Jpn. J. Appl. Phys.* **39**, Part 2, L1127 (2000).

[48] A.C. Masset, C.Michel, A. Maignan, M. Hervieu, O. Toulemonde, F. Studer, B. Raveau, and J. Hejtmanek. *Phys. Rev. B* **62**, 166 (2000).

[49] Y. Miyazaki, K. Kudo, M. Akoshima, Y. Ono, Y. Koike, and T. Kajitani. *Jpn. J. Appl. Phys.* **39**, Part 2, L531 (2000).

[50] S. Lambert, H. Leligny, and D. Grebille. *J. Solid state Chem.* **160**, 491 (2001).

[51] T. Yamamoto, I. Tsukada, K. Uchinokura, M. Takagi, T. Tsubone, M. Ichihara, and K. Kobayashi. *Jpn. J. Appl. Phys.* **39**, Part 2, L747 (2000).

[52] I. Tsukada, T. Yamamoto, M. Takagi, T. Tsubone, S. Konno, and K. Uchinokura. *J. Phys. Soc. Jpn.* **70**, 834 (2001).

[53] P.M. Chaikin, and G. Beni. *Phys. Rev. B* **13**, 647 (1976).

[54] R.R. Heikes, and R.W. Ure Jr. *Thermoelectricity: Science and Engineering.* Interscience Publishers, New York-London. 1961.

[55] W. Koshibae, K. Tsutsui, and S. Maekawa. *Phys. Rev. B* **62**, 6869 (2000).

[56] Y. Wang, N.S. Rogado, R.J. Cava, and N.P. Ong. *Nature* **423**, 425 (2003).

[57] D.J. Singh. *Phys. Rev. B* **61**, 13397 (2000).

[58] R. Ray, A. Ghoshray, and K. Ghoshray. *Phys. Rev. B* **59**, 9454 (2003).

[59] J.D. Jorgensen, M. Avdeev, D.G. Hinks, P.W. Barnes, and S. Short. *Phys. Rev. B* **72**, 224515 (2005).

[60] Q. Huang, B. Khaykovich, F.C. Chou, J.H. Cho, J.W. Lynn, and Y. S. Lee. *Phys. Rev. B* **70**, 134115 (2004).

[61] Q. Huang, M.L. Foo, R.A. Pascal Jr., J.W. Lynn, B.H. Toby, Tao He, H.W. Zandbergen, and R.J. Cava. *Phys. Rev. B* **70**, 184110 (2004).

[62] S.P. Bayrakci, C. Bernhard, D.P. Chen, B. Keimer, R.K. Kremer, P. Lemmens, C.T. Lin, C. Niedermayer, and J. Strempfer. *Phys. Rev. B* **69**, 100410 (2004).

[63] M. L. Foo, Y. Wang, S. Watauchi, H. W. Zandbergen, T. He, R. J. Cava, and N. P. Ong. *Phys. Rev. Lett.* **92**, 247001 (2004).

[64] T. Motohashi, R. Ueda, E. Naujalis, T. Tojo, I. Terasaki, T. Atake, M. Karppinen, and H. Yamauchi. *Phys. Rev. B* **67**, 064406 (2003).

[65] J. Sugiyama, J.H. Brewer, E.J. Ansaldo, B. Hitti, M. Mikami, Y. Mori, and T. Sasaki. *Phys. Rev. B* **69**, 214423 (2004).

[66] D. Prabhakaran, A.T. Boothroyd, R. Coldea, and N.R. Charnley. *J. Cryst. Growth.* **271**, 74 (2004).

[67] J.L. Luo, N.L. Wang, G.T. Liu, D. Wu, X.N. Jing, F. Hu, and T. Xiang. *Phys. Rev. Lett.* **93**, 187203 (2004).

[68] F.C. Chou, J.H. Cho, P.A. Lee, E.T. Abel, K. Matan, and Y.S. Lee. *Phys. Rev. Lett.* **92**, 157004 (2004).

[69] M.N. Iliev, A.P. Litvinchuk, R.L. Meng, Y.Y. Sun, J. Cmaidalka, and C.W. Chu. *Physica C* **402**, 239 (2004).

[70] J. Tarabek. Dissertation, TU Desden 2004.

[71] C. Delmas, J.-J. Braconnier, C. Fouassier, and P. Hagemuller. *Solid State Ionics* **3/4**, 165–169 (1981).

[72] R.E. Schaak, T. Klimczuk, M.L. Foo, and R.J. Cava. *Nature* **424**, 527 (2003).

[73] O.I. Motrunich, and P.A. Lee. *Phys. Rev. B* **70**, 024514 (2004).

[74] J. Kunes, K.-W. Lee, and W.E. Picket. *New Challenges in Superconductivity: Experimental Advances and Emerging Theories* edited by J. Ashkenazi, M.V. Eremin, J. L. Cohn, I. Eremin, D. Manske, D. Pavuna, and F. Zuo (Kluwer Academic, Boston, 2004), 235–242 (2003).

[75] I.R. Mukhamedchine, H. Alloul, G. Collin, and N. Blanchard. *Phys. Rev. Lett.* **93**, 167601 (2004).

[76] H.W. Zandbergen, M. Foo, Q. Xu, V. Kumar, and R.J. Cava. *Phys. Rev. B* **70**, 024101 (2004).

[77] K. Ishida, Y. Ihara, Y. Maeno, C. Michioka, M. Kato, K. Yoshimura, K. Takada, T. Sasaki, H. Sakurai, and E. Takayama-Muromachi. *J. Phys. Soc. Jpn.* **72**, 3041 (2003).

[78] R. Jin, B.C. Sales, P. Khalifah, and D. Mandrus. *Phys. Rev. Lett.* **91**, 217001 (2003).

[79] T. Fujimoto, G.Q. Zheng, Y. Kitaoka, R.L. Meng, J. Cmaidalka, and C.W. Chu. *Phys. Rev. Lett.* **92**, 047004 (2004).

[80] W. Higemoto, K. Ohishi, A. Koda, R. Kadono, K. Ishida, K. Takada, H. Sakurai, E. Takayama-Muromachi, and T. Sasaki. *Phys.Rev. B* **70**, 134508 (2004).

[81] M. Kato, C. Michioka, T. Waki, Y. Itoh, K. Yoshimura, K. Ishida, H Sakurai, E. Takayama-Muromachi, K. Takada, and T. Sasaki. *J. Phys.: Condens. Matter* **18**, 669 (2006).

[82] P.W. Anderson. *Science* **235**, 1196 (1987).

[83] G. Baskaran. *Phys. Rev. Lett.* **91**, 097003 (2003).

[84] B. Kumar, and B.S. Shastry. *Phys. Rev. B* **68**, 104508 (2003).

[85] M. Ogata. *J. Phys. Soc. Jpn.* **72**, 1839 (2003).

[86] C. Honerkamp. *Phys. Rev. B* **68**, 104510 (2003).

[87] Q.H. Wang, D.H. Lee, and P.A. Lee. *Phys. Rev. B* **69**, 092504 (2004).

[88] Y. Kobayashi, H. Watanbe, M. Yokoi, T. Moyoshi, Y. Mori, and M. Sato. *J. Phys. Soc. Jpn.* **74**, 1800 (2005).

[89] A. Tanaka, and X. Hu. *Phys. Rev. Lett.* **91**, 257006 (2003).

[90] H. Ikeda, Y. Nisikawa, and K. Yamada. *J. Phys. Soc. Jpn.* **73**, 17 (2004).

[91] Y. Tanaka, Y. Yanase, and M. Ogata. *J. Phys. Soc. Jpn.* **73**, 319 (2004).

[92] A. Kanigel, A. Keren, L. Patlagan, K.B. Chashka, P. King, and A. Amato. *Phys. Rev. Lett.* **92**, 257007 (2004).

[93] D.J. Singh. *Phys. Rev. B* **68**, 020503 (2003).

[94] M.D. Johannes, I.I. Mazin, D.J. Singh, and D.A. Papaconstantopoulos. *Phys. Rev. Lett.* **93**, 097005 (2004).

[95] M.Z. Hasan, Y.D. Chuang, A.P. Kuprin, Y. Kong, D. Qian, Y.W. Li, B.L. Mesler, Z. Hussain, A.V. Fedorov, R. Kimmerling, E. Rotenberg, H. Koh, M. Rogado, M.L. Foo, and R.J. Cava. *Phys. Rev. Lett.* **92**, 246402 (2004).

[96] H.B. Yang, S.C. Wang, A.K.P. Sekharan, H. Matsui, S. Souma, T. Sato, T. Takahashi, T. Takeuchi, J.C. Campuzano, R. Jin B.C. Sales, D. Mandrus, Z. Wang, and H. Ding. *Phys. Rev. Lett.* **92**, 246403 (2004).

[97] H.B. Yang, Z.-H. Pan, A.K.P. Sekharan, T. Sato, S. Souma, T. Takahashi, R. Jin, B.C. Sales, D. Mandrus, A.V. Fedorov, Z. Wang, and H. Ding. *Phys. Rev. Lett.* **95**, 146401 (2005).

[98] A.T. Boothroyd, R. Coldea, D.A. Tennant, D. Prabhakaran, L.M. Helme, and C.D. Frost. *Phys. Rev. Lett.* **92**, 197201 (2004).

[99] S.P. Bayrakci, I. Mirebeau, P. Bourges, Y. Sidis, M. Enderle, J. Mesot, D.P. Chen, C.T. Lin, and B. Keimer. *Phys. Rev. Lett.* **94**, 157205 (2005).

[100] K. Takada, K. Fukuda, M. Osada, I. Nakai, F. Izumi, R.A. Dilanian, K. Kato, M. Takata, H. Sakurai, E. Takayama-Muromachi, and T. Sasaki. *J. Mater. Chem.* **14**, 1448 (2004).

[101] C.J. Milne, D.N. Argyriou, A. Chemseddine, N. Aliouane, J. Veira, and D. Alber. *Phys. Rev. Lett.* **93**, 247007 (2004).

[102] P.W. Barnes, M. Avdeev, J.D. Jorgensen, D.G. Hinks, H. Claus, and S. Short. *Phys. Rev. B* **72**, 134515 (2005).

[103] H. Sakurai, N. Tsujii, O. Suzuki, H. Kitazawa, G. Kido, K. Takada, T. Sasaki, and E. Takayama-Muromachi. *Phys. Rev. B* **74**, 092502 (2006).

[104] H. Sakurai, K. Takada, T. Sasaki, and E. Takayama-Muromachi. *J. Phys. Soc. Jpn.* **74**, 2909 (2005).

[105] Y. Ihara, K. Ishida, C. Michioka, M. Kato, K. Yoshimura, K. Takada, T. Sasaki, H. Sakurai, and E. Takayama-Muromachi. *J. Phys. Soc. Jpn.* **74**, 867 (2005).

[106] G. Gasparovic, R.A. Ott, J.-H. Cho, F.C. Chou, Y. Chu, J.W. Lynn, and Y.S. Lee. *Phys. Rev. Lett.* **96**, 046403 (2006).

[107] Q. Huang, M.L. Foo, J.W. Lynn, H.W. Zandbergen, G. Lawes, Y. Wang, B.H. Toby, A.P. Ramirez, N.P. Ong, and R.J. Cava. *Journal of physics: Condensed matter* **16**, 5803 (2004).

[108] N.L. Wang, Dong Wu, G. Li, X.H. Chen, C.H. Wang, and X.G. Luo. *Phys. Rev. Lett.* **93**, 147403 (2004).

[109] F.C. Chou, J.H. Cho, and Y.S. Lee. *Phys. Rev. B* **70**, 144526 (2004).

[110] M. Yokoi, T. Moyoshi, Y. Kobayashi, M. Soda, Y. Yasui, M. Sato, and K. Kakurai. *J. Phys. Soc. Jpn.* **74**, 3046 (2005).

[111] L. Balicas, M. Abdel-Jawad, N.E. Hussey, F.C. Chou, and P.A. Lee. *Phys. Rev. Lett.* **94**, 236402 (2005).

[112] K.W. Lee, J. Kunes, and W.E. Pickett. *Phys. Rev. B* **70**, 045104 (2004).

[113] T.-P. Choy, D. Galanakis, and P. Phillips. *cond-mat/* (2005).

[114] A.J. Williams, J.P. Attfield, M.L. Foo, L. Viciu, and R. J. Cava. *Phys. Rev. B* **73**, 134401 (2006).

[115] P. Zhang, R.B. Capaz, M.L. Cohen, and S.G. Louie. *Phys. Rev. B* **71**, 153102 (2005).

[116] P. Zhang, W. Luo, V.H. Crespi, M.L. Cohen, and S.G. Louie. *Phys. Rev. B* **70**, 085108 (2004).

[117] M. Roger, D.J.P. Morris, D.A. Tennant, M.J.Gutmann, J.P. Goff, D.Prabhakaran, N. Shannon, B.Lake, R. Coldea, and P.P. Deen. *Cond-mat/* 0507040 (2005).

[118] M. Roger, D.J.P. Morris, D.A. Tennant, M.J. Gutmann, J.P. Goff, D. Prabhakaran, N. Shannon, B. Lake, A.T. Boothroyd, R. Coldea, and P. Deen. *Cond-mat/* 0510468 (2005).

[119] H. Eschrig, and K. Koepernik. accepted at Physica C.

[120] J.L. Gavilano, D. Rau, B. Pedrini, J. Hinderer, H.R. Ott, S. Kazakov, and J. Karpinski. *Phys. Rev. B* **69**, 100404(R) (2004).

[121] P. Carretta, M. Mariani, C.B. Azzoni, M.C. Mozzati, I. Bradaric, I. Savic, A. Feher, and J. Sebek. *Phys. Rev. B* **70**, 024409 (2004).

[122] G. Caimi, L. Degiorgi, H. Berger, N. Barisic, L. Forró, and F. Bussy. *Eur. Phys. J. B* **40**, 231 (2004).

[123] S.Y. Li, L. Taillefer, D.G. Hawthorn, M.A. Tanatar, J. Paglione, M. Sutherland, R.W. Hill, C.H. Wang, and X.H. Chen. *Phys. Rev. Lett.* **93**, 056401 (2004).

[124] M. Brühwiler, B. Batlogg, S.M. Kazakov, and J. Karpinski. *Physica B: Condensed Matter* **378**, 630 (2006).

[125] J. Geck, M. v. Zimmermann, H. Berger, S.V. Borisenko, H. Eschrig, K. Koepernik, M. Knupfer, and B. Büchner. *Phys. Rev. Lett.* **97**, 106403 (2006).

[126] Y.S. Meng, A. Van der Ven, M.K.Y. Chan, and G. Ceder. *Phys. Rev. B* **72**, 172103 (2005).

[127] J. Geck (University of British Columbia, Vancouver, Canada). *private communication.*

[128] Y. Ono, R. Ishikawa, Y. Miyazaki, and T. Kajitani. *J. Phys. Soc. Jpn.* **70**, 235 (2001).

[129] J. Sugiyama, J.H. Brewer, E.J. Ansaldo, H. Itahara, T. Tani, M. Mikami, Y. Mori, T. Sasaki, S. Hebert, and A. Maignan. *Phys. Rev. Lett.* **92**, 017602 (2004).

[130] S. Hébert, S. Lambert, D. Pelloquin, and A. Maignan. *Phys. Rev. B* **64**, 172101 (2001).

[131] A. Maignan, S. Hébert, D. Pelloquin, C. Michel, and J. Hejtmanek. *J. Appl. Phys.* **92**, 1964 (2002).

[132] D. Pelloquin, A. Maignan, S. Hébert, C. Michel, and B. Raveau. *J. Solid State Chem.* **170**, 374 (2003).

[133] J. Sugiyama, H. Itahara, T. Tani, J.H. Brewer, and E.J. Ansaldo. *Phys. Rev. B* **68**, 134423 (2002).

[134] J. Sugiyama, J.H. Brewer, E.J. Ansaldo, H. Itahara, K. Dohmae, Y. Seno, C. Xia, and T. Tani. *Phys. Rev. B* **68**, 134423 (2003).

[135] I. Tomeno, and M. Oguchi. *J. Phys. Soc. Jpn.* **67**, 318 (1998).

[136] J. Sugiyama, H. Itahara, J.H. Brewer, E.J. Ansaldo, T. Motohashi, M. Karppinen, and H. Yamauchi. *Phys. Rev. B* **67**, 214420 (2003).

[137] K.M. Kojima, Y. Fudamoto, M. Larkin, G.M. Luke, J.Merrin, B. Nachumi, Y.J. Uemura, Y. Ajiro, A. Revcolevschi, and J.-P. Renard. *Phys. Rev. Lett.* **79**, 503 (1997).

[138] C. Bernhard, A.V. Boris, N.N. Kovaleva, G. Khaliullin, A. Pimenov, L. Yu, D.P. Chen, C.T. Lin, and B. Keimer. *Phys. Rev. Lett.* **93**, 167003 (2004).

[139] O. Toulemonde, N. N'Guyen, F. Studer, and A. Traverse. *Journal of Solid State Chemistry* **158**, 208–217 (2001).

[140] C. Zobel, M. Kriener, D. Bruns, J. Baier, M. Grüninger, T. Lorenz, P. Reutler, and A. Revcolevschi. *Phys. Rev. B* **66**, 020402 (2002).

[141] S. Yamaguchi, Y. Okimoto, H. Taniguchi, and Y. Tokura. *Phys. Rev. B* **53**, R2926 (1996).

[142] S. Yamaguchi, Y. Okimoto, and Y. Tokura. *Phys. Rev. B* **55**, R8666 (1997).

[143] N.N. Loshkareva, E.A. Ganshina, B.I. Belevtsev, Y.P. Sukhorukov, E.V. Mostovshchikova, A.N. Vinogradov, V.B. Krasovitsky, and I.N. Chukanova. *Phys. Rev. B* **68**, 024413 (2003).

[144] L.M. Helme, A.T. Boothroyd, R. Coldea, D. Prabhakaran, D.A. Tennant, A. Hiess, and J. Kulda. *Phys. Rev. Lett.* **94**, 157206 (2005).

[145] M.D. Johannes, I.I. Mazin, and D.J. Singh. *Phys. Rev. B* **71**, 214410 (2005).

[146] L.M. Helme, A.T. Boothroyd, R. Coldea, and D. Prabhakaran. *Phys. Rev. B* **73**, 054405 (2006).

[147] J.M. Tranquada, G. Shirane, B. Keimer, S. Shamoto, and M. Sato. *Phys. Rev. B* **40**, 4503 (1989).

[148] T. Kroll, M. Knupfer, J. Geck, C. Hess, T. Schwieger, G. Krabbes, C. Sekar, D.R. Batchelor, H. Berger, and B. Büchner. *Phys. Rev. B* **74**, 115123 (2006).

[149] P. Monthoux, and G.G. Lonzarich. *Phys. Rev. B* **59**, 14598 (1999).

[150] P. Monthoux, and G.G. Lonzarich. *Phys. Rev. B* **63**, 054529 (2001).

[151] T. Moriya, and K. Ueda. *Rep. Prog. Phys.* **66**, 1299 (2003).

[152] J. Geck, P. Wochner, D. Bruns, B. Büchner, U. Gebhardt, S. Kiele, P. Reutler, and A. Revcolevschi. *Phys. Rev. B* **69**, 104413 (2004).

[153] J.M. Luttinger, and J.C. Ward. *Phys. Rev.* **118**, 1417 (1969).

[154] A. Chainani, T. Yokoya, Y. Takata, K. Tamasaku, M. Taguchi, T. Shimojima, N. Kamakura, K. Horiba, S. Tsuda, S. Shin, D. Miwa, Y. Nishino, T. Ishikawa, M. Yabashi, K. Kobayashi, H. Namatame, M. Taniguchi, K. Takada, T. Sasaki, H. Sakurai, and E. Takayama-Muromachi. *Phys. Rev. B* **69**, 180508 (2004).

[155] J. Zaanen, G.A. Sawatzky, and J.W. Allen. *Phys. Rev. Lett.* **55**, 418 (1985).

[156] V.I. Anisimov, J. Zaanen, and O.K. Anderson. *Phys. Rev. B* **44**, 943 (1991).

[157] P. Zhang, W. Luo, M.L. Cohen, and S.G. Louie. *Phys. Rev. Lett.* **93**, 236402 (2004).

[158] J. Ni, and G.M. Zhang. *Phys. Rev. B* **69**, 214503 (2004).

[159] W. Koshibae, and S. Maekawa. *Phys. Rev. Lett.* **91**, 257003 (2003).

[160] A. Bourgeois, A.A. Aligia, T. Kroll, and M.D. Núñez-Regueiro. *cond-mat/* 0610173, submitted to Phys. Rev. Lett. (2006).

[161] A. Ferraz, E. Kochetov, and M. Mierzejewski. *Phys. Rev. B* **73**, 064516 (2006).

[162] M. Mochizuki, Y. Yanasa, and M. Ogata. *Phys. Rev. Lett.* **94**, 147005 (2005).

[163] Y. Yanase, M. Mochizuki, and M. Ogata. *J. Phys. Soc. Jpn.* **74**, 430 (2005).

[164] Z. Li, J. Yang, J.G. Hou, and Q. Zhu. *Phys. Rev. B* **71**, 024502 (2005).

[165] W.B. Wu, D.J. Huang, J. Okamoto, A. Tanaka, H.J. Lin, F.C. Chou, A. Fujimori, and C.T. Chen. *Phys. Rev. Lett.* **94**, 146402 (2005).

[166] M. Indergand, Y. Yamashita, H. Kusunose, and M. Sigrist. *Phys. Rev. B* **71**, 214414 (2005).

[167] M.D. Johannes, and D.J. Singh. *Phys. Rev. B* **70**, 014507 (2004).

[168] H. Rosner, S.-L. Drechsler, G. Fuchs, A. Handstein, A. Wälte, and K.H. Müller. *Braz. Jour. Phys.* **33**, 718 (2003).

[169] V.V. Poltavets, M. Croft, and M. Greenblatt. *Phys. Rev. B* **74**, 125103 (2006).

[170] B.C. Sales, R. Jin, K.A. Affholter, P. Khalifah, G.M. Veith, and D. Mandrus. *Phys. Rev. B* **70**, 174419 (2004).

[171] C. Sekar *et al.* (unpublished).

[172] G.A. Sawatzky. *in Solid State Chemistry 1982, Proceeding of the 2nd European Conference, Veldhoven, Netherlands, 1982,* edited by R. Metselaar, H.J.M. Heijligers, and J. Schoonman, Studies in inorganic Chemistry Vol. 3 (Elsevier, Amsterdam, 1983).

[173] H. Eskes, and G.A. Sawatzky. *Phys. Rev. B* **43**, 119 (1991).

[174] T. Böske, O. Knauff, R. Neudert, M. Kielwein, M. Knupfer, J. Fink, H. Eisaki, S. Uchida, K. Okada, and A. Kotani. *Phys. Rev. B* **56**, 3438 (1997).

[175] F.M.F. de Groot, M. Grioni, J.C. Fuggle, J. Ghijsen, G. A. Sawatzky, and H. Petersen. *Phys. Rev. B* **40**, 5715 (1989).

[176] F.M.F. de Groot. *Coordination Chemistry Reviews* **249**, 31 (2005).

[177] W.D. Johnston, R.R. Heikes, and D. Sestrich. *J. Phys. Chem. Solids* **7**, 1 (1958).

[178] J. van Elp, J.L. Wieland, H. Eskes, P. Kuiper, G.A. Sawatzky, F.M.F. de Groot, and T.S. Turner. *Phys. Rev. B* **44**, 6090 (1991).

[179] T. Kroll, A.A. Aligia, and G.A. Sawatzky. *Phys. Rev. B* **74**, 115124 (2006).

[180] Z. Hu, G. Kaindl, S.A. Warda, D. Reinen, F.M.F. de Groot, and B.G. Muller. *Chemical Physics* **232**, 63 (1998).

[181] Z. Hu, H. Wu, M.W. Haverkort, H.H. Hsieh, H.-J. Lin, T. Lorenz, J. Baier, A. Reichl, I. Bonn, C. Felser, A. Tanaka, C.T. Chen, , and L.H. Tjeng. *Phys. Rev. Lett.* **92**, 207402 (2004).

[182] T. Mizokawa, L.H. Tjeng, H.-J. Lin, C.T. Chen, R. Kitawaki, I. Terasaki, S. Lambert, and C. Michel. *Phys. Rev. B* **71**, 193107 (2005).

[183] M. Kubota, K. Takada, T. Sasaki, H. Kumigashira, J. Okabayashi, M. Oshima, M. Suzuki, N. Kawamura, M. Takagaki, K. Fukuda, and K. Ono. *Phys. Rev. B* **70**, 012508 (2004).

[184] M. Haverkort (University of Cologne, Germany). *private communication.*

[185] D.G. Hawthorn, and J. Geck (University of British Columbia, Vancouver, Canada). *private communication.*

[186] M.S. Hybertsen, E.B. Stechel, W.M.C. Foulkes, and M. Schlüter. *Phys. Rev. B* **45**, 10032 (1992).

[187] F.C. Zhang, and T.M. Rice. *Phys. Rev. B* **37**, 3759 (1988).

[188] H. Eskes, and G.A. Sawatzky. *Phys. Rev. Lett.* **61**, 221 (1988).

[189] A.A. Aligia, M.E. Simon, and C.D. Batista. *Phys. Rev. B* **49**, 13061 (1994).

[190] L.F. Feiner, J.H., Jefferson, and R. Raimondi. *Phys. Rev. B* **53**, 8751 (1996).

[191] M.E. Simon, A.A. Aligia, and E.R. Gagliano. *Phys. Rev. B* **56**, 5637 (1997).

[192] T. Kroll, R. Klingeler, J. Geck, B. Büchner, W. Selke, M. Hücker, and A. Gukasov. *Jour. of Magnetism and Magnetic Materials* **290**, 306 (2005).

[193] C.D. Batista, A.A. Aligia, and J. Eroles. *Europhys. Lett.* **43**, 71 (1998).

[194] P. Petrone, and A.A. Aligia. *Phys. Rev. B* **66**, 104418 (2002).

[195] K.W. Blazey, and K.A. Müller. *J. Phys. C* **16**, 5491 (1983).

[196] G. Khaliullin, W. Koshibae, and S. Maekawa. *Phys. Rev. Lett.* **93**, 176401 (2004).

[197] J.C. Slater, and G.F. Koster. *Phys. Rev.* **94**, 1498 (1954).

[198] R.R. Sharma. *Phys. Rev. B* **19**, 2813 (1979).

[199] Y. Kakehashi, and A. Kotani. *Phys. Rev. B* **29**, 4292 (1984).

[200] J.W. Negele, and H. Orland. *Quantum Many-Particle Systems* (Addison–Wesley, New York, 1988).

[201] A.A. Aligia, and M.A. Gusmão. *Phys. Rev. B* **70**, 054403 (2004).

[202] T. Tohyama, and S. Maekawa. *J. Phys. Soc. Jpn.* **60**, 53 (1991).

[203] K. Okada, and A. Kotani. *J. Phys. Soc. Jpn.* **66**, 341 (1997).

[204] R. Neudert, S.-L. Drechsler, J. Malek, H. Rosner, M. Kielwein, Z. Hu, M. Knupfer, M. S. Golden, J. Fink, N. Nücker, M. Merz, S. Schuppler, N. Motoyama, H. Eisaki, S. Uchida, M. Domke, and G. Kaindl. *Phys. Rev. B* **62**, 010752 (2000).

[205] G. Lang, J. Bobroff, H. Alloul, P. Mendels, N. Blanchard, and G. Collin. *Phys. Rev. B* **72**, 094404 (2005).

[206] S. Landron, and M.-B. Lepetit. *Phys. Rev. B* **74**, 184507 (2006).

[207] *Atomic Energy Levels* edited by C.E. Moore (MBS, Washington D.C., 1958).

[208] M. Karppinen, I. Asako, T. Motohashi, and H. Yamauchi. *Phys. Rev. B* **71**, 92105 (2005).

[209] G.A. Sawatzky, and A. Lenselink. *Chem. Physica* **72**, 3748 (1980).

[210] M. Feiner. *Phys. Rev. B* **48**, 16857 (1993).

[211] M.E. Simon, A.A. Aligia, C.D. Batista, E. Gagliano, and F. Lema. *Phys. Rev. B* **54**, R3780 (1996).

[212] F. Lema, and A.A. Aligia. *Phys. Rev. B* **55**, 14092 (1997).

[213] J.M. Eroles, C.D. Batista, and A.A. Aligia. *Phys. Rev. B* **59**, 14092 (1999).

[214] W. Gawelda, M. Johnson, F.M.F. de Groot, R. Abela, C. Bressler, and M. Chergui. *Jour. Am. Chem. Soc.* **128**, 5001 (2006).

[215] T. Xiang, and J.M. Wheatley. *Phys. Rev. B* **54**, R12653 (1996).

[216] V.I. Belinicher, A.L. Chernyshev, and V.A. Shubin. *Phys. Rev. B* **54**, 14914 (1996).

[217] O.P. Sushkov, G.A. Sawatzky, R. Eder, and H. Eskes. *Phys. Rev. B* **56**, 11769 (1997).

[218] S. Rigamonti, C.R. Proetto, and F.A. Reboredo. *Europhys. Lett.* **70**, 116 (2005).

[219] S. Zhou, M. Gao, H. Ding, P.A. Lee, and Z. Wang. *Phys. Rev. Lett.* **94**, 206401 (2005).

[220] H. Ishida, M.D. Johannes, and A. Liebsch. *Phys. Rev. Lett.* **94**, 196401 (2005).

[221] D.J. Singh, and D. Kasinathan. *Phys. Rev. Lett.* **97**, 016404 (2006).

[222] G. Kotliar, and A.E. Ruckenstein. *Phys. Rev. Lett.* **57**, 1362 (1986).

[223] R. Frésard, and G. Kotliar. *Phys. Rev. B* **61**, 52909 (1997).

[224] T.G. Trippe, A. Barbaro-Galtieri, R.L. Kelly, A. Rittenberg, A.H. Rosenfeld, G.P. Yost, N. Barash-Schmidt, C. Bricman, R.J. Hemingway, M.J. Losty, M. Roos, V. Chaloupka, and B. Armstrong. *Rev. Mod. Phys.* **48**, S1–S245 (1976).

List of Publications

1. *Ising magnets with mobile defects*,
   W. Selke, V.L. Pokrovsky, B. Büchner, and T. Kroll,
   The European Physical Journal B **30**, 83-92 (2002)

2. *Magnetism of low-doped spin chains in* $La_x(Sr,Ca)_{14-x}Cu_{24}O_{41}$,
   T. Kroll, R. Klingeler, J. Geck, B. Büchner, W. Selke, M. Hücker, and A. Gukasov,
   Journal of Magnetism and Magnetic Materials 290–291 (2005) 306–309

3. *X-ray absorption spectroscopy of* Na_xCoO_2 *layered cobaltates*,
   T. Kroll, M. Knupfer, J. Geck, C. Hess, T. Schwieger, G. Krabbes, C. Sekar, D. R. Batchelor, H. Berger, and B. Büchner,
   Physical Review B **74**, 115123 (2006)

4. *Polarization dependence of X-ray absorption spectra of* Na_xCoO_2*: Electronic structure from cluster calculations*,
   T. Kroll, A.A. Aligia, and G.A. Sawatzky,
   Physical Review B **74**, 115124 (2006)

5. *Quasiparticle dispersion near the Fermi surface in* Na_xCoO_2,
   A. Bourgeois, A.A. Aligia, T. Kroll, and M.D. Núñez-Regueiro
   accepted at Physica C; cond-mat/0609759

6. *Spectroscopic investigations on layered sodium cobaltates*,
   T. Kroll, A.A. Aligia, M. Knupfer, J. Geck, C. Hess, T. Schwieger, G. Krabbes, C. Sekar, D.R. Batchelor, H. Berger, G.A. Sawatzky, and B. Büchner
   accepted at Physica C

7. *Electronic structure and Fermi surface tolopogy of* Na_xCoO_2,
   A. Bourgeois, A.A. Aligia, T. Kroll, and M.D. Núñez-Regueiro
   submitted to Physical Review Letters; cond-mat/0610173

Experimental reports:

1. *Doping dependence of magnetic excitations in* $(La,Ca,Sr)_{14}Cu_24O_{41}$
   R. Klingeler, J. Geck, T. Kroll, B. Büchner, and M. Enderle
   Institut Laue Langevin, Grenoble, Experimental report No. 4-03-1288 (2003)

2. *$La \leq 5(Sr, Ca) \leq 9Cu_{24}O_{41}$: A 1D toy model for hole doped cuprates*
R. Klingeler, A. Gukasov, T. Kroll, J. Geck, M. Hücker, U. Ammerahl, A. Revcolevschi, B. Büchner
Laboratoire Léon Brillouin, Saclay, Experimental report (2003)

3. *X-ray absorption spectroscopy on layered cobaltates*
T. Kroll, J. Geck, C. Hess, T. Schwieger, G. Krabbes, C. Sekar, D. Batchelor, M. Knupfer, J. Fink, and B. Büchner
Bessy - Annual report 2004

Acknowledgements

This thesis could not have been written without the help of numerous people. For one person the field is way too large and complicated. Physics is teamwork, the better the team, the better the work.

I would like to thank the people I worked with for all their help and patience. First of all, its Bernd Büchner I have to thank, who convinced me to come to Dresden to the IFW and placed me into the right group. Furthermore, I had his support when going abroad, and it seems that he wrote a good report for the DAAD proposal. I am more than grateful for this possibility. While I was in Dresden he was a good source of inspiration, and the times we really discussed the data, it was truly fruitful.

After about one year at the IFW, I got the opportunity to go to Armando A. Aligia in Bariloche, Argentina. During the six month I spent there, I learned so much and started to understand so much more about things I did before. I am very thankful for his incredible patience for my non–understanding and all his explanations until I grasped the point. I am still amazed by his knowledge, insight and talent in physics and many other things. Thanks a lot, Armando!

Leaving Bariloche after that summer the next destination was Vancouver, Canada, (summer again!) right into the AMPEL institute and the group of George A. Sawatzky. What we started in Bariloche, has been finished (almost) in Vancouver. It was an amazing experience to work with George. What I learned from Armando I had to discuss with George and I had to justify what I did. And again, I learned so much about the theory and the experiments. The hours in his office discussing the data and solid state physics in general were more than a great source of help and inspiration for me.

Also the time with the whole group in Vancouver was great. Mainly I worked with David Hawthorn and I have to say that it was real fun to work with him. I had a great time in Vancouver because I had a great group to work with, beside David, it was mainly Andrea Damascelli, Ilya Elfimov, Suman Hossain and Kyle Shen, but also my room mates at the 4th floor office, Sujay and Leandro, as well as Ryan down the corridor.
Now Jochen Geck is part of the group in Vancouver and I hope he enjoys it as much as I did. We had some cool beamtimes together, and I am thankful for all his explanations and help.

Back in Dresden, I would like to thank Martin Knupfer for his open office (the door was literally open) and his will to answer my questions almost whenever I had one.

After returning to Dresden I am sharing a room with Ingo Hellmann and almost the first thing we did was buying a (large) black board for our room. Since then we constantly use it to think about little problems and vividly discuss it. Learning is nice, but if you cannot discuss about it, it is quickly forgotten. Furthermore, I would like to thank the people in Dresden for the good atmosphere, especially Hajo Grafe for his hospitality and the cool barbecues, and Hajo, I loved it having Döner at your place, Thomas Pichler for the good Tennis matches and his help with some experimental details, as well as the people from the 4th floor room Hendrik Rauf, Eva Borowiak-Palen, Xianje Liu, and Kati Biedermann, and also Mark Rümmeli, Andreas Koitsch, and Torsten Schwieger for a good working atmosphere and lots of cake. Roland Hübel is a great help when it comes to technical and computer problems, together with Herr Stefan Leger, Ronny Schönfelder, and Kerstin Müller. Christian Hess and Rüdiger Klingeler were always willing to answer questions and give remarks. I would also like to thank the people in my actual room in the 2nd floor for the good atmosphere, namely Gregory Schorsch Urbanik, Ingo Hellmann, Sergei Biryukov, Anderi Sotnikov, and Uwe Schaufuss.

But also away from Dresden there are some people who deserve to be thanked for their help. These are the beamline scientists we worked with, namely David Batchelor (Bessy, Berlin), Jonathan Dendlinger (ALS, Berkeley), Martin v. Zimmermann (DESY, Hamburg) and Ralf Feyerherm (Bessy, HMI, Berlin). Last but not least, I am happy that I went to Frank de Groot's multiplet course in Berkeley, California, and got some inside into the cluster program of Cowan and T. Thole. I am really thankful for his continuous help for me and my little problems with the input files. It is a pitty that the trigonal distortion project did not lead to the result I hoped it would.

As a direct consequence of our work in Bariloche I met Antonin Bourgeois who also visited Armando in Bariloche. It was really cool meeting him here in Dresden on the M^2S. I hope we can do something together sometime in the future.

Writing a thesis is a tough work and English can be a difficult language, so I am very thankful for all the people who helped me with the corrections, especially my Dad for the erasure of most of my mistakes in the writing.

My schedule for handing in this thesis was rather tight, but it finally worked out, but only because of Kat's help with some of the figures (sometimes converting a figure into good quality .eps can be a drama). Thank you so much for that and so much more!

Versicherung

Die vorliegende Arbeit wurde unter Betreuung von Prof. Dr. Bernd Büchner am Institut für Festkörperforschung (IFF) des Leibniz–Instituts für Festkörper- und Werkstoffforschung Dresden (IFW Dresden) angefertigt. Teile dieser Dissertation wurden im Rahmen eines DAAD Stipendiums im Centro Atomico Bariloche, Bariloche, Argentinien, bei Prof. Dr. Armando A. Aligia und im Advanced Materials and Process Engineering Laboratory (AMPEL) an der University of British Columbia, Vancouver, Canada, bei Prof. Dr. George A. Sawatzky durchgeführt.

Hiermit versichere ich, dass ich die vorliegende Arbeit ohne unzulässige Hilfe Dritter und ohne Benutzung anderer als der angegebenen Hilfsmittel angefertigt habe; die aus fremden Quellen direkt oder indirekt übernommenen Gedanken sind als solche kenntlich gemacht. Die Arbeit wurde bisher weder im Inland noch im Ausland in gleicher oder in ähnlicher Form einer anderen Prüfungsbehörde vorgelegt.

Die Promotionsordnung der Technischen Universität Dresden erkenne ich hiermit an.